CFD Investigations on Sluice Gate Flows with Application of the Momentum Balance for Discharge Computations

Michael Steppert

Vollständiger Abdruck der von der Fakultät für Bauingenieurwesen und Umweltwissenschaften der Universität der Bundeswehr München zur Erlangung des akademischen Grades eines

Doktor-Ingenieurs (Dr.-Ing.)

genehmigten Dissertation.

Gutachter:

Univ.-Prof. Dr.-Ing. Andreas Malcherek
Universität der Bundeswehr München
Fakultät für Bauingenieurwesen und Umweltwissenschaften
Institut für Wasserwesen

Prof. Dr.-Ing. Philipp Epple
Hochschule Coburg
Fakultät Maschinenbau und Automobiltechnik
Strömungsmechanik und Strömungsmaschinen

Die Dissertation wurde am 14.12.2022 bei der Universität der Bundeswehr München eingereicht und durch die Fakultät für Bauingenieurwesen und Umweltwissenschaften am 11.07.2023 angenommen. Die mündliche Prüfung fand am 16.08.2023 statt.

Acknowledgements

First of all, I would like to thank Prof. Dr.-Ing. Andreas Malcherek, Department of Civil Engineering and Environmental Sciences, Institute of Hydrosciences Bundeswehr University Munich for taking over the supervision of the doctoral thesis as well as the review of this work. It was an exciting task for me to work on this topic of hydraulic engineering as a mechanical engineer. The work could be described as interdisciplinary, whereby the connection is fluid mechanics, whose laws of course apply to hydraulic engineering problems as well as to mechanical engineering problems.

I would also like to thank Prof. Dr.-Ing. Philipp Epple for his willingness to supervise the work on the part of Coburg University of Applied Sciences and for reviewing this work. It was Prof. Dr. Philipp Epple who first brought the idea of a doctorate to my attention and put me in contact with Prof. Dr.-Ing. Andreas Malcherek. He has always motivated me with his passion for fluid mechanics and provided me with the necessary expertise to write this scientific thesis.

This thesis was written cooperatively with the Bundeswehr University Munich during my work at Coburg University of Applied Sciences at the Faculty of Mechanical and Automotive Engineering.

I would like to thank my colleagues at the Institute of Hydrosciences Bundeswehr University Munich and my colleagues at the Faculty of Mechanical and Automotive Engineering at Coburg University, who always provided me with advice and support and created a pleasant working environment, thus contributing to the success of this work.

Finally, I would like to thank my family and friends for their support during the writing of this dissertation and for their understanding that I was not always available at that time.

Abstract

In this work, sluice gate flows are investigated in detail using CFD simulations and an approach based on the integral momentum balance is elaborated for the calculation of the discharge under standard and inclined sluice gates. For this purpose, different control volumes are first analyzed and rated. To solve the momentum balance of the most suitable control volume, the pressure forces at the control volume boundaries in the upstream region, at the sluice gate wall and at the sluice gate opening as well as the momentum coefficients at the control volume boundaries in the headwater and at the sluice gate opening are required. To determine these, CFD simulations are first performed and analyzed for common relative gate opening heights ε and angles of inclination α. To determine the pressure forces, the pressure distributions from the CFD simulations are parameterized as a function of relative sluice gate opening and angle of inclination. By integrating the parameterized pressure distributions, it is then possible to determine the pressure forces relevant for the integral momentum balance as a function of the relative sluice gate opening and the angle of inclination. The momentum coefficients are also first determined from the CFD simulations and then parameterized as a function of the relative sluice gate opening and angle of inclination.

With the parameterization formulas for pressure forces and momentum coefficients determined in this way, the discharge of standard and inclined sluice gates can be calculated with the aid of the integral momentum balance. The plausibility of the approach was confirmed by comparison with measured values and calculations available in the relevant literature.

The pressure distributions and momentum coefficients, initially assumed to be constant across the width, are further investigated for the 3D case for different relative sluice gate widths. Deviations in the pressure distributions and velocity profiles were found due to three-dimensional flow structures, which in previous work were shown to be constant across the width. Likewise, for very narrow sluice gates, the ever-increasing influence of the frictional forces of the sidewalls was found. To take these 3D effects into account in the momentum balance, a 3D coefficient is introduced. With this coefficient, accurate calculations can be made for narrow sluice gates where 3D effects are relevant.

Kurzfassung

In dieser Arbeit werden Schützströmungen anhand von CFD Simulationen detailliert untersucht und ein auf der integralen Impulsbilanz basierender Ansatz zur Berechnung des Durchflusses unter senkrechten und geneigten Schützen wird ausgearbeitet. Hierzu werden zunächst verschiedene Kontrollvolumen analysiert und bewertet. Zur Lösung der Impulsbilanz des am besten geeigneten Kontrollvolumens, werden die Druckkräfte an den Kontrollvolumengrenzen im Oberwasser, der Schütztafel und an der Schützöffnung sowie die Impulsbeiwerte an den Kontrollvolumengrenzen im Oberwasser und an der Schützöffnung benötigt. Um diese zu ermitteln, werden zunächst CFD Simulationen für gängige relative Schützöffnungshöhen ε und Neigungswinkel α durchgeführt und analysiert. Um die Druckkräfte zu ermitteln, werden die Druckverteilungen aus den CFD Simulationen in Abhängigkeit der relativen Schützöffnung und des Neigungswinkels parametrisiert. Durch Integration der parametrisierten Druckverteilungen können anschließend die für die integrale Impulsbilanz relevanten Druckkräfte in Abhängigkeit der relativen Schützöffnung und des Neigungswinkels ermittelt werden. Die Impulsbeiwerte werden auch zunächst aus den CFD Simulationen ermittelt und dann in Abhängigkeit der relativen Schützöffnungshöhen und der Neigungswinkel parametrisiert.

Mithilfe der so ermittelten Parametrisierungsformeln für Druckkräfte und Impulsbeiwerte kann der Durchfluss von senkrechten sowie geneigten Schützen mithilfe der integralen Impulsbilanz berechnet werden. Beim Vergleich mit Messwerten und Berechnungen einschlägiger Literatur konnte die Plausibilität/Richtigkeit des Ansatzes bestätigt werden.

Die zunächst als über die Breite konstant angenommenen Druckverteilungen und Impulsbeiwerte werden im Weiteren für den 3D Fall für verschiedene relative Schützbreiten untersucht. Dabei konnten Abweichungen in der Druck- und Geschwindigkeitsverteilung aufgrund von dreidimensionalen Strömungsstrukturen festgestellt werden, die in bisherigen Arbeiten als konstant über die Breite dargestellt wurden. Ebenfalls konnte für sehr schmale Schütze der immer stärker zunehmende Einfluss der Reibungskräfte der Seitenwände festgestellt werden. Um diese 3D Effekte in der Impulsbilanz zu berücksichtigen, wurde ein 3D Koeffizient eingeführt. Mit diesem können auch schmale Schütze, bei denen 3D Effekte relevant sind, genau berechnet werden.

Content

List of Abbreviations

Latin Letters

A	[m²]	surface area
a	[m]	gate opening
B	[m]	channel width
C_c	[-]	contraction coefficient
$c_{D,T}$	[-]	Torricelli discharge coefficient
$c_{D,dB}$	[-]	du Buat discharge coefficient
e	[-]	error
F	[N]	force
g	[kg m/s]	gravitational acceleration
h	[m]	water level
h_p	[m]	pressure head
Δh	[m]	water level increase at gate
H	[m]	energy head
I	[N s]	momentum
k	[-]	fitting parameter
L	[m]	length (dimensional analysis)
l	[m]	length
M	[kg]	mass (dimensional analysis)
m	[kg]	mass
$\dot{m}$	[kg/s]	mass flow rate
n	[-]	fitting exponent
n_{gird}	[-]	fraction of cell edge length
P	[Pa]	dimensionless pressure
p	[Pa]	pressure
p_0	[Pa]	total pressure
Q	[m³/s]	discharge rate
q	[m²/s]	specific discharge
r	[m]	roughness
T	[s]	time (dimensional analysis)
t	[s]	time
U	[m/s]	velocity
u	[m/s]	x-velocity
V or $\cancel{V}$	[m³]	volume
v	[m/s]	y-velocity
w	[m/s]	z-velocity
X	[-]	dimensionless z-coordinate
x	[m]	x-coordinate
y	[m]	y-coordinate
Z	[-]	dimensionless z-coordinate
z	[m]	z-coordinate

Greek Symbols

α	[°]	angle of inclination
β	[-]	momentum coefficient
Δ	[m]	cell edge length
ε	[-]	relative gate opening
ζ	[-]	relative gate width
ϑ	[-]	3D coefficient
Π	[-]	relative pressure force
ρ	[kg/m³]	density
τ	[N/m²]	wall shear stress

Subscripts

a	attached flow
B	bottom
dB	du Buat
D	downstream
e	eddy
G	gate
S	shock
SW	side wall
T	Torricelli
U	upstream
V	viscous
l	limit
x	x-component
O	opening
$0\ or\ \emptyset$	upstream
1	downstream supercritical
2	downstream subcritical
I	downstream supercritical
II	downstream subcritical

Abbreviations

CFD	Computational Fluid Dynamics
CV	Control Volume
DES	Detached Eddy Simulation
$HRIC$	High Resolution Interface Capturing
MB	Momentum Balance
MSE	Mean Squared Error
Para	Parameterization
$RANS$	Reynolds-Averaged Navier-Stokes equations
$RMSE$	Root Mean Squared Error
SSE	Sum of Squared Errors
U$RANS$	Unsteady Reynolds-Averaged Navier-Stokes equations
VOF	Volume of Fluid

1 About Sluice Gates

Sluice gates are control structures in hydraulic engineering that can be used to dam the upstream water level of a channel or river or to regulate the discharge. Figure 1 shows two application examples. Figure 1 a) shows a sluice gate in front of the Jonitzer Mühle in Dessau, Germany, which today houses a hydroelectric power plant. The sluice gate can be used to control the flow of water to the hydroelectric power plant. Another application is shown in Figure 1 b), where the sluice gate is used for irrigation in agriculture.

Figure 1: Application examples for sluice gates a) sluice gate in front of a former mill, now a hydroelectric power plant b) sluice gate for controlling irrigation ditches

The classic sluice gate consists of a flat plate that is immersed in the water. If the gate is arranged perpendicular to the ground, the gate is also referred to as a standard sluice gate. The distance between the bottom and the gate lip is called the opening height a and can be varied by the drive of the sluice gate. Figure 2 a) shows the main dimensions of a sluice gate at free outflow. In the upstream region of the sluice gate, the water level is dammed up to the height h_0. The water flows out through the gate opening with the height a. If the water level h_1 in the tailwater is lower than the opening height a, this is called free outflow, and if the water level in the tailwater is higher than the opening height or gate lip, this is called submerged outflow. In the case of free outflow, a jet contraction forms downstream of the gate edge, the smallest water level is also called vena contracta. The angle between the bottom of the channel and the gate is referred as the angle of inclination α. Figure 2 b) shows an example of the gate flow of a standard sluice gate ($\alpha = 90°$) with free outflow in a laboratory flume. The jet contraction in the tailwater is clearly visible. Another main dimension of the sluice gate is the width B. In a rectangular channel, this also corresponds to the channel width.

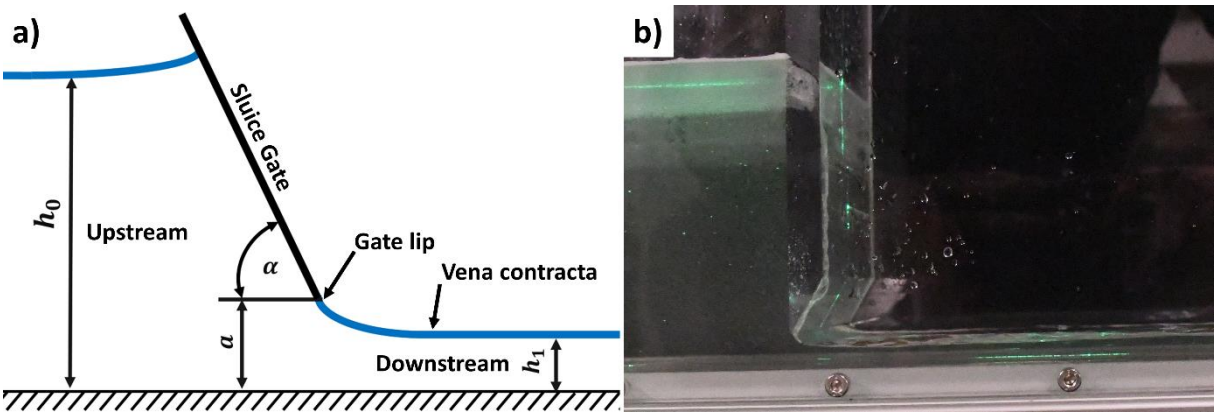

Figure 2: Sluice gate with supercritical outflow a) schematic drawing with main dimensions b) laboratory flume

In Figure 3, the flow for a standard sluice gate was visualized using particles and a laser sheet in a laboratory flume. For different opening heights a, the type of outflow changes. In Figure 3 a) and b) the outflow is submerged. It can be seen, however, that a jet with a jet contraction is nevertheless formed, only underwater. In Figure 3 c) there is still supercritical outflow, but very close to the opening there is a hydraulic jump, the transition from supercritical to subcritical flow. In Figure 3 d) there is also supercritical outflow, but here there is no hydraulic jump in the image. The flow phenomena shown will be described in more detail in the following fundamentals chapter. However, the main focus of this thesis is on the free outflow, as shown in Figure 3 d).

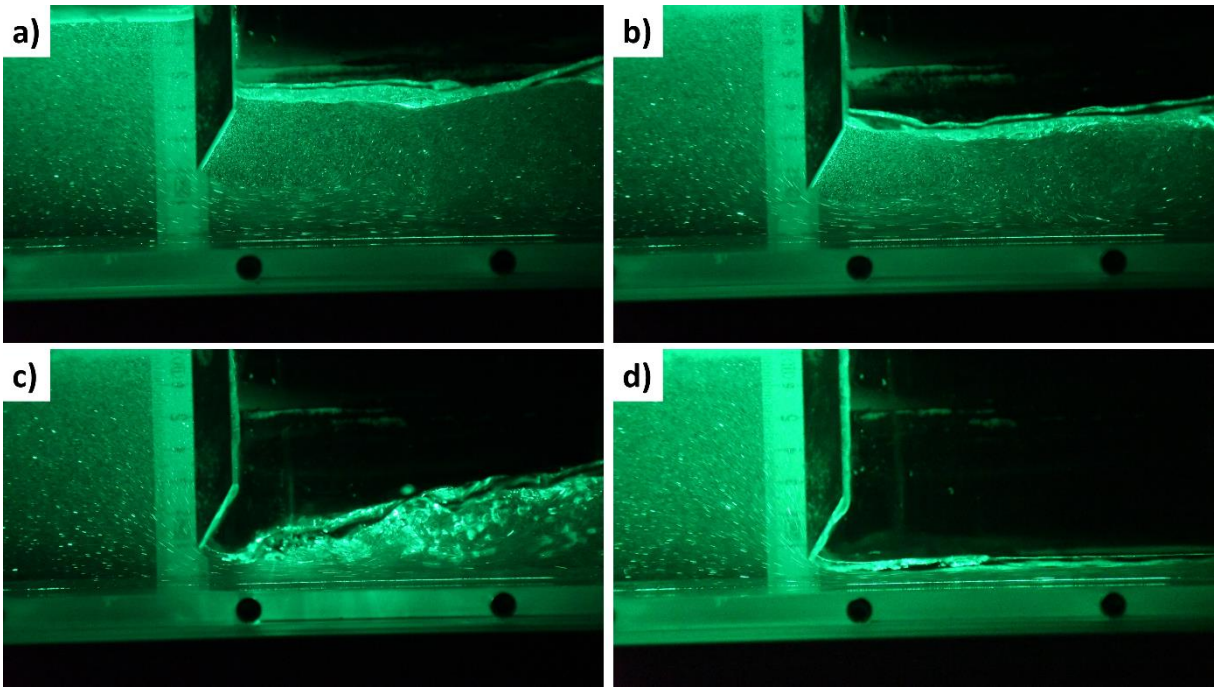

Figure 3: Different types of discharge of a standard sluice gate in a small-scale laboratory flume a) submerged outflow ($a = 20$ mm)b) submerged outflow ($a = 15$ mm)c) free outflow with hydraulic jump ($a = 10$ mm) d) free outflow ($a = 8$ mm)

To control the discharge or the water level, the opening height a can be adjusted on the sluice gates. Figure 4 shows two examples of how the adjustment is performed. In Figure 4 a), the sluice gate is driven by a hand crank, and a gear transmission. At this gate a worm gear first transmits the rotary motion so that less power is needed to drive it. A lantern pinion then converts the rotational motion into the translational lifting motion. The wooden gate is guided in a steel U-profile. Figure 4 b) shows a newer sluice gate with electrical drive. The gate is moved by an electric motor with worm gear in order to change the opening height a. In this case, a trapezoidal-threaded spindle is used to convert the rotational movement into the lifting movement. The bearing of the steel gate is implemented by U-profiles made of steel.

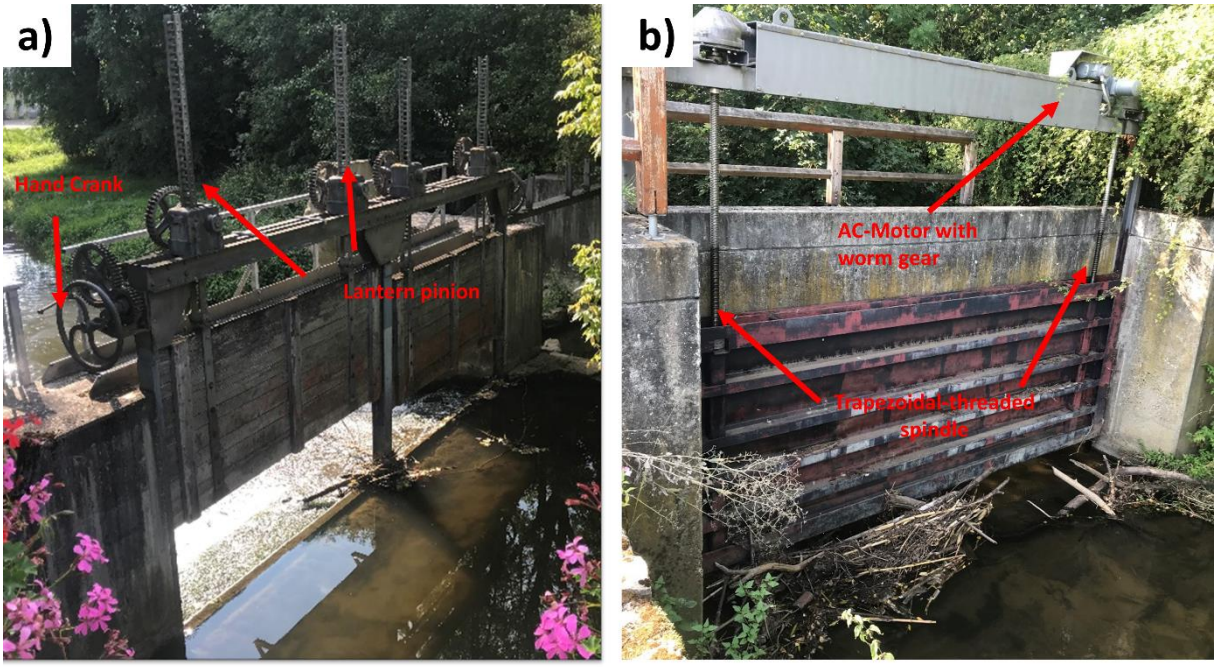

Figure 4: Standard sluice gate a) with hand crank and lantern pinion b) with AC-Motor and trapezoidal-threaded spindle

The preceding pages are intended to provide a general overview of sluice gate design and application examples. The core of this work is the fluid mechanics analysis of sluice gates using computational fluid dynamics (CFD) simulations to investigate a new calculation approach for the discharge under sluice gates with free outflow based on the conservation of mass and momentum, whereby the basic approach, the calculation of the discharge of sluice gates by momentum balance, has already been carried out with simplified pressure distributions by Malcherek [1].

A further elaboration of the calculation approach for sluice gate flows on the basis of the momentum balance is necessary, since for the calculation of sluice gate flows in most textbooks a theory based on the Torricelli outflow velocity derived from the Bernoulli equation

is used, which leads to incorrect results for the calculation of sluice gate flows and must therefore be corrected by an outflow coefficient. However, incorrect use of the Bernoulli equation for fluid mechanics problems is not uncommon. The best known is the widely used explanation for the lift of airfoils, see [2], where it is wrongly assumed that the flow splits at the leading edge of the airfoil and meets again at the trailing edge at the same time (same transit time assumption). The path at the upper side of the airfoil is longer than at the lower side. Based on the same transit time assumption, the Bernoulli equation is used to describe a pressure difference between the upper and lower side of the airfoil. The argumentation with the Bernoulli equation using the same transit time is wrong. In fact, the flow along the upper path, reaches the trailing edge faster than at the lower path, for more details, see Epple et al. [2]. When calculating lift, it is therefore preferable to use the momentum balance instead of the Bernoulli equation, and the same applies to sluice gate flows, which is discussed in more detail below.

The momentum balance approach has several advantages compared to Bernoulli's energy conservation principle, which was used in previous work on sluice gate discharge calculations. Bernoulli's energy conservation principle has two major drawbacks: It is only valid along streamlines, it works with the magnitude of the velocity vector and flow directions cannot be distinguished. But on the other hand, the discharge is an integral quantity of the normal component of the velocity over the opening cross section. Therefore, outflow problems where the velocity is not perpendicular to the opening cross section have to be solved adequately using the integral momentum balance. Furthermore, the momentum equation is also valid for flows where the energy is not conserved as is the case for flows under sluice gates. However, it is more complicated since it is an integral vector equation whereas the energy equation is a scalar equation. In the case of the momentum equation, the pressure distributions must be known on all the control volume boundaries and the momentum fluxes on all open boundaries. As a result, the discharge can be determined without any empirical flow coefficient, which is used by the conservation of energy approach to correct the wrong assumptions. The integral momentum balance method is closed by the determination of the missing pressure distributions and momentum coefficients using CFD computations. The momentum balance method to calculate the discharge is applicable to the standard sluice gate as well as to the inclined sluice gate. For this purpose, the following work is structured as follows: In chapter 2 of this thesis, the commonly used calculation approaches of the discharge will be discussed again, as well as different types of sluice gates are introduced. In addition, the detailed flow phenomena that occur during the free outflow of the sluice gate are discussed in detail and the current state of research is presented. In Chapter 3, the momentum balance for the sluice gate

is derived. To calculate the discharge with the formula resulting from the integral momentum balance, the pressure force at the opening and at the gate as well as the momentum coefficient at the opening must be known. For this purpose, CFD simulations of the sluice gate for different relative gate openings a/h_0 and different angles of inclination α are performed as described in chapter 4. The analysis and parameterization of the pressure distributions and pressure forces determined in the CFD simulations as well as the momentum coefficient are carried out in chapter 5 and chapter 6, respectively. In chapter 7, the derived pressure forces and the momentum coefficient are then used in the momentum balance to calculate the discharge. The discharge calculated in this way is also compared with relevant literature values and the results are discussed. In chapter 8, the elaborated momentum balance approach is further extended to include 3D effects.

2 Fundamentals on Sluice Gate Hydraulics

In this chapter, the fundamentals of sluice gate flows are discussed, and various types of sluice gates are shown and explained. The sluice gate with sharp gate lip and supercritical outflow dealt with in this thesis is explained in detail.

2.1 Sluice Gate Discharge

The calculation of the sluice gate discharge Q is presented in established textbooks e. g. [3], [4] and [5] based on the assumption of a constant velocity at the opening u_O, calculated by Torricelli's law:

$$u_{Torricelli} = \sqrt{2gh_P} \tag{2-1}$$

where g is the gravitational acceleration and h_p is the pressure head. The discharge can then be calculated by multiplying the Torricelli velocity $u_{Torricelli}$ with the area of the gate opening $A_O = a\,B$. As this assumption deviates from experimental observations by up to 40 % [6], the discharge coefficient c_D was introduced in the early 19th century to correct this deviation. The resulting equation for the discharge can then be written as:

$$Q = c_D\, a\, B \sqrt{2gh_P} \tag{2-2}$$

An early determination of the discharge coefficient was made by Weisbach [7] in 1855. His experiments with different opening heights and slopes enabled him to determine a constant value for this coefficient. Later, in 1871 [8] and 1880 [9], Bornemann presented different equations to calculate discharge coefficients for the free and the submerged outflow, respectively. In developing these equations, Bornemann referred to his own experimental data as well as experimental data from other authors such as Boileau [10], Weisbach [11], Linnebrügge [12] and Lesbros (published by Rühlmann [13]). Based on this data, he established equations for the discharge coefficients and demonstrated the dependence of these on the relative gate opening ε, finding different coefficients for the different experimental setups. The relative gate opening ε is a crucial parameter in sluice gate flows and defined as the ratio of the gate opening height a divided by the upstream water level h_0, see Eq.(2-3).

$$\varepsilon = \frac{a}{h_0} \tag{2-3}$$

In the works of e. g. Bornemann [8] or Rühlmann [13], the pressure head $h_P = h_0 - \frac{a}{2}$ was assumed to be the difference in height between the upstream water level h_0 and the center of the gate opening a. In later works (e.g. Fawer 1937 [14]) the upstream water level $h_p = h_0$

or the energy head $h_p = h_0 + \frac{u_0^2}{2g}$ was used as the pressure head for the calculation of the Torricelli velocity $u_{Torricelli}$ (Eq. (2-1)). The authors have chosen as pressure head $h_P = h_0 - a$, which was first introduced by du Buat [15] and also used by e. g. Weisbach [11], with the discharge coefficient $c_{D,dB}$:

$$c_{D,dB} = \frac{Q}{a\,B\sqrt{2g(h_0 - a)}} \tag{2-4}$$

Note that the discharge coefficient depends on the chosen pressure head, but the discharge coefficient of a specific pressure head can also be converted to the discharge coefficient of another pressure head. For example, the Torricelli discharge coefficient $c_{D,T}$, with $h_p = h_0$, can be derived from the du Buat discharge coefficient $c_{D,dB}$, with $h_p = h_0 - a$, see Eq. (2-5):

$$c_{D,T} = c_{D,dB}\sqrt{1 - \frac{a}{h_0}} \tag{2-5}$$

2.1.1 Free Sluice Gate Flow

Free flow under a sluice gate is when a jet contraction forms in the tailwater of the sluice gate and the water flows through the gate under supercritical condition. Various publications e. g. [16], [17], [18], [19] and textbooks e. g. [3], [4], [20], [21] use an energy conservation approach to calculate the discharge coefficient for the free sluice gate flow. Based on the findings of Keutner's [6] study from 1932 who found that the velocity at the supercritical flow u_1 downstream of the gate is almost constant, the discharge can be calculated, if the downstream water level h_1 or the contraction coefficient $c_C = \frac{h_1}{a}$ is known. Figure 5, shows that the potential and kinetic energy upstream and downstream of the sluice gate in terms of the energy head:

$$h_0 + \frac{u_0^2}{2g} = h_1 + \frac{u_1^2}{2g} \tag{2-6}$$

Further the continuity equation for the up- and downstream region can be written as:

$$h_0 \cdot B \cdot u_0 = h_1 \cdot B \cdot u_1 \tag{2-7}$$

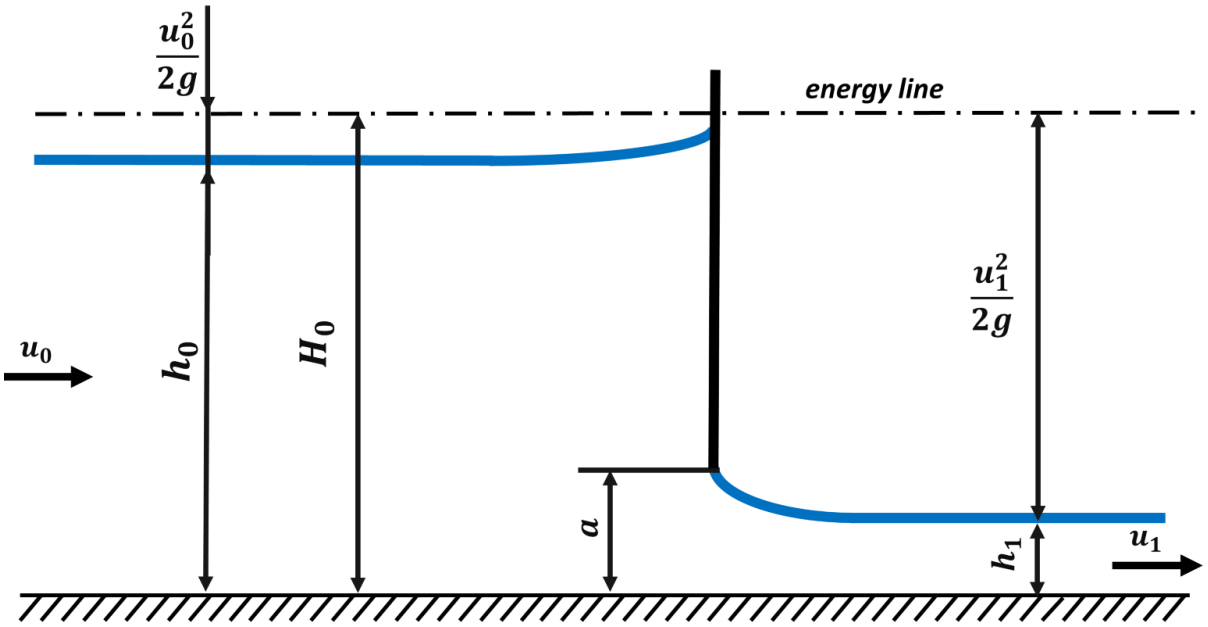

Figure 5: Frequently used sluice gate theory assuming energy conservation

By rearranging Eq. (2-6) and inserting the continuity equation (Eq. (2-7)) we get:

$$u_1 = \sqrt{\frac{2gh_0}{1+\frac{h_1}{h_0}}} \tag{2-8}$$

With the downstream velocity u_1, the specific discharge Q can be calculated by multiplying with the downstream flow cross-section $h_1 B$ as follow:

$$Q = h_1\, B\, u_1 = h_1\, B \sqrt{\frac{2gh_0}{1+\frac{h_1}{h_0}}} \tag{2-9}$$

By rearranging Eq. (2-9) and substituting the contraction coefficient c_C, we get:

$$Q = a\, c_C\, B\, u_1 = a\, c_C\, B \sqrt{\frac{2gh_0}{1+\frac{a\, c_C}{h_0}}} \tag{2-10}$$

By inserting the calculated discharge Q from Eq. (2-10) into Eq. (2-4), the discharge coefficient $c_{D,dB}$ can be calculated by the energy approach as follows:

$$c_{D,dB} = c_C \sqrt{\frac{1}{(1+c_C\varepsilon)(1-\varepsilon)}} \tag{2-11}$$

Using Helmholtz's theory of free streamlines, in 1935 Müller [16] calculated the theoretical contraction of the tailwater using a simplified model neglecting the acceleration due to gravity and the frictional losses. He was able to show that, the contraction coefficient c_C and thus also the discharge coefficient $c_{D,dB}$ depend solely on the relative gate opening ε. This approach to use the theory of free streamlines was further refined and extended to include inclined sluice gates by Werner [22] in 1963. An approximation function for calculating the contraction coefficient, based on the work of Müller [16] and Werner [22], was defined by Voigt [23] for the standard sluice gate as follows:

$$c_C = \frac{1}{1 + 0.64\sqrt{1-\varepsilon^2}} \tag{2-12}$$

Based on experimental data of Gentilini [24] and own measurements, Aigner and Horlacher [25] have developed formulas for the parameterization of the jet contraction of inclined sluice gates. First, for the case $\varepsilon = 0$, the jet contraction is calculated as a function of the angle of inclination α as follows:

$$c_{C,\varepsilon=0} = 1.3 - 0.8\sqrt{1-\left(\frac{\alpha-205}{220}\right)^2} \tag{2-13}$$

In addition, the approach to calculate the jet contraction for the standard sluice gate by Voigt (Eq. (2-12)) which represents the dependence of the contraction coefficient on the relative gate opening ε, was adapted in such a way that the jet contraction for the inclined sluice gate can finally be calculated as follows:

$$c_C = \frac{1}{1 + \left(\frac{1}{c_{C,\varepsilon=0}} - 1\right)\sqrt{1-\varepsilon^{\frac{210}{\alpha}}}} \tag{2-14}$$

To calculate the discharge coefficient from the contraction coefficient, Aigner and Horlacher use a modified form of equation Eq. (2-11):

$$c_{D,dB,AignerHorlacher} = c_C\sqrt{\frac{1}{\left(1 + \frac{c_C}{\frac{1}{\varepsilon} - 0.5}\right)(1-\varepsilon)}} \tag{2-15}$$

In Figure 6 a), the contraction coefficient is plotted according to the formula of Voigt and Aigner et al. as a function of the relative gate opening ε. Figure 6 b) shows the measurement results of Gentilini [24] and the parameterization of Aigner and Horlacher [25] for the discharge coefficient of the standard and inclined gate are plotted as an example.

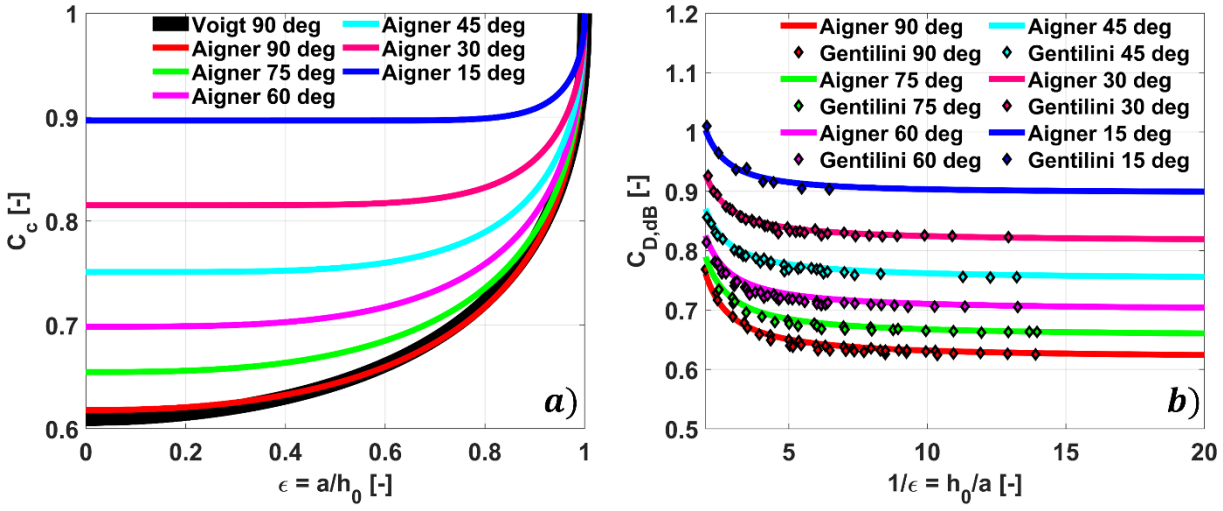

Figure 6: a) contraction coefficient and b) discharge coefficient for standard and inclined sluice gates from literature

The parameterization of Aigner and Horlacher, which was calibrated with the measured values of Gentilini, agrees with them very well. However, compared to other literature values by Swamee [26], Rouse [3], Henry [27], Roth and Hager [28] as well as Rajaratnam [29], who only investigated the standard sluice gate, the parameterization by Aigner and Horlacher is above the other widely cited literature values for the discharge coefficient, as can be seen in Figure 7. Which of the shown discharge coefficients is the correct one cannot be said conclusively, since the discharge coefficient varies among other things also by the inflow condition, scaling effects, wall roughness, channel width etc. of the channel.

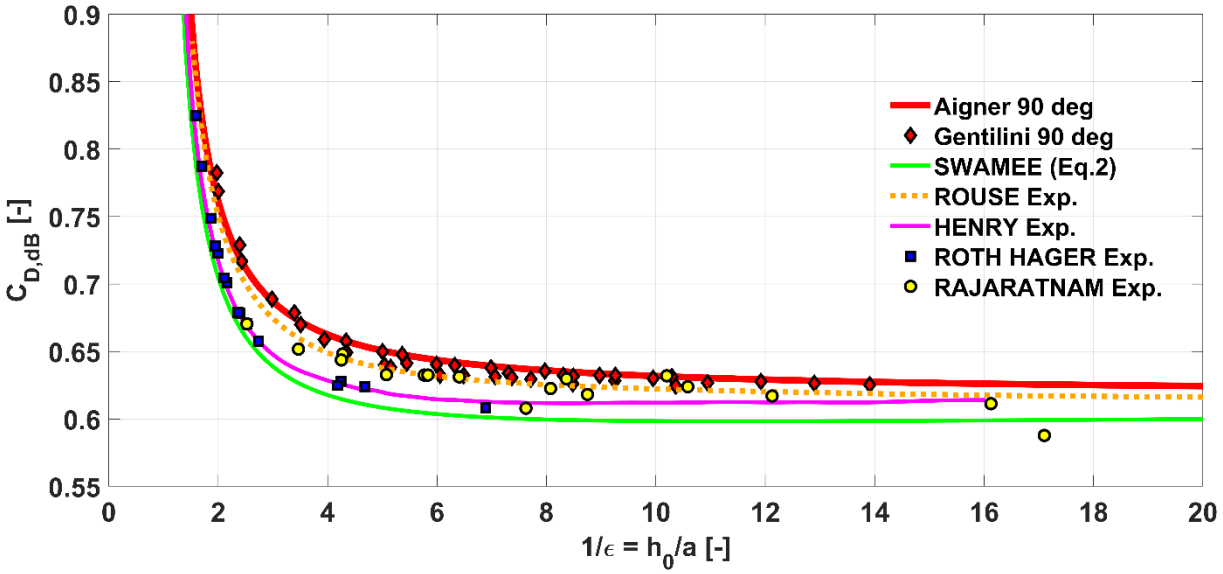

Figure 7: Discharge coefficient $c_{D,dB}$ of the standard sluice gate in dependency of the inverse relative gate opening $1/\varepsilon$

2.1.2 Submerged Sluice Gate Flow

If the downstream water level is above that of the sluice gate opening ($h_1 > a$), this is referred to as a submerged flow. A schematic drawing of a submerged sluice gate is shown in Figure 8 a). Due to the larger water column of the backwater h_2, the pressure head difference between the upstream and downstream water level is smaller and therefore the flow through the gate opening is reduced. If the flow is submerged, a jet with a jet contraction also forms at the opening of the sluice gate, but this is normally not visible because the discharge takes place underwater. In Figure 8 b), the jet was therefore made visible with glass hollow spheres and a laser sheet. In the downstream area above the jet directly behind the gate, eddies form and the water level are slightly lowered. As the distance to the sluice gate increases, these eddies disappear and a velocity profile develops along the entire water depth.

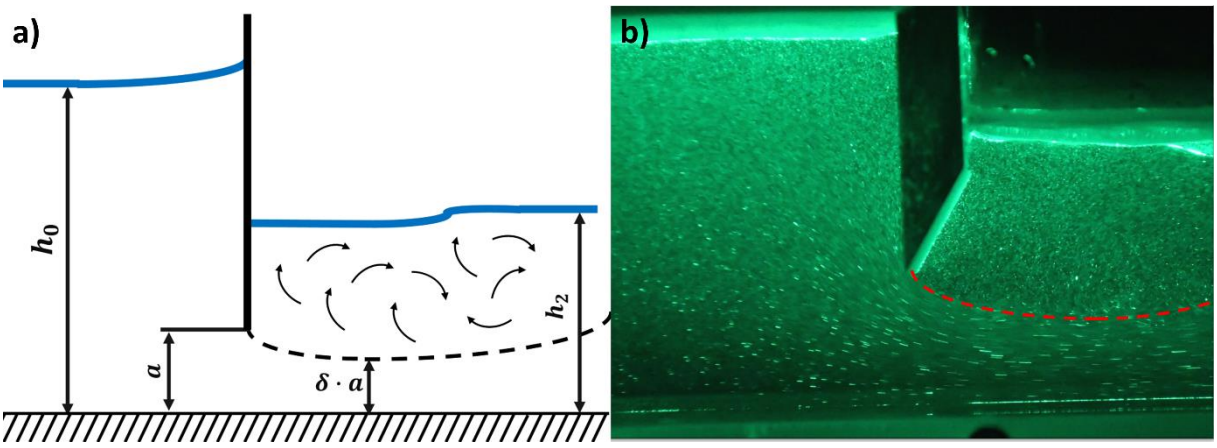

Figure 8: Submerged sluice gate a) schematic drawing b) flow visualization

To calculate the discharge of submerged gates, the Torricelli outflow formula is also used here and corrected with a discharge coefficient for submerged sluice gate flows $c_{D\ sub,dB}$. The discharge coefficient for the submerged gate depends on both the ratio of the upstream water level to the opening height $\frac{1}{\varepsilon} = \frac{h_0}{a}$ and the ratio of the downstream water level to the opening height $\frac{h_2}{a}$. Frequently cited studies on this subject were carried out by Henry [12]. The discharge coefficient $c_{Dsub,dB}$ for the submerged gate from Henry [12] is shown in Figure 9. Also shown in Figure 9 is the discharge coefficient $c_{D\ sub,dB}$ for $\frac{h_0}{a} = 4$ and $\frac{h_2}{a} = 3$ calculated by own CFD simulations, which agrees with the results of Henry [12].

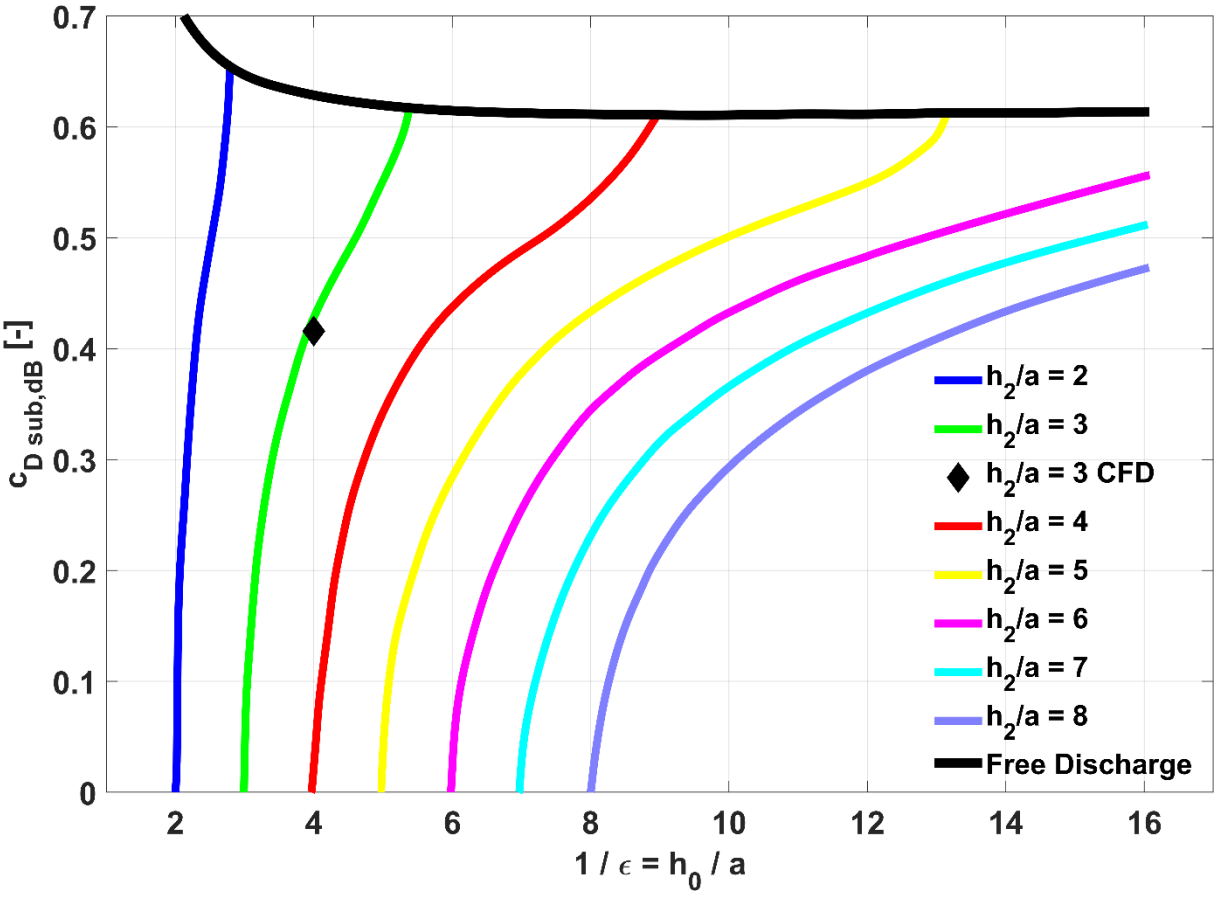

Figure 9: Discharge coefficient $c_{Dsub,dB}$ in dependency of the inverse relative gate opening $1/\varepsilon$ for submerged sluice gates

If we look at the CFD simulation plots, showing the volume fraction of water and the streamlines, see Figure 10, it can be seen that the streamlines are similar in both cases. For both discharge types, the water jet exiting the gate opening is similarly contracted, but in the case of the submerged gate, the exiting water jet is underwater. However, the velocities of the backwater discharge are significantly lower due to the smaller difference between the upstream and downstream water levels. If the streamlines are also compared further downstream, they diverge further in the case of the submerged gate than in the case of the gate with free discharge, and thus the jet becomes wider until it is distributed over the complete downstream water level h_2. However, this is no longer shown in Figure 10.

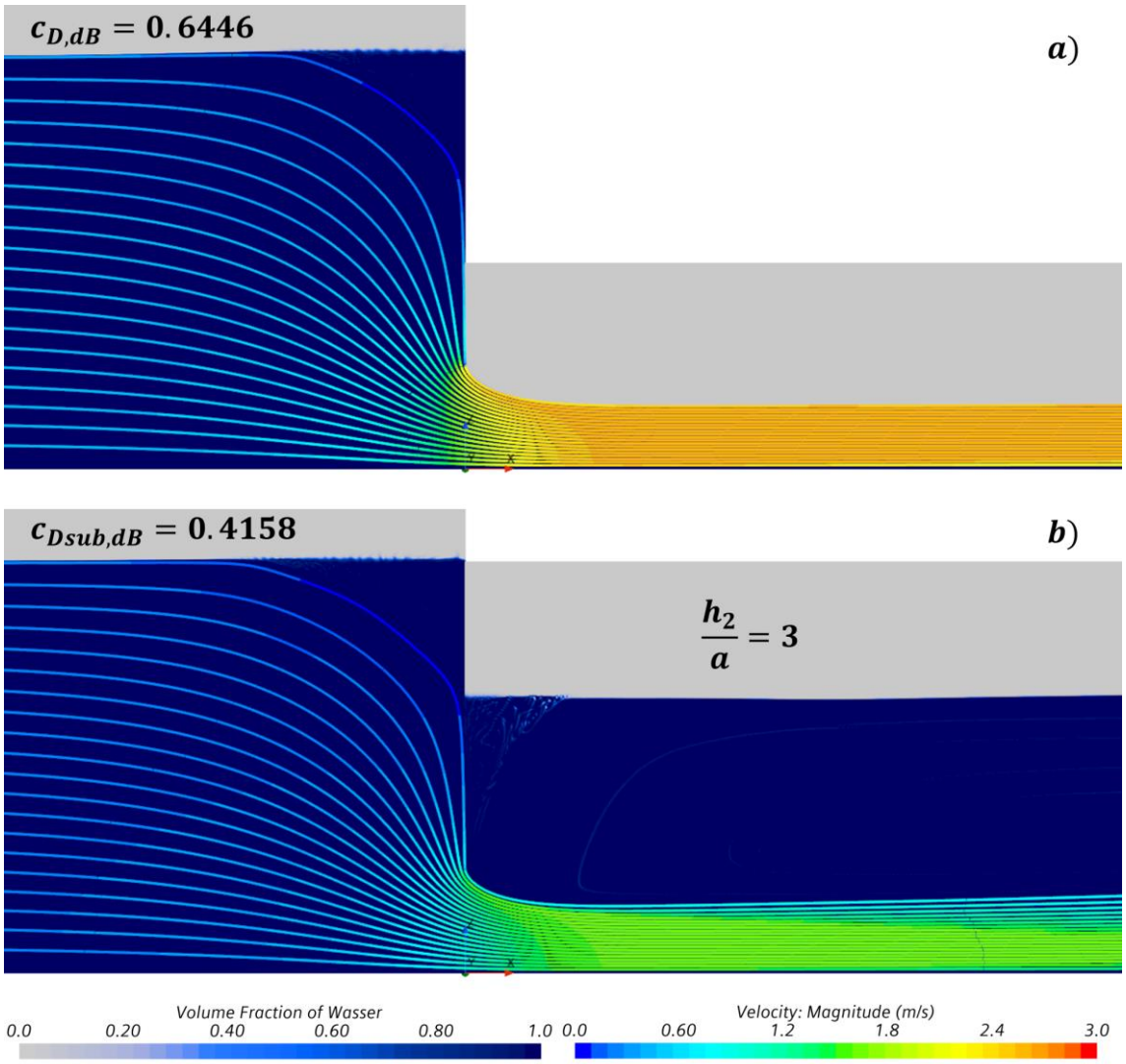

Figure 10: Volume fraction of water contour plot and streamlines for $h_0/a = 4$: a) free flow b) submerged flow ($h_2/a = 3$)

2.1.3 Other Sluice Gate Types

In addition to the plane sluice gates with a sharp gate lip, which is examined both vertically (standard sluice gate) and in inclined positions in this work, there are also other sluice gate types. A common variation of the plane sluice with sharp gate lip is the plane sluice gate with rounded gate lip at the opening. This is discussed, for example, in the textbook by Aigner and Bollrich [30]. The discharge coefficient $c_{D,dB}$ for the sluice gate with rounded edge, calculated using the formula of Aigner and Bollrich [30], is shown in Figure 11 as a function of the relative edge radius $\frac{r}{a}$. Also shown in Figure 11 are own simulation results for $\frac{r}{a} = 0$, which corresponds to the sharp-edged sluice gate, for $\frac{r}{a} = 0.5$, for $\frac{r}{a} = 1$ and for $\frac{r}{a} = 3$. For $\frac{r}{a} = 0.5$ the CFD results and the parameterization from Aigner and Bollrich agree, while for $\frac{r}{a} = 0$, for $\frac{r}{a} = 1$ and for $\frac{r}{a} = 3$ the CFD values are overestimated.

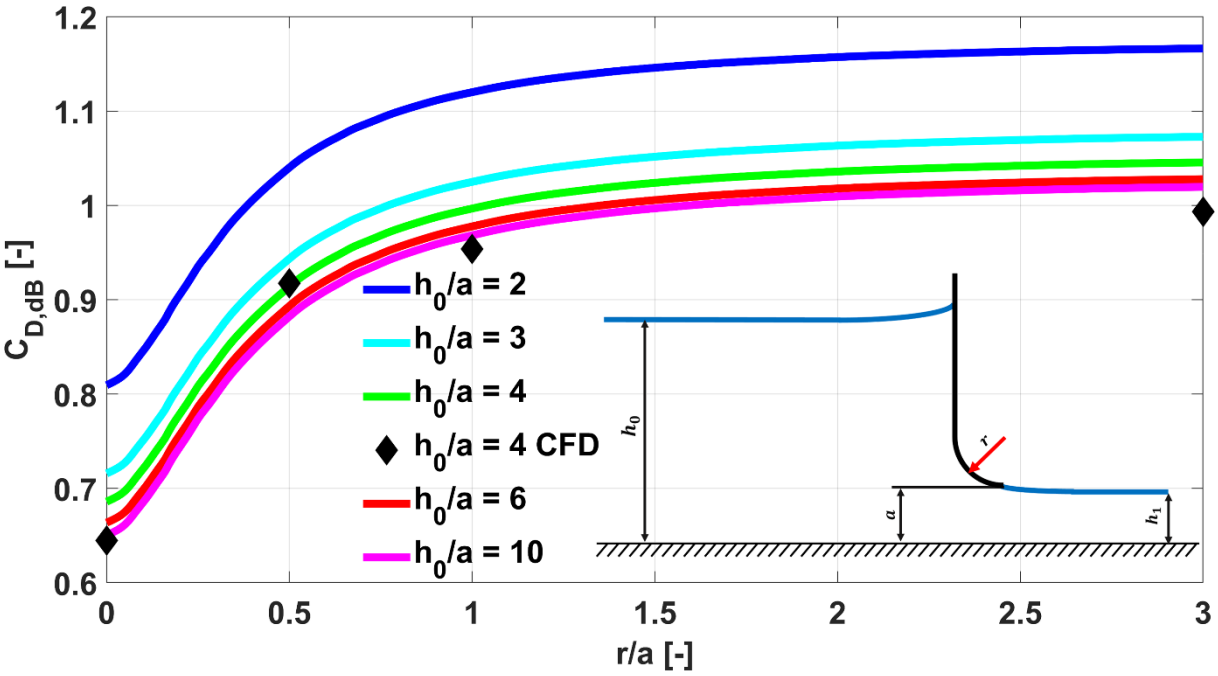

Figure 11: Rounded edge discharge coefficient $c_{D,dB}$ in dependency of the relative gate edge radius r/a

The volume fraction of water contour plot and the streamlines of the CFD simulations of the sluice gate with rounded edge are shown in Figure 12. Since with the increasing radius, the streamlines are already deflected upstream of the sluice gate opening a, the vena contracta becomes much smaller and the downstream water level h_1 approaches the sluice gate opening height a with increasing radius r, which is indicated by an increasing contraction coefficient c_C.

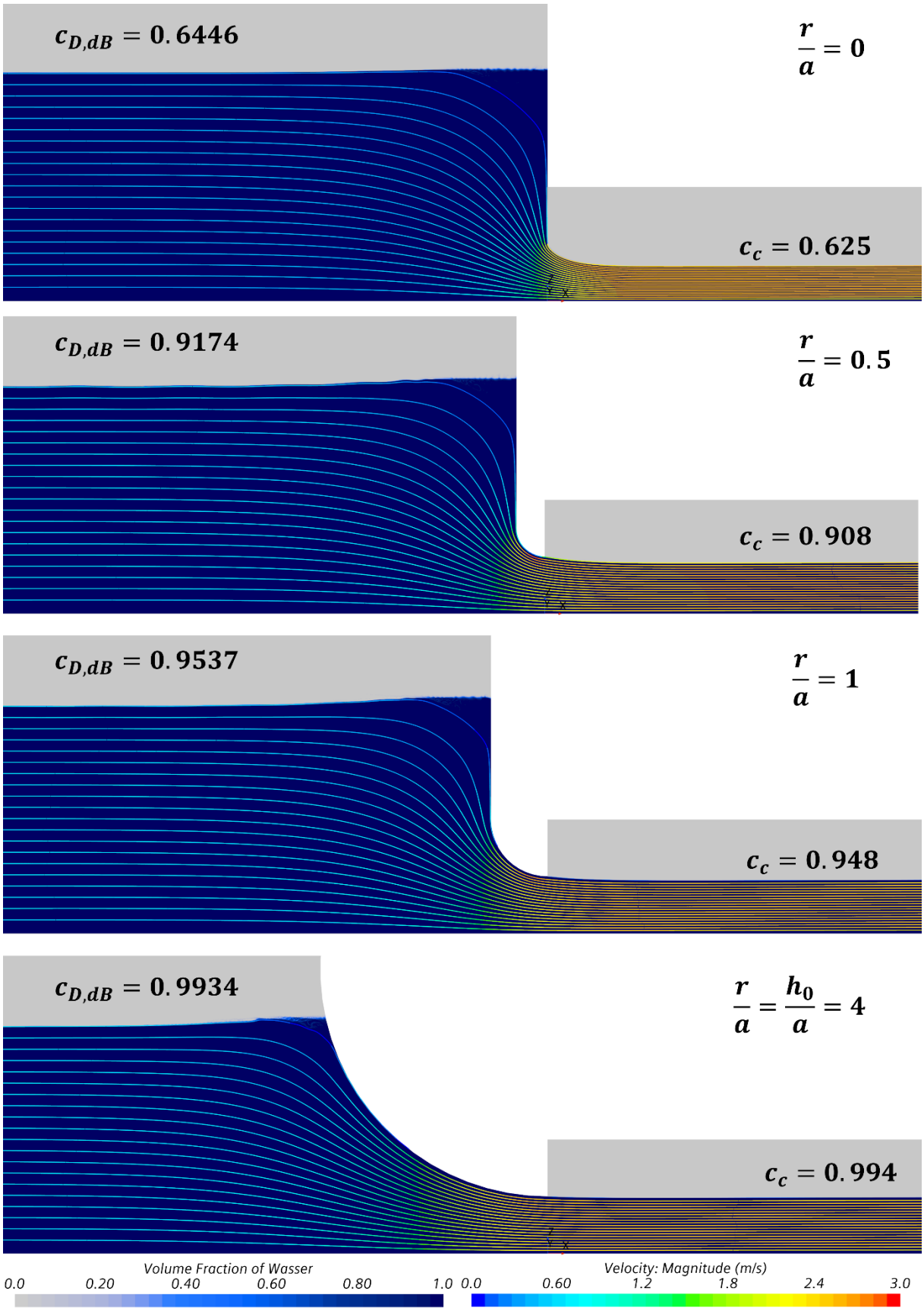

Figure 12: Volume fraction of water contour plot and streamlines of sluice gate with rounded edge for $h_0/a = 4$

The sluice gate with $\frac{r}{a} = \frac{h_0}{a}$, shown in Figure 12, no longer has a straight part and also corresponds to a radial gate which is also a widely used sluice gate type. The radial sluice gate is treated e.g. in the textbook of Zanke [20]. In contrast to the plane gates, which are opened by a translatory movement, this one is opened and closed by rotation around a fixed pivot point. The discharge coefficient for the radial gate is given in dependency of the gate opening angle α_R and the values for the discharge coefficient from Zanke [20] are shown in Figure 13. Also shown in Figure 13 are the results of own CFD calculations, with $R = h_0 = 0.4$ m. Both the literature values and the CFD calculations show that the discharge coefficient increases with decreasing angle at the opening α_R. Note: The radial gate with an opening angle of $\alpha_R = 0°$ cannot be closed by rotation.

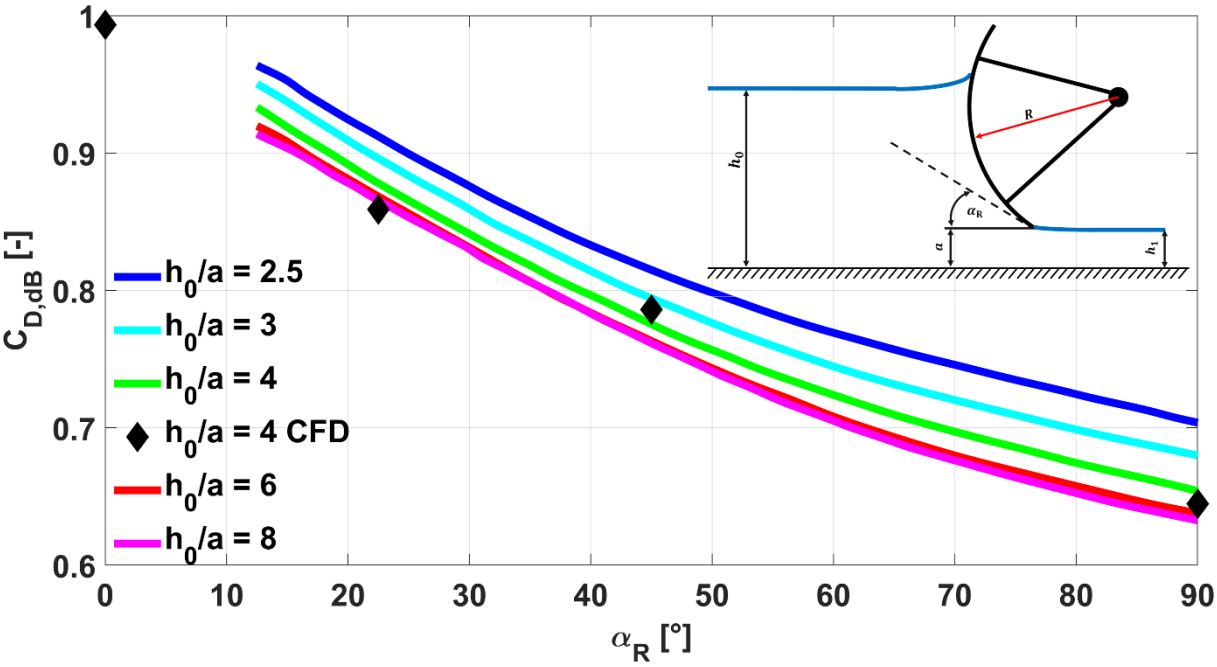

Figure 13: Discharge coefficient $c_{D,dB}$ of radial in dependency of the opening angle α_R

The volume fraction of water contour plot and the streamlines of the CFD simulations of the radial sluice gate are shown in Figure 14. The contraction coefficient c_c of the jet also decreases with decreasing opening angle α_R, since the jet is already aligned in the main flow direction. The radius of the radial sluice gate also has an influence on the flow variables, but this is considered to be of secondary importance in the practical books.

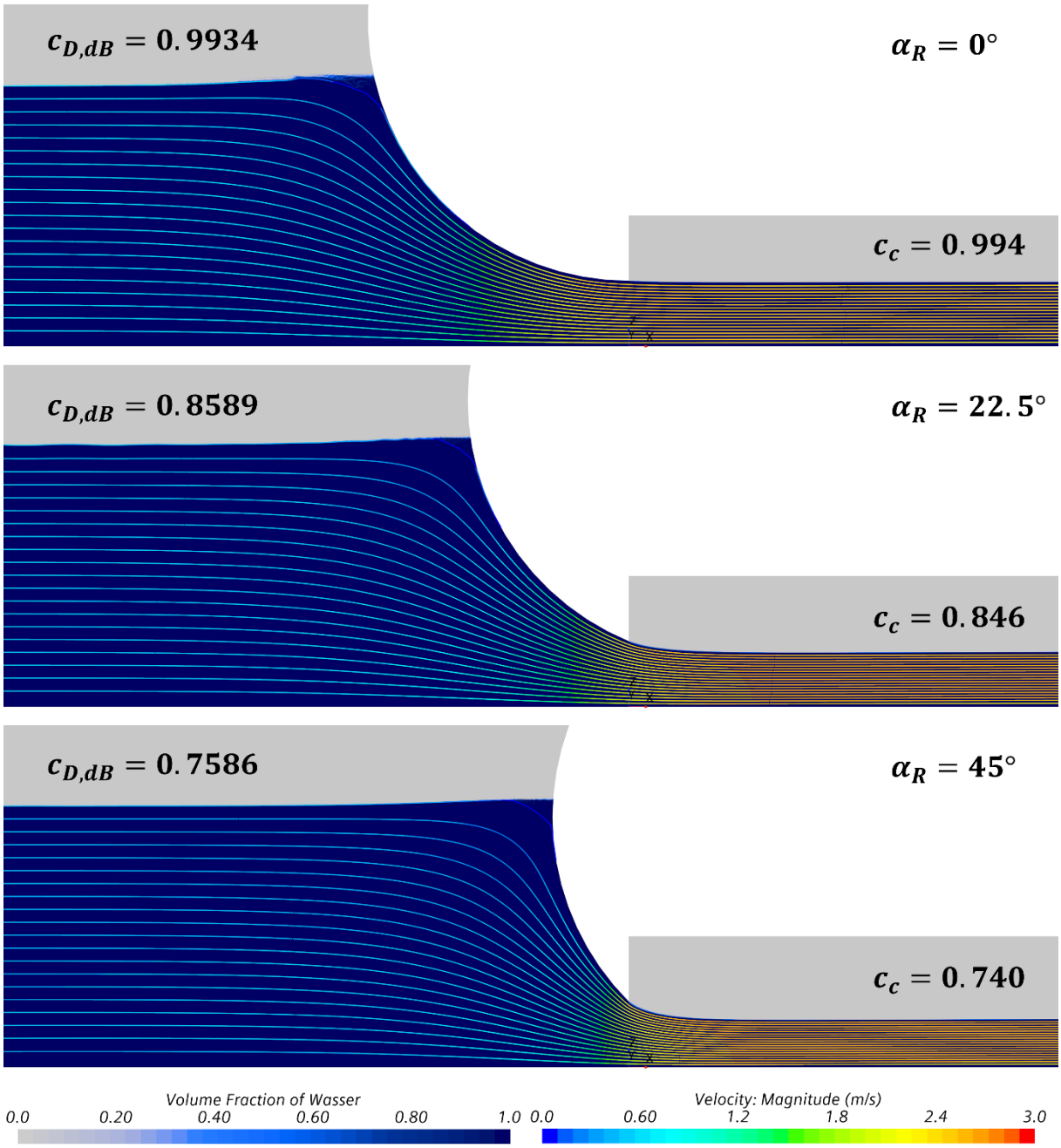

Figure 14: Volume fraction of water contour plot and streamlines of radial sluice gate for $h_0/a = 4$

2.2 Detailed Flow Characteristics of Free Outflow

In the previous considerations, theoretical models of gate flows were shown, as they are often described in a simplified way in textbooks. Classically, gate flows are considered as two-dimensional flows, which can be assumed for the flow of broad gates ($B \gg a$) at sufficient distance from the side walls. This approach is not uncommon in fluid mechanics and can be compared, for example, with the infinit wing theroy for airfoils. The flow phenomena occurring in the two-dimensional observation of gate flows are shown in Figure 15. The water level increases at the gate wall and the water level there is greater than the upstream water level h_0 by Δh_0. Further, an eddy is formed at the upstream water surface at the sluice gate wall. In this area, the flow is detached, further downstream the flow attaches at the gate wall.

The height of the eddy h_{Ge}, the height of the attached flow h_{Ga} as well as the height of the water level increase Δh_0 have an influence on the pressure distribution at the sluice gate wall [31] and are described in detail in chapter 5.3. In the downstream region, the vena contracta already described in the previous chapter is formed.

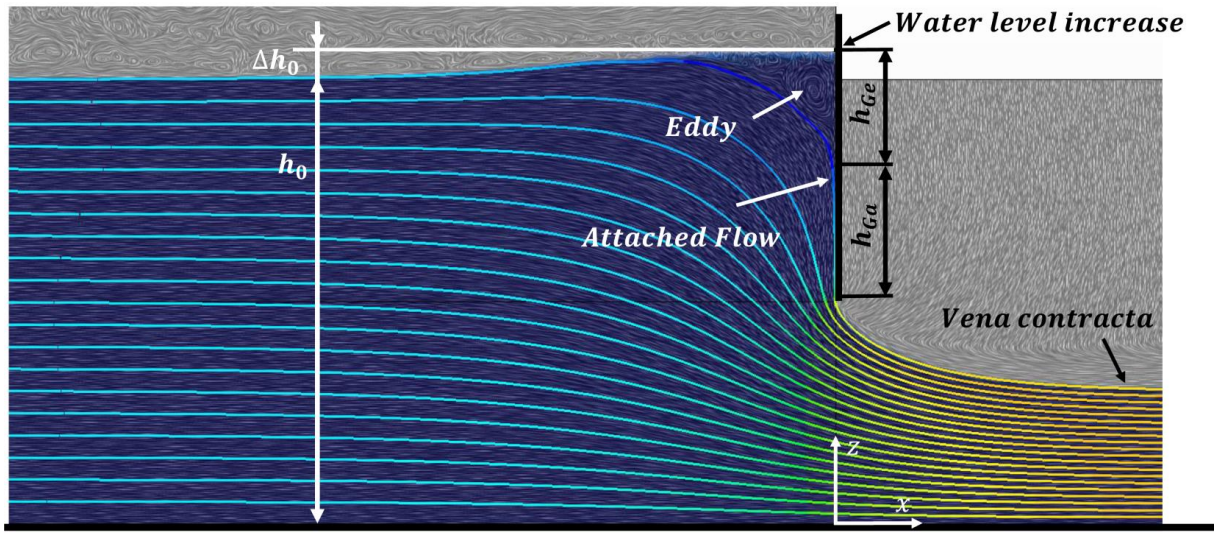

Figure 15: Detailed 2D flow characteristics of sluice gates, visualized by line integral convolution and streamlines

In addition to the described flow characteristics, which also occur in a two-dimensional view, three-dimensional effects also occur due to the side walls. These effects depend on the relative gate width ζ, defined in Eq. (2-16).

$$\zeta = \frac{B}{a} \tag{2-16}$$

For $\zeta = 4$, the 3D simulation results are shown in Figure 16 in a representative way to explain these 3D effects in more detail. In Figure 16, the streamlines and the pressure distribution are shown in a resampled volume that only shows the cells in the simulation domain

with a volume fraction of water >1 %. The most important 3D effects are the forming corner vortices (Figure 16 (I)), which are the cause of the 3D effects on the pressure distributions. The water level increase at the sluice gate wall Δh_0, initially assumed to be constant for the 2D case along the y-coordinate, fluctuates near the corners due to the corner vortices. At the centers of the corner vortices, a surface vortex forms at the water surface (Figure 16 (II)), as also observed experimentally by Roth and Hager [28]. This can be explained by the energy conservation equation. Since due to the larger velocities in the vortex, the kinetic energy increases and hence the potential energy (water level) must decrease. The figure also shows that the pressure distribution on the gate (Figure 16 (IV)) and the sidewalls (Figure 16 (V)) deviates in the area of the corner vortices. Furthermore, the pressure distributions at the opening and at the bottom are also influenced by the corner vortices. Since the pressure distributions are crucial for the momentum balance, 3D effects on the pressure distribution will be also considered in this work.

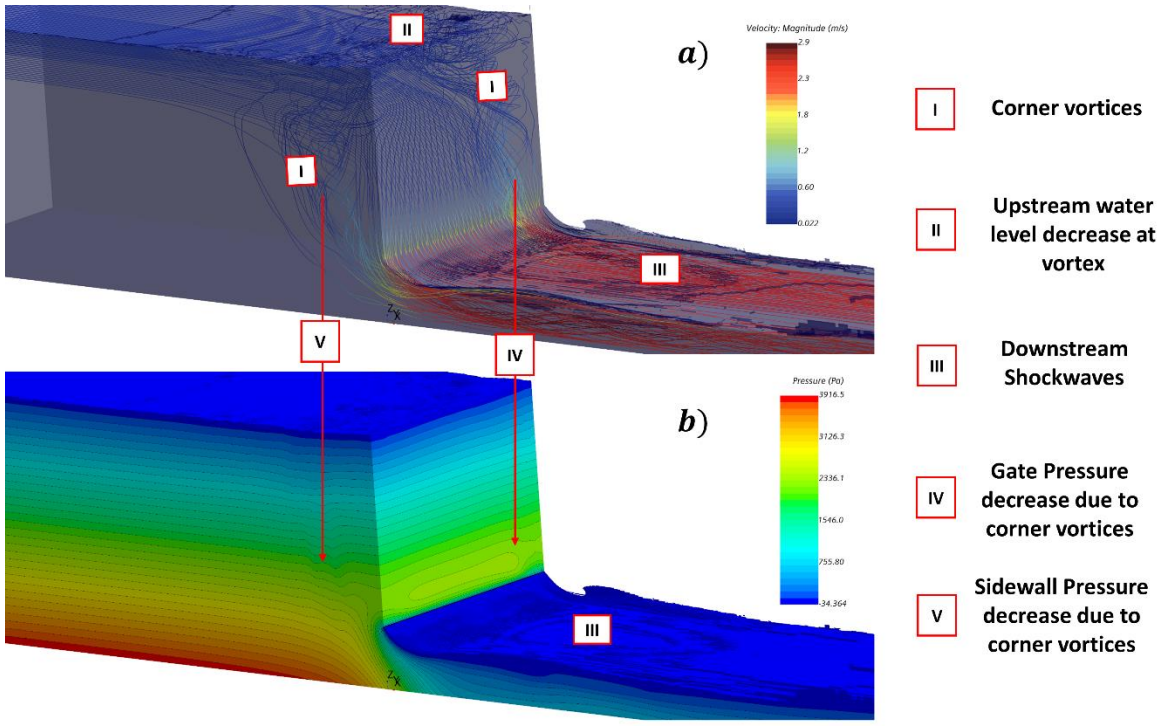

Figure 16: 3D Sluice gate CFD simulation for the standard sluice gate with $h_0 = 0.4\ m$, $a = 0.1\ m$ and $B = 0.4\ m$ a) streamlines and b) pressure contour plot

In the following sections, the mentioned flow phenomena will be discussed in more detail and previous work on them will be presented.

2.2.1 Surface Eddy and Water Level Increase at the Gate

Figure 15 shows that a surface eddy forms in the upper part of the sluice gate near the water surface. An experimental analysis of the upstream sluice gate flow characteristics was done by Rajaratnam and Humphries [32]. They parametrized the height and the length of the eddy at the upper sluice gate edge. Rajaratnam and Humphries [32] assumed that the height of the eddy at the sluice gate wall increases with increasing upstream water level h_0 and doesn't depend on the relative gate opening ε. They described only a dependency of the length of the eddy l_e on the relative gate opening ε and also on the surface tension. Harber et. al [33] and Roth et. al [28] described a Reynolds ridge at the upstream end of the surface eddy. The distance of this Reynolds ridge from the sluice gate wall, was defined by Rajaratnam and Humphries as the eddy length l_e. Later Cassan and Belaud [34] found out, that the length of the ridge is also a function of the upstream water level h_0.

The upstream water level at the gate also increases by Δh_G at the sluice gate. In Figure 17 the water level increase is shown by the graphic from Keutners work from 1932 [6]. The water level increase is often determined by using the energy conservation approach, but it is lower due to losses, which was also found by Keutner.

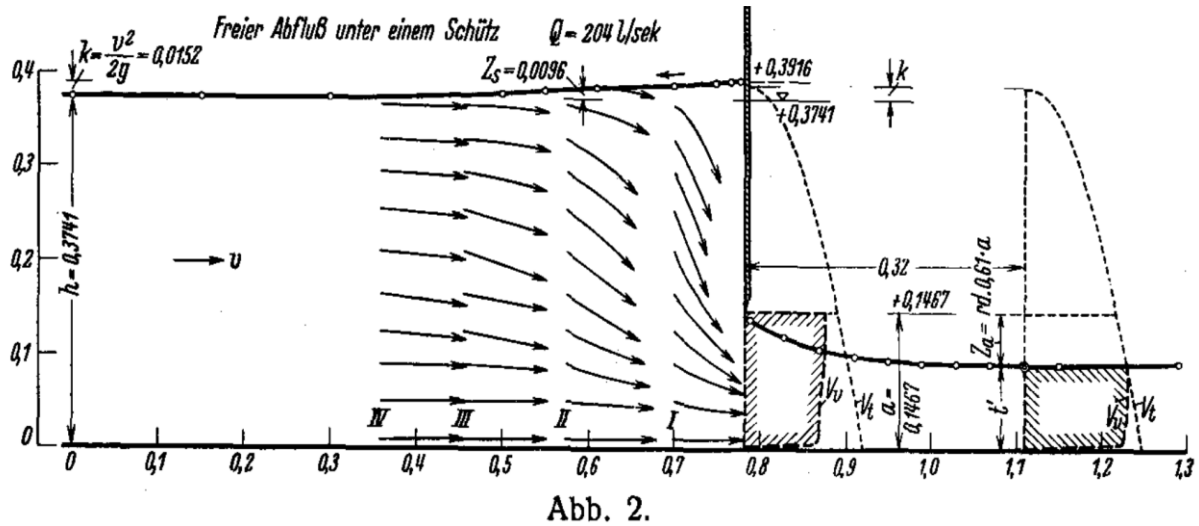

Abb. 2.

Figure 17: Sluice gate flow description from Keutner 1932 [6]

2.2.2 Corner Vortices

The corner vortices are occurring at the corners between the sluice gate wall and the side walls, as shown in Figure 18 a). Looking perpendicularly at this vortex formation, see Figure 18 b), it can be seen, that the surface eddy combined with the corner vortices form a horseshoe shaped vortex, which was also described by Montes [35]. The corner vortices continue in the downstream region and run into infinity (Helmholtz's third theorem [36]).

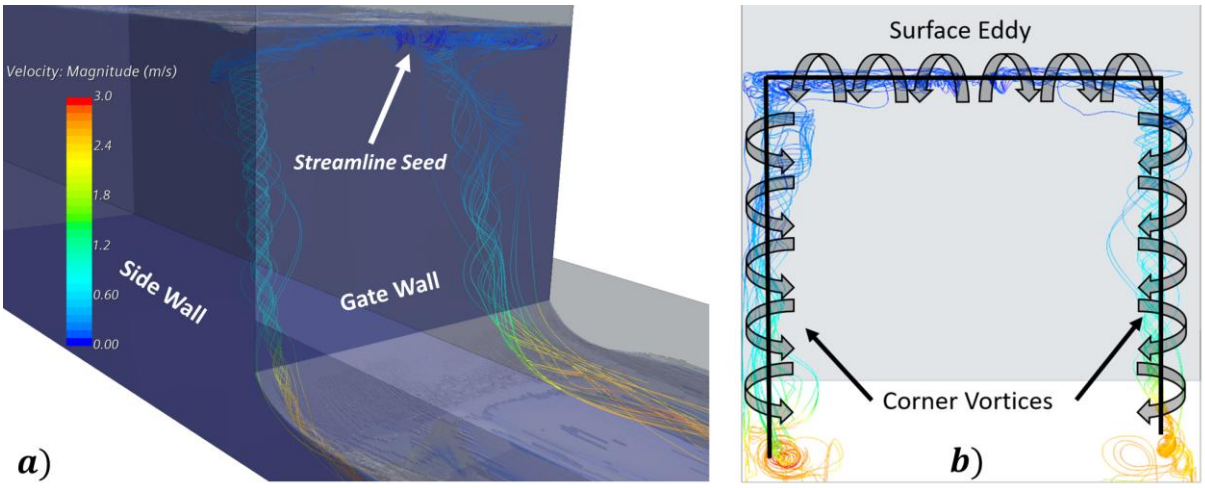

Figure 18: Streamlines showing corner vortices and surface eddy a) perspective view and b) frontal view

The velocity at the corner vortices is larger as at the middle of the sluice gate. Also, at the center of the vortices the velocity increases and since the surface pressure is constant, due to energy conservation, the water level has to drop. The water level drop can be seen by a surface vortex in the simulations. The water level decrease was also shown by Roth and Hager [28], who also derived equations for the upstream position of the surface vortices. Roth and Hager also investigated anti-vortex elements with the aim of attenuating the shock waves generated by the corner vortices downstream. Further possibilities to display the corner vortices are shown in Figure 19. Figure 19 a) shows the magnitude of the vorticity from $10\frac{1}{s}$ to $50\frac{1}{s}$ and in Figure 19 b) the Q-Criterion from $10\frac{1}{s^2}$ to $1000\frac{1}{s^2}$ is shown.

However, the previous studies that analyzed the pressure distribution at the sluice gate, have not yet dealt with the influence of the corner vortices on the pressure distributions of sluice gates. This is also the subject of this thesis and is dealt with in Chapter 5.

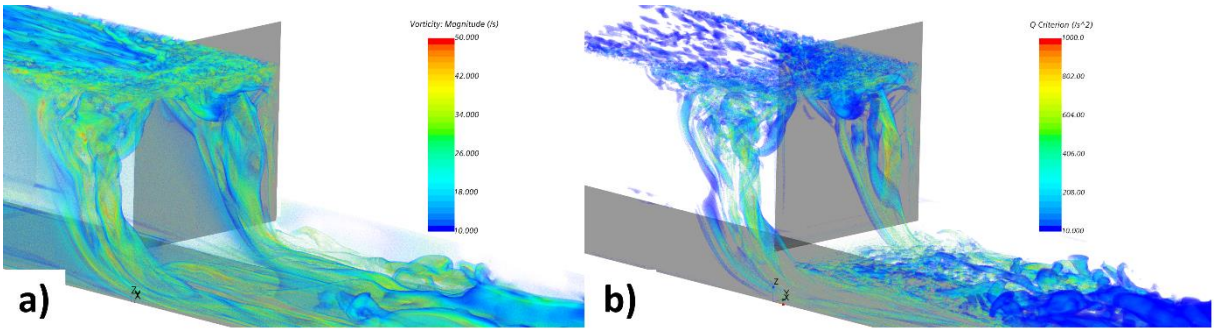

Figure 19: Visualization of the corner vortices by a) vorticity magnitude and b) Q-Criterion

2.2.3 Shock Waves

The local water level increases at the sidewalls, which are referred to as shockwaves in the literature, occur downstream of sluice gate in the supercritical flow region. Figure 20 shows a section perpendicular to the main flow direction or x-axis at the location of a shock wave at the dimensionless x-coordinate $X = x/a = 2.5$ from 3D CFD simulations. The water level towards the wall is initially lower at the corner vortices. At the wall, the water is then forced upwards again, forming a shock wave with a secondary eddy, also shown in Figure 20.

Roth and Hager [28] described a dependence of the dimensionless shock position X_S and the dimensionless shock height Z_S of the shockwaves in dependence of the relative gate opening ε and proposed calculation formulas. Roth and Hager also studied anti-vortex elements, which are attached to the sluice gate and can reduce the shockwaves caused by the vortices by 50 %.

Due to the shockwaves and the corner vortices, the measurement of an exact single value of the downstream water level h_1 or the contraction coefficient c_C is not possible for three-dimensional sluice gate flows. This difficulty was also described in the work of Aigner and Horlacher [25], who determined the discharge coefficient based on the contraction coefficient c_c, see Eq. (2-15).

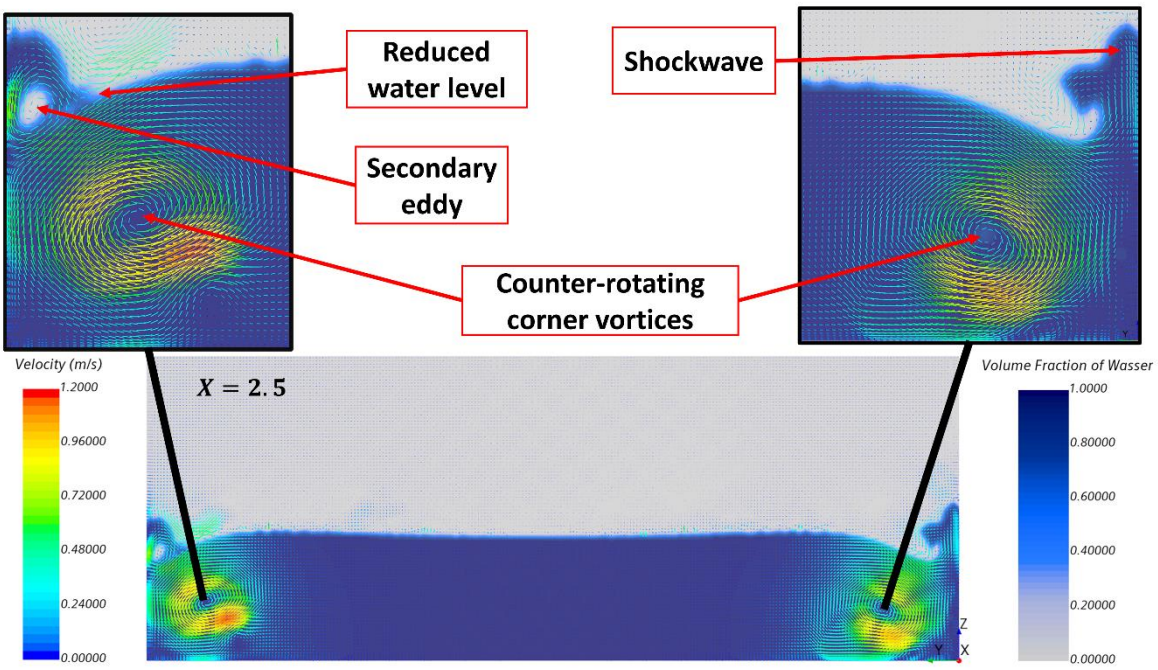

Figure 20: Tangential velocity vectors and volume fraction of water at $X = 2.5$ for shockwave visualization

2.3 Similarity Laws and Scaling Effects for Sluice Gate Flows

Similarity laws are used in fluid mechanics to transfer laboratory experiments on a model scale to real applications. With the help of a dimensional analysis by applying the Buckingham PI theorem, see e.g. [37], the dimensionless parameters can be determined, which must coincide in the laboratory model and in the real flow, so that a dynamic similarity exists. The theorem states that N physical variables with K dimensions can be represented in $N - K$ dimensionless products Π. The theorem is applied to the sluice gate in the following and the dimensionless varibals are determined.

The relevant physical variables to describe the sluice gate flow are the density of water ρ, the viscosity of water μ, the gravity acceleration g, the flow velocity e.g. the upstream velocity u_0 and a characteristic length e.g. the upstream water level h_0 ($N = 5$).

$$f_1(\rho, u_0, \mu, g, h_0) = 0 \tag{2-17}$$

The fundamental dimensions to describe the physical variables are the mass (M), length (L) and time (T) (K=3). The dimensions of the physical variables, are shown in Table 1.

Table 1: Physical variables with their dimensions for sluice gate flows

ρ	u_0	h_0	g	μ
ML^{-3}	LT^{-1}	L	LT^{-2}	$ML^{-1}T^{-1}$

Eq. (2-17) can be expressed in $N - K = 5 - 3 = 2$ dimensionless Π products, see Eq. (2-18).

$$f_2(\Pi_1, \Pi_2) = 0 \tag{2-18}$$

Following the Buckingham PI theorem, both dimensionless Π products Π_1 and Π_2 can be written as:

$$\Pi_1 = f_3(\rho, u_0, h_0, \mu) \tag{2-19}$$

$$\Pi_2 = f_4(\rho, u_0, h_0, g) \tag{2-20}$$

In the next step, exponents are introduced for the physical variables, which are then determined in such a way that the product of the physical variables becomes dimensionless.

$$\Pi_1 = \rho u_0^z h_0^y \mu^x \tag{2-21}$$

$$\Pi_2 = \rho^w u_0^v h_0^u g \tag{2-22}$$

To determine the exponents, write Eq. (2-21) and Eq. (2-22) in dimensional terms, see Eq. (2-23) and Eq. (2-24).

$$[\Pi_1] = (\mathrm{ML}^{-3})\ (L\mathrm{T}^{-1})^z (L)^y\ (ML^{-1}\mathrm{T}^{-1})^x \tag{2-23}$$

$$[\Pi_2] = (\mathrm{M}L^{-3})^w\ (\mathrm{L}T^{-1})(\mathrm{L})^v\ (LT^{-2})^u \tag{2-24}$$

The exponents of each fundamental dimension must add to zero for each equation. If we first consider Eq. (2-23), the following system of equations results for the exponents:

M: $1 + x = 0$

L: $-3 + z + y - x = 0$

T: $-z - x = 0$

If you solve the system of equations the results are $x = -1$, $y = 1$ and $z = 1$. If these values are inserted into Eq. (2-21), one obtains:

$$\Pi_1 = \frac{\rho u_0 h_0}{\mu} \tag{2-25}$$

The dimensionless product Π_1 corresponds to the Reynolds number Re. The Reynolds number is the ratio of inertia forces to viscous forces in a flow and is an important dimensionless number in fluid mechanics. If we further consider Eq. (2-25), the following system of equations is obtained:

M: $w = 0$

L: $-3w + 1 + v + u = 0$

T: $-1 - 2u = 0$

From the system of equations, we obtain for the exponents $w = 0$, $v = -\frac{1}{2}$ and $u = -\frac{1}{2}$. Substituting these values into Eq. (2-22), we obtain:

$$\Pi_2 = \frac{u}{\sqrt{g h_0}} \tag{2-26}$$

The dimensionless product Π_2 corresponds to the Froude number Fr. The dimensional analysis has thus shown that for model investigations both the Froude number (Eq. (2-27)) and the Reynolds number (Eq. (2-28)) have to match the real application.

$$\mathrm{Fr} = \frac{\mathrm{u}}{\sqrt{\mathrm{gl}}} \tag{2-27}$$

$$\mathrm{Re} = \frac{\rho \mathrm{ul}}{\mu} \tag{2-28}$$

Similar to compressible flows in aerodynamics where simultaneous Mach number and Reynolds number similarity cannot be established by model scaling, simultaneous Froud number and Reynolds number similarity cannot prevail in sluice gate flows by geometric scaling. This is shown in Figure 21, where the Froude and Reynolds numbers are plotted as a function of a characteristic length $\mathrm{l_{char}}$, for $\mathrm{u} = 1\ \frac{\mathrm{m}}{\mathrm{s}}$, $\mathrm{g} = 9.81\ \frac{\mathrm{m}}{\mathrm{s}}$, $\rho = 1000\ \frac{\mathrm{kg}}{\mathrm{m}^3}$ and $\mu = 8.89 \cdot 10^{-4}$ Pa s. Since both Froud number and Reynolds number are directly proportional to velocity, there is no change in the shape of the two dimensionless ratios as velocity is varied. The only way to achieve dynamic similarity between the model and the real application would be to experiment with different fluids to change the viscosity or density.

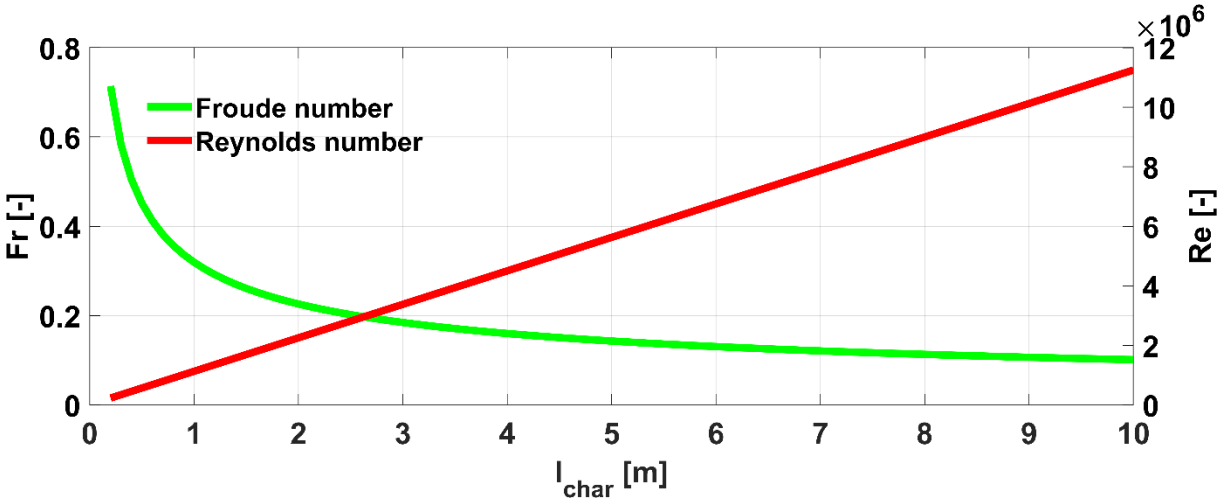

Figure 21: Behavior of Froude number and Reynolds number for different characteristic lengths

To calculate the Froude number for the sluice gate, the discharge equation (Eq. (2-4)) is applied to calculate the average flow velocity $\overline{\mathrm{u_0}} = \mathrm{Q}/\mathrm{h_0 B}$ in the upstream region as follows:

$$\overline{\mathrm{u_0}} = \mathrm{c_{D,dB}}\ \varepsilon \sqrt{2\mathrm{g}(\mathrm{h_0} - \mathrm{a})} \tag{2-29}$$

If the average upstream velocity $\overline{\mathrm{u_0}}$ (Eq. (2-29)) is substituted into the formula for the Froude number Fr (Eq. (2-27)), the upstream Froude number $\mathrm{Fr_0}$ is obtained:

$$\mathrm{Fr}_0 = \sqrt{2}\, c_{D,dB}\ \varepsilon \sqrt{(1-\varepsilon)} \tag{2-30}$$

From Eq. (2-30) it is clear that with geometric similarity $\varepsilon = \text{const.}$ and constant discharge coefficient $c_{D,dB}$, Froud number similarity also prevails. With the mean upstream velocity $\overline{u_0}$, see Eq. (2-29), the upstream Reynolds number Re_0 can also be calculated from Eq. (2-28):

$$\mathrm{Re}_0 = \frac{\rho\, c_{D,dB}\, a \sqrt{2g(h_0 - a)}}{\mu} \tag{2-31}$$

As can be seen from the equation above, the upstream Reynolds number Re_0 changes with the scaling. In the literature, the discharge coefficient is generally considered constant for $\varepsilon = \text{const.}$ and thus the Reynolds number dependency is neglected and only the Froud number similarity is prevailed. Nago [38] as well as Roth and Hager [27] have carried out investigations for different gate openings a to examine the scaling effects on the discharge coefficient. Nago [38] investigated the flow of standard sluice gates with opening heights $a = 1.0$ cm to $a = 12.0$ cm and gate widths from $B = 10$ cm to $B = 40$ cm and found that the discharge coefficient converges to a fixed value, when the gate opening is above a limit opening height a_l, for constant ε and is thus independent of the Reynolds number. For $a_l > 6.0$ cm and $\varepsilon < 0.5$ he could no longer detect any appreciable influence of scaling effects on the flow. The discharge coefficient measured by Nago, which converges for large sluice gate openings a, agrees well with the measurements of Henry [27]. For small sluice gate openings $a_l < 6.0$ cm, however, Nago found a clear dependence of the discharge on the model scaling and thus on the Reynolds number. Furthermore, Nago could not find a clear dependence of the discharge coefficient on the channel width B. The smallest relative gate width investigated by Nago was $\zeta = \frac{10\text{ cm}}{8\text{ cm}} = 1.25$, as shown by Steppert, Epple and Malcherek [39] and as will be described in more detail in this thesis, significant width effects on the discharge coefficient only occur at $\zeta < 1$.

Furthermore, Nago also suspected a dependence of the jet contraction on the surface tension σ or the Weber number We, see Eq. (2-32), which can also be derived from the dimensional analysis when the surface tension σ is taken into account. However, in Nago's experiments, which are supposed to prove this dependence, he also varied the Froude number Fr with the Weber number We.

$$\mathrm{We} = \frac{\rho u^2 l_{char}}{\sigma} \tag{2-32}$$

Roth and Hager [28] also investigated the discharge of standard sluice gates with different opening heights in the range $a = 10$ mm to $a = 120$ mm. They found no significant scaling effects or Reynolds number dependencies on the discharge coefficient for $a_l \geq 50$ mm. Nago did not carry out any investigations at $a = 50$ mm, but found that at $a = 60$ mm there is no longer any significant Reynolds number dependence and at the next smaller opening height $a = 40$ mm the Reynolds number has an influence on the discharge. Although he stated the limit at $a_l = 60$ mm, his test results would also confirm the limit of Roth and Hager at $a_l = 50$ mm. It should be noted here that this is not a hard limit anyway, but rather a flowing (or smooth) transition where the Reynolds number dependence becomes vanishingly small and is practically negligible. According to Roth and Hager [28], the influence of the surface tension only occurs at much smaller relative sluice gate openings than those investigated, which means that the dependence on the Weber number We can be neglected for practical applications in hydraulic engineering. The dependence on the Reynolds number is also practically negligible for most real applications, as sluice gate flows outside of laboratories are typically operated at gate openings larger than $a = 50$ mm.

In order to calculate the discharge coefficient for small sluice gate openings $a < 50$ mm taking into account viscous effects, formulas were derived by Roth and Hager [28]. They found that if the Torricelli discharge coefficient $c_{D,T}$ for small gate openings $a < 50$ mm is plotted as a function of the relative gate opening ε, a minimum value for $c_{D,T}$ occurs. This minimum value $c_{D,T,min}$, is at the relative gate opening ε_{min} , and depends on the gate Reynolds number Re_a introduced by Roth and Hager. The calculation formulas for $c_{D,T,min}$ (Eq. (2-33)), ε_{min} (Eq. (2-34)) and Re_a (Eq. (2-35)) according to Roth and Hager are given in the following equations:

$$c_{D,T,min} = 0.60 - \frac{1}{18}\log\left(\frac{Re_a}{1000}\right) \tag{2-33}$$

$$\varepsilon_{min} = 0.05 + 0.40\log\left(\frac{Re_a}{1000}\right) \tag{2-34}$$

$$Re_a = \frac{\rho a\sqrt{2ga}}{\mu} \tag{2-35}$$

Furthermore, according to Roth and Hager, the scaling effects or the Reynolds number dependence disappear for small epsilons ($\varepsilon \to 0$) and the discharge coefficient assumes the base value $c_{D,T0} = 0.594$ for $\varepsilon \to 0$ independent of the opening height a. With these newly

introduced values the discharge coefficient $c_{D,dB,Re}$ for small gate openings ($a < 50$ mm) can be calculated considering the Reynolds number dependence using Eq. (2-36):

$$c_{D,dB,Re} = \frac{\left(1 - \frac{\varepsilon}{\varepsilon_{min}}\right)^2 \left(c_{D,T0} - c_{D,T,min}\right) + c_{D,T,min}}{\sqrt{1 - \frac{a}{h_0}}} \tag{2-36}$$

The results of Eq. (2-36) for $a = 0.05$ m, $a = 0.01$ m and $a = 0.005$ m are plotted in Figure 22. Due to the scaling effects, the discharge becomes larger for small ε according to Roth and Hager.

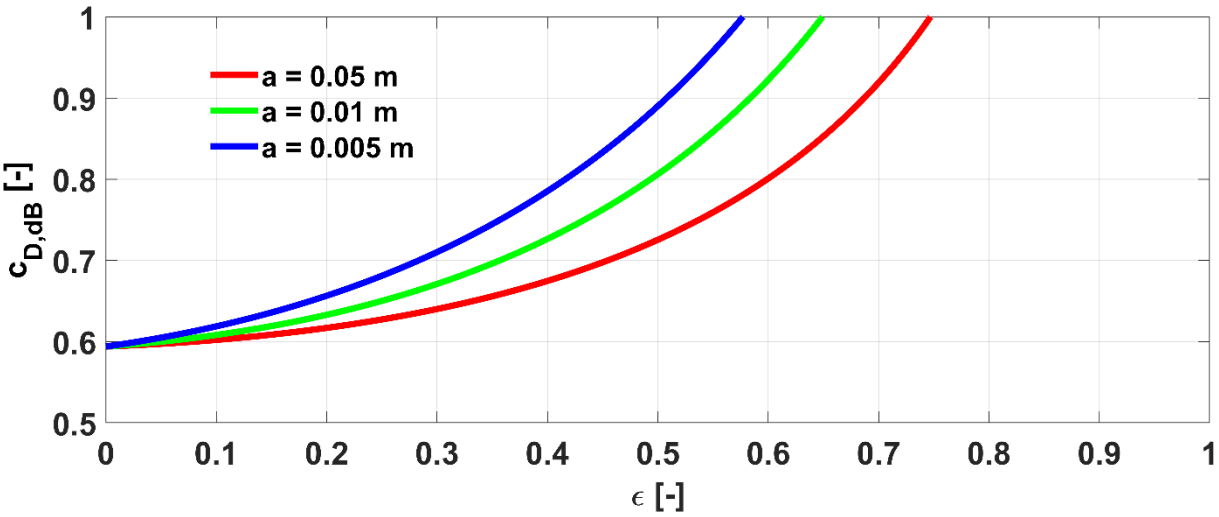

Figure 22: Discharge coefficient $c_{D,dB,Re}$ of the standard sluice gate in dependency of the relative gate ε opening for various gate opening height a

In summary, it can be said that for geometrically similar sluice gates with opening heights $a > 50$ mm, only the Froud number Fr similarity must be given. The influence of the Reynolds number Re is not significant here. In this work, sluice gate flows with opening height of $a = 100$ mm are analyzed in CFD, which allows the Reynolds number dependence to be neglected. In applications in hydraulic engineering, also usually only flows with $a > 50$ mm are of practical importance, whereby the results of this work can be directly transferred to these applications via the Froude number similarity.

2 .4 Hydraulic Jump Downstream of Sluice Gates

As shown in the previous chapter, the outflow can basically be divided into free and submerged outflow. If the outflow is free, the flow is supercritical. However, it does not remain supercritical forever, but becomes subcritical again sooner or later when, for example, the normal water depth changes or an obstruction or hydraulic structure is located downstream. This water depth change is abrupt and is called hydraulic jump. Figure 23 shows the image of a laboratory flume with a standard sluice gate. On the left side the gate and a small part of the upstream region can be seen. In the tailwater of the gate in the center of the image, the free outflow is clearly visible. Further downstream, the high turbulent hydraulic jump can be seen, where the flow changes from supercritical to subcritical.

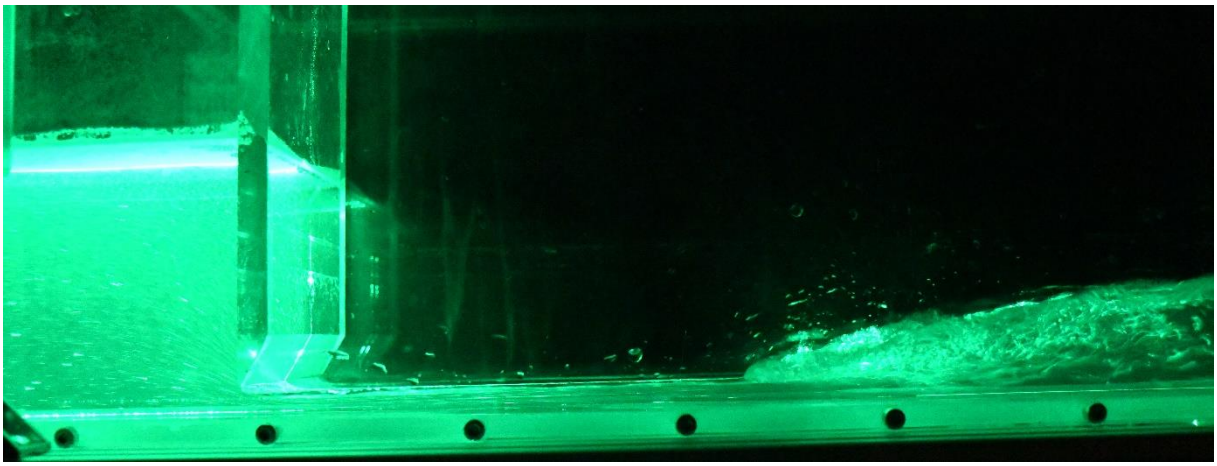

Figure 23: Standard sluice gate with supercritical outflow and hydraulic jump downstream of the gate

Figure 24 shows the schematic drawing of the hydraulic jump. The water height of the supercritical flow upstream of the hydraulic jump h_I would correspond to the water depth of the supercritical outflow h_1 at the sluice gate. The water height downstream of the hydraulic jump is designated h_{II}. This water height downstream of the hydraulic jump h_{II} can be calculated by means of the integral momentum balance. The integral momentum balance and the mass conservation equation are presented in detail in chapter 3.1, but are already applied here as an example.

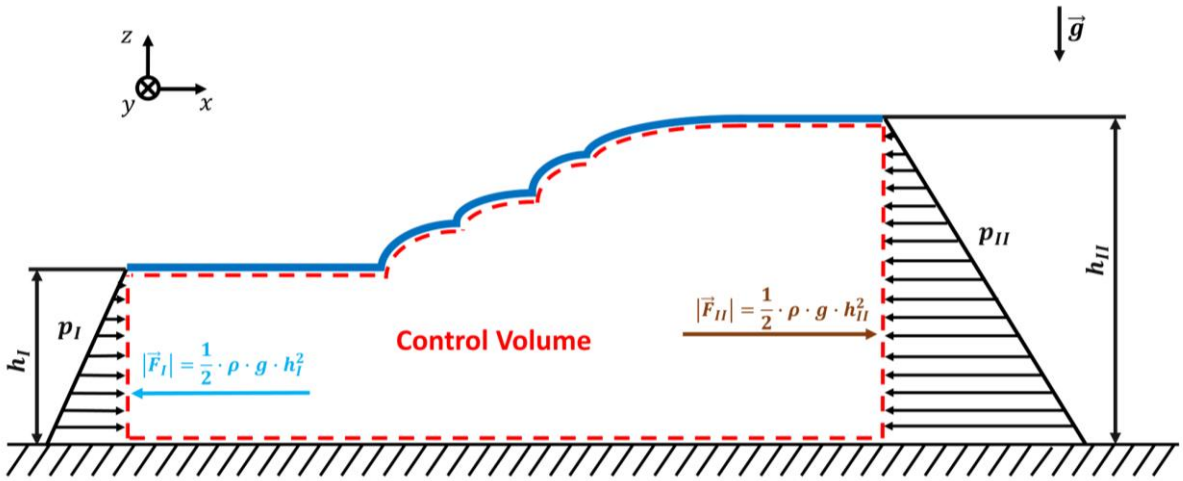

Figure 24: Schematic drawing of a hydraulic jump with control volume

To calculate the hydraulic jump, a control volume is introduced as shown in Figure 24. The limits of the control volume were set immediately upstream of the jump at the supercritical flow and immediately downstream of the hydraulic jump at the subcritical flow, see also Figure 24. Since the size of the control volume is thus small, friction losses at the walls of the control volume can be neglected in the momentum balance. In addition, we consider the flow direction to be horizontal, which eliminates the term of the gravity forces, and the flow is assumed to be stationary, which eliminates the transient term of the momentum equation. Finally, the momentum balance for the hydraulic jump is:

$$0 = -\int_{\partial\Omega} p\,\vec{n}\,dA - \int_{\partial\Omega} \rho\vec{V}\left(\vec{V}\cdot\vec{n}\right) dA \tag{2-37}$$

The streamlines in the head- and tailwater of the hydraulic jump are assumed to be parallel to the ground, resulting in a hydrostatic pressure distribution at the control volume boundaries. In addition, a constant velocity profile can be assumed upstream and downstream of the hydraulic jump. With these conditions, the following notation results for the momentum equation:

$$-\rho u_I^2 h_I B + \rho u_{II}^2 h_{II} B = \frac{1}{2}\,\rho g h_I^2 B - \frac{1}{2}\,\rho g h_{II}^2 \tag{2-38}$$

The continuity equation for the hydraulic jump can be written as follows:

$$\rho B h_I u_I = \rho B h_{II} u_{II} \tag{2-39}$$

By substituting Eq. (2-39) into Eq. (2-38) gives:

$$u_I^2 \left(\frac{h_I^2}{h_{II}} - h_I\right) = \frac{g}{2}\,(h_I^2 - h_{II}^2) \tag{2-40}$$

The flow velocity in the supercritical flow u_I is replaced by the dimensionless Froude number Fr_I with $u_I = Fr_I\sqrt{gh_I}$, resulting in the following equation:

$$2Fr_I^2\left(\frac{h_I}{h_{II}}\right)^3 - (2Fr_I^2 + 1)\left(\frac{h_I}{h_{II}}\right)^2 + 1 = 0 \tag{2-41}$$

The equation contains a total of three solutions, one of which is $\frac{h_I}{h_{II}} = 1$. With this one, there is no change in the flow. By polynomial division with the trivial solution $\frac{h_I}{h_{II}} = 1$ and subsequent application of the solution formula for quadratic equations, the flow can be solved analytically (see Malcherek [1]):

$$\left(\frac{h_2}{h_1}\right)_{1/2} = \frac{1}{2}\left(\pm\sqrt{8Fr_I^2 + 1} - 1\right) \tag{2-42}$$

The negative solution is not possible, because one of the water depths would have to be negative. The positive solution of Eq. (2-42), is shown in Figure 25. The solutions of the equation for $Fr_I < 1$ are also not possible in real flows since a spontaneous jump from the subcritical to supercritical flow is not possible. For the sake of completeness, this solution, and the trivial solution $\frac{h_I}{h_{II}} = 1$ are nevertheless also shown in Figure 25.

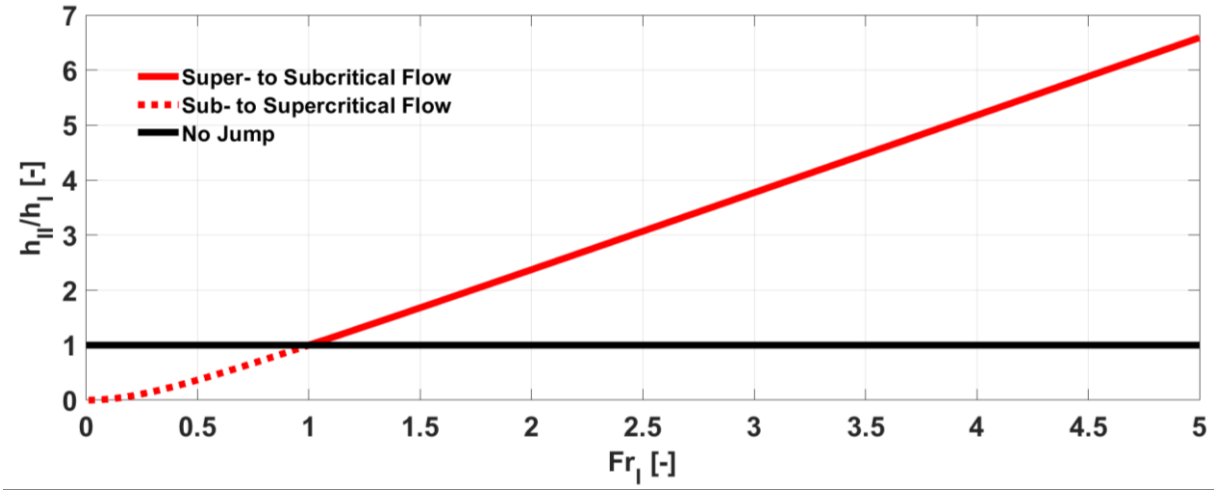

Figure 25: Water level ratio according to the integral momentum balance of hydraulic jumps for different Froude numbers Fr_I upstream of the jump

To calculate the energy losses due to the hydraulic jump, the energy heights up- and downstream of the hydraulic jump are calculated first. For the velocity $u_I = Fr_I\sqrt{gh_I}$ the Froude number formulation is used again. Thus, for the energy height upstream of the hydraulic jump we get:

$$H_I = h_I + \frac{u_I^2}{2g} = h_I\left(1 + \frac{Fr_I^2}{2}\right) \tag{2-43}$$

Before the energy height H_{II} is determined, first from the continuity equation Eq. (2-39) the velocity u_{II} downstream of the hydraulic jump is calculated. The water height downstream of the hydraulic jump h_{II} is calculated by Eq. (2-42), which finally gives the velocity u_{II} downstream of the hydraulic jump:

$$u_{II} = \frac{u_I h_I}{h_{II}} = \frac{Fr_I\sqrt{g\,h_I}}{\frac{\sqrt{8Fr_I^2+1}-1}{2}} \tag{2-44}$$

From Eq. (2-42) and Eq. (2-44) finally results for the energy height H_{II} downstream of the hydraulic jump:

$$H_{II} = h_{II} + \frac{u_{II}^2}{2g} = h_I\left(\frac{\sqrt{8Fr_I^2+1}-1}{2} + \frac{1}{2}\left(\frac{Fr_I}{\frac{\sqrt{8Fr_I^2+1}-1}{2}}\right)^2\right) \tag{2-45}$$

From the energy height H_I in the upstream region of the hydraulic jump (Eq. (2-43)) and the energy height H_{II} in the downstream region of the hydraulic jump (Eq. (2-45)), the relative energy height loss $H_{L,rel}$ can be calculated.

$$H_{L,rel} = \frac{H_{II} - H_I}{H_I} = \frac{\left(\frac{\sqrt{8Fr_I^2+1}-1}{2} + \frac{1}{2}\left(\frac{Fr_I}{\frac{\sqrt{8Fr_I^2+1}-1}{2}}\right)^2\right)}{\left(1 + \frac{Fr_I^2}{2}\right)} - 1 \tag{2-46}$$

As can be seen from Eq. (2-46), the relative energy height loss $H_{L,rel}$ depends only on the Froud number Fr_I upstream of the hydraulic jump. The relative energy height loss as a function of the Froud number Fr_I is shown in Figure 26. Here it becomes again clear that with the solution $Fr < 1$ a spontaneous energy gain takes place, which is not possible according to the laws of thermodynamics. For $Fr = 1$, no jump takes place and therefore the energy loss $H_{L,rel} = 0$. For $Fr > 1$, a hydraulic jump with energy losses takes place. The energy height losses $H_{L,rel}$ increases, as can be seen in Figure 26, with increasing supercritical flow Froud number Fr_I.

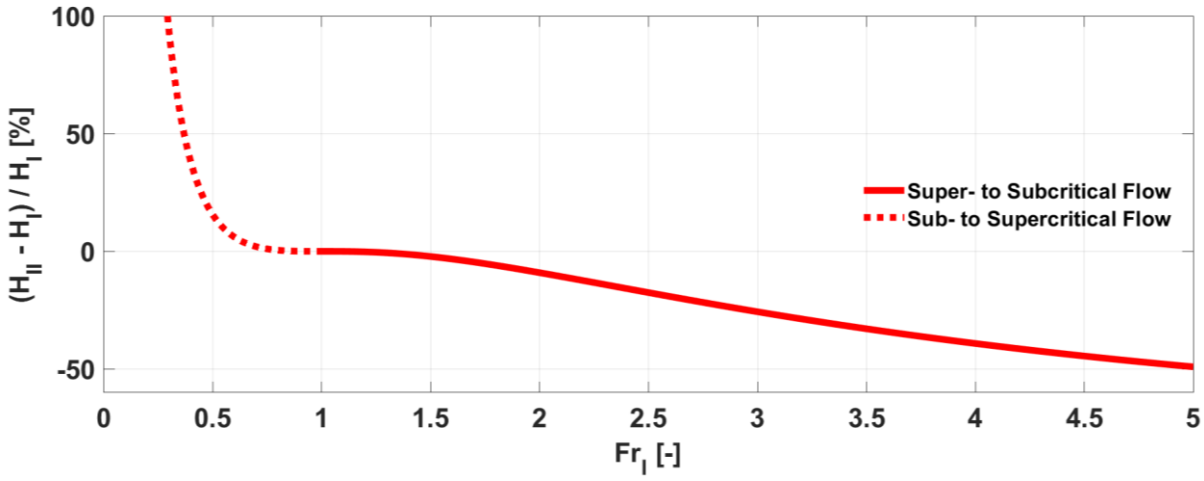

Figure 26: Energy loss through hydraulic jumps as a function of the Froude number Fr_I upstream of the jump

As the example shows, using the conservation of energy would have resulted in significant errors due to the neglect of energy losses. With the help of the momentum balance, however, the water depth downstream of the jump h_{II} can be calculated correctly. The example shows the significant advantage of using the momentum balance. The energy losses do not have to be known, a priori, which raises the question why sluice gate flows are also not calculated using the momentum balance, but why the approach of energy conservation shown in Figure 5 is still used. This question will probably not be answered in this work, but here the momentum balance for the standard and inclined sluice gate is worked out to provide the possibility of discharge calculation directly from the momentum balance. The elaboration for this is described in the following chapters.

3 Integral Conservation Equations Applied on Sluice Gates

In this chapter, the conservation laws for mass and momentum are applied to sluice gates. The equations are generally suitable for solving all fluid mechanical problems. For some problems, such as supersonic (compressible) flows, additional conservation equations such as the conservation of energy are required. In hydraulics and hydrodynamics, however, the conservation equations of mass and momentum are often sufficient. As an example, the hydraulic jump from supercritical to subcritical flow was already shown in the previous chapter, which takes place in the tailwater of sluice gates with supercritical outflow. The water height downstream of the hydraulic jump was calculated by solving the integral equations of mass and momentum conservation. It was also shown the error that would have been made if the conservation of energy equation had been used without taking dissipation losses into account, as is the case with the calculation of sluice gates. In the following, the conservation equations for mass and momentum are described in more detail and are applied on sluice gate flows. For this purpose, various control volumes are also examined and a formula for calculating the discharge of sluice gates is derived from the conservation of mass and momentum.

3.1 Conservation Equations

The two basic physical principles required to calculate sluice gate flows are conservation of mass and conservation of momentum. Mass conservation states that mass can neither be destroyed nor generated. For a closed system it follows that,

$$\left.\frac{dM}{dt}\right|_{system} = 0 \tag{3-1}$$

where

$$M_{system} = \int_{M(system)} dm = \int_{\forall(system)} \rho \, d\forall \tag{3-2}$$

Further we want to consider the conservation of momentum. That is based on Newton's second law, which states that the force is equal to the time rate of change of momentum. For a closed system, the conservation of momentum can be written as follows,

$$\left.\frac{d\vec{I}}{dt}\right|_{system} = \vec{F} \tag{3-3}$$

where

$$\vec{I}_{system} = \int_{M(system)} \vec{V} dm = \int_{V(system)} \vec{V}\, \rho\, dV \tag{3-4}$$

In order to transfer the conservation equations for a closed system (Eq. (3-1) and Eq. (3-3)) to an open system, through whose system boundaries mass as well as momentum can flow in and out, the Reynolds transport theorem is applied, see e. g. [40]. For mass conservation for an arbitrary control volume Ω with the open boundary $\partial\Omega$ can be written:

$$\left.\frac{dM}{dt}\right|_{\Omega} = -\int_{\partial\Omega} \rho\left(\vec{V}\cdot\vec{n}\right) dA \tag{3-5}$$

For the conservation of momentum, the following equation results analogously:

$$\left.\frac{d\vec{I}}{dt}\right|_{\Omega} = \vec{F} - \int_{\partial\Omega} \rho\vec{V}\left(\vec{V}\cdot\vec{n}\right) dA \tag{3-6}$$

The forces $\vec{F}$ that occur in hydrodynamics can be divided into volume forces and surface forces. Volume forces are caused by fields. Relevant for hydrodynamics is the effect of the gravitational field of the earth with the gravitational acceleration $\vec{g}$ on the mass M stored in the control volume Ω. Further, pressure forces and viscous forces act on the boundaries $\partial\Omega$ of the control volume and therefore are surface forces. Substituting these into Eq. (3-7), one obtains for the time rate change of the momentum in the control volume.

$$\left.\frac{d\vec{I}}{dt}\right|_{\Omega} = M\vec{g} - \int_{\partial\Omega} p\,\vec{n}\, dA + \vec{F}_{viscous} - \int_{\partial\Omega} \rho\vec{V}\left(\vec{V}\cdot\vec{n}\right) dA \tag{3-7}$$

As can be seen from the mass conservation equation Eq. (3-5) and the momentum conservation equation Eq. (3-7), the mass and momentum flux through the control volume boundaries have a negative sign. This is due to the fact, that the normal vector $\vec{n}$ always points outward away from the control volume surface. If the normal vector $\vec{n}$ and the velocity vector $\vec{V}$ are opposed, the transport quantity flows into the control volume and the scalar product $\vec{n}\cdot\vec{V}$ becomes negative. However, since there is an increase in transport size, the momentum change must be positive. This is corrected by the negative sign. The same applies vice versa for outflowing mass and outflowing momentum.

3.2 Control Volumes for Calculating the Discharge of Sluice Gates

In order to apply the momentum balance for the sluice gate and to determine the discharge from it, the selection of a suitable control volume (CV) is essential. There are several possible control volumes, the advantages, and disadvantages for three different control volumes will be discussed in this chapter. The first control volume shown in Figure 27 is similar to the control volume introduced by Malcherek [41] [42], who was the first to calculate the discharge of standard sluice gates using the momentum balance, but with simplified pressure distributions.

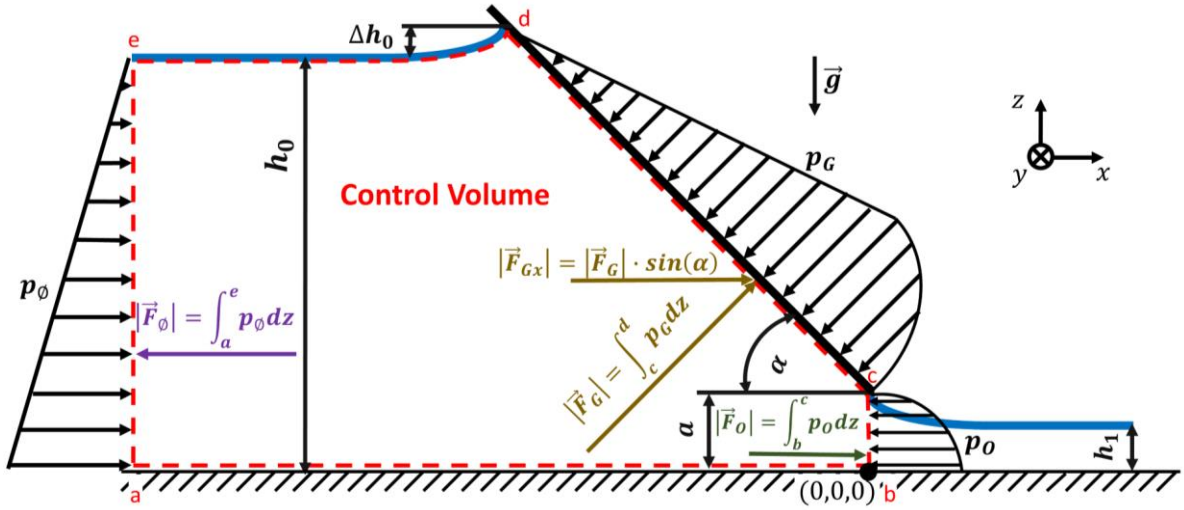

Figure 27: Control volume I - large control volume with boundary at the opening

For the calculation of the sluice gate discharge, it is sufficient only to look at the horizontal x-component of the momentum equation. Therefore, gravity cancels out in Eq. (3-7). Further, it was assumed, that the flow is inviscid $\vec{F}_{viscous} = 0$ and steady $\frac{d}{dt} = 0$. Comparable to the sudden contraction in pipe flows, which was studied by Malcherek and Müller [43], the momentum balance reduces to a balance of momentum fluxes and pressure forces:

$$\left.\frac{d\vec{I}}{dt}\right|_\Omega = 0 = -\int_{\partial\Omega} p\,\vec{n}\,dA - \int_{\partial\Omega} \rho\vec{V}\left(\vec{V}\cdot\vec{n}\right) dA \tag{3-8}$$

The pressure force acting on the control volume I, shown in Figure 27, is the sum of the upstream hydrostatic pressure force $F_\emptyset$, the x-component of the gate pressure force $F_G \sin(\alpha)$ and the pressure force at the opening F_O. Because the surface vectors between a-e and b-c are parallel to the x-axis, see Figure 27 and the fluid is assumed as incompressible, i.e. the density ρ is constant and considering also the pressure p and velocity u as constant along the width B, Eq. (3-8) becomes:

$$B\int_b^c \rho u^2\ dz - B\int_a^e \rho u^2\ dz = F_\emptyset - F_G\cos(\alpha) - F_O \tag{3-9}$$

The integrals on the left side can be also written by mean velocities $\bar{u}$, if the momentum coefficient β (Boussinesq coefficient) is introduced for every velocity profile u at the control volume boundaries:

$$\beta = \frac{B\int_{z_1}^{z_2} u^2\ dz}{A\ \bar{u}^2} \tag{3-10}$$

The limits of the integral, shown in Eq. (3-10), are the lower z-coordinate z_1 of the control volume boundary and the upper z-coordinate z_2 of each control volume boundary, at the corresponding x-coordinate. Further, by using mean velocities $\bar{u} = Q/A$ and assuming constant density $\rho = \text{const.}$ the continuity equation, Eq. (3-5), can be written as:

$$A_\emptyset\ \overline{u_\emptyset} = A_O\overline{u_O} \tag{3-11}$$

Where in Eq. (3-11) $A_\emptyset = h_\emptyset\ B$ is the upstream flow cross sectional area, $\overline{u_\emptyset}$ is the mean upstream velocity, $A_O = a\ B$ is the area of the gate opening and $\overline{u_O}$ is the mean opening velocity. Substituting Eq. (3-10) and Eq. (3-11) in Eq. (3-9) and rearranging, Eq. (3-9) becomes:

$$\beta_O A_O\ \bar{u}_O{}^2 - \beta_\emptyset A_\emptyset\left(\frac{A_O\overline{u_O}}{A_\emptyset}\right)^2 = \frac{F_\emptyset - F_G\cdot\cos(\alpha) - F_O}{\rho} \tag{3-12}$$

$$A_O^2\ \overline{u_O}^2\left(\frac{\beta_O}{A_O} - \frac{\beta_\emptyset}{A_\emptyset}\right) = \frac{F_\emptyset - F_G\cos(\alpha) - F_O}{\rho} \tag{3-13}$$

with $Q = A_O\overline{u_O}$ Eq. (3-13) becomes:

$$Q = \sqrt{\frac{F_\emptyset - F_G\cos(\alpha) - F_O}{\rho\left(\frac{\beta_O}{A_O} - \frac{\beta_\emptyset}{A_\emptyset}\right)}} \tag{3-14}$$

and with $A_\emptyset = h_\emptyset\ B$ and $A_O = a\ B$, Eq. (3-14) finally becomes:

$$Q = \sqrt{\frac{F_\emptyset - F_G\ \cos(\alpha) - F_O}{\frac{\rho}{B}\left(\frac{\beta_O}{a} - \frac{\beta_\emptyset}{h_\emptyset}\right)}} \tag{3-15}$$

Eq. (3-15) can be used to calculate the discharge under standard and inclined sluice gates from the integral momentum balance for control volume I (Figure 27). However, the pressure forces $F_\emptyset$, F_G and F_O as well as the momentum coefficients β_O and $\beta_\emptyset$ must be known.

Because, upstream of the sluice gate the streamlines are parallel to the x-coordinate and hence the pressure distribution has to be hydrostatic and therefore the upstream pressure integral can be written as $F_{\emptyset} = \frac{1}{2}\,\rho\,g\,h_0^2\,B$. The pressure integral at the gate F_G and at the opening F_O are depending on the angle of inclination α and on the relative gate opening ε. To determine these forces, the pressure distribution at the gate p_G and at the opening p_O were first parametrized based on CFD computations and then integrated. Also, the momentum coefficients are parametrized based on CFD data.

The necessary parameterizations for forces and momentum coefficients depend on the choice of the control volume. To avoid the parameterization of the gate force F_G, a control volume as shown in Figure 28 could be chosen. If applying Eq. (3-8) for this control volume, we get:

$$B\int_b^c \rho u^2\ dz - B\int_a^f \rho u^2\ dz + B\int_f^c \rho u(\vec{v}\cdot\vec{n})\,dx = F_{\emptyset} - F_O \qquad (3\text{-}16)$$

Eq. (3-16) shows that although the pressure force on the sluice gate wall is no longer needed, another term is added for the momentum flux at the boundary of the control volume, c-f. While the force on the sluice gate wall is a descriptive quantity and is also relevant, for example, for static calculations, the momentum flux at the control volume boundary c-f is less descriptive.

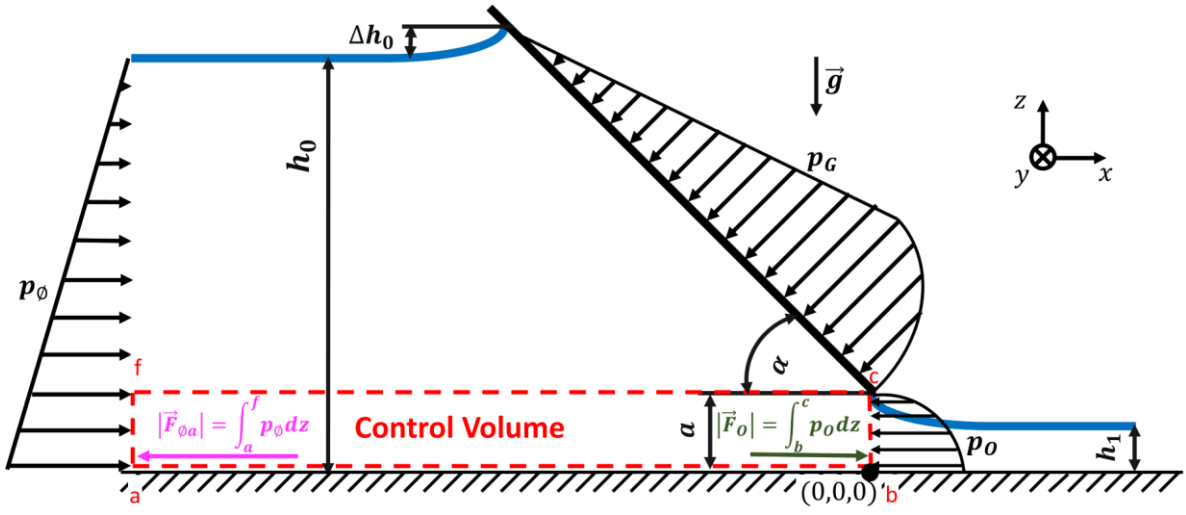

Figure 28: Control volume II: small control volume with boundary at the opening

Another possible control volume is shown in Figure 29. Here, instead of the control volume boundary at the opening, the control volume boundary in the downstream area was selected. Applying equation Eq. (3-8) to the control volume, the result is:

$$B\int_{h}^{g}\rho u^{2}\ dz - B\int_{a}^{e}\rho u^{2}\ dz = F_{\emptyset} - F_{G}\cos(\alpha) - F_{1} \tag{3-17}$$

Instead of the pressure force and the velocity at the opening, the two quantities in the downstream area must be known for this control volume. These are dependent on the jet contraction. Since the jet contraction c_C and thus the downstream water level h_0 changes depending on the angle of inclination α and relative gate opening ε, the control volume would also change for each calculation.

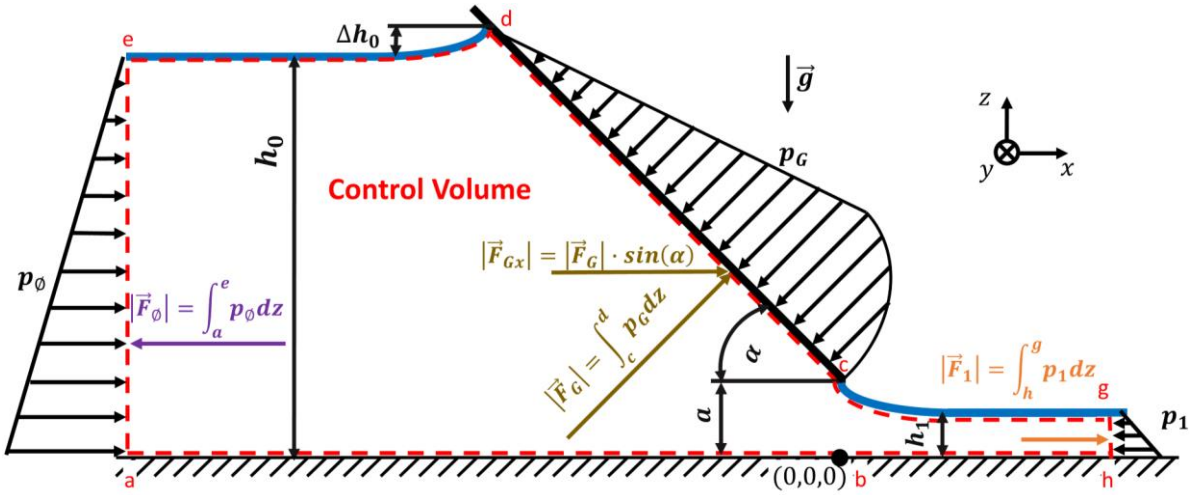

Figure 29: Control volume III: large control volume with downstream boundary

In contrast to control volume I, where the flow is calculated directly at the opening of the gate, in control volume III the flow is determined in the tailwater. In the derivation of Eq. (3-17), a frictionless flow was assumed for simplification ($F_{Viscous} = 0$). In reality, frictional forces occur at the control volume boundaries due to the wall shear stresses, which is why the control volume should be selected as small as possible. In addition, the wall shear stresses in the supercritical flow are much greater than in the subcritical flow, as shown in Figure 30, because of the high velocities at supercritical flows. For the example shown in Figure 30, the friction forces at the bottom when choosing CV III with a total of 5.3 N/m, is 4.8 times as large when choosing CV I with 1.1 N/m. In order to keep the error in neglecting the friction forces as small as possible, it is recommended to select CV I. Since the subject of wall shear stress distribution has only been dealt with to a limited extent in the literature, the wall shear stress at the bottom and at the side walls for various relative sluice gate widths ζ has been investigated and is shown in appendix A.

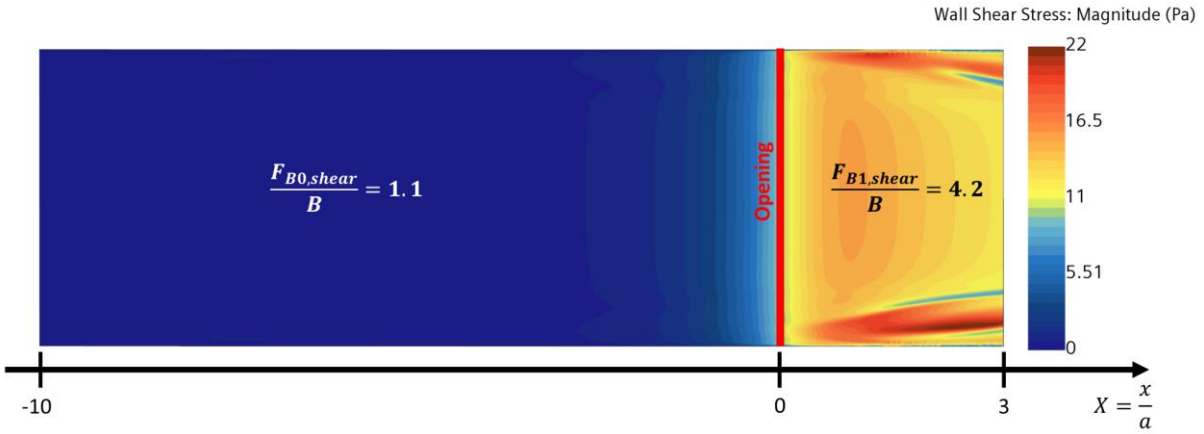

Figure 30: Up- and downstream bottom wall shear stress from CFD ($h_0 = 0.4$, $a = 0.1$ and $\zeta = 4$)

The comparison of the different control volumes has shown that the CV I, shown in Figure 27, is best suited for the discharge determination of sluice gates by momentum balance. As already mentioned, the forces F_G and F_O as well as the momentum coefficients $\beta_\emptyset$ and β_O must be determined in order to calculate the discharge. To determine these quantities, CFD simulations for different relative gate openings ε and angles of inclination α are first performed in this work. The CFD simulations are described in the following chapter. Based on the simulation results, parameterizations of the pressure distributions are carried out, from which the pressure forces can be determined by integration. Furthermore, the parameterization of the momentum coefficients is also carried out based on the CFD simulations in order to be able to determine the sluice gate discharge from momentum balance.

4 CFD Simulation of Sluice Gate Flows

To become a detailed insight into the flow processes of sluice gate flows, CFD simulations were performed using the commercial CFD solver Simcenter Star CCM+ from Siemens PLM Software. In the following sections, the used models, the simulation setup and the grid study are presented. For detailed information on the used models, refer to the Simcenter Star CCM+ product documentation [44].

4.1 Numerical Models

Sluice gate flows are gravity-driven flows in an open channel. From a fluid mechanics perspective, the channel is partially filled with water (liquid) and partially filled with air (gas). To model this multiphase flow with free surfaces in CFD, the Volume of Fluid (VOF) method is applied. The flow is calculated using the Unsteady Reynolds Averaged Navier-Stokes (URANS) equations [45]. The solution is quasi-steady, but the solver diverges by using the steady solver with the RANS equations. In the URANS solution, the free surface develops in the downstream region first, starting from the initial condition where no water is at the downstream region, see Figure 34. This URANS method of solution showed to be stable, for all investigated relative gate openings ε and angles of inclination α.

For the closure of the governing equations (URANS), the k-ω SST Menter two-equation turbulence eddy viscosity model ([46] [47] [48]) was selected. In Figure 31 the results of the chosen k-ω SST Menter two-equation turbulence model are compared by the discharge coefficient $c_{D,dB}$, the gate force F_G and the opening force F_O with other two-equation turbulence models such as the standard k-ω model [49], the standard k-ε model [50], the realizable k-ε Two-Layer model [51] and also with the one-equation Spalart-Allmaras turbulence model [52]. While the standard k-ω model overestimates F_G and F_O and underestimates the discharge coefficient $c_{D,dB}$, the other investigated models were underestimating F_G and F_O and overestimating $c_{D,dB}$. The biggest deviations were found for the standard k-ε model, which is the oldest of the investigated models and the one-equation model of Spalart and Allmaras. The absolute deviations are small (<0.3%) and for the more recent standard k-ω model and realizable k-ε two-layer model, the deviations are even smaller (<0.11%). Comparing the results of all other turbulence models with the k-ω SST model, it can be seen that the deviations are small, in the order of 0,1% or 0,2%. Since also the k-ω SST is a very well tested, robust, well documented, and widely recommended turbulence model it was used throughout the computations in this work. For the wall treatment, the all-y^+ model was chosen.

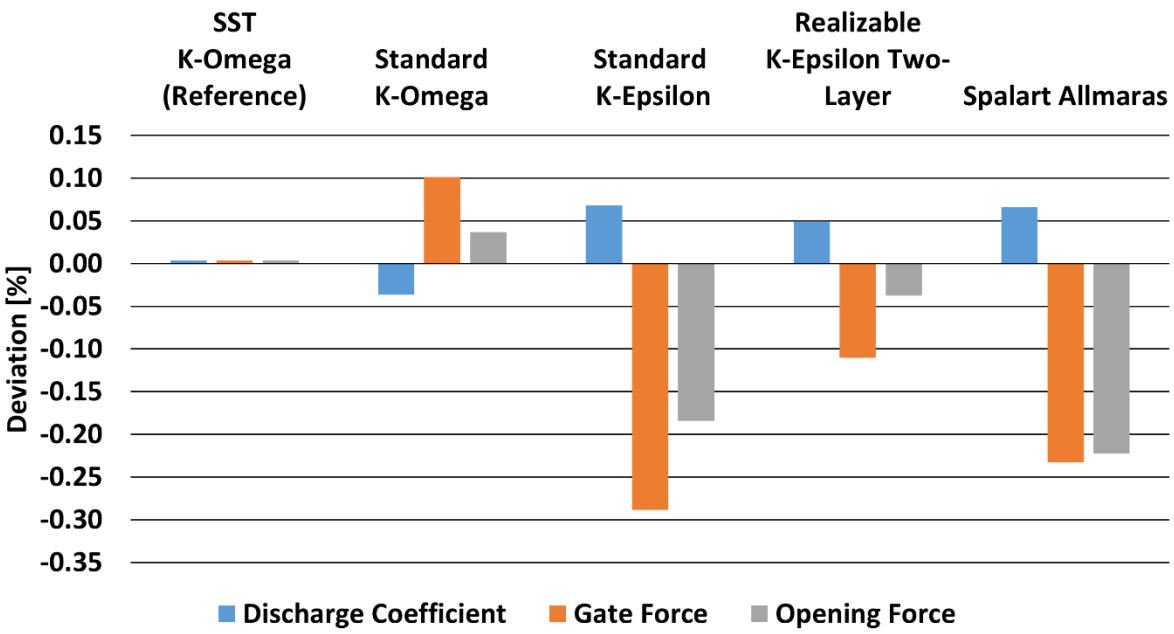

Figure 31: Deviation of discharge coefficient, gate force and opening force for investigated turbulence models compared to SST k-Omega model (ε=0.25)

The free surface was modeled using the multiphase model with the Volume of Fluid (VOF) [53] approach. Former CFD investigations e. g. Kim [54], Cassan et al. [34] and Oner [55] have shown that the chosen numerical models are very well suited to calculate sluice gate flows. The fluids were treated as incompressible for both phases. The assumption of incompressibility for the simulation of sluice gates is also valid for the gas phase (air), because the pressure of the gas phase is ambient pressure, and the velocities are low compared to the speed of sound and therefore the Mach number is small (M<0.1).

4.2 Solvers

The segregated solver of Star-CCM+ was used to solve the differential equation. The conservation equations are solved sequentially. To avoid mixing of the two phases in the VoF model, the High Resolution Interface Capturing (HRIC) method is used for solving the multiphase flow. The sharpening factor of the HRIC solver was set to 0.5. The time step was chosen as $\Delta t=0.1$ s and 15 iterations are calculated per time step. The simulation has been shown to run stable and converge well with these settings, with a comparatively low computational cost for the high spatial resolution simulations. The simulations were computed on the Emmy parallel cluster of the Erlangen National High Performance Computing Center [56]. As convergence criteria the mass flow balance between inlet and opening, see Eq. (3-5) and the momentum balance between inlet and opening/gate, see Eq. (3-7) were monitored.

4.3 Simulation Domain and Boundary Conditions

The simulation domain is shown in Figure 32. The simulation domain is divided into an upstream and a downstream region, which are connected by an internal interface. Care has been taken so that the cell nodes on both sides of the interface coincide perfectly, as it can be seen in Figure 33. The benefit of such an interface is, that the scalar values can be directly evaluated at the interface, in contrast to e. g. a plane section were the values have to be mapped into the plane section from adjacent cells. As a result, the opening pressure distribution and the opening momentum coefficient would not be evaluated exactly at the opening under the gate lip. In addition, the two regions with interface can be used to represent a sluice gate with a thickness of zero in the simulations, which means that the effects of the thickness of the gate lip can be excluded. For wide gate lips, there is a suction at the lower sluice gate edge which affects the flow as shown by Patt and Gonsowski [61] or Ahmed and Moayed [62].

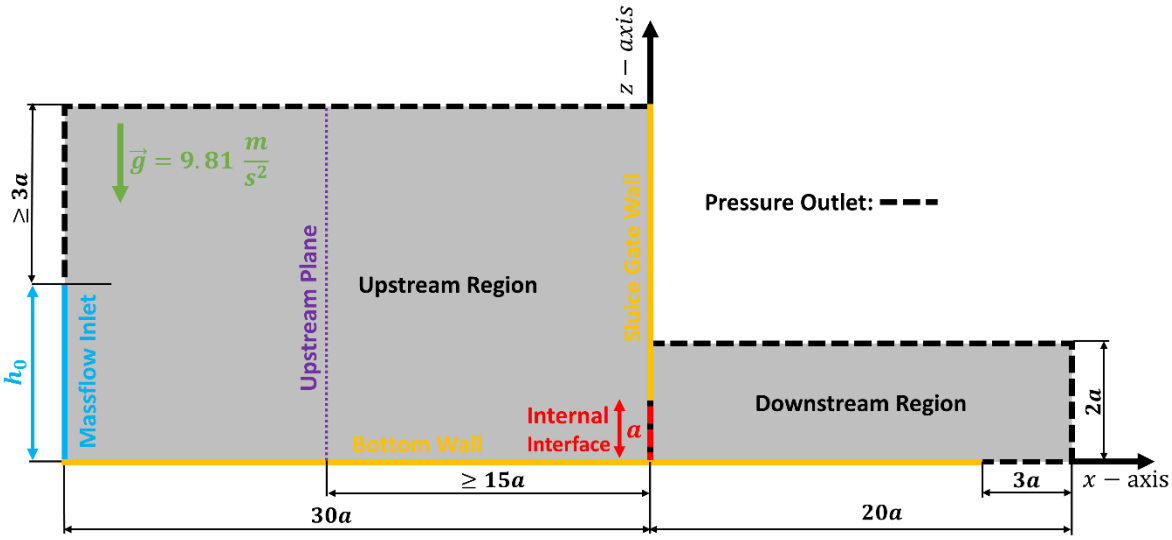

Figure 32: Simulation domain for sluice gates with boundary conditions

The height of the mass flow inlet is set equal to the desired sluice gate upstream water level h_0, which is constant for each simulation case (for each ε). The height of the downstream water level h_1 is not specified as a boundary condition and is calculated by the CFD solver. In the first iteration loop, the mass flow rate at the mass flow inlet is calculated with an initial estimated discharge coefficient of $c_{D,dB} = 0.6$, which is a typical value see e.g. [30], using the du Buat discharge equation Eq. (2-4). After a first simulation loop, the water level is evaluated at the upstream plane, see Figure 32. With this water level a new discharge coefficient is calculated, using the du Buat discharge equation Eq. (2-4), and the mass flow rate is corrected based on the new discharge coefficient. The mass flow rate correction is repeated until the

difference between the evaluated upstream water level and the target upstream water level h_0 is smaller than 0.1 %. The simulations were carried out fully automatically using a java macro.

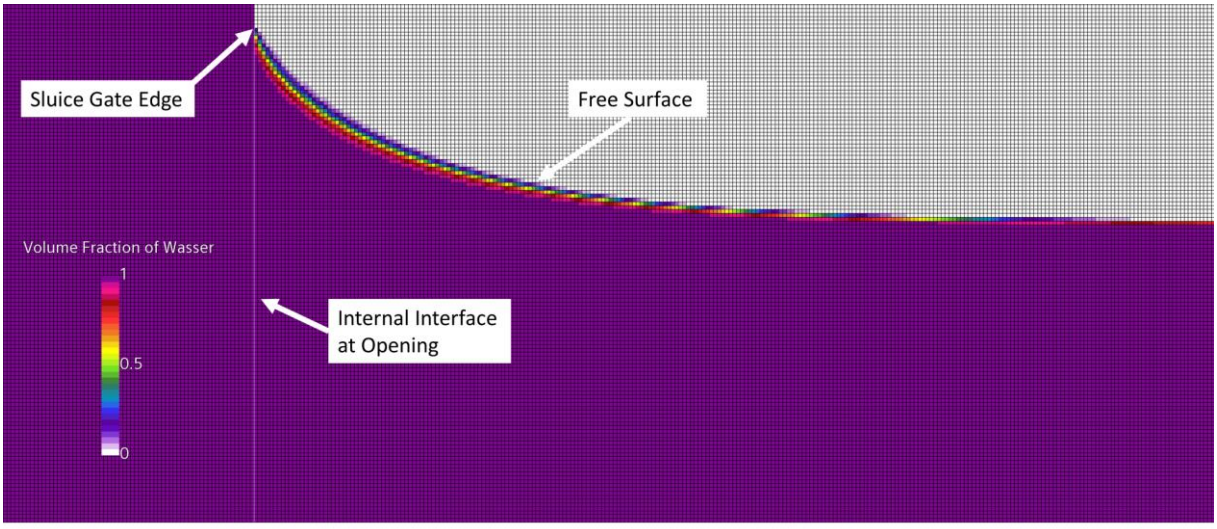

Figure 33: Mesh and volume fraction of Water near the sluice gate opening

At the pressure outlets, the relative pressure was set to 0 Pa, i.e. it was set equal to the environmental pressure and air was set to 100 % as backflow phase. The gravity vector was defined as $\vec{g} = \left(0\,,0\,,-9.81\ \frac{m}{s^2}\right)$. The fluid properties of the two phases, water and air, are shown in Table 2.

Table 2: Fluid properties for CFD simulations

	Water	Air
Density ρ [kg/m^3]	1000.00	1.18
Dynamic Viscosity μ [Pa s]	$8.89 \cdot 10^{-4}$	$1.86 \cdot 10^{-5}$

4.4 Initial Conditions

The stability, convergence behavior and the solution of CFD simulations are also depending on the initial conditions. For the simulations to converge quickly, it has been shown that the initial conditions are well suited as shown in Figure 34, setting the initial upstream water level equal to h_0 and assuming hydrostatic pressure for the upstream region. The initial velocity was set to zero in the complete simulation domain. It was found that the solver runs stable for a wide range of the simulated inverse relative gate openings $\frac{1}{\varepsilon} = 2$ to 20 and angles of inclinations $\alpha = 15$ deg to 90 deg, using $\Delta t = 0.1$ s ($a = 0.1\ m$) and the initial conditions as shown in Figure 34.

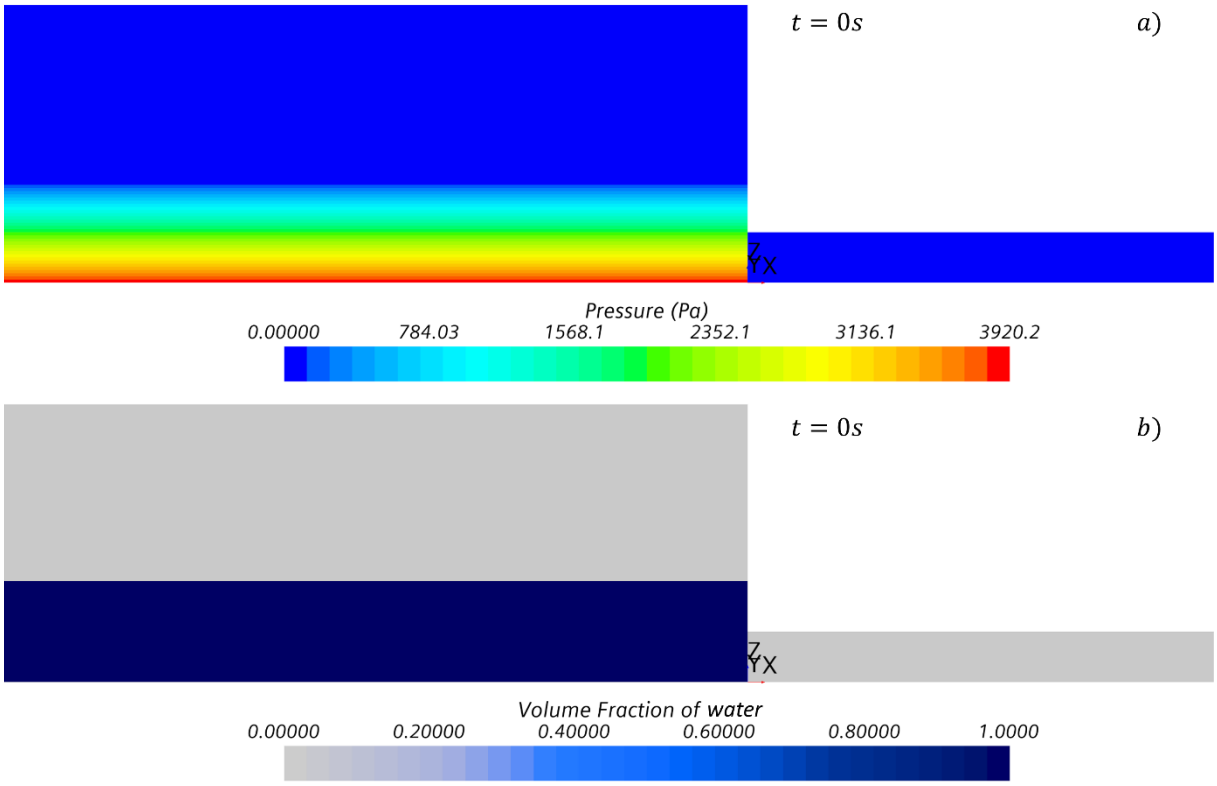

Figure 34: Initial conditions for sluice gate flow simulation a) pressure contour plot b) volume fraction of water contour plot

4.5 Grid Study

For the discretization of the fluid domain, a structured grid with cubic volume cells (aspect ratio 1) was generated, using the directed mesher in Star-CCM+. For the grid study, the edge length of the cells $\Delta_{grid} = \frac{a}{n_{grid}}$, was varied in fractions of the gate opening a and the discharge coefficient $c_{D,dB}$ was monitored. Simulations for relative edge lengths of $1/8a$, $1/16a$, $1/32a$, $1/64a$ and $1/128\,a$ were done using first and second order discretization schemes. For the first order discretization scheme the Richardson extrapolation ([57], [58]) was computed, to estimate the result of an infinite small grid. The results of the grid study are shown Figure 35.

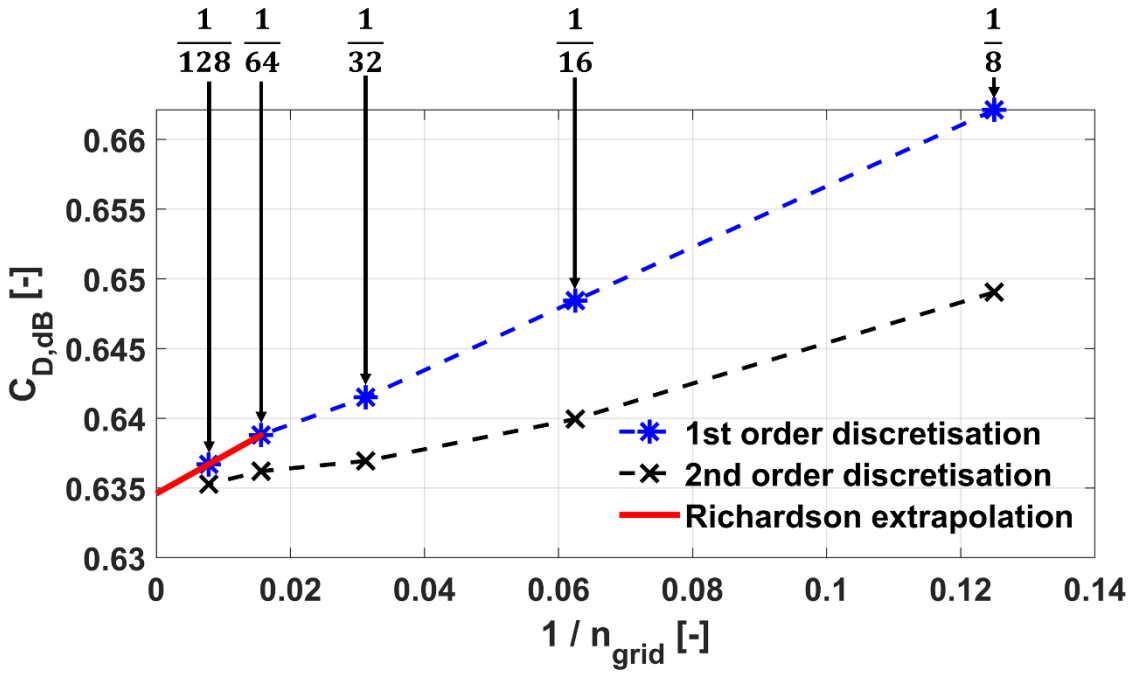

Figure 35: Grid study and discretization error estimation

The discretization error $e_{Cd,DB}$ of the calculated discharge coefficient from the second order discretization with $\frac{\Delta_{grid}}{a} = \frac{1}{n_{grid}} = \frac{1}{128}$ has been calculated with $e_{Cd,dB} = 0.04\%$. For the simulation results shown in this work, the simulations were done with a relative cell edge length of $\frac{\Delta_{grid}}{a} \leq \frac{1}{128}$ and the second order simulation scheme was used. For $\Delta_{grid} = 1/128\,a$ the 2D grid consists of 4.259.840 volume cells. The structured mesh near the opening is shown in Figure 33.

5 Sluice Gate Pressure Distributions

To solve the momentum balance for the control volume I, shown in Figure 27, the pressure forces at the sluice gate and at the opening must be determined. These forces are the integrals of the respective pressure distribution, which can be determined by CFD simulations. For this purpose, CFD simulations were carried out for different relative gate openings $\varepsilon^{-1} = \{2, 3, 4, 5, 6, 7, 8, 10, 12, 14, 16, 18, 20\}$ and for different angles of inclination $\alpha = \{90°, 75°, 60°, 45°, 30°, 15°\}$. The CFD setup was described in detail in the previous chapter. For the angles of inclination $\alpha = \{30°, 15°\}$ the sluice gate was only investigated for $\varepsilon^{-1} = \{3, 4, 5, 6, 7, 8, 10\}$. Larger values of ε^{-1} are not relevant for these angles in practice, since the sluice gates would become very long and thus cause large construction costs and additionally require an enormous amount of space. Likewise, the computational grid and thus the required computational cost would become very large, which is why these were not simulated. The CFD results presented in the following chapters always refer to own computations unless another author was explicitly named.

Before considering the pressure distributions at the control volume boundaries in more detail, the pressure distribution of the sluice gate flow calculated by CFD will be presented here in general. Figure 36 shows the pressure contour plot for $\varepsilon^{-1} = 4$ and $\alpha = 90°$. At the red marked positions, shown in Figure 36, at different positions of the dimensionless X-coordinate (Eq. (5-1)), the pressure distribution along the z-coordinate was evaluated.

$$X = \frac{x}{a} \tag{5-1}$$

These pressure distributions are shown in Figure 37 a), for the upstream region, and in Figure 37 b), for the downstream region.

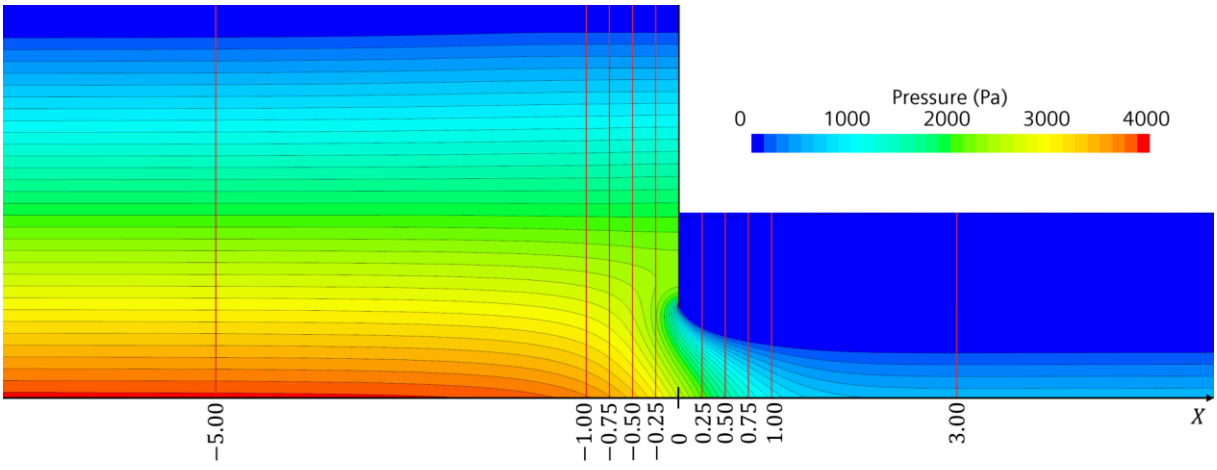

Figure 36: Pressure contour plot from CFD simulations

In the upstream region, hydrostatic pressure distribution prevails at a sufficient distance from the gate opening, see $X = -5.00$. As the distance from the gate opening decreases, the pressure at and near the bottom ($z = 0$) initially decreases. With increasing distance to the ground, the pressure distribution changes back to the linearly increasing hydrostatic pressure distribution. For $X = -1.00$, $X = -0.75$ and $X = -0.50$, the pressure decreases steadily with increasing distance from the ground. If one approaches the sluice gate opening even further, see $X = -0.25$, the pressure initially decreases and then increases again before the pressure falls again. The pressure distribution thus continuously changes to the pressure distribution at the sluice gate and at the opening at $X = 0.00$. The drop at the lower edge of the gate at $z = a = 0.1$ is striking, as this is where the outflow into the environment takes place and thus ambient pressure prevails.

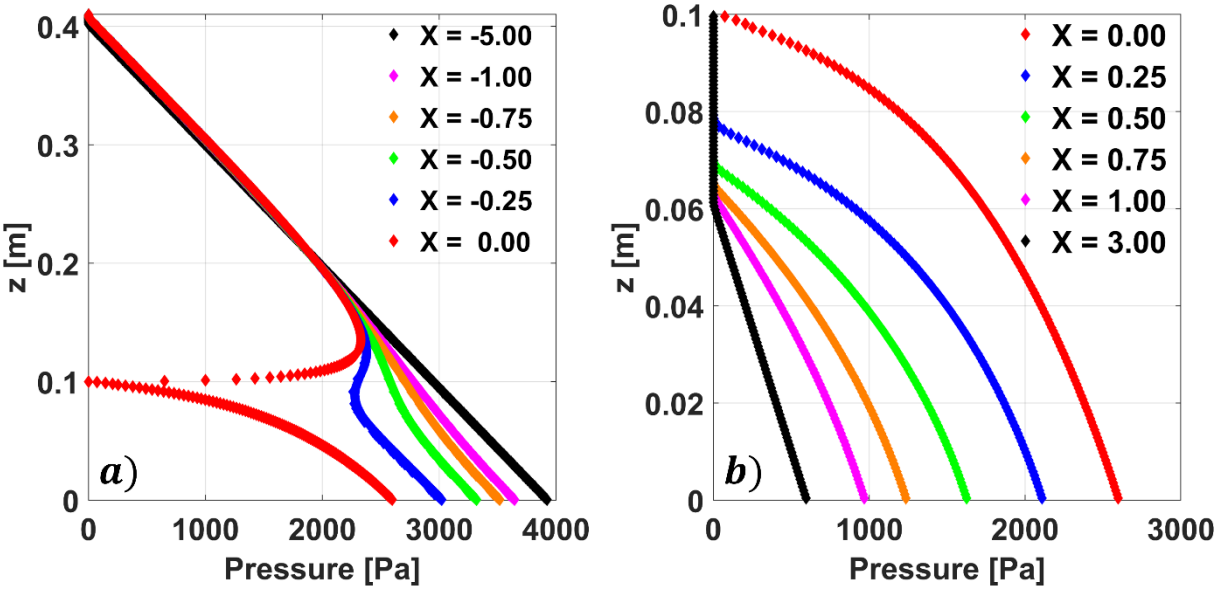

Figure 37: Pressure distributions at different locations of the dimensionless X-coordinate a) at the upstream region b) at the downstream region

In the downstream region, see Figure 37 b), the water level as well as the pressure at the bottom decreases continuously with increasing distance to the opening ($X = 0.00$) and approaches the hydrostatic pressure distribution at the vena contracta. With the selected control volume I for calculating the discharge from the momentum balance, the pressure forces in the upstream region, at the gate and at the opening are required.

As already described, the pressure at the bottom drops from the hydrostatic pressure through the water column in the upstream region h_0, to the hydrostatic pressure of the water column in the downstream region, the height of the vena contracta h_1. The distribution of the bottom pressure for the example $\varepsilon^{-1} = 4$ is shown in Figure 39. An important parameter for

the parameterization of the pressure distribution at the opening is the bottom pressure at the point $X = 0$.

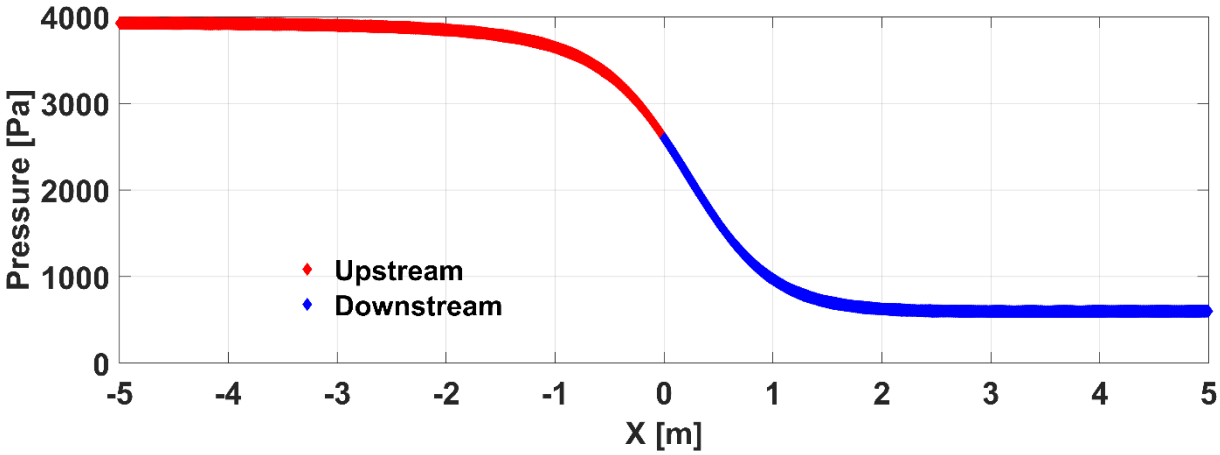

Figure 38: Bottom pressure distribution

A graphical representation of the pressure force is shown in Figure 39. For the two-dimensional case, this can be represented as the area "under" the pressure distribution multiplied by the width B. For the vertical sluice gate (Figure 39 a)) and for the inclined sluice gate with $\alpha = 45°$ (Figure 39 b)), the pressure distribution at the points $X = -5.00$ and $X = 0.00$, i.e. the pressure distribution at the opening and at the sluice gate, are plotted along the z-coordinate. For the inclined sluice gate, the pressure distribution on the gate was projected onto the z-axis. The area difference of the plotted pressure distributions multiplied by the gate width corresponds to the pressure integral $\int_{\partial\Omega} p\,\vec{n}\,dA$ of control volume I of the momentum balance along the x-coordinate. For the areas colored blue in the upper region, the pressure distribution at the gate is initially larger than the hydrostatic pressure distribution in the upstream region because the water level increases by Δh_G at the gate, generating an additional hydrostatic pressure. This water level increase will be discussed in more detail when parameterizing the pressure distribution at the sluice gate. As a result of the water level increase the area difference is negative $\Delta A_2 < 0$. In the lower region, the pressure at the gate decreases and is smaller than the hydrostatic pressure at the upstream control volume boundary at $X = -5.00$. The pressure at the gate decreases to ambient pressure at the lower gate edge. At the opening, between the lower edge of the gate and the bottom, the pressure increases again, but always remains lower than the hydrostatic pressure at $X = -5$. Thus, the area difference ΔA_1 shown in red in Figure 39 is positive $\Delta A_1 > 0$.

For the resulting force, this gives $\Delta F = (|\Delta A_1| - |\Delta A_2|) \cdot B$. From Eq. (3-15) it can be seen that the larger the force difference ΔF, the larger the discharge Q through the sluice gate. Qualitatively comparing the area differences of the standard (Figure 39 a)) and inclined (Figure 39 b)) sluice gates, it can be seen that this is greater for the inclined one and therefore the discharge must also be greater.

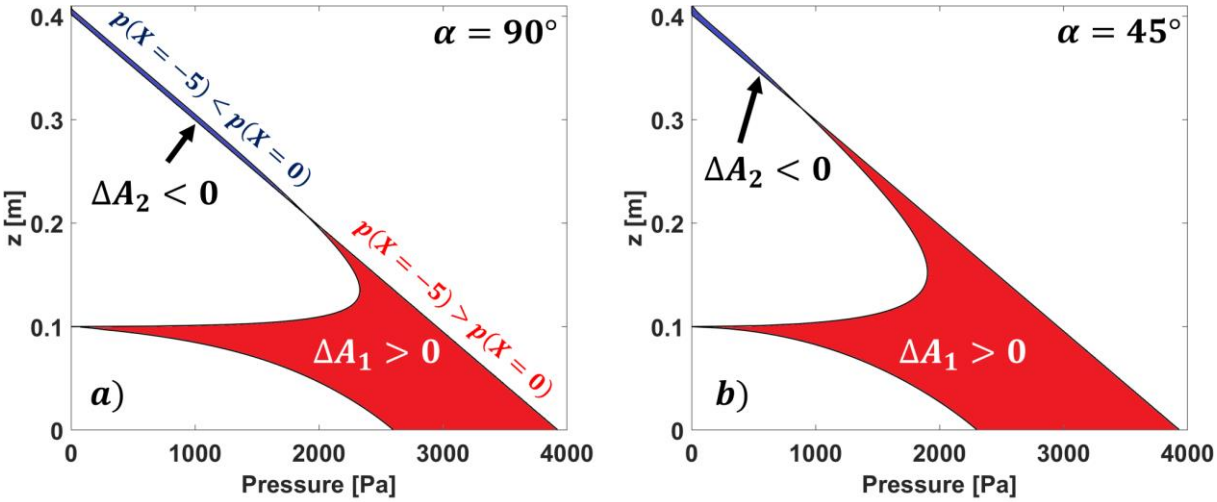

Figure 39: Graphical representation of the resulting pressure forces on the control volume a) for the standard sluice gate ($\alpha = 90°$) b) for the inclined sluice gate with $\alpha = 45°$

In order to calculate the pressure forces qualitatively, parameterization formulas are derived for the pressure distributions in the following chapters, which take into account the dependence on the relative gate opening ε and the angle of inclination α. We start with the bottom pressure distribution p_B. This is not directly needed for the calculation of the flow from the momentum balance, but the value of the bottom pressure distribution at the position X = 0 will be used later for the parameterization of the opening pressure distribution p_O. The opening pressure distribution p_O is parameterized in chapter 5.2 and by integration of this, the pressure force at the opening F_O is determined. In chapter 5.3, the pressure distribution at the sluice gate is determined and its characteristics are discussed in detail. In order to determine a calculation formula for the pressure force on the gate F_G, the newly derived formula for the gate pressure distribution p_G is subsequently integrated.

5.1 Bottom Pressure Distribution

The pressure at the bottom of the sluice gate decreases smoothly from the upstream hydrostatic pressure $\rho \cdot g \cdot h_0$ to the downstream hydrostatic pressure $\rho \cdot g \cdot h_1$. To compare the bottom pressure distributions for different relative gate openings, the dimensionless bottom pressure distribution P_B is introduced in dependency of the dimensionless x-coordinate $X = \frac{x}{a}$ as:

$$P_B(X) = \frac{p_B(x) - \rho \cdot g \cdot h_1}{\rho \cdot g \cdot (h_0 - h_1)} \tag{5-2}$$

Parameterization approaches for the bottom pressure have also been developed by other authors for the standard sluice gate, which emphasizes the importance of this parameter. Rajaratnam and Humphries [32] suggested an exponential approach for the parameterization of the upstream part of the dimensionless bottom pressure distribution, shown in Eq. (5-3):

$$P_{B,RaHu}(X) = 1 - \left(e^{-\frac{3 \cdot X}{2.42}} \cdot (1 - k)\right) \quad \text{with } k = 0.605 \tag{5-3}$$

In a previous study, Rajaratnam [29] investigated also the bottom pressure distribution downstream of the gate, where he found out that the pressure distribution for different relative gate openings can be described by a single curve and that at $X \approx 2$, the bottom pressure becomes equal to the hydrostatic pressure of the downstream supercritical flow. Roth and Hager [28] introduced a new approach for the bottom pressure distribution, using a Gaussian function. They also mentioned, that the non-hydrostatic pressure part of the bottom pressure distribution is confined to $-2 < X < 2$.

$$P_{B,RoHa}(X) = 1 - e^{-\frac{1}{3}(X-1.7)^2} \tag{5-4}$$

These both approaches of Rajaratnam et al. and Roth et al. are assuming, that the dimensionless bottom pressure distribution $P_B(X)$ does not vary with the relative gate opening ε. In Figure 40, the determined dimensionless bottom pressure distributions from CFD simulations for $\varepsilon = 0.05$ and $\varepsilon = 0.5$ were compared with the empirical equations of Rajaratnam et al. [29] and Roth et al. [28] and also with the numerical solution of Montes [35]. Looking at the CFD results, it can be seen, that for small values of the relative gate opening ε, the pressure at the bottom starts to decrease further upstream as compared to large values of ε, which results in a shift of the pressure distribution in negative X-direction for decreasing ε.

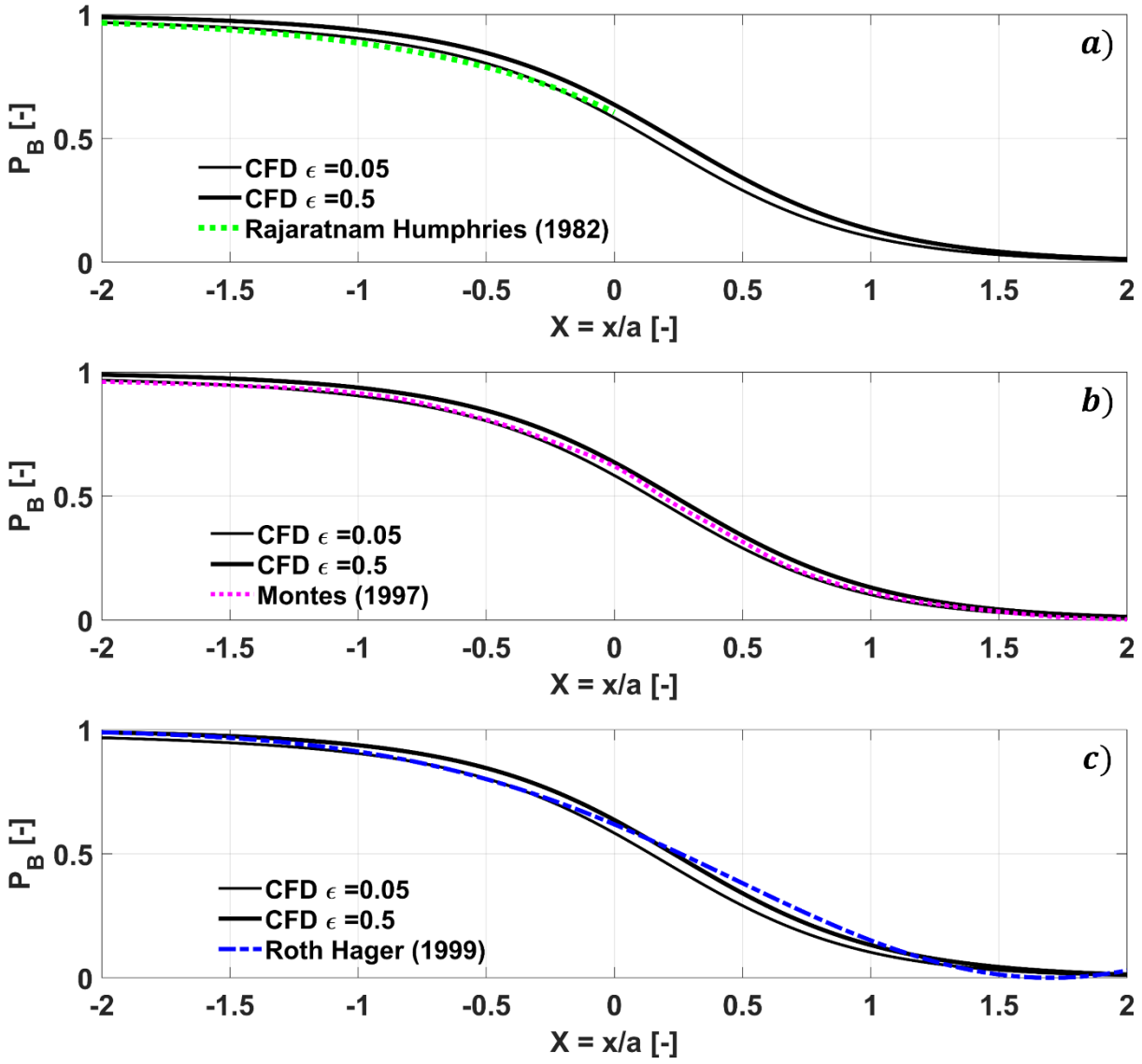

Figure 40: Comparison of the dimensionless bottom pressure distribution P_B from CFD with literature values from a) Rajaratnam et al., b) Montes and c) Roth et al.

This phenomenon can be explained by the increase in length of the surface eddy l_e with decreasing ε, which was also observed by Rajaratnam [43] and is exemplarily shown in Figure 41 for $\varepsilon = 0.5$ and $\varepsilon = 0.05$. To compare the length of the eddies l_e, a grid (black vertical lines) with constant x-spacing is shown in Figure 41 and it can be seen, that the ratio of the eddy lengths $l_{e,0.05} \; / \; l_{e,0.5} \approx 18$. Because of the eddy, the streamlines are deflected in bottom direction and hence the effective flow cross section decreases, which leads to an increase in velocity (continuity equation). The velocity increase at the bottom as computed with CFD starts even further upstream of the position of the eddy starting point l_e. The dimensionless bottom pressure distribution of Rajaratnam et al. [29], Roth et al. [28] and Montes [35] have an better agreement with the CFD results for $\varepsilon = 0.05$ in the upstream region, while for the downstream region, Roth et al. approach agrees better with the CFD results for $\varepsilon = 0.5$. However, for a

precise description of the bottom pressure, the described dependency on the relative gate opening ε, has to be taken into account.

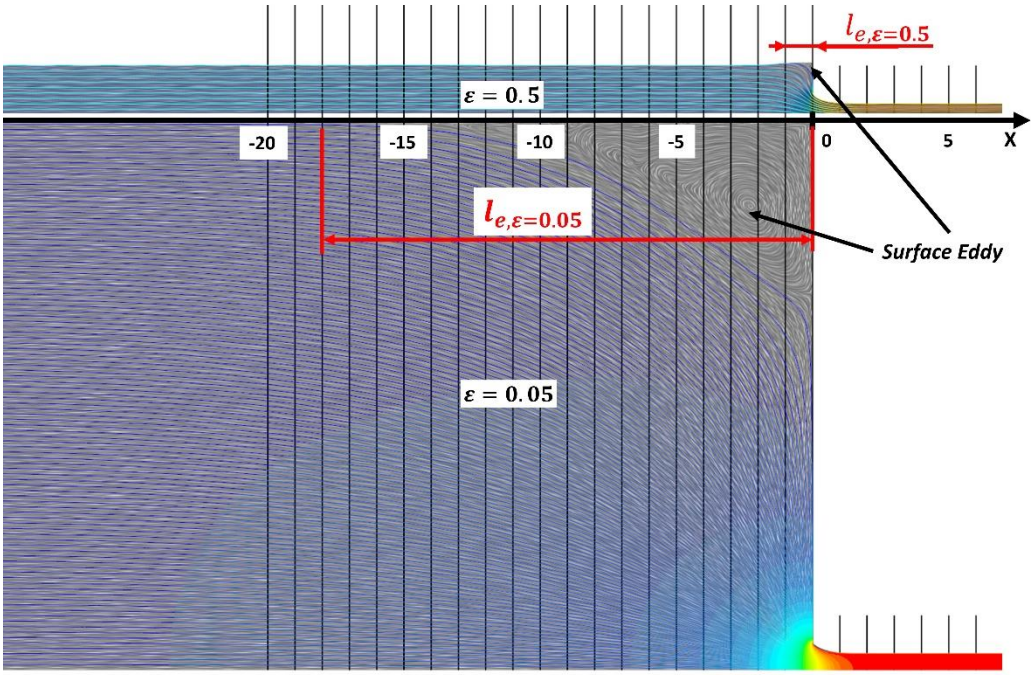

Figure 41: Comparison of standard sluice gate surface eddy length l_e for $\varepsilon = 0.5$ and $\varepsilon = 0.05$

In the following subchapters, first the bottom pressure at the opening is analyzed and a parameterization approach is derived. Based on this approach a new parameterization approach for the upstream bottom pressure distribution for the standard and inclined sluice gates is derived.

5.1.1 Parameterization of the Bottom Pressure at the Opening

Like the bottom pressure distribution, also the pressure at the bottom of the opening $p_{BO} = p_B(X = 0)$ (immediately under the gate lip) varies with the relative gate opening ε. To compare the bottom pressure at the opening for different relative gate openings ε, the dimensionless bottom pressure at the opening is defined as $P_{BO} = \frac{p_{BO}}{\rho \cdot g \cdot a}$. Experimental investigations on the pressure at the bottom of the opening p_{BO} were done by Valentin [59], who described a nearly linear increase of p_{BO} with $1/\varepsilon$ for $1/\varepsilon > 2$ and derived a formula for this relation, see Eq. (5-5).

$$P_{BO,Va}(\varepsilon) = 0.575 \cdot \frac{1}{\varepsilon} + 0.325 \tag{5-5}$$

The bottom pressure at the opening can be also determined by evaluating the bottom pressure distribution of Rajaratnam et al. [32] at $X = 0$, see Eq. (5-3). The resulting formula is shown in Eq. (5-6).

$$P_{BO,RaHu}(\varepsilon) = k \cdot \frac{1}{\varepsilon} + (1 - k) \cdot c_c \tag{5-6}$$

Hence Rajaratnam et al. assumed c_c=const., this approach is similar to Valentin's linear approach, but with different coefficients. In the same way, the bottom pressure at the opening can be derived from the bottom pressure distribution of Roth and Hager [28], see Eq. (5-4). It can be seen in Eq. (5-7), that this approach is similar to Rajartanams and Humphries approach but has different coefficients.

$$P_{BO,RoHa}(\varepsilon) = 0.6184 \cdot \frac{1}{\varepsilon} + (1 - 0.6184) \cdot c_c \tag{5-7}$$

These approaches, if c_c is assumed as constant, underestimate the hydrostatic pressure for the limiting case of $\varepsilon = 1$, were the gate is not immersed into the water and the pressure at the bottom has to be equal to the hydrostatic pressure of the opening height, as shown in Figure 42.

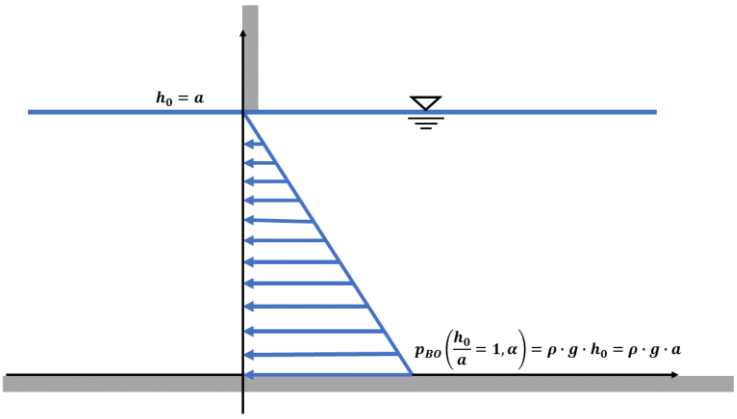

Figure 42: Limiting case: pressure distribution for $h_0 = a$ (ε=1)

To determine a new approach, that is more accurate and satisfies the condition for the limiting case ($P_{BO}(\varepsilon = 1) = 1$), the CFD results and the experimental results of Valentin [59] were used. In the first step, the linear approach which was suggested by other authors (Eq. (5-5), Eq. (5-6) and Eq. (5-7)) was used. Considering the limiting case, this linear approach reduces to:

$$P_{BO}(\varepsilon) = k_{BO} \cdot \frac{1}{\varepsilon} + (1 - k_{BO}) \tag{5-8}$$

The coefficient was determined as $k_{BO} = 0.566$ using the non-linear least square method. The sum of square errors (SSE) and the root mean square error (RMSE) are used to quantitatively evaluate the goodness of this and further parameterization in this work. The definition of the SSE and the RMSE can be found in Appendix B. For the bottom pressure parameterization at the opening, using Eq. (5-8), the errors were calculated with $SSE = 0.2548$ and $RMSE = 0.07286$. As it can be seen in Figure 43 a), the new linear approach does overestimate the CFD and experimental values and the approaches of the other authors for $\frac{1}{\varepsilon} < 4$. For $\frac{1}{\varepsilon} > 4$, shown in Figure 43 b), the new approach agrees well with the experimental and CFD results as well with the approach of Valentin, because both approaches have a similar slope. For small values of $1/\varepsilon$, the approaches of Roth et al. and Rajaratnam et al. are underestimating the CFD and the experimental results of Valentin, while for larger values, $\frac{1}{\varepsilon} > \sim 3$ their approaches are overestimating them. Note that as contraction coefficient for the Rajaratnam and Humphries approach c_c=0.61 was used and for the approach of Roth and Hager c_c=0.595 was used.

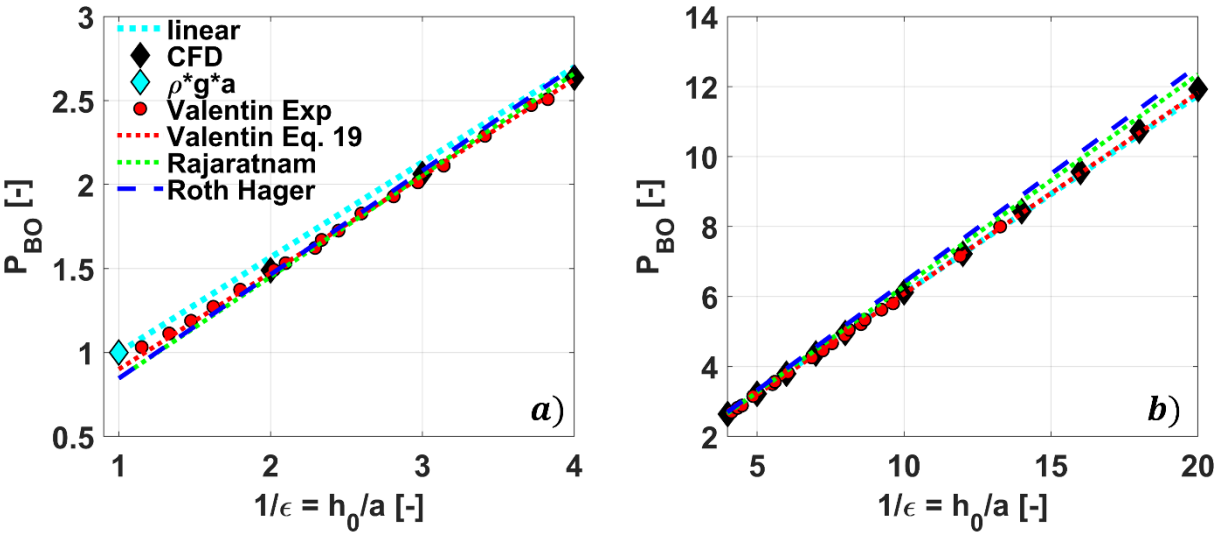

Figure 43: Comparison of bottom pressure parameterization approaches at the opening with CFD and experimental results for a) $\frac{1}{\varepsilon} < 4$ and b) $\frac{1}{\varepsilon} > 4$

Hence the linear approach does not predict the bottom pressure under the sluice gate edge precisely enough, the approach was extended adding an inverse proportional term $k_{BO,2}\ \varepsilon^n$ which corrects the bottom pressure for small values of $\frac{1}{\varepsilon}$. By including the limiting case ($P_{BO}(\varepsilon = 1) = 1$), the extended approach becomes:

$$P_{BO}(\varepsilon) = k_{BO,1}\frac{1}{\varepsilon} + k_{BO,2}\ \varepsilon^n + (1 - k_{BO,1} - k_{BO,2}) \tag{5-9}$$

The parameters $k_{BO,1}$ and $k_{BO,2}$ of Eq. (5-9) were determined for $n = 1$, $n = 2$, $n = 3$ and also for n as an independent parameter, where n was determined as $n = 2.833$. The resulting parameters as well as the SSE and RMSE of the fittings are shown in Table 3. It can be seen, that the SSE and the RMSE of the new approach (Eq. (5-9)), are noticeable lower for all values of n, than for the linear approach (Eq.(5-8)).

Table 3: Fitting parameters for the parameterization of the bottom pressure at the opening

	Eq. (5-8)	Eq. (5-9) n=1	Eq. (5-9) n=2	Eq. (5-9) n=3	Eq. (5-9) n=2.833
$k_{BO,1}$	0.566	0.5829	0.5801	0.5791	0.5792
$k_{BO,2}$	-	0.1777	0.1317	0.1194	0.1207
SSE	0.2548	0.02981	0.02588	0.02537	0.02535
RMSE	0.07286	0.02519	0.02347	0.02323	0.02348

The results of the five approaches for the parameterization of the bottom pressure under the sluice gate edge are shown in Figure 44. It can be seen that the approaches from Eq. (5-9), agree well with the experimental results of Valentin and with the CFD results over the complete range of the inverse relative gate opening $1/\varepsilon$. Especially for small inverse relative gate openings, see Figure 44 a), the new parameterization approach agrees very well with the experimental values.

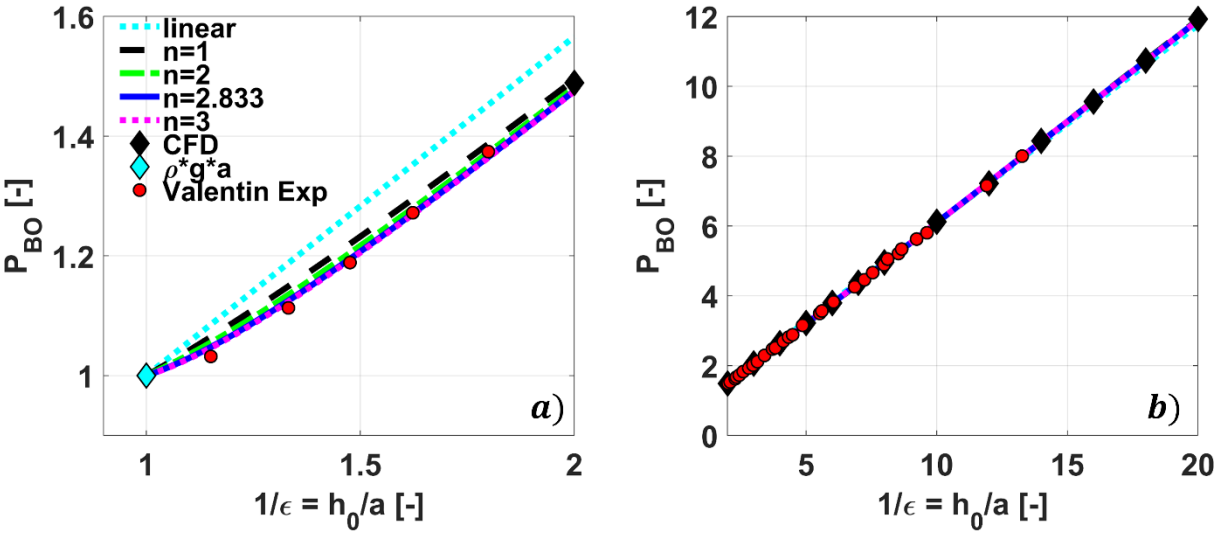

Figure 44: New parameterization approaches of the bottom pressure at the opening

Based on this new approach, the parameterization of P_{BO} was extended for inclined sluice gates. For this, first the bottom pressure distributions of the inclined sluice gates were analyzed. An example of the dimensionless bottom pressure distribution for the investigated angles of inclination α for $\varepsilon = 0.25$ is shown in Figure 45.

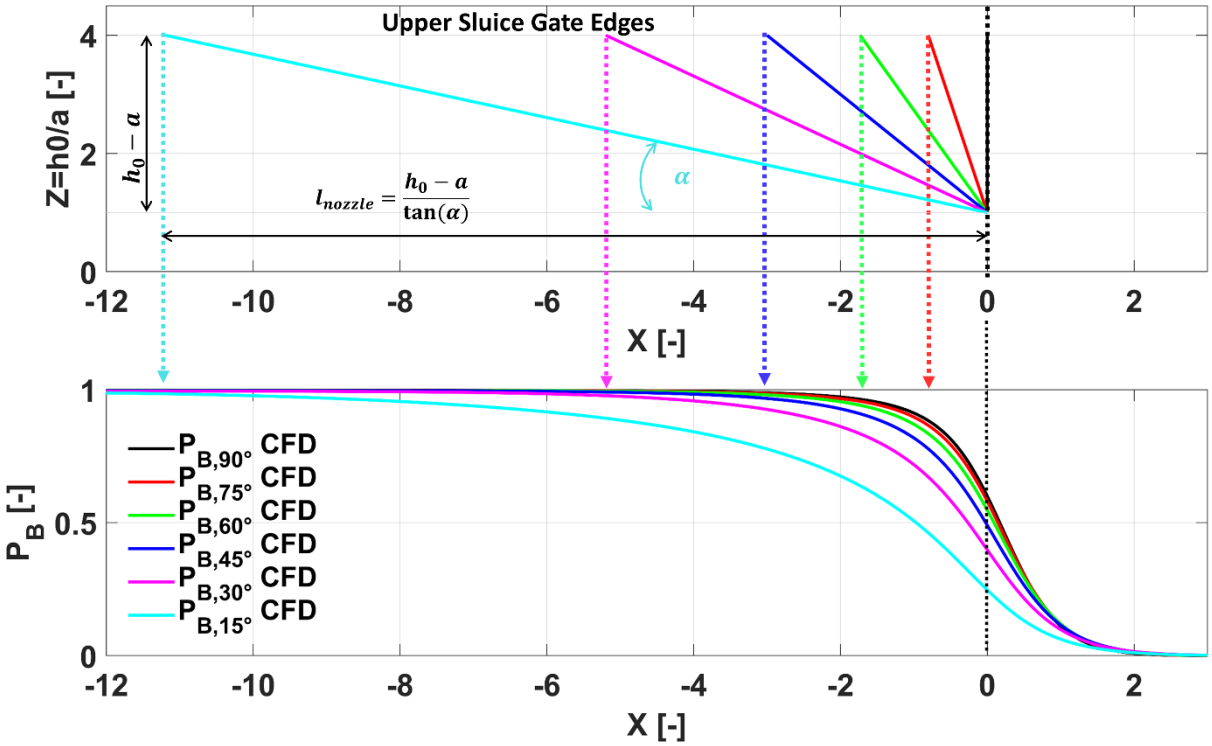

Figure 45: Bottom pressure distribution for various angles of inclination for ε=0.25

The pressure decrease starts further upstream for small angles of inclination, because the inclined sluice gate forms a kind of nozzle with the bottom and the length of this "nozzle" increases with decreasing angle of inclination, see also Figure 45. For angles of inclination close to $\alpha = 90°$ and for the standard sluice gate ($\alpha = 90°$), the surface eddy also reduces the effective flow cross-section significantly. The surface eddy is less pronounced, the more the sluice gate is inclined, as can be seen in Figure 46.

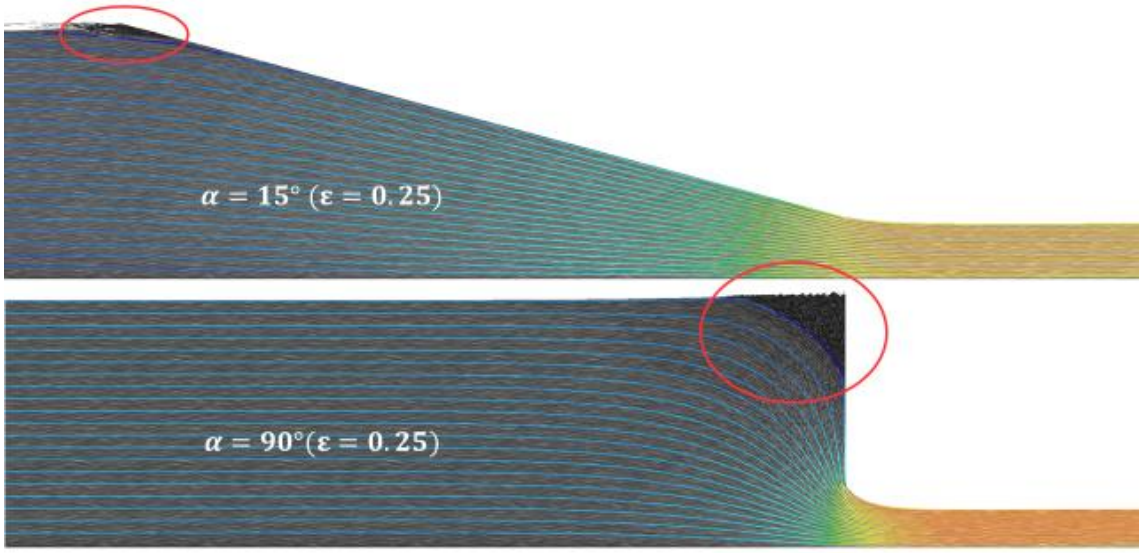

Figure 46: Comparison of surface eddies for α=15° and α=90° (ε=0.25)

If the flow cross-section is reduced, through the inclined sluice gate or the surface eddy, the flow velocity increases to satisfy the continuity equation and with increasing velocity at the bottom, the pressure at the bottom decreases (energy conservation). If the pressure decrease starts further upstream, the pressure at the bottom of the opening, see Figure 45 at $X = 0$, is also lower. For the parameterization of the bottom pressure at the opening ($X = 0$) the parameterization approach for the standard sluice gate Eq. (5-9) can also be used, but the parameters $k_{BO,1}(\alpha)$ and $k_{BO,2}(\alpha)$ are depending on the angle of inclination α. The parameter $k_{BO,1}(\alpha)$ does mainly represent the impact of the "nozzle" length, the parameter $k_{BO,2}(\alpha)$ does mainly represent the impact of the surface eddy. The parameterization approach for the bottom pressure under the sluice gate edge (Eq. (5-9)) is now applied on the inclined sluice gate. The parameters $k_{BO,1}$ and $k_{BO,2}$ are determined for each angle of inclination α based on CFD data using the parameterization approach of Eq. (5-9) with $n = 1$ and are shown in Table 4.

Table 4: Fitting parameters for bottom pressure at X=0 for the investigated angles of inclination α

	$\alpha = 90$	$\alpha = 75$	$\alpha = 60$	$\alpha = 45$	$\alpha = 30$	$\alpha = 15$
$k_{BO,1}$	0.5829	0.5553	0.5170	0.4570	0.3640	0.2254
$k_{BO,2}$	0.1777	0.1035	0.0849	0.0504	0.0167	0.0049
SSE	0.0298	0.0015	0.0048	0.0002	0.0001	0.0001
RMSE	0.0252	0.0113	0.0200	0.0043	0.0039	0.0038

The determined parameters are also shown in Figure 47 in dependency of the angle of inclination α. For the parameterization of the parameter $k_{BO,1}(\alpha)$ the first approach is shown in Eq. (5-10). This approach considers the decrease in bottom pressure at the opening with increasing nozzle length.

$$k_{BO,1}(\alpha) = 0.5829 - \frac{0.1028}{\tan(\alpha)} \tag{5-10}$$

The approach from Eq. (5-10) does show the trend of $k_{BO,1}(\alpha)$ with a $SSE = 0.002929$ and a $RMSE = 0.0242$, but overestimates the parameter in the range between $\alpha = 30°$ and $\alpha = 60°$, see Figure 47 a). Hence the approach of Eq. (5-10) was further improved to determine the parameters more accurate. The resulting approach is shown in Eq. (5-11) which shows a very good agreement ($SSE = 0.0001465$ and $RMSE = 0.005414$) with the values from Table 4.

$$k_{BO,1}(\alpha) = 0.5829 - 0.06459 \cdot \left(\frac{1}{\tan(\alpha)} + 2 \cdot \cos(\alpha)^2\right) \tag{5-11}$$

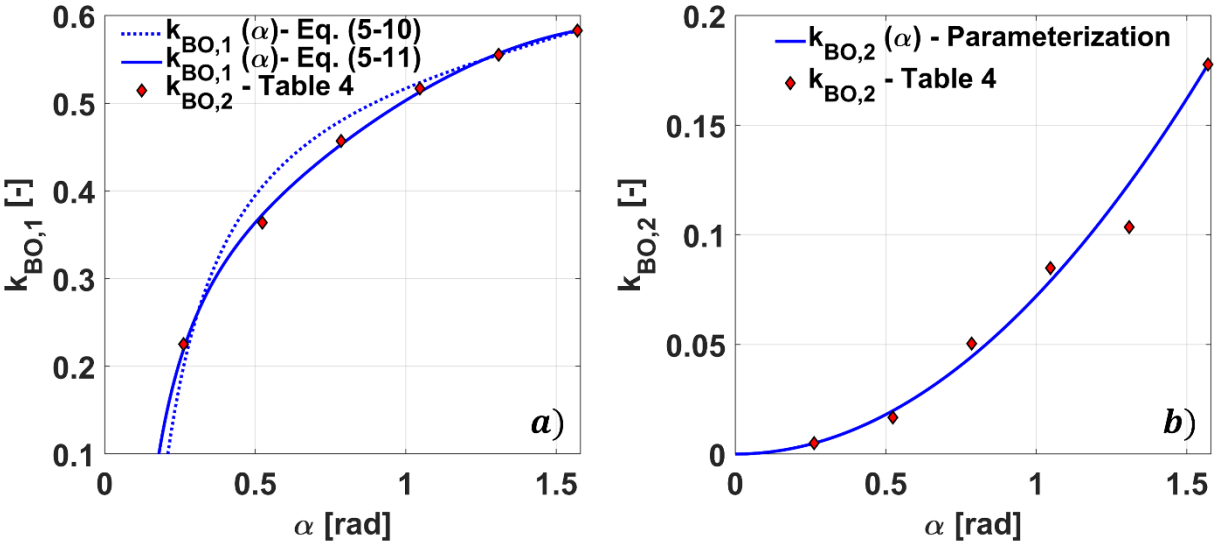

Figure 47: Fitting parameters for the parameterization of the bottom pressure at the opening a) $k_{BO,1}(\alpha)$ and b) $k_{BO,2}(\alpha)$

Looking at the parameter $k_{BO,2}(\alpha)$, see Figure 47 b), it can be seen that the points are following a parabola approach with the vertex at the origin of the coordinate system. Inserting $k_{BO,2}\left(\frac{\pi}{2}\right)$ =0.1777, the resulting formula for $k_{BO,2}(\alpha)$ with $SSE = 0.0004756$ and $RMSE = 0.008903$ becomes:

$$k_{BO,2}(\alpha) = 0.1777\left(\frac{\alpha}{\frac{\pi}{2}}\right)^2 \tag{5-12}$$

In Figure 48, a comparison of the CFD simulation results and the new developed parameterization approach for the bottom pressure at the opening P_{BO} (Eq. (5-9)) with the parameters of Eq. (5-11) and Eq. (5-12) is shown. The derived parameterization has a very good agreement with the CFD results over the complete investigated range of the inverse relative gate opening $\frac{1}{\varepsilon}$ and for all investigated angles of inclination α. With the new parameterization approach, the pressure at the opening can now be calculated more accurately as a function of both the relative gate opening ε and the angle of inclination α. With the parameterization approaches known so far, it was only possible to determine the bottom pressure at the opening for the standard sluice gate.

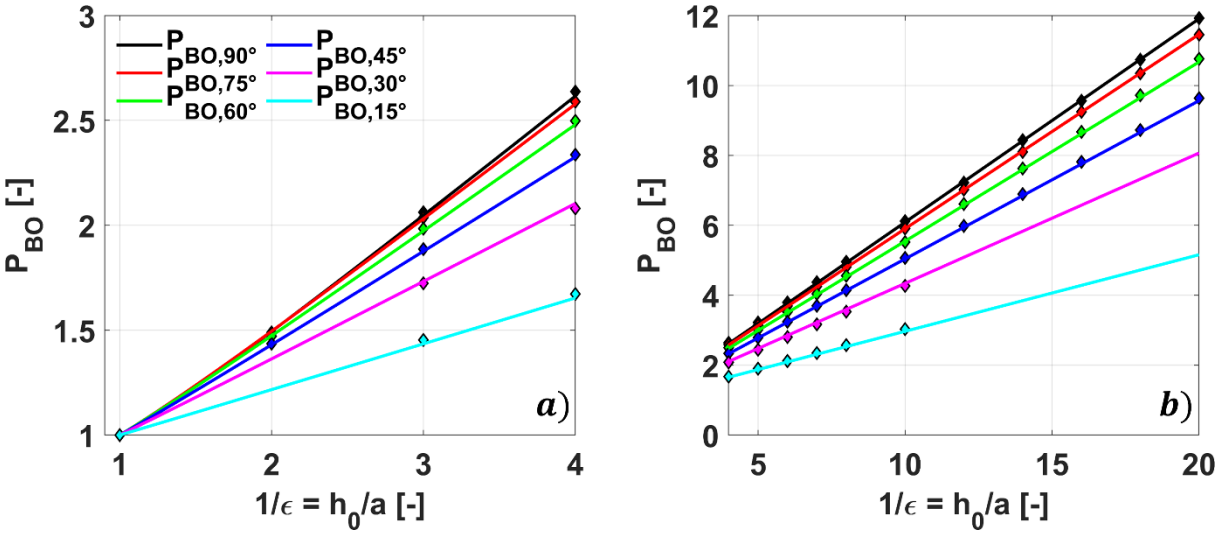

Figure 48: Comparison of dimensionless bottom pressure at the opening P_{BO} from CFD (diamonds) with parameterization approach (lines) for the investigated angles of inclination α for a) $\frac{1}{\varepsilon} < 4$ and b) $\frac{1}{\varepsilon} > 4$

5.1.2 Parameterization of the Bottom Pressure Distribution

The parameterizations of the bottom pressure distribution of Rajaratnam/Humphries see Eq. (5-3) and Roth/Hager see Eq. (5-4) are already shown in Figure 40. While these approaches are only valid for a certain region of the bottom close to the sluice gate opening at $X = 0$, Malcherek [1] suggested a hyperbolic tangent approach, see Eq. (5-13), that is valid for the complete range. The parameter $X_0 = \frac{x_0}{a}$ for this approach was determined by Malcherek based on measurement results of Roth and Hager [28].

$$P_{B,Ma}(X) = \frac{1}{2}(1 - \tanh(X - X_0)) \text{ with } X_0 = \frac{x_0}{a} = 0.24 \tag{5-13}$$

Based on this approach, a modified bottom pressure distribution was derived by inserting Eq. (5-9) into Eq. (5-13) ($P_{B,Ma}(X = 0) = P_{BO}$) to determine the parameter X_0. The resulting equation for the parameter X_0 is shown in Eq. (5-14). The parameter depends now on the relative gate opening ε and as well on the contraction coefficient C_c.

$$X_0(\varepsilon) = -\operatorname{atanh}\left(\frac{2(P_{B0}(\varepsilon) - C_c)}{\frac{1}{\varepsilon} - C_c}\right) \tag{5-14}$$

The contraction coefficient was determined by CFD simulations and is shown in dependency of the relative gate opening ε in Figure 49 a). For the calculation of the bottom pressure distribution parameter X_0 between or outside the investigated relative gate openings, C_C was linearly inter- and extrapolated from the CFD results. The resulting parameter X_0 is

shown in Figure 49 b). Also shown in Figure 49 b) is the original approach of Malcherek, which is equal with the new approach for $\varepsilon = 0.392$.

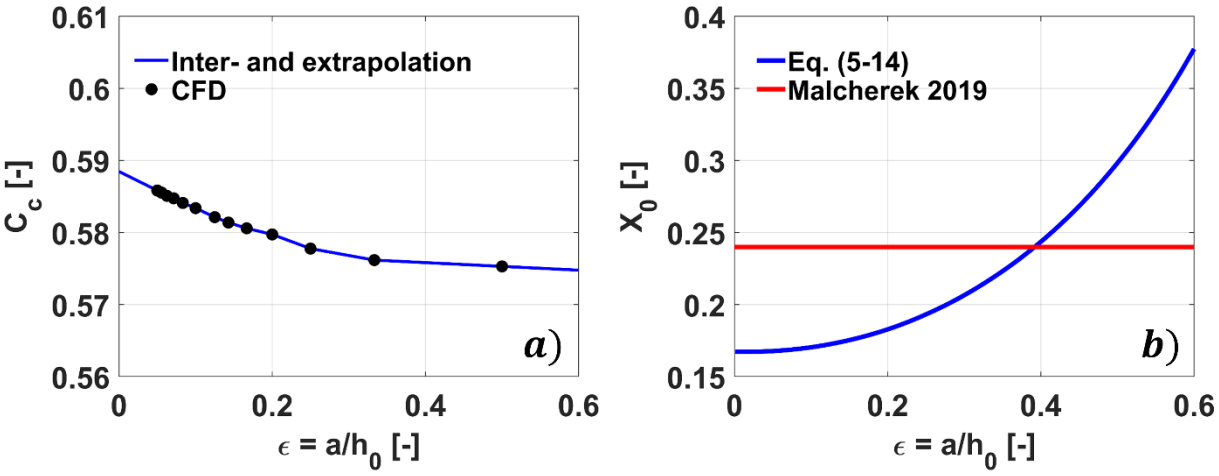

Figure 49: a) Contraction coefficient and b) bottom pressure distribution parameter X_0 for the standard sluice gate

The bottom pressure distribution can now be calculated using the new parameter X_0. Figure 50 shows a comparison of the original hyperbolic tangent approach of Malcherek, the new approach which is also based on Malcherek's approach and the CFD values. At $X = 0$ the hyperbolic tangent approach with the parameter from Eq. (5-14) agrees well with the CFD values for both investigated relative gate openings ε, which can be returned on the well selected factor X_0. The original approach of Malcherek ($X_0(0.392) = X_{0,\text{Malcherek}}$) lays between the values of the new approach. For $X > 0$ the hyperbolic tangent approach of Eq. (5-13) overestimates the CFD values. For $X < 0$ the CFD approach agrees well with the new approach, while the agreement is even better for big relative gate openings ε, because the earlier decrease in bottom pressure due to lager surface eddies for small relative gate openings, as shown in Figure 41, is not considered here.

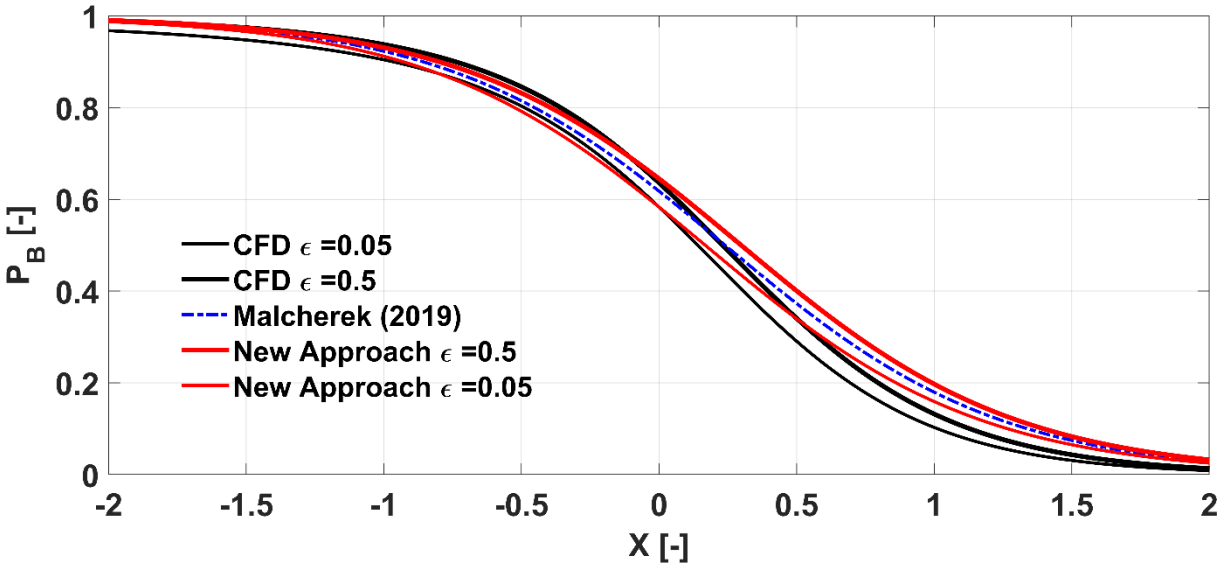

Figure 50: Comparison of bottom pressure distribution P_B of the hyperbolic tangent approaches with CFD values

To determine the bottom pressure distribution for the inclined sluice gate, the bottom pressure distribution for $\varepsilon = 0.25$ is first shown for various angles of inclination α in Figure 51. Also shown in the figure is the hyperbolic tangent approach from Eq. (5-13) where X_0 was determined by Eq. (5-14) and is shown in Figure 52. The contraction coefficient C_c that was used to determine X_0 is also shown in Figure 52.

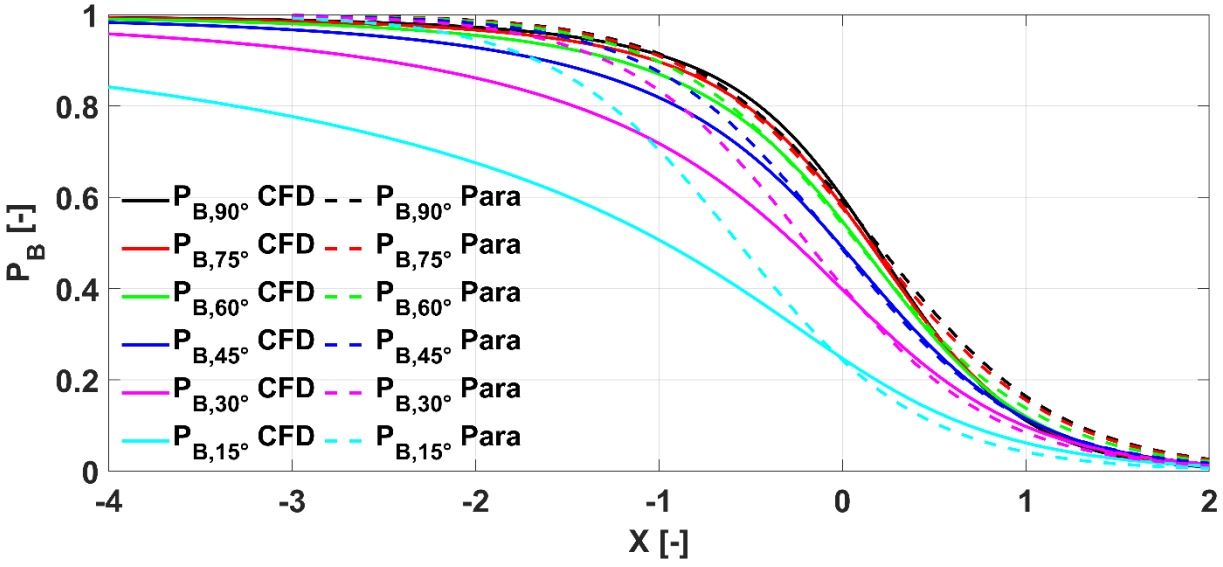

Figure 51: Comparison of hyperbolic tangent approach for various angles of inclination α ($\varepsilon = 0.25$)

At the opening, see $X = 0$ in Figure 51, the approach agrees again well because the factor X_0 was determined with Eq. (5-14), which shifts the bottom pressure distribution so that it coincides at the point $X = 0$. For $X > 0$ and $\alpha = 45°$, the hyperbolic tangent approach agrees very well with the simulation values. For $X > 0$ and $\alpha > 45°$, the hyperbolic tangent approach overestimates the bottom pressure and for $X > 0$ and $\alpha < 45°$ the approach underestimates it.

Upstream of the sluice gate ($X < 0$), the hyperbolic tangent approach Eq. (5-13) agrees best at $\alpha = 90°$.

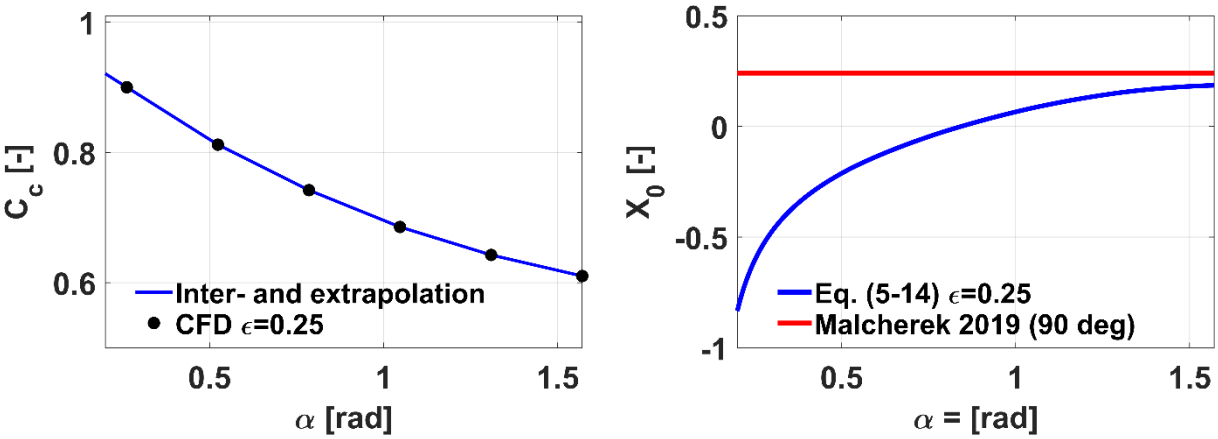

Figure 52: Contraction coefficient C_C and bottom pressure distribution parameter X_0 for inclined sluice gate ($\varepsilon = 0.25$)

Due to the "nozzle" that is generated by the sluice gate, see Figure 45, the pressure decreases start further upstream of the gate with increasing angle of inclination α and the pressure gradient is smaller, which is not considered by Eq. (5-13). To take this behavior into account, a new section wise defined equation is suggested. For the upstream region ($X < 0$), the parameterization approach shown in Eq. (5-15) with the four fitting parameters $k_{BU,1}$, $k_{BU,2}$, $k_{BU,3}$ and $k_{BU,4}$ is suggested, which is an extension of the hyperbolic tangent approach of Malcherek, see Eq. (5-13), for inclined sluice gates.

$$P_{BU}(X) = \frac{1}{2}\left(1 - \tanh\left(k_{BU,1} \cdot X - k_{BU,2}\right)\right) + \frac{1}{k_{BU,3} \cdot X - k_{BU,4}} \tag{5-15}$$

The four parameters were determined, using the non-linear least square method and are shown in Table 1. The resulting bottom pressure distribution for $\varepsilon = 0.25$ is shown in Figure 53. There is a good agreement with the CFD results over the complete range. The largest deviations are found at the opening ($X = 0$), which is, however, an important value, which is why the parameterization should be correct at this point in particular.

Table 5: Determined parameters for the upstream bottom pressure distribution

	90°	75°	60°	45°	30°	15°
$k_{BU,1}$	0.8930	0.8269	0.7381	0.6199	0.4579	0.2487
$k_{BU,2}$	0.4188	0.3844	0.3276	0.2471	0.1504	0.0241
$k_{BU,3}$	35.4326	32.1650	27.5335	20.3202	11.8761	5.0547
$k_{BU,4}$	9.3293	8.9416	8.2039	6.9016	5.0524	3.3059
SSE	0.0038	0.0043	0.0058	0.0097	0.0213	0.0997
RMSE	0.0016	0.0017	0.0018	0.0017	0.0030	0.0066

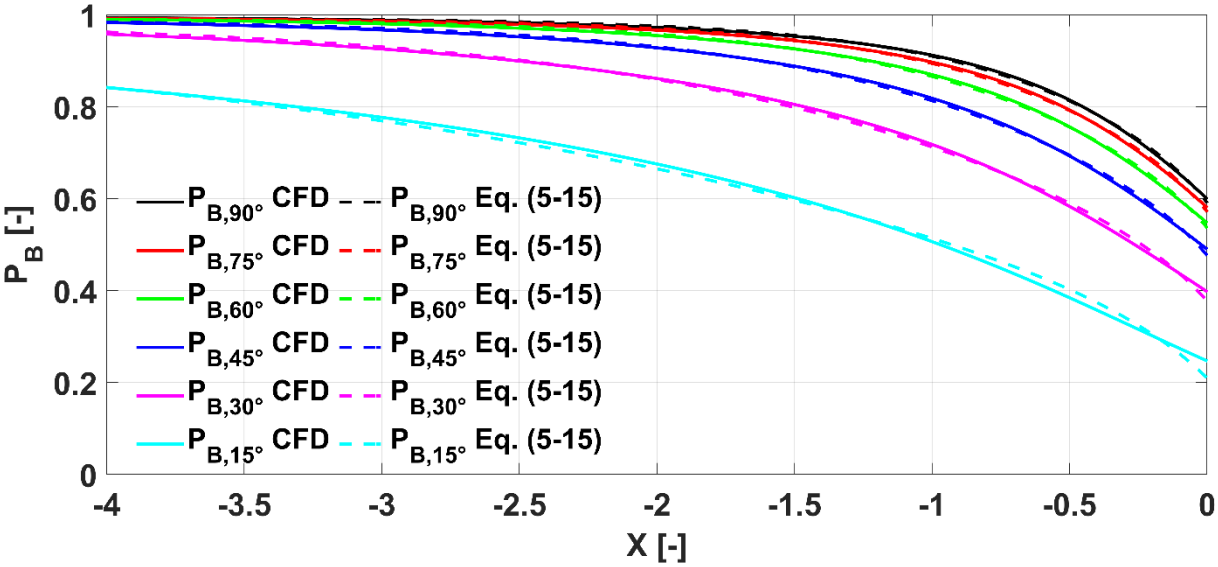

Figure 53: Comparison of extended hyperbolic tangent approach (Eq. (5-15)) for various angles of inclination α ($\varepsilon = 0.25$)

Hence the bottom pressure at the opening is given by Eq. (5-9), one fitting parameter of Eq. (5-15) can be determined using this condition. The resulting equation can be solved for $k_{BU,2}$, see Eq. (5-16) or for $k_{BU,4}$, see Eq. (5-17):

$$k_{BU,2} = -\operatorname{atanh}\left(1 - 2\left(\frac{P_{B0} - C_c}{\frac{1}{\varepsilon} - C_c} + \frac{1}{k_{BU,4}}\right)\right) \tag{5-16}$$

$$k_{BU,4} = \frac{1}{\frac{1}{2}(1 - \tanh(-k_{BU2})) - \frac{P_{B0} - C_c}{\frac{1}{\varepsilon} - C_c}} \tag{5-17}$$

The resuming parameters are then again determined using the non-linear least square method. For the approach from Eq. (5-16), the resulting parameters are shown in Table 6. A plot of the resulting parameterization function compared to the CFD results is shown in Figure 54. Comparing the errors in Table 6 and the curves in Figure 54 with the previous results

(Table 5 and Figure 53), it can be seen that the parameters determined in Table 6 give a much poorer representation of the upstream bottom pressure distribution. Only at the opening ($X = 0$) the parameterization of the upstream bottom pressure distribution P_{BU} with $k_{BU,2}$ from Eq. (5-16) agrees better with the CFD values. Also, the errors are partly two orders of magnitude higher than in the previous approach.

Table 6: Determined parameters for the upstream bottom pressure distribution with k_{BU2} constrained

	90°	75°	60°	45°	30°	15°
$k_{BU,1}$	0.66796	0.60663	0.56492	0.48042	0.36530	0.25949
$k_{BU,2}$	1.56176	2.06675	1.28557	1.01395	0.90917	-0.01790
$k_{BU,3}$	14.07377	11.55954	10.98330	9.23706	5.73018	6.64704
$k_{BU,4}$	2.73000	2.45206	2.57896	2.51446	2.19693	4.03166
SSE	0.18985	0.26992	0.25506	0.30208	0.45509	0.15130
RMSE	0.01104	0.01316	0.01187	0.00951	0.01377	0.00815

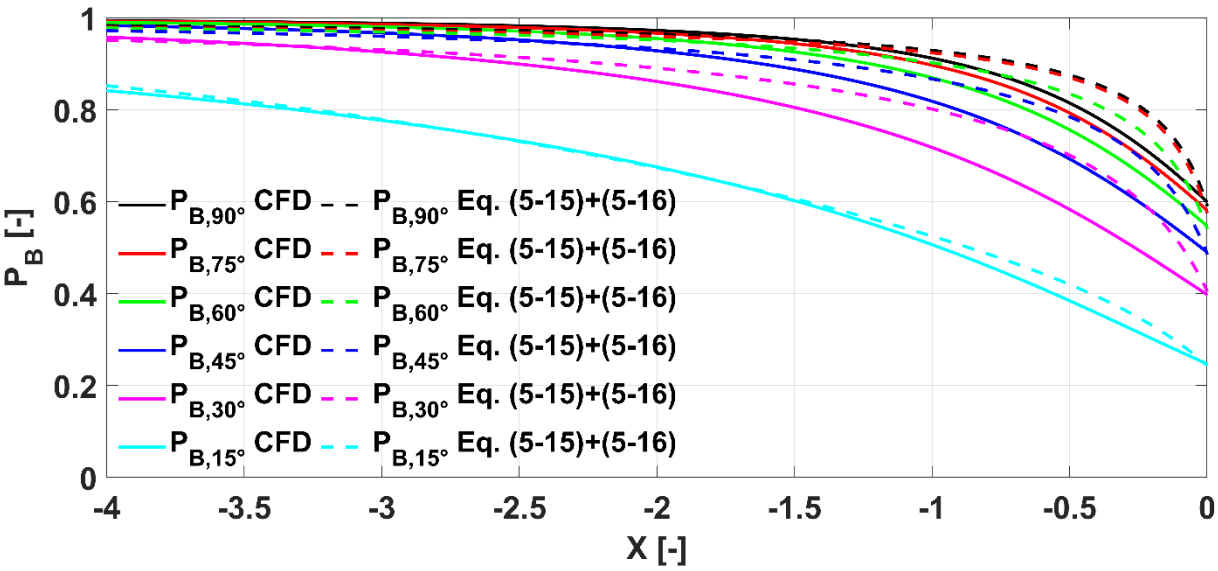

Figure 54: Comparison of extended hyperbolic tangent approach (Eq. (5-15)) with $k_{BU,2}$ Eq. (5-16) for various angles of inclination α ($\varepsilon = 0.25$)

Looking at the results of the parameterization with $k_{BU,4}$ determined from Eq. (5-17), on the other hand, see Table 7 and Figure 55, the course of the upstream bottom pressure distribution for the inclined sluice gate is well reproduced and also the values at the opening ($X = 0$) agree very well with the CFD values. The calculated errors correspond to the same order of magnitude as for the independent parameters in Table 5.

Table 7: Determined parameters for the upstream bottom pressure distribution with k_{BU4} constrained

	90°	75°	60°	45°	30°	15°
$k_{BU,1}$	0.8950	0.8398	0.7478	0.6341	0.4858	0.2598
$k_{BU,2}$	0.4166	0.3691	0.3144	0.2244	0.0914	-0.0253
$k_{BU,3}$	35.4334	32.0959	27.5558	20.3410	11.7717	5.2342
$k_{BU,4}$	9.4812	9.9800	9.0094	8.0427	7.1219	4.0930
SSE	0.0038	0.0046	0.0060	0.0109	0.0357	0.1303
RMSE	0.0016	0.0017	0.0018	0.0018	0.0039	0.0076

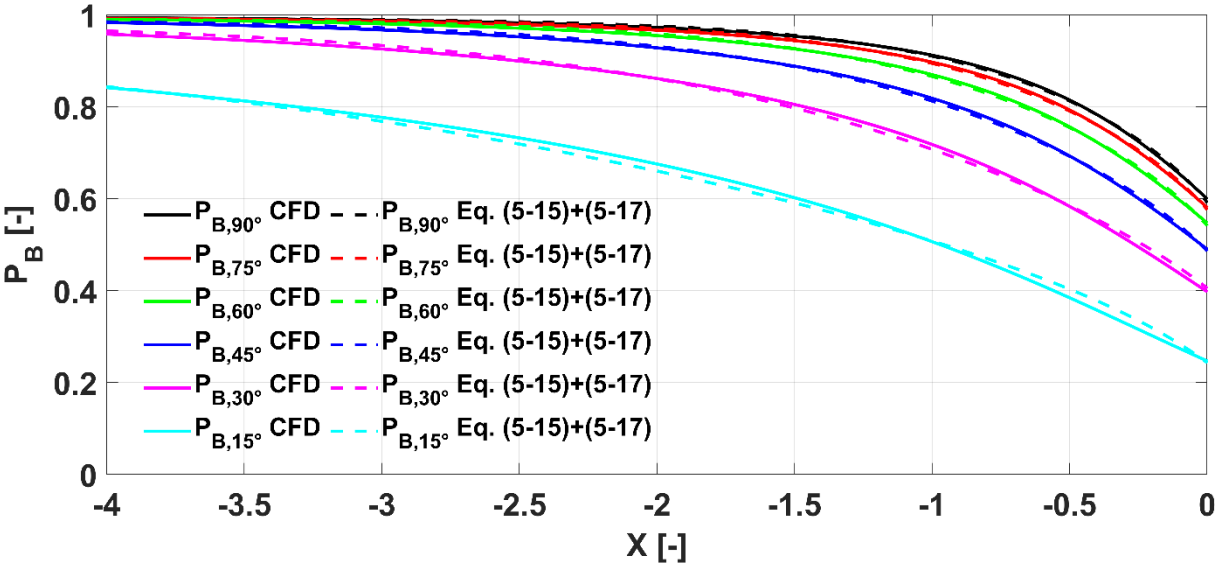

Figure 55: Comparison of extended hyperbolic tangent approach (Eq. (5-15)) with $k_{BU,4}$ Eq. (5-17) for various angles of inclination α ($\varepsilon = 0.25$)

In summary, it can be said that with the parameterization approach from Eq. (5-15), the upstream bottom pressure distribution of the inclined sluice gate can be represented very well. If Eq. (5-17) is used to determine the parameter $k_{BU,4}$ in Eq. (5-15), it can be ensured that the bottom pressure at the opening $P_{BU}(X = 0)$ agrees with the parameterization approach of the bottom pressure at the opening P_{BO} (Eq. (5-9)) and the CFD values. The resulting formula for the calculation of the upstream bottom pressure distribution for standard and inclined sluice gates is finally shown in Eq. (5-18):

$$P_{BU}(X) = \frac{1}{2}\left(1 - \tanh\left(k_{BU,1} \cdot X - k_{BU,2}\right)\right) + \frac{1}{k_{BU,3} \cdot X - \frac{1}{\frac{1}{2}\left(1 - \tanh(-k_{BU2})\right) - \frac{P_{B0} - C_c}{\frac{1}{\varepsilon} - C_c}}} \qquad (5\text{-}18)$$

5.2 Opening Pressure Distribution

For the parameterization of the opening pressure distribution p_O, first the opening pressure distribution p_O was nondimensionalized using the bottom pressure at the opening p_{BO}, see Eq. (5-19), which is the maximum pressure at the opening.

$$P_O = \frac{p_O}{p_{BO}} \tag{5-19}$$

The dimensionless opening z-coordinate Z_O is defined in Eq.(5-20):

$$Z_O = \frac{z}{a} \tag{5-20}$$

A schematic drawing of the dimensionless opening pressure distribution P_O along the dimensionless z-coordinate Z_O is shown in Figure 56 a).

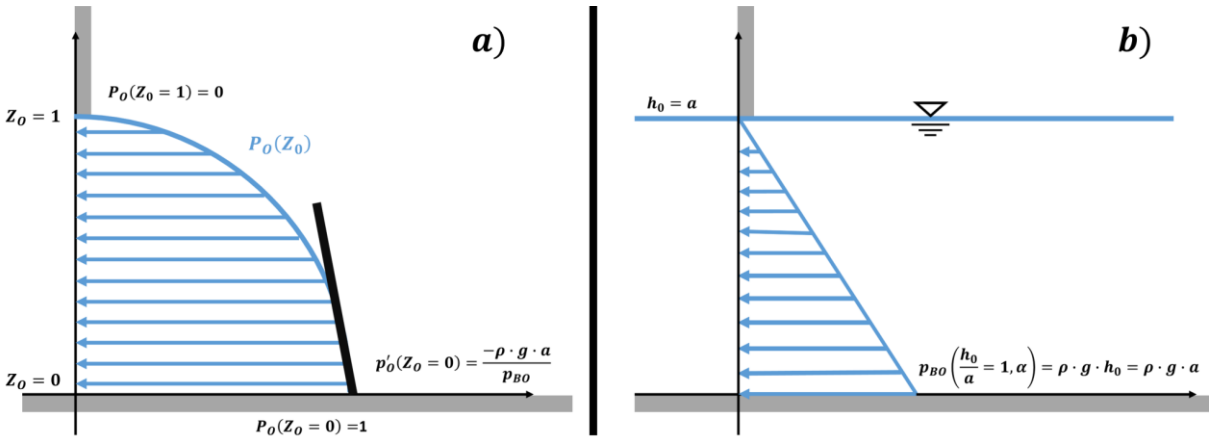

Figure 56: a) Schematic dimensionless pressure distribution at the opening with constrains and b) opening pressure distribution for the special case $h_0 = a = h_1$

A special case for the opening pressure distribution is when the gate lip is at the water surface and hence the upstream water level is equal to the gate opening and also equal to the downstream water level ($h_0 = a = h_1$), as shown in Figure 56 b). In this case, the opening pressure distribution p_O is hydrostatic.

5.2.1 General Parameterization Approach for the Opening Pressure Distribution

The pressure distribution at the opening p_O can be well described by a polynomial function, see Eq. (5-21), as suggested by Malcherek [1].

$$P_O(Z_O) = k_O(\varepsilon) \cdot Z_O^n + k_{O,1}\, Z_O^2 + k_{O,2}\, Z_O + k_{O,3} \tag{5-21}$$

The boundary conditions of the opening pressure distribution which must be satisfied by the parameterization approach are shown in Figure 56 a). The bottom pressure p_{BO} at the opening, was already determined in section 5.1.1 and the formula is shown in Eq. (5-9) with the parameters given in Eq. (5-11) and Eq. (5-12).

Inserting the bottom pressure distribution ($p_O(z = 0) = p_{BO}$ or $P_O(Z = 0) = 1$) in Eq. (5-21) the parameter $k_{O,3}$ can be determined as:

$$k_{O,3} = 1 \tag{5-22}$$

At the gate lip ($p_O(z = a) = 0$ or $P_O(Z = 1) = 0$), the pressure is equal to the ambient pressure, since the flow direction at the edge, is parallel to the wall and air is in the adjacent region. Inserting this condition in Eq. (5-22) and Eq. (5-21), $k_{O,1}$ can be written as:

$$k_{O,1} = -k_O(\varepsilon) - k_{O,2} - 1 \tag{5-23}$$

The change in pressure is the sum of the hydrostatic pressure increase and the change in pressure due to the curvature of the streamline $\left(\frac{dp}{dr} = \rho\, \frac{U^2}{R}\right)$. Since the streamlines at the bottom are parallel to the bottom $R \to \infty$, the pressure increases are hydrostatic there $\left(\frac{dp_O}{dz} = -\rho\, g \text{ or } \frac{P_O}{dZ} = \frac{-\rho\, g\, a}{p_{BO}}\right)$. With this boundary condition, the opening pressure distribution parameter $k_{O,2}$ can be determined:

$$k_{O,2} = -\frac{\rho\, g\, a}{p_{BO}} \tag{5-24}$$

Inserting Eq. (5-22), Eq. (5-23) and Eq. (5-24) in Eq. (5-21) and rearranging gives Eq. (5-25):

$$P_O(Z_O) = k_O(\varepsilon)(Z_O^n - Z_O^2) + \frac{\rho\, g\, a}{p_{BO}} \cdot (Z_O^2 - Z_O) - Z_O^2 + 1 \tag{5-25}$$

With the boundary conditions, only the parameter $k_O(\varepsilon)$ and the exponent n has to be determined.

5.2.2 Parameterization of the Standard Sluice Gate Opening Pressure Distribution

The pressure distributions, which are used for the parameterization were calculated using CFD. Figure 57 a) shows the opening pressure distribution p_O for the different investigated upstream water levels h_0. As can be seen, the pressure increases with increasing upstream water level. With Eq. (5-19) and Eq. (5-20) the opening pressure distribution p_O is first nondimensionalized to perform the parameterization. Figure 57 b) shows the dimensionless opening pressure distribution P_O. Looking at the dimensionless opening pressure distribution, it can be seen that with decreasing upstream water levels h_0 (increasing relative gate openings ε), the opening pressure distribution is approaching the hydrostatic pressure distribution, see black line in Figure 57 b). For decreasing relative gate openings, it seems that the opening pressure distribution approaches a constant value. The parameterization approach for the dimensionless opening pressure distribution P_O was already introduced, see Eq. (5-21), and is carried out in the following on the basis of the values shown in Figure 57.

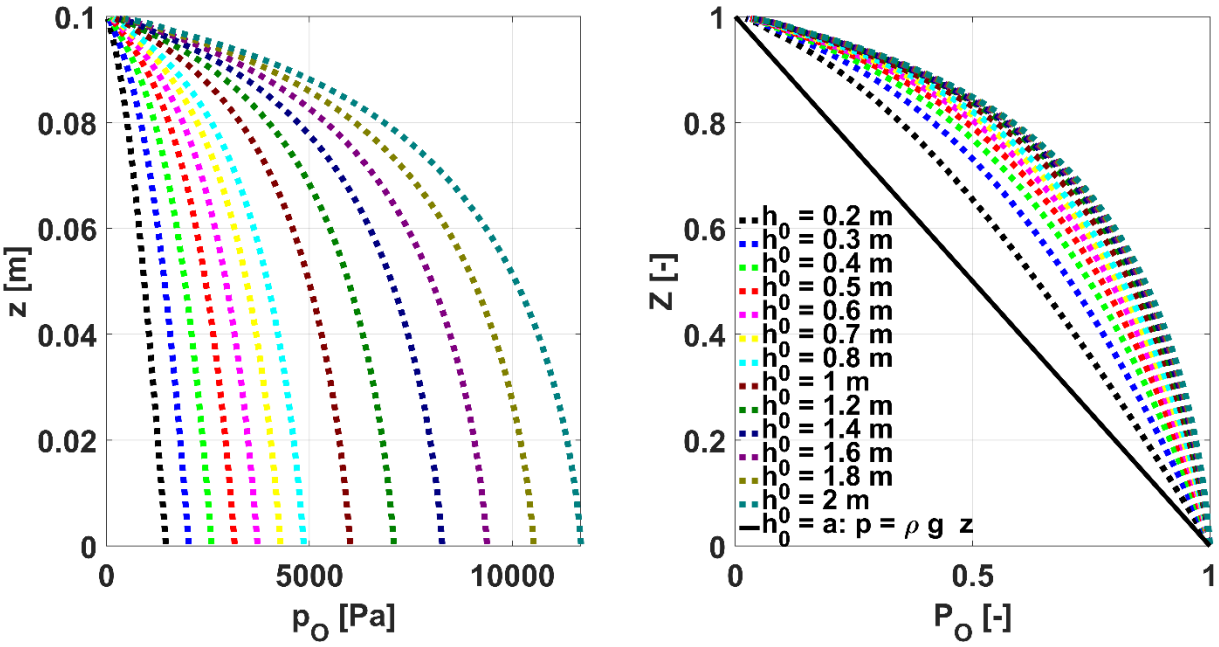

Figure 57: a) Opening pressure distribution p_O and b) nondimensionalized opening pressure distribution P_O of the standard sluice gate from CFD for $a = 0.1\ m$

In the first step, the exponent n from Eq. (5-21) was analyzed using the non-linear least square method to fit the data from the CFD simulations shown in Figure 57. The fit was done for n = [3,4,5,6,7,8,9,10] for all investigated relative gate openings ε and the corresponding SSE and the RMSE were calculated. Then the mean values of the SSE and the RMSE were calculated for each exponent n. The mean errors are shown in Figure 58. The mean errors

initially decrease with decreasing exponent n up to $n = 8$, where the errors are minimal. As the exponent n increases further, the mean SSE and the mean RMSE are increase again. Since both the SSE and the RMSE are smallest for $n = 8$, this is used for the further parameterization.

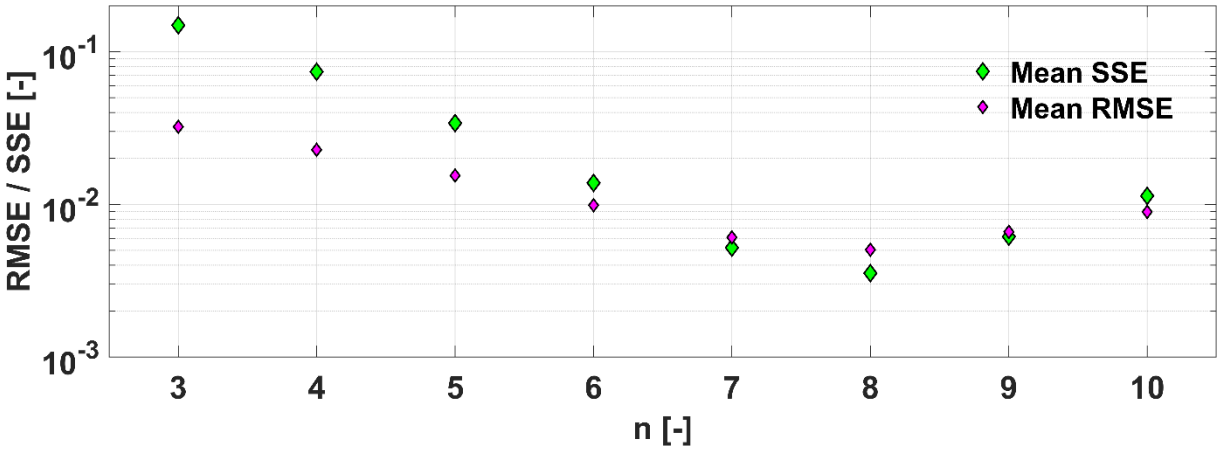

Figure 58: RMSE and SSE for the investigates exponents n of the parameterization approach for the opening pressure distribution

Inserting the previously determined exponent $n = 8$ into Eq. (5-21), the resulting function is used to determine the coefficient $k_O(\varepsilon)$, for the dimensionless opening pressure distribution P_O. For the relative gate openings ε investigated in CFD, the fitting parameter k_O is shown in Figure 59. To satisfy the special case $h_0 = a = h_1$, see Figure 56 b), where the pressure distribution is hydrostatic, the fitting parameter $k_O(\varepsilon)$ has to become zero.

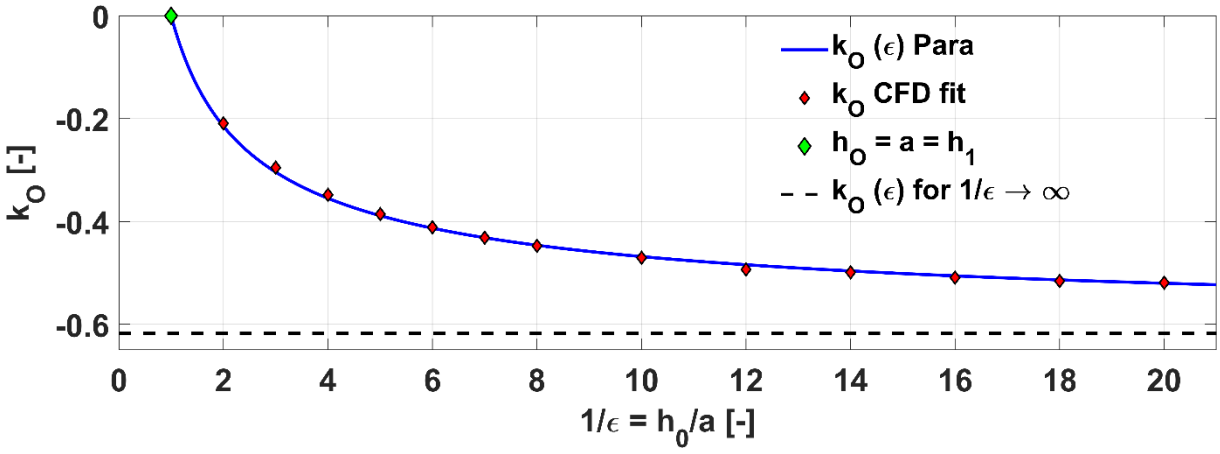

Figure 59: Opening pressure distribution fitting parameter $k_O(\varepsilon)$ for α=90°

To parameterize the opening pressure distribution fitting parameter $k_O(\varepsilon)$ the function shown in Eq. (5-26) was introduced.

$$k_O(\varepsilon) = k_O^* \left(1 - \left(\frac{1}{\varepsilon}\right)^{k_O^*}\right) \qquad \text{with} \qquad k_O^* = -0.6172 \tag{5-26}$$

The fitting constant k_O^* from Eq. (5-26) was determined as $k_O^* = -0.6172$ using the non-linear least square method with $SSE = 2.761 \cdot 10^{-4}$ and $RMSE = 4.797 \cdot 10^{-3}$. The parameterization approach from Eq. (5-26) is also shown in Figure 59. For the limiting case $\frac{1}{\varepsilon} \to \infty$, the parameter $k_O(\varepsilon)$ tends to the constant limit $k_O(\varepsilon) = k_O^* = -0.6172$.

The quality of the new opening pressure parameterization approach was checked by comparing it with results from the literature. Figure 60 shows the results of the standard sluice gate parameterization in comparison with the results of Werner [22] for the limit case $\varepsilon \to 0$, Han et al. [60] for $\varepsilon = 0.395$ and Montes [35] for $\varepsilon = 0.2546$. There is a good agreement of the parameterization results with the results of other authors.

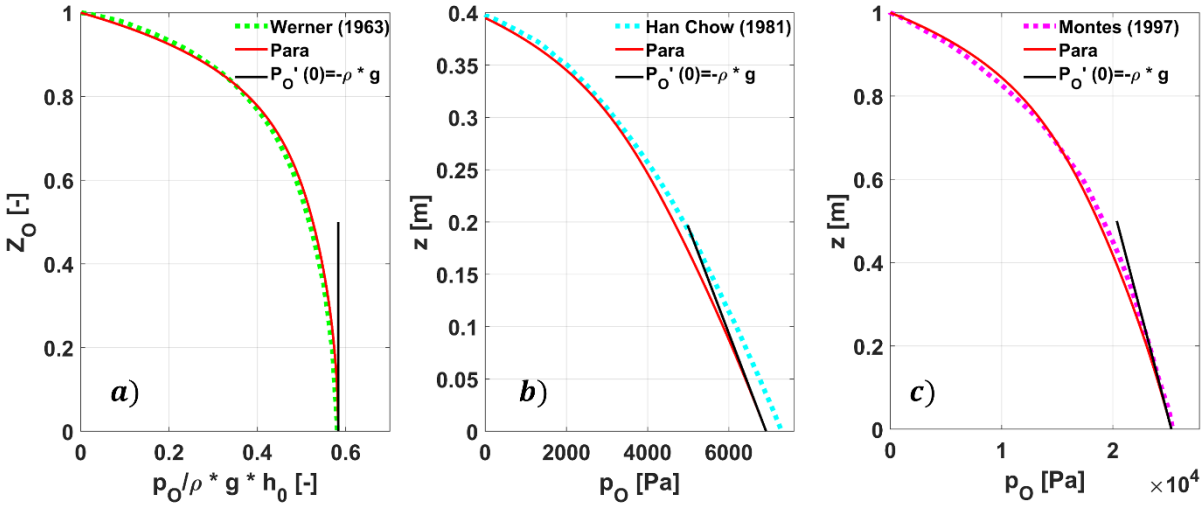

Figure 60: Parameterization approach of opening pressure distribution for standard sluice gate compared with results from a) Werner for ε=0 b) Hand Chow for ε=0.395 and c) Montes for ε=0.2546

As shown, the new parameterization approach is very well suited to calculate the pressure distribution at the opening for the standard sluice gate. Eq. (5-27) shows again the parameterization approach for the opening pressure distribution of the standard sluice gate (Eq. (5-25)) with inserted coefficient $k_O(\varepsilon)$ (Eq. (5-26)) and exponent ($n = 8$):

$$P_O(Z_O) = -0.6172\left(1 - \left(\frac{1}{\varepsilon}\right)^{-0.6172}\right)(Z_O^8 - Z_O^2) + \frac{\rho\, g\, a}{p_{BO}} \cdot (Z_O^2 - Z_O) - Z_O^2 + 1 \qquad (5\text{-}27)$$

5.2.3 Parameterization of the Inclined Sluice Gate Opening Pressure Distribution

The opening pressure distribution p_O of the inclined sluice gates is exemplarily shown in Figure 61 a) for ε=0.25. The values of the opening pressure distribution become smaller as the angle of inclination α becomes smaller. To perform the parameterization, the pressure distribution p_O and the opening z-coordinate are first nondimensionalized, using again Eq. (5-19) and Eq. (5-20). The dimensionless opening pressure distribution P_O is shown in Figure 61 b). The deviations of the curves of the dimensionless pressure distributions P_O for the shown angles of inclination α are small, compared with the deviations of the curves of the dimensionless opening pressure distribution P_O for different relative gate openings ε, see Figure 57 b). Because of the small dependency of P_O on the angle of inclination α, two methods were introduced for the following investigations on the parameterization of the inclined sluice gate opening pressure distribution. A simplified approach, which assumes that the dimensionless pressure distribution does not depend on the angle of inclination α and a detailed approach which includes the (small) deviations of the dimensionless opening pressure profile due to the angle of inclination α. Even if there is no dependence of the angle of inclination α on the dimensionless opening pressure distribution P_O in the simplified approach, the opening pressure distribution p_O changes with the angle of inclination since the angular dependence of the bottom pressure is also taken into account here.

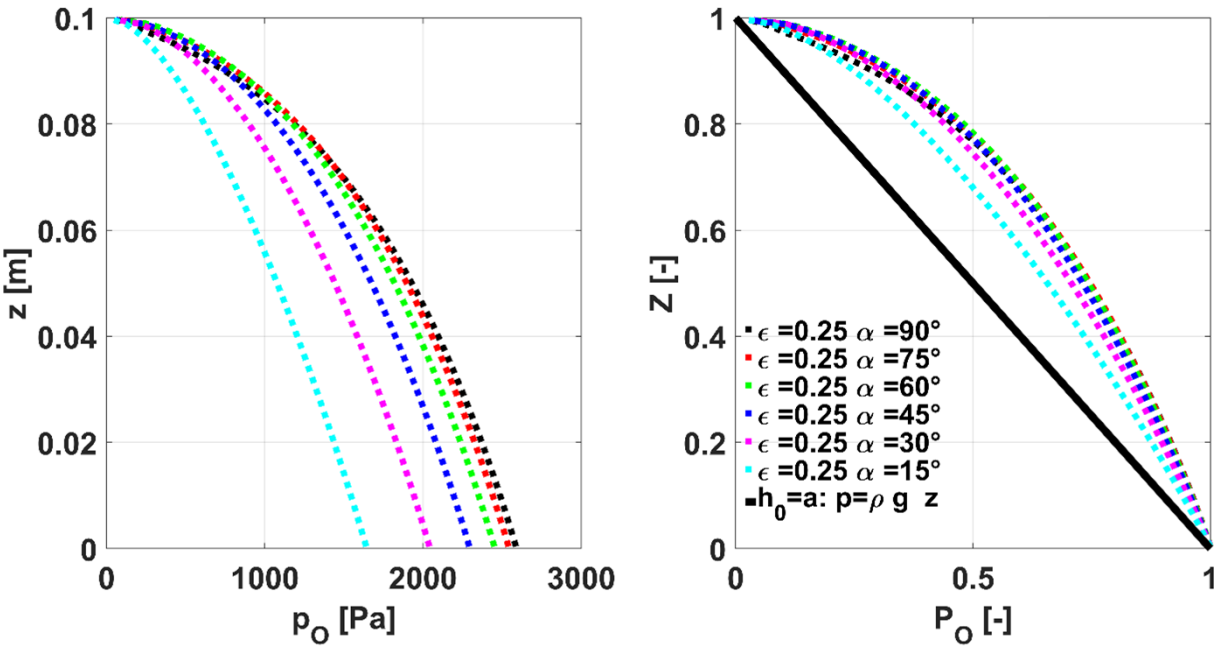

Figure 61: a) Opening pressure distribution p_O and b) dimensionless opening pressure distribution P_O for the inclined sluice gate with ε=0.25

Simplified Approach

The introduced parameterization approach of the opening pressure distribution of the standard sluice gate with the parameter $k_O(\varepsilon)$ (Eq. (5-26)) and the exponent $n = 8$ is also applicable for the parameterization of the opening pressure distribution of the inclined sluice gate. In a first approximation, the angle dependence is only considered via the dependency of the bottom pressure at the opening. The bottom pressure at the opening can be calculated with Eq. (5-9) derived in chapter 5.1.1.

The opening pressure distribution p_O for the inclined sluice gate and the CFD results are shown exemplary in Figure 62 a) for $\varepsilon = 0.1$ and in Figure 62 b) for $\varepsilon = 0.25$. The parameterization fits well over all values of α. Only close to the gate lip, near $z = 0.1$, the profile of the opening pressure distribution is influenced by the angle of inclination due to a smaller curvature of the streamlines, but since this influence is small, it can be neglected in this approach. The opening pressure distribution p_O of the inclined sluice gate was not shown yet by other authors, therefore a comparison with the literature is not possible here.

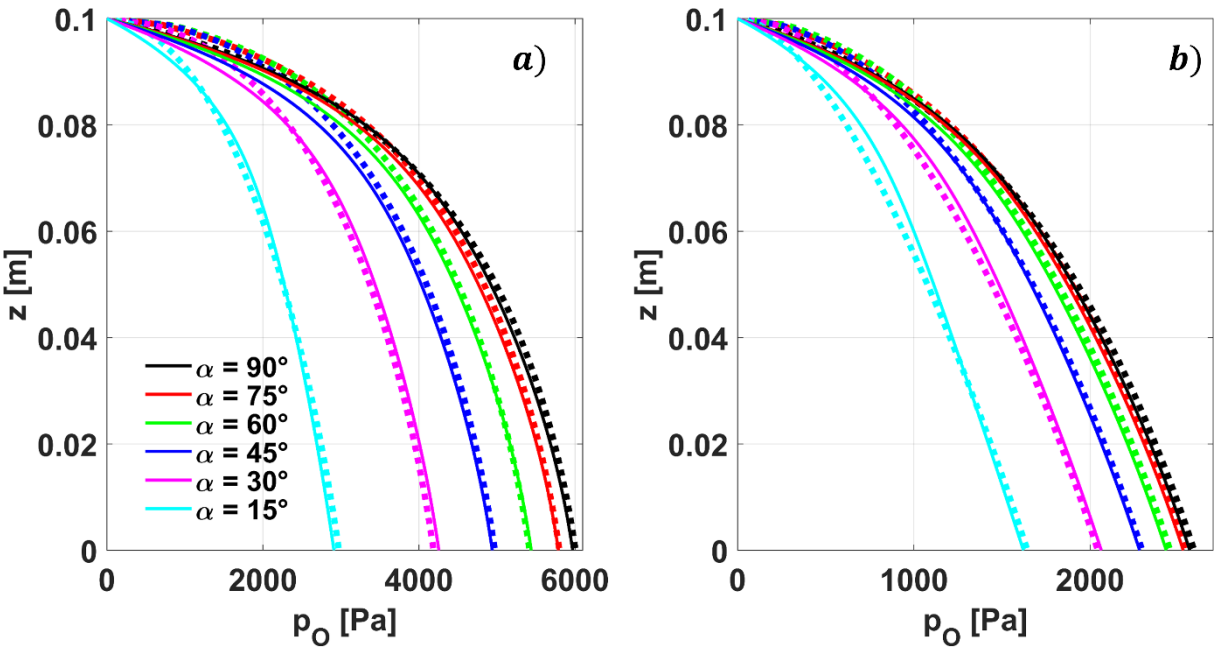

Figure 62: Comparison of the parametrization results of the simplified approach (solid line) with CFD simulation results (dashed line) of the opening pressure distribution for a) ε=0.1 and b) ε=0.25 for various angles of inclination α

Detailed Approach

For the detailed approach, both the exponent n and the parameter k_0 (ε) are determined for the different angles of inclination α. As the exponent n for the standard sluice gate was determined, also the exponent for the inclined sluice gate was determined using the non-linear least square method to fit Eq. (5-25) with the CFD data for the inclined sluice gate. The mean RMSE and the mean SSE over the exponents n are shown in Figure 63 for the investigated angles of inclination.

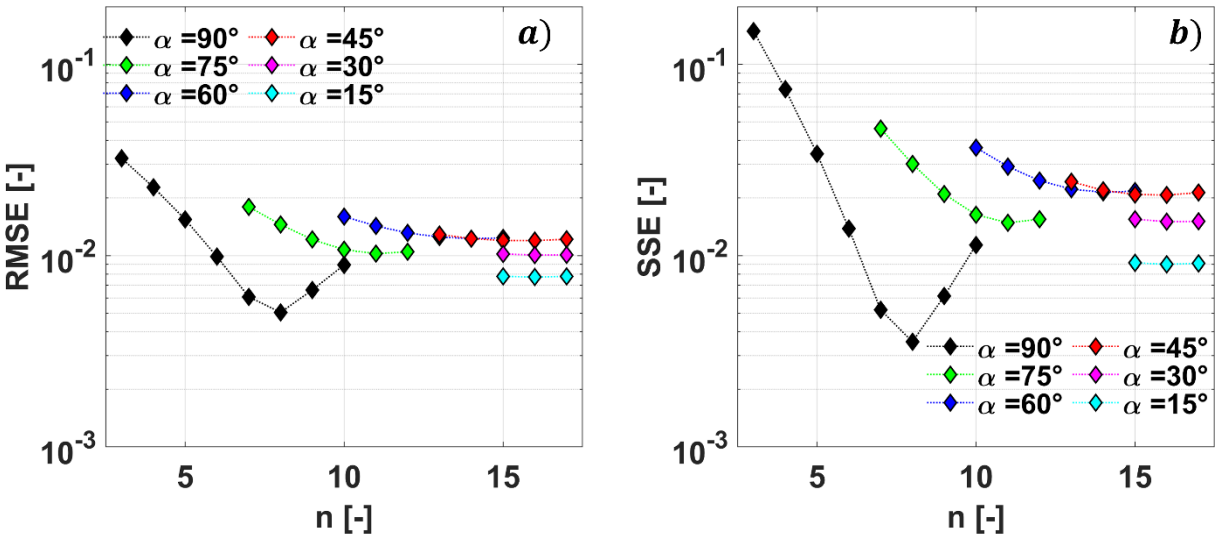

Figure 63: Mean RMSE and mean SSE for inclined opening pressure exponent determination

The exponents n with the smallest errors are also shown in Table 8. The exponent n is increasing with the angel of inclination from $n = 8$ for $\alpha = 90°$ until $n = 16$ for $\alpha = 45°$. For smaller values ($\alpha < 45°$), the exponent n does not increase further and the best agreement with the CFD results can be obtained for $n = 16$.

Table 8: Determined opening pressure distribution exponent n and errors for various angles of inclination

	$\alpha = 90$	$\alpha = 75$	$\alpha = 60$	$\alpha = 45$	$\alpha = 30$	$\alpha = 15$
n	8	11	14	16	16	16
$\overline{SSE}$	0.003544	0.014851	0.021423	0.020733	0.015051	0.009000
$\overline{RMSE}$	0.005046	0.010244	0.012268	0.011977	0.010063	0.007725

For the different angles of inclination α with the corresponding exponent n (see Table 8) and the investigated relative gate openings ε, the fitting parameter $k_0(\varepsilon)$ was now determined with the non-linear least square method, using the CFD simulations of the inclined sluice gate. The values determined in this way for the parameter k_0 are shown in Figure 64.

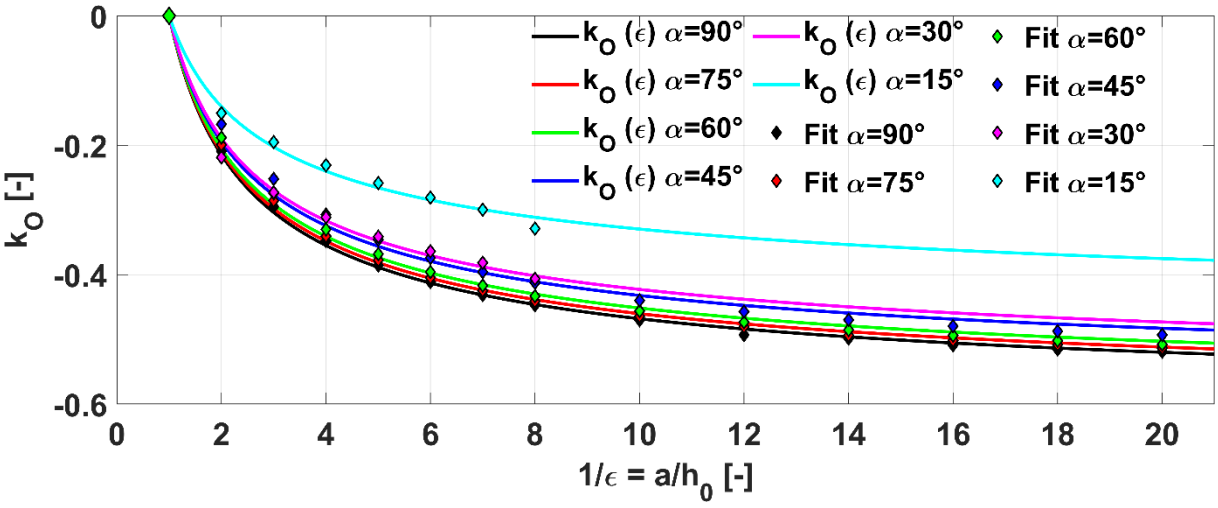

Figure 64: Fitting parameter $k_{0,\alpha}(\varepsilon)$ for inclined sluice gates

The dependency on the relative gate opening ε of the parameter k_O can be again good approximated by Eq. (5-26). The fitting constant k_O^* was determined, using the non-linear least square method. The results for k_O^* are shown with the corresponding SSE and RMSE in Table 9. The resulting parameter curves from Eq. (5-26) with k_O^* from Table 9 are also shown in Figure 64 for the investigated angles of inclination α.

Table 9: Fitting constant $k_{0,\alpha}^*$ for inclined sluice gates

	α = 90	α = 75	α = 60	α = 45	α = 30	α = 15
$k_{O,\alpha}^*$	-0.6172	-0.6101	-0.6022	-0.5844	-0.5758	-0.4883
SSE	0.000276	0.000450	0.000939	0.002393	0.001040	0.000622
RMSE	0.004608	0.005882	0.008499	0.013570	0.012190	0.009425

With the determined fitting constants in Table 9 and the exponent in Table 8, the opening pressure distribution p_O for the detailed approach can be calculated using Eq. (5-25). Figure 65 shows the comparison of the detailed parameterization approach with the CFD values. The opening pressure distributions determined in the CFD and the detailed approach of the opening pressure distribution parameterization agree well. However, deviations also occur here and the approach matches the CFD values only slightly better than the simplified approach, but is much more complex. For the determination of the opening force F_O in the following chapter, the simplyfied approach is therefore used.

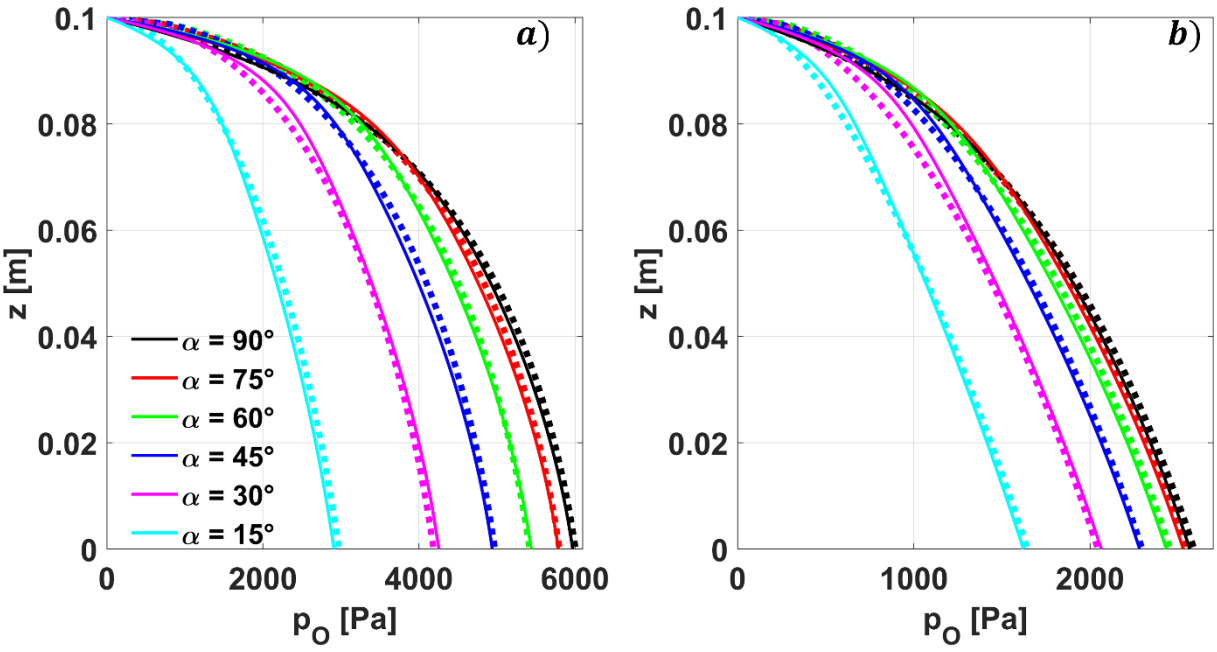

Figure 65: Comparison of the parametrization results of the detailed approach (solid line) with CFD simulation results (dashed line) of the opening pressure distribution for various angles of inclination α for a) ε=0.1 and b) ε=0.25

5.2.4 Integral of the Opening Pressure Distribution

The force at the opening F_O can be determined by integrating the pressure distribution at the opening p_O from the bottom ($z = 0$) to the gate lip ($z = a$). With the definition of the dimensionless opening pressure Eq. (5-19) and the dimensionless gate coordinate Eq.(5-20), the opening force F_O can be determined by integrating the dimenionless opening pressure distribution p_O, see Eq. (5-28).

$$F_O = \int_0^a p_O \, dz = p_{BO} \cdot a \cdot B \cdot \int_0^1 P_O \, dZ_O \tag{5-28}$$

The general approach for the dimensionless opening pressure distribution P_O was introduced in Eq. (5-25). Substituting this equation into Eq. (5-28) gives the following equation:

$$F_O = p_{BO} \, a \, B \int_0^1 \left(k_O(\varepsilon) \left(Z_O^n - Z_O^2 \right) + \frac{\rho \, g \, a}{p_{BO}} \left(Z_O^2 - Z_O \right) - Z_O^2 + 1 \right) dZ_O \tag{5-29}$$

Solving the integral in Eq. (5-29) yields Eq. (5-30):

$$F_O = p_{BO} \; a \; B \left(k_O(\varepsilon) \frac{2 - n}{3(n + 1)} - \frac{\rho \, g \, a}{6 \, p_{BO}} + \frac{2}{3} \right) \tag{5-30}$$

Determining the bottom pressure at the opening p_{BO} from Eq. (5-9) and using the simplified approach with $n = 8$ and $k_O(\varepsilon)$ from Eq. (5-26), the force at the opening can be determined from Eq. (5-30). The results for F_O obtained in this way are shown in Figure 66. Also shown in Figure 66 are the CFD results. These are in excellent agreement with the parameterization. A comparison with literature values is not possible since a parameterization of the opening force as a function of the angle of inclination α and the relative gate opening ε was carried out for the first time in this work.

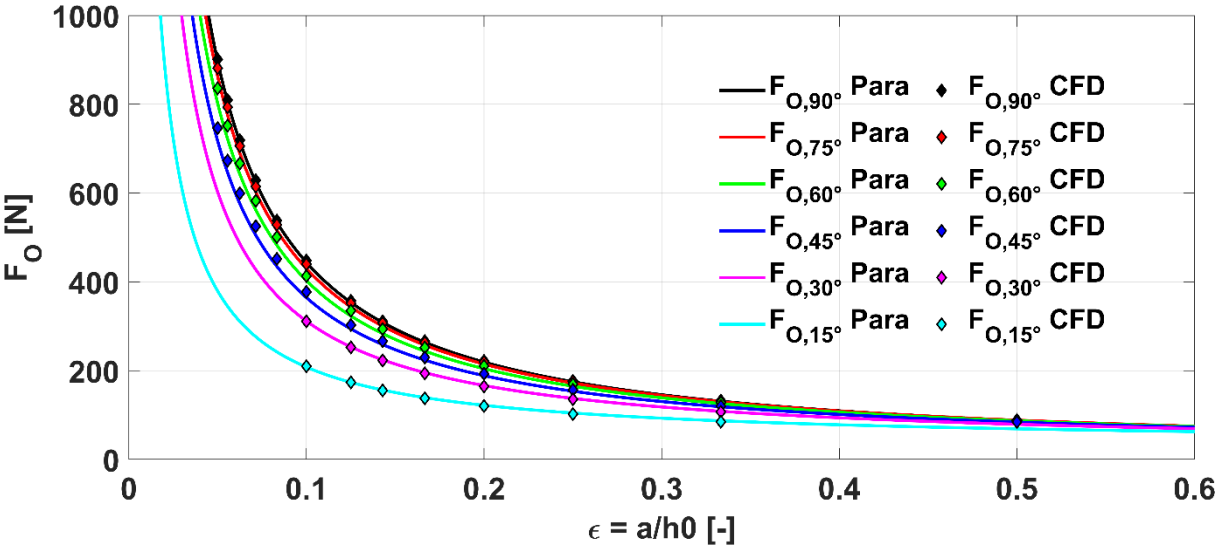

Figure 66: Pressure integral at the opening F_O for standard and inclined sluice gates

5.3 Gate Pressure Distribution

The gate pressure distribution is probably the most studied pressure distribution on sluice gates, as it is not only important from a fluid mechanics point of view, but also for structural mechanics calculations. Early investigations on the gate pressure distribution were done by Koch and Carstanjen [61], who described a decrease of the pressure at the gate, due to the increase in velocity and hence the dynamic pressure. Kulka [62] integrated the approach of Koch and Carstanjen [61] and derived a formula for the pressure force at the sluice gate wall F_G, for mechanical calculations. Later, Pajer [63], Cheng et. al [64], Han/Chow [60], Montes [35] and Belaud/Litrico [65] calculated the pressure distribution at the sluice gate using numerical approaches. Experimental results of the pressure distribution were given by Gentilini [24] (for the inclined sluice gate with $\alpha = 45°$), Finnie/Jeppson [66] and Roth/Hager [28]. Castro-Orgaz/Hager [67] calculated the pressure distribution based on an exponential increase of the velocity at the sluice gate wall, where the exponent was determined by applying momentum balance for a known contraction coefficient C_c and discharge coefficient c_D.

The main characteristics of the pressure distribution are the water level increase at the sluice gate wall Δh_G, the Z_{Ga} or Z_{Ge} coordinate, where the flow attaches at the sluice gate wall or the surface eddy height and P_{Gm} at Z_{Gm}, where the gate pressure reaches its maximum value.

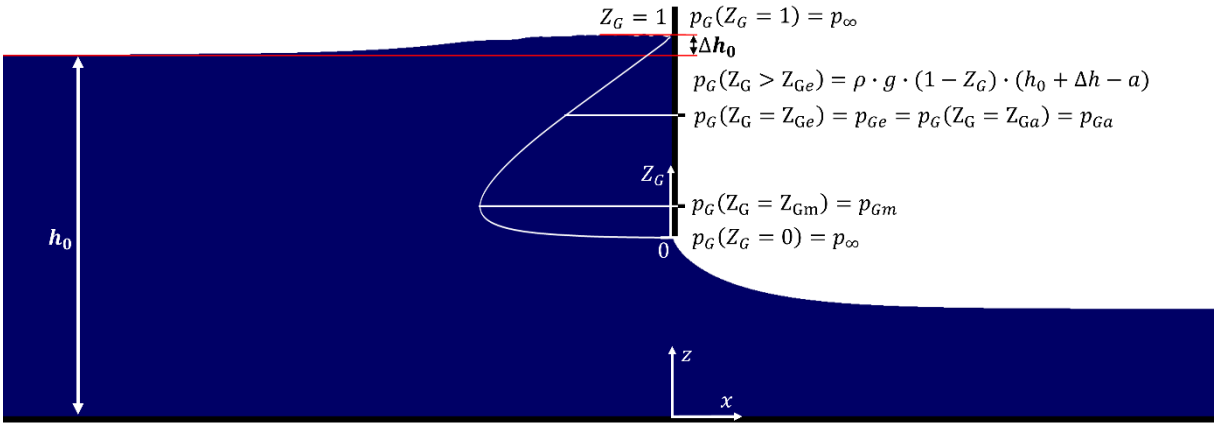

Figure 67: Main characteristics of the gate pressure distribution

While from $Z_G = 1$ to Z_{Ge}, the pressure increase is hydrostatic, from Z_{Ge} to $Z_G = 0$ the pressure is smaller than the hydrostatic pressure. The characteristic properties of the pressure distribution on the sluice gate shown in Figure 68 will be discussed in the following chapters. At first, the dimensionless representation of the pressure distribution and the dimensionless gate coordinate will be shown. Then the water level increase at the sluice gate Δh_G, the attached flow coordinate or eddy height $Z_{Ga} = Z_{Ge}$ as well as the maximum pressure p_{Gm} and the location of the maximum pressure Z_{Gm} of the pressure distribution are investigated.

5.3.1 Dimensionless Sluice Gate Pressure Distribution

To analyze and parametrize the gate pressure distribution along the sluice gate wall, the gate pressure distribution p_G and the z-coordinate at the gate were first normalized, so that at the gate lip the normalized gate coordinate $Z_G = 0$ and at the upstream water level at the sluice gate wall, the normalized gate coordinate $Z_G = 1$. The gate pressure distribution was normalized by dividing the gate pressure distribution p_G by the hypothetical hydrostatic pressure at the gate lip. The water column of this hypothetical hydrostatic pressure distribution is equal to the upstream water level h_0 plus the water level increase at the sluice gate wall Δh_G minus the height of the gate opening a. The equation for calculating the dimensionless Z-coordinate Z_G is shown in Eq. (5-31) and the equation for calculating the dimensionless gate pressure P_G is shown in Eq. (5-32).

$$Z_G = \frac{(z - a)}{h_0 + \Delta h_G - a} \tag{5-31}$$

$$P_G(Z_G) = \frac{p_G(Z_G)}{\rho\, g\, (h_0 + \Delta h_G - a)} \tag{5-32}$$

5.3.2 Water Level Increase at the Sluice Gate Wall

At the sluice gate wall, the water level increases and is higher than the upstream water level h_0 of the sluice gate flow. The water level increase depends on the relative gate opening ε. The difference between the water level at the sluice gate and the upstream water level is introduced as Δh_G. In early studies, it was assumed, that the upstream water level h_0 at the sluice gate wall decreases or is constant ([61], [62], [68]). Later on, e.g. Keutner [6] described an increase of the upstream water level near the sluice gate wall due to a reduced flow velocity near the water surface until a point in a distance upstream of the sluice gate. Between this point and the sluice gate wall, an eddy occurs, which was described by Keutner as “Deckwalze”. In this region a further increase in the upstream water level was described. The eddy itself was observed earlier e. g. by Koch and Carstanjen [61], but the water level increase was not mentioned there. For the calculation of the upstream water level increase at the sluice gate wall a stagnation point was assumed at the sluice gate wall, and it was also assumed that the upstream water level at this point is equal to the total energy head H_0. This relation was found by E. Lindquist from Stockholm, published later in Germany at the “Zentralblatt der Bauverwaltung” in 1930 [69]. In later works e. g. [63], [16], [70], [71] on sluice gate flows, this approach was used in this time to calculate the water level increase at the sluice gate, from the

upstream velocity u_0. This method is commonly used until today. The water level increase at the sluice gate from this approach can be calculated using Eq. (5-33):

$$\Delta h_G = \frac{u_0^2}{2\ g} \tag{5-33}$$

Naudascher [72] [5] assumed a lower water level than the upstream energy head (Eq. (5-33)), due to dissipation losses caused by the eddy and due to a non-uniform upstream velocity distribution.

In this work Δh_G was determined using values from the CFD simulations. The water level increase was calculated with the energy conservation approach Eq. (5-33) as well as the actual water level increase from the CFD simulations was determined. To determine the water level increase from CFD, the pressure at the sluice gate p_G at the position h_0 was determined, which corresponds to the hydrostatic pressure of the water level increase. From this, the water level increase can be determined as follows:

$$\Delta h_G = \frac{p_G(h_0)}{\rho\ g} \tag{5-34}$$

The representation of the water level increases Δh_G at the sluice gate wall is done dimensionless by dividing it by $h_0 - a$. The CFD results of the dimensionless water level increase $\frac{\Delta h_G}{h_0 - a}$ in dependency of the relative gate opening ε are shown in Figure 68 for both approaches Eq. (5-33) and Eq. (5-34).

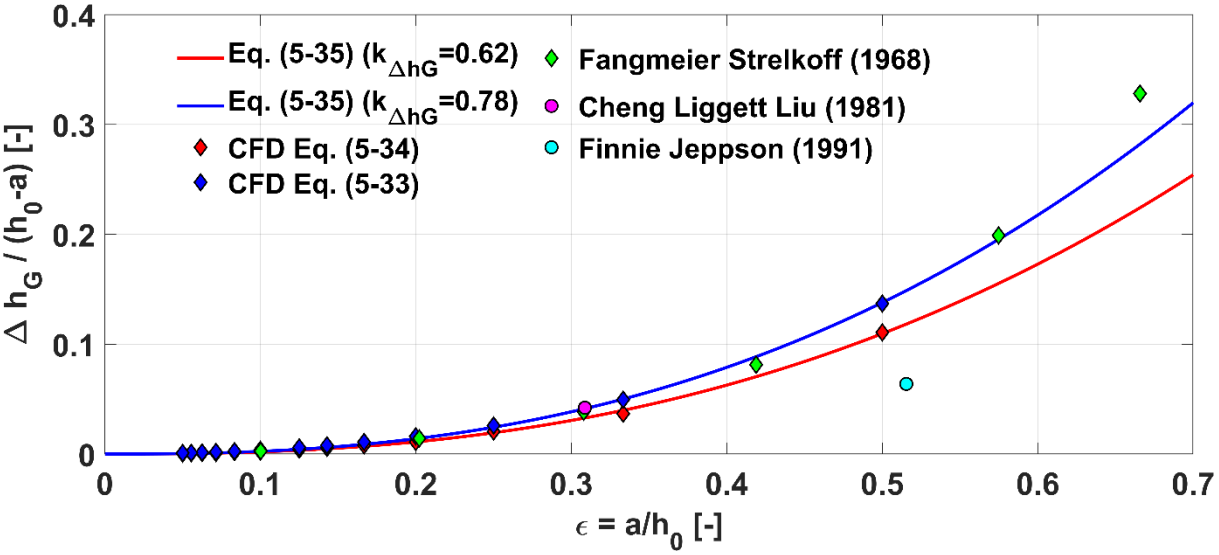

Figure 68: Water level increase Δh_G at the sluice gate wall in dependency of the relative gate opening ε

As shown in Figure 68, the dimensionless water level increase $\frac{\Delta h_G}{(h_0 - a)}$ increases with increasing relative gate opening ε for both approaches. The dependence of the dimensionless

water level increase $\frac{\Delta h_G}{(h_0-a)}$ on ε can be represented by a power function passing through the origin $(0,0)$. With the coefficient $k_{\Delta hG}$, the function shown in Eq. (5-35), is used as parameterization approach for the dimensionless water level increase $\frac{\Delta h_G}{(h_0-a)}$.

$$\frac{\Delta h_G}{(h_0 - a)} = k_{\Delta hG}\, \varepsilon^{\frac{5}{2}} \tag{5-35}$$

The coefficient $k_{\Delta hG}$ is determined for both approaches (Eq. (5-33) and Eq. (5-34)) with the non-linear least square method. For the energy conservation approach (Eq. (5-33)), $k_{\Delta hG} = 0.78$ is obtained with the errors $SSE = 2.48 \cdot 10^{-5}$ and $RMSE = 0.001438$. For the real water level increase determined with Eq. (5-34) directly at the sluice gate wall, the coefficient $k_{\Delta hG} = 0.62$ is obtained with the erros $SSE = 1.44 \cdot 10^{-5}$ and $RMSE = 0.001095$. The errors are small for both calculation methods, from which it can be concluded that the approach introduced in Eq. (5-35) is well suited for the calculation of the dimensionless water level rise $\frac{\Delta h_G}{(h_0-a)}$. Also shown in Figure 68 are the dimensionless water level increases calculated by the authors Fangmeier and Strelkoff [73], Cheng, Liggett and Liu [64] and Finnie and Jeppson [66]. Investigations from Fangmeier et. al and Cheng et. al, do agree well with the energy approach. Only for large relative gate openings ε the approach of Fangmeier et. al does significantly overestimate the parameterization function (Eq. (5-35)) with $k_{\Delta hG} = 0.78$. The calculations of Finnie et al. do underestimate both approaches and the other literature values. The difference between the energy conservation approach and the real water level increase are caused by dissipation losses of the surface eddy. The dissipation losses were also already observed by Naudascher [5]. For the parametrization of the gate pressure distribution later in this work, the water level increase including dissipation losses (Eq. (5-35) with $k_\Delta = 0.62$) will be used.

5.3.3 Eddy Height and Attachment Point at the Sluice Gate Wall

An important parameter in the analysis of the sluice gate pressure distribution is the point at which the flow attaches to the gate, this point is called the attachment point with the dimensionless gate coordinate Z_{Ga} and is shown schematically in Figure 69. Between the water surface $Z_G = 1$ and Z_{Ga}, an eddy occurs, where the dynamic pressure is low and has no significant impact on the sluice gate pressure distribution, hence for $Z_G > Z_{Ga}$ the sluice gate pressure $p_G(Z_G)$ is hydrostatic. The height of this eddy at the sluice gate is measured in the Z-direction and is referred to as h_{Ge}.

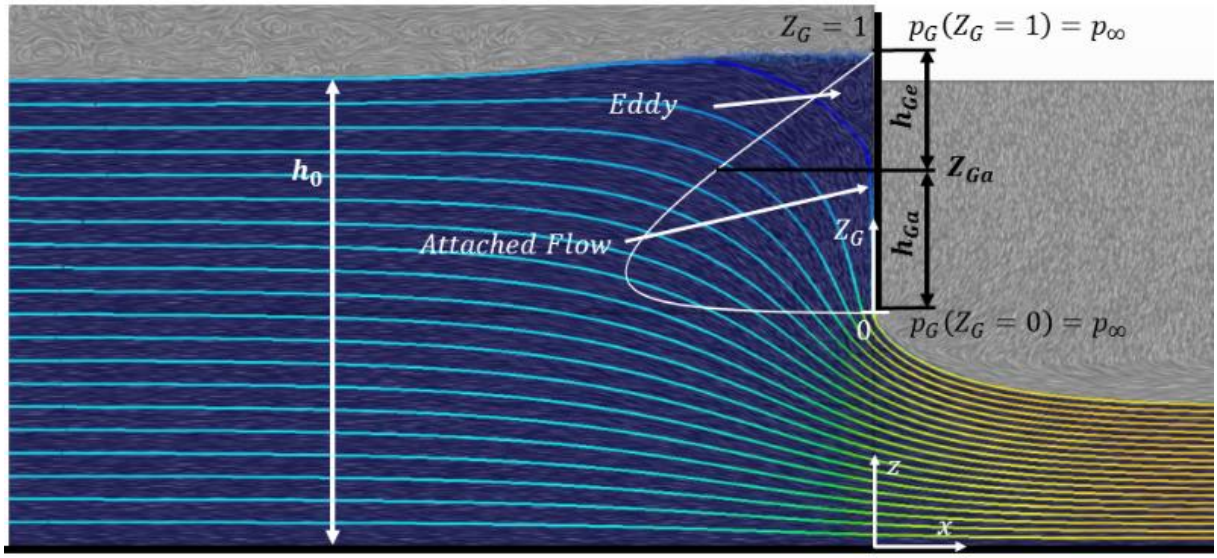

Figure 69: Pressure distribution at sluice gate wall with attachment point Z_{Ga} and eddy height h_{Ga}

Between the gate lip $Z_G = 0$ and Z_{Ga}, the flow is attached and the velocity and hence the dynamic pressure increases along the streamline near the sluice gate wall through gravity. For the calculation of Z_{Ga}, a field function was created in Star CCM+, with which the deviation of the pressure at the sluice gate $p_G(z)$ from the theoretical occurring hydrostatic pressure $(h_0 + \Delta h_G - z)\ \rho\ g$ is calculated. This corresponds quasi to the dynamic pressure at the sluice gate, but since the velocity is equal to zero at the sluice gate due to the no slip condition, it cannot be designated in this way. Since the pressure through the boundary layer is constant in a direction perpendicular to the surface, the dynamic pressure thus determined is the dynamic pressure of the streamline adjacent to the boundary layer in the free flow. Figure 70 shows a schematic plot of the dynamic pressure determined in this way. In addition, streamlines have been shown in the figure, which show that a stagnation point occurs at Z_{Ga}.

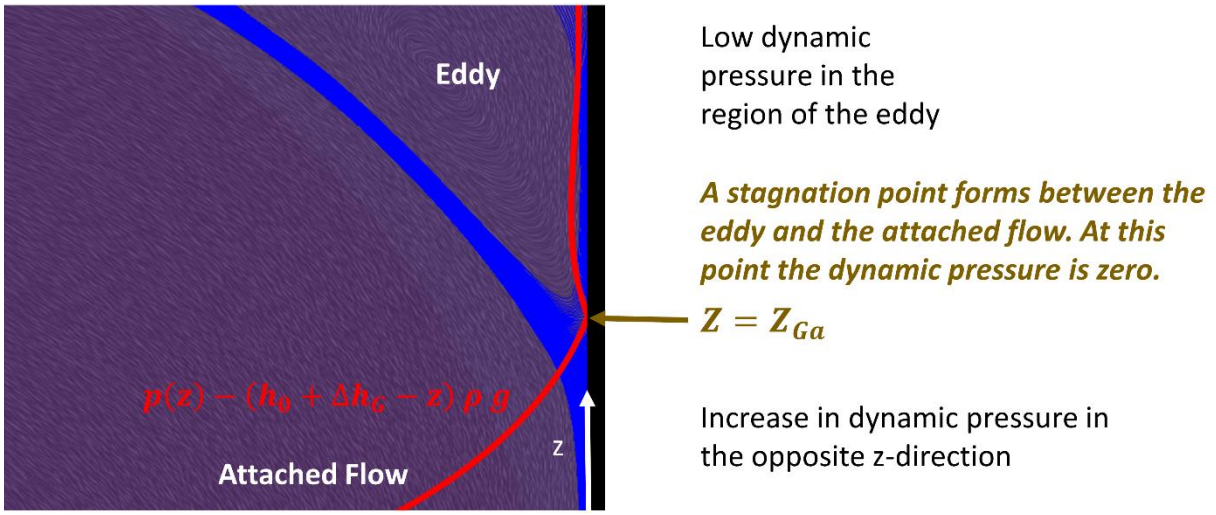

Figure 70: Gate flow characteristics: eddy, stagnation point and attached flow

At the stagnation point the velocity and thus the dynamic pressure is zero. The position of the stagnation point, which is equal to the position of Z_{Ga}, can thus finally be calculated from the CFD simulations with Eq. (5-36):

$$Z_{Ga} = Z_G(p_G = \min\big((h_0 + \Delta h_G - z)\,\rho\,g - p_G(z)\big)) \tag{5-36}$$

With Z_{Ga}, the eddy height h_{Ge} can be calculated with the help of Eq. (5-37) by first calculating the dimensionless distance from Z_{Ga} to the water surface $Z_G = 1$ and then converting this back to normal coordinates with the help of Eq. (5-31).

$$h_{Ge} = (1 - Z_{Ge})(h_0 + \Delta h_G - a) + a \tag{5-37}$$

The values calculated in this way for the standard sluice gate are nondimensionalized by dividing them by the upstream water level h_0. Rajaratnam and Humphries [32] also nondimensionalized the eddy height in this way. They found in their experiments that for the investigated relative gate openings from $\varepsilon = 0.04$ to $\varepsilon = 0.4$ the nondimensionalized eddy height can be given as constant with $\frac{h_{Ge}}{h_0} = 0.28$. Figure 71 shows the CFD values and the result of Rajaratnam and Humphries. The dimensionless eddy heights read out from the CFD seem to increase with decreasing relative gate opening. Therefore, for a parameterization of the dimensionless eddy height h_{Ge}/h_0 a function depending on the relative gate opening ε might be chosen. Nago [38] also described scale effects on the size of the eddy. Because the eddy height h_{Ge} is not needed for further calculations, no parameterization is performed for it in this work. Note: The eddy height was evaluated here at a random time step, but since the eddies are subject to large fluctuations, a time-resolved analysis is suggested here for more detailed investigations.

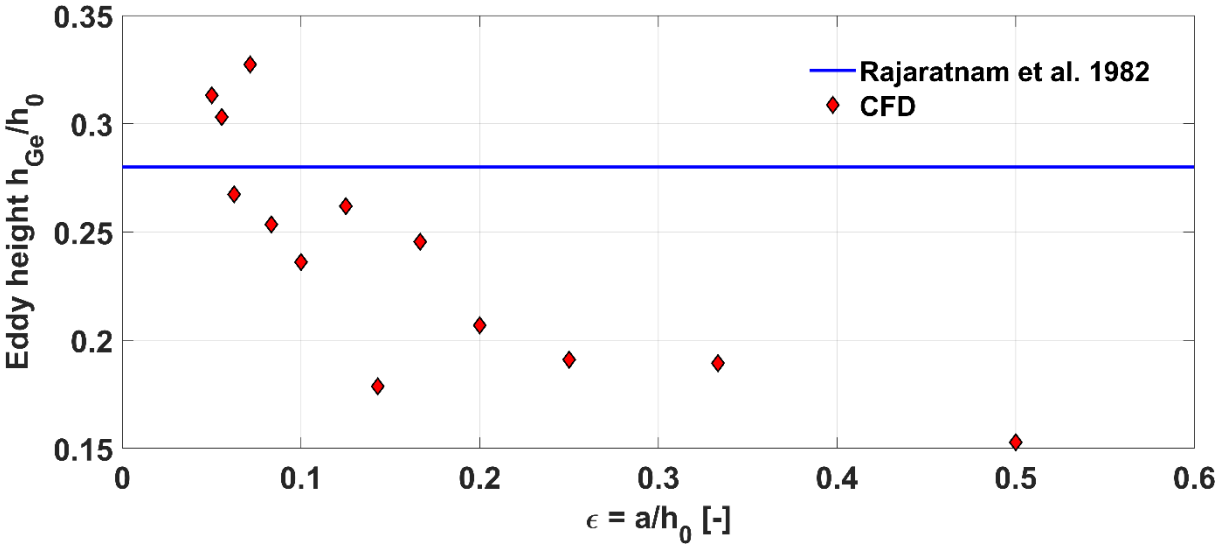

Figure 71: Relative eddy height h_{Ge}/h_0 in dependency of the relative gate opening ε

5.3.4 Maximum Gate Pressure

The pressure at the sluice gate initially increases hydrostatically from the water surface in negative z-direction to the gate lip. At the point Z_{Ga}, where the flow attaches to the gate, the pressure continues to increase but no longer as strongly as at the beginning. This increase takes place until the maximum pressure p_{Gm} is reached at the position $Z_G = Z_{Gm}$. The maximum pressure at the gate is reached when the change of the dynamic pressure at the gate is equal to the change of the quasi hydrostatic pressure, see Eq. (5-38). However, since the no-slip condition exists at the gate wall, it is actually the dynamic pressure of the streamline above the boundary layer. From Eq. (5-38) it follows that the maximum value of the pressure at the gate can be calculated with Eq. (5-39).

$$\frac{d}{dz}\left((h_0 + \Delta h_G - z)\,\rho\,g - p_G(z)\right) = \frac{d}{dz}\left(\rho\,g\,(h_0 + \Delta h - z)\right) \tag{5-38}$$

$$\frac{dp_G(z)}{dz} = 0 \tag{5-39}$$

The values for the nondimensionalized maximum gate pressure P_{Gm} calculated in the CFD as well as those given by Roth and Hager [28], Belaud and Litrico [65] and Castro-Orgaz and Hager [67] are shown in Figure 72 as a function of the relative gate opening ε. The maximum nondimensionalized gate pressure P_{Gm} from the three papers ([28], [65], [67]) were determined from the pressure distributions given in these papers. These pressure distributions will be discussed in more detail in the following chapters when parameterizing the gate pressure distribution. As can be seen in Figure 72, the dimensionless maximum gate pressure increases with decreasing relative gate opening. While for $\varepsilon = 0$, which means the

gate is closed, the maximum gate pressure is $P_{Gm} = 1$ and equal to the hydrostatic pressure at the bottom. The maximum pressure P_{Gm} agrees well for all studies for small relative gate openings ($\varepsilon < 0.1$). Whereas for larger relative gate openings ε, the maximum pressure P_{Gm} calculated in CFD is larger than that calculated by the other authors. All the results shown diverge for increasing relative gate openings ε.

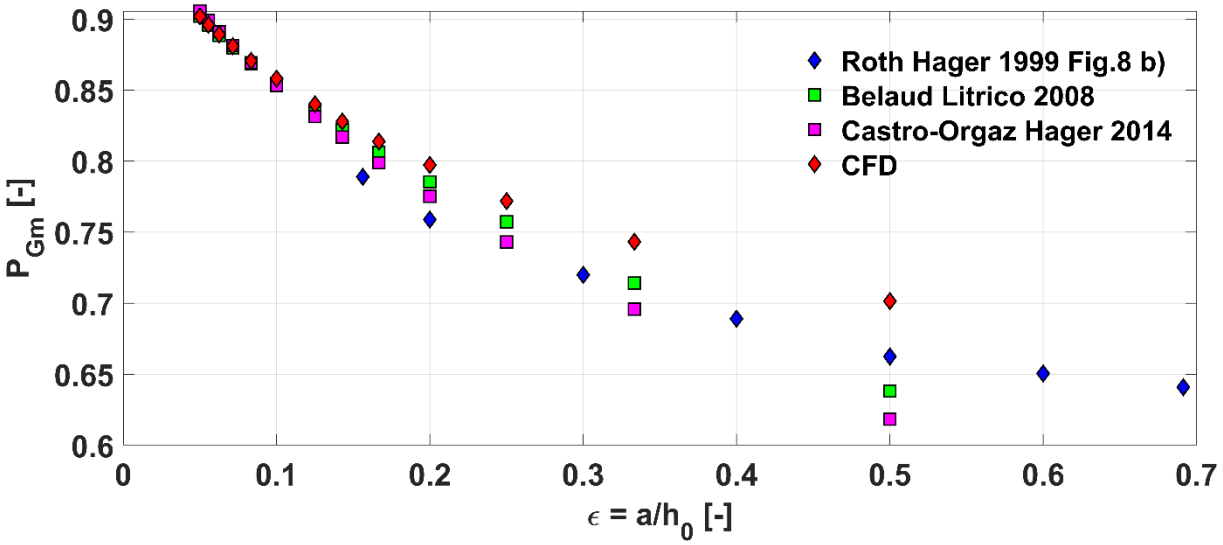

Figure 72: Nondimensionalized maximum gate pressure P_{Gm} in dependency of the relative gate opening ε

Figure 73 further shows the position of the maximum pressure Z_{Gm} as a function of the relative gate openings ε. The position of the maximum pressure Z_{Gm} decreases with decreasing relative gate opening ε in the direction of the gate lip. For the limiting case $\varepsilon = 0$, which corresponds to the closed gate with hydrostatic pressure distribution, the position of the maximum pressure Z_{Gm} is at the gate lip or at the bottom. This tendency is also satisfied by the pressure distributions of Belaud and Litrico [65] and Castro-Orgaz and Hager [67], while in the parameterization of Roth and Hager [28] the position of the maximum pressure is assumed to be constant. For small relative gate openings $\varepsilon < 0.1$, Z_{Gm} from the CFD simulations agrees very well with the results of Belaud and Litrico [65]. In the parameterization of Castro-Orgaz and Hager, the position of the maximum gate pressure Z_{Gm} is lower compared to Belaud and Litrico over the whole investigated range. The position of the dimensionless maximum gate pressure Z_{Gm} obtained from the CFD simulations, on the other hand, agrees better with the values of Castro Orgaz and Hager for $\varepsilon > 0.3$ than with those of Belaud and Litrico.

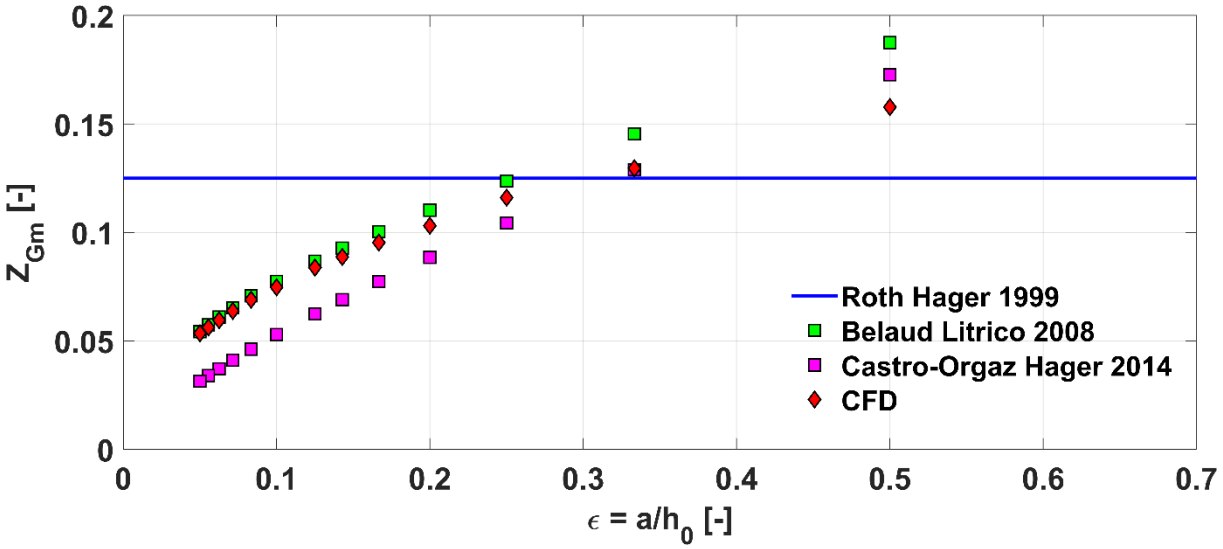

Figure 73: Position of the maximum gate pressure Z_{Gm} in dependency of the relative gate opening ε

5.3.5 Parameterization of the Standard Gate Pressure Distribution

For the parametrization of the standard sluice gate pressure distribution, first the hydrostatic pressure component $P_{GS}(Z_G)$ and the quasi dynamic pressure part $P_{GD}(Z_G)$ were separated. The dimensionless hydrostatic pressure component $P_{GS}(Z_G)$, can be calculated using Eq. (5-40):

$$P_{GS}(Z_G) = 1 - Z_G \tag{5-40}$$

To determine the dynamic pressure distribution, the gate pressure p_G from the CFD simulations was first nondimensionalized using Eq. (5-31) and Eq. (5-32). The thus calculated dimensionless gate pressure $P_G(Z_G)$ is shown in Figure 74 a). To calculate the quasi dimensionless dynamic gate pressure $P_{GD}(Z_G)$, the dimensionless gate pressure $P_G(Z_G)$ is subtracted from the dimensionless hydrostatic pressure $P_{GS}(Z_G)$, see Eq. (5-41). The quasi dimensionless dynamic gate pressure $P_{GD}(Z_G)$ determined in this way is shown in Figure 74 b) for the investigated inverse relative gate openings $1/\varepsilon$. In the following, the quasi-dimensionless dynamic gate pressure is referred to as dimensionless dynamic gate pressure.

$$P_{GD}(Z_G) = P_{GS}(Z_G) - P_G(Z_G) \tag{5-41}$$

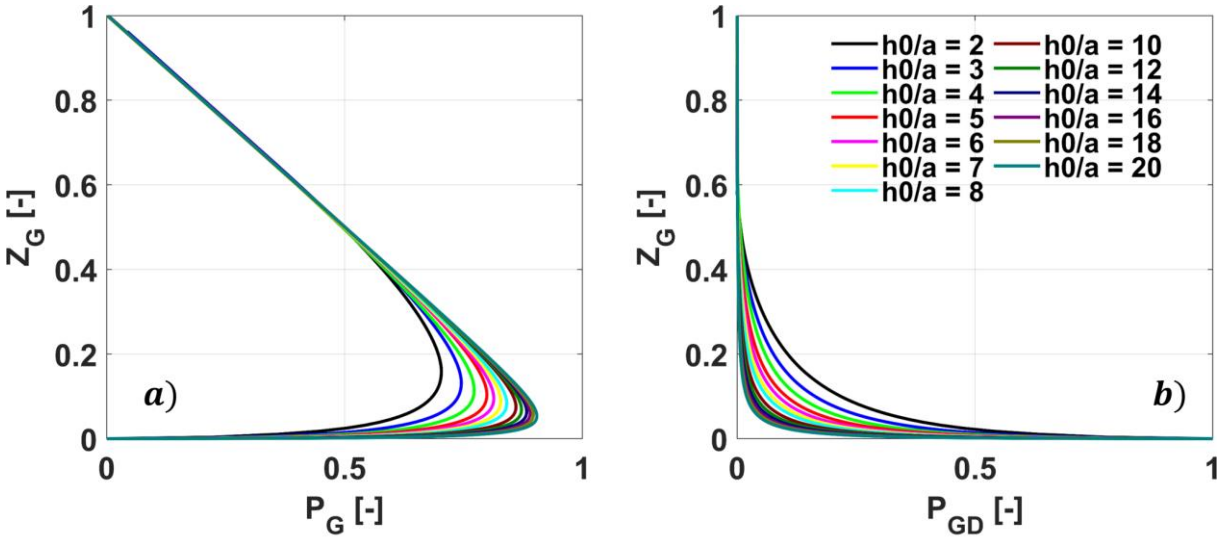

Figure 74: a) Dimensionless gate pressure $P_G(Z_G)$ and b) dimensionless dynamic gate pressure $P_{GD}(Z_G)$ of the standard sluice gate from CFD

At the upstream water level at the gate, the dynamic pressure is zero. The dynamic pressure increase starts when the flow is attached at $Z_G = Z_{Ga}$. Hence for an exact definition of the gate pressure distribution, a piecewise-defined function is necessary, as shown in Eq. (5-42):

$$P_{GD}(Z_G) = \begin{cases} f(Z_G) & \text{for} \quad 0 < Z_G < Z_{Ga} \\ 0 & \text{for} \quad Z_{Ga} < Z_G \end{cases} \tag{5-42}$$

For practical applications, it is useful to define a continuous function for $P_{GD}(Z_G)$ over the complete sluice gate wall, because the position of Z_{Ga} depends on the relative gate opening ε and also on the upstream water level h_0. Other authors such as Roth and Hager [28], Belaud and Litrico [65] and Castro-Orgaz and Hager [67] have also used a continuous function to parameterize the gate pressure distribution. In this work the dimensionless dynamic pressure $P_{GD}(Z_G)$ at the sluice gate wall, is parametrized using the following equation with the parameter $k_G(\varepsilon)$:

$$P_{GD}(Z_G) = \frac{1}{\frac{1}{k_G(\varepsilon)} \cdot Z_G + 1} - k_G(\varepsilon) \cdot Z_G \tag{5-43}$$

The parameter $k_G(\alpha = 90°)$ for the standard sluice gate was determined for all relative gate openings ε investigated in CFD using the non-linear least square method. The parameter $k_G(\alpha = 90°)$ for each investigated relative gate opening ε, determined in this way, is shown in Figure 75 (blue diamonds).

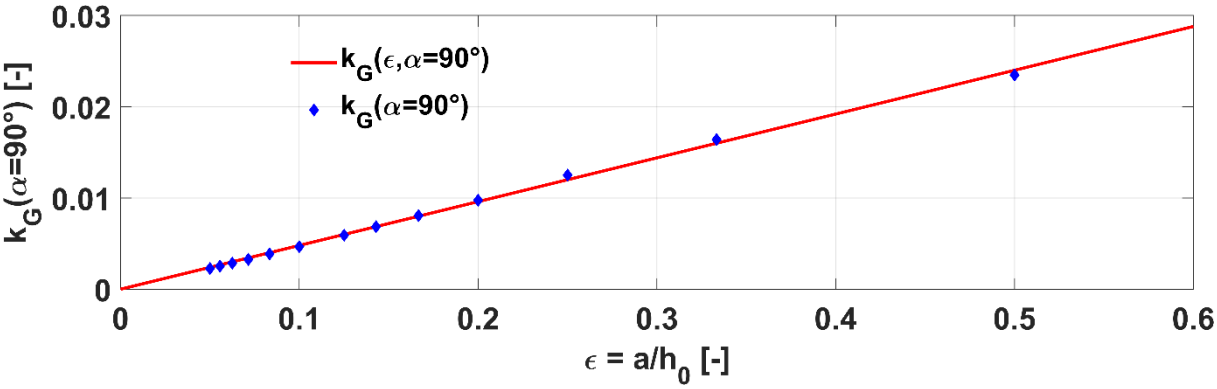

Figure 75: Parameter $k_G(\alpha = 90°)$ for gate pressure parameterization of the standard sluice gate

As it can be seen in the Figure 75, the parameter $k_G(\alpha = 90°)$ increases linearly with increasing relative gate opening ε. For the limiting case $\varepsilon = 0$, the parameter k_G must be zero, because the gate is closed and the dynamic pressure $P_{GD}(Z_G) = 0$ must be equal to zero. The course of the parameter $k_G(\alpha = 90°)$ can be mapped with Eq. (5-44), where the parameter $k_{G,90°}$ was calculated with the non-linear least square method as $k_{G,90°} = 0.48$ with an $R^2 = 0.9982$. The parameterization errors were calculated with $SSE = 8.4028 \cdot 10^{-7}$ and $RMSE = 2{,}6462 \cdot 10^{-4}$.

$$k_G(\varepsilon, \alpha = 90°) = k_{G,90°} \cdot \varepsilon \tag{5-44}$$

Substituting Eq. (5-43) and Eq. (5-40) into (5-41), and converting them to $P_G(Z_G)$, we obtain the following function for the dimensionless gate pressure distribution $P_G(Z_G)$:

$$P_G(Z_G) = 1 + k_G(\varepsilon, \alpha) \cdot Z_G - \left(Z_G + \frac{1}{\frac{1}{k_G(\varepsilon, \alpha)} \cdot Z_G + 1} \right) \tag{5-45}$$

With Eq. (5-31) and Eq. (5-32) the dimensionless gate pressure distribution (Eq. (5-45)) can be returned to the dimensioned form. For the cases $a = 0.1$ m, that was also investigated in CFD simulations, the pressure distributions were calculated with the new parameterization approach from Eq. (5-45). These are compared with the values from the CFD simulations in Figure 76. The pressure distributions from the CFD simulations and the new parameterization approach generally agree well.

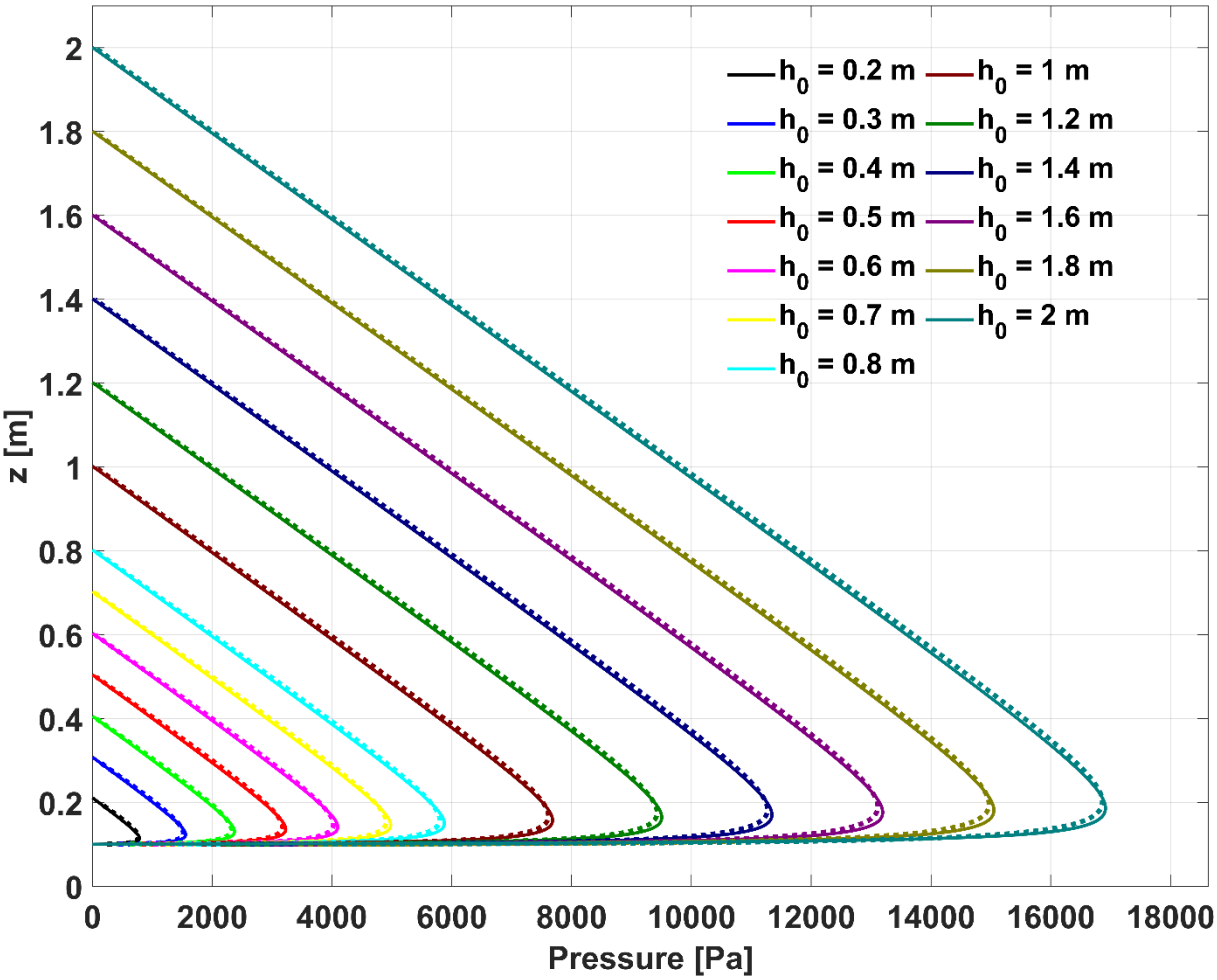

Figure 76: Comparison of the gate pressure distribution from the parametrization (solid line) and from the CFD simulations (dashed line) for α=90° and a=0.1m

The gate pressure distribution for the standard sluice gate has also been studied by other authors. In the following, the new parameterization approach is compared with these literature values, whereby these works are divided into two categories. The works of Pajer [63], Han and Chow [60], Cheng, Liggett and Liu [64] and Finnie and Jeppson [66], shown in Figure 77, have calculated the gate pressure distribution for a specific example, while the works of Roth and Hager [28], Belaud and Litrico [65] and Castro Orgaz and Hager [67], have proposed general parameterization formulas for the vertical sluice gate. These are exemplarily shown for $\varepsilon = 0.5$ and $\varepsilon = 0.05$ in Figure 78.

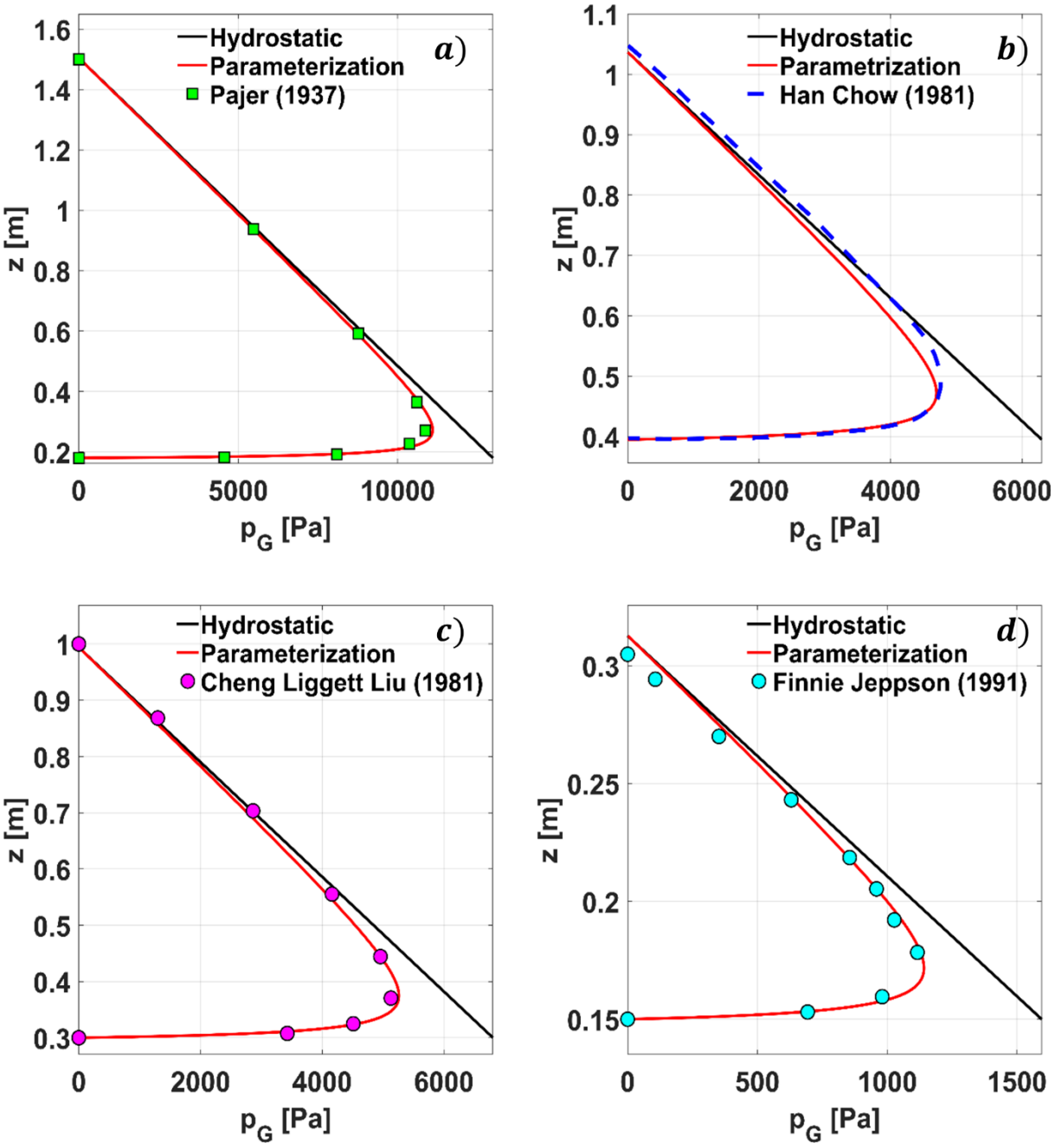

Figure 77: Parameterization approach compared with data from a) Pajer [63] with $\varepsilon = 0.12$, b) Han and Chow [60] with $\varepsilon = 0.395$, c) Cheng, Liggett and Liu [64] with $\varepsilon = 0.309$ and d) Finnie and Jeppson [66] with $\varepsilon = 0.507$

The work of Pajer (Figure 77 a) and Cheng et al. (Figure 77 c) agrees very well with the parameterization formula over the entire course. The gate pressure calculated by Han et. al (Figure 77 b) is slightly larger than the gate pressure calculated with the parameterization in the region between the water surface $z = h_0 + \Delta h_G$ and the position of the maximum pressure z_{Gm}. In the region below z_{Gm}, the values of Han et. al are in excellent agreement with the parameterization. The values of Finnie et al. are also very well reproduced by the new

parameterization. Only near the water surface $z = h_0 + \Delta h_G$ the values of Finnie et al. are lower, because the authors have determined a smaller Δh_G, as shown in Figure 68.

Comparing the derived parameterization with the parameterization approaches from the literature ([65] [67] [28]), additional data for the parameterization approaches of these authors have to be provided first. For the approach of Belaud et al. no relation is given for the upstream water level h_0 and the water level at the sluice gate wall $h_0 + \Delta h_G$, because only $h_0 + \Delta h_G$ is used in the formula. However, since the upstream water level h_0 must be known to calculate the realtive gate opening ε, the water level increase is calculated using Eq. (5-35) with $k_{\Delta hG} = 0.62$. In the work of Roth and Hager, the water level increase Δh_G at the gate is calculated using the conservation of energy approach, see Eq. (5-33). To use this approach, however, the discharge must be known. In the approach of Belaud and Litrico, the discharge must also be known since it occurs as a parameter in their parameterization approach. To work on the same data basis, the discharge determined from the CFD simulations was used for all parameterization approaches. Castro-Orgaz et al. assumed a constant value of the contraction coefficient $c_C = 0.61$ for the parameterization of the pressure distribution to calculate the discharge from the energy conservation equation. For the calculation of the water level increase at the sluice gate Δh_G, the energy conservation approach was also used by Castro-Orgaz et al. In Figure 78 the parameterization approach derived in this work (Eq. (5-45)) and the CFD results are compared with the parameterization approaches of Roth and Hager [28], Belaud and Litrico [65] and Castro-Orgaz and Hager [67] for $\varepsilon = 0.5$ (Figure 78 a))and $\varepsilon = 0.05$ (Figure 78 b)). For $\varepsilon = 0.5$, the results of the new parameterization and the CFD results are in between the parameterization results of the other authors, with Roth and Hager calculating a larger pressure and with the parameterization approaches of Castro-Orgaz and Hager and Belaud and Litrico calculating smaller pressures. For $\varepsilon = 0.05$, the results of the new parameterization, the CFD results, and the parameterization results of Castro-Orgaz and Hager and Belaud and Litrico agree very well. The parameterization of Roth and Hager deviates from the other results and takes in places larger values than the hydrostatic pressure distribution, which is physically not possible.

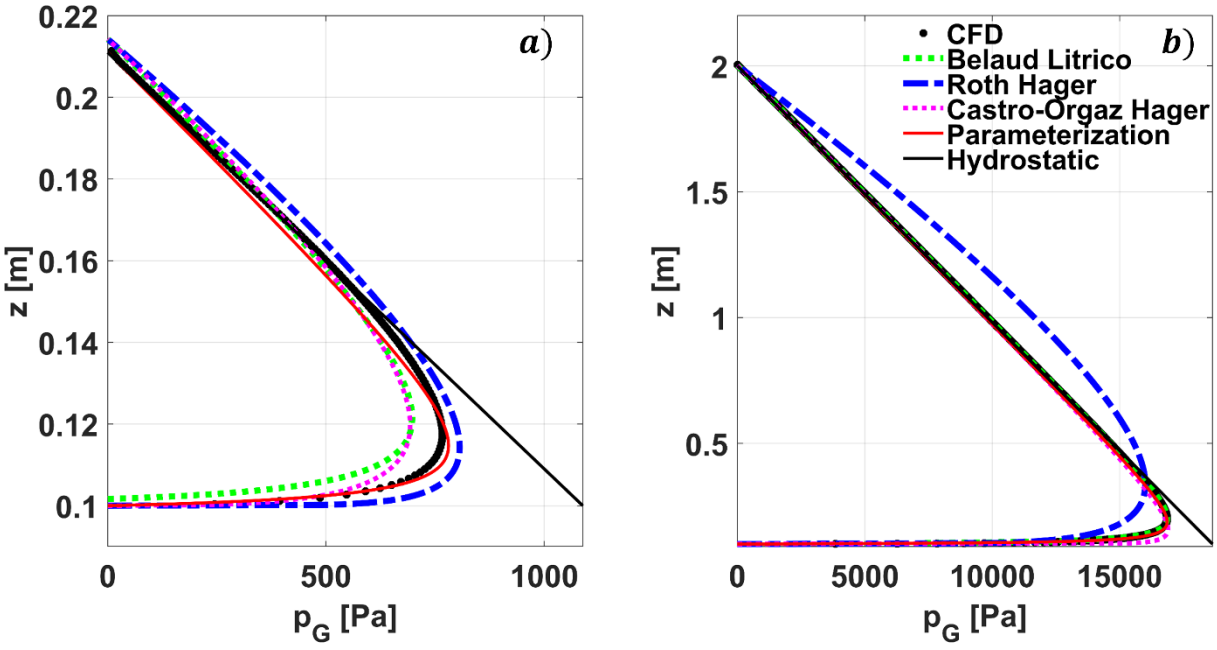

Figure 78: Comparison of the parameterization approach with parameterization approaches from literature ([65] [67] [28]) a) for $\varepsilon = 0.5$ and b) for $\varepsilon = 0.05$

It was shown that the new parameterization approach is very well suited for parameterizing the gate pressure at the standard sluice gate. This has been confirmed both by own CFD results and by gate pressure data from other authors.

5.3.6 Parameterization of the Inclined Gate Pressure Distribution

The results presented so far have been limited to the standard sluice gate with $\alpha = 90°$. Since the new parameterization approach (Eq. (5-45)) is also to be used to calculate the pressure distributions for inclined sluice gates, which is not yet possible with the parameterization approaches known in the literature, the approach is extended to include the inclined sluice gate. For this purpose, the pressure distribution of the inclined sluice gate is first nondimensionalized with Eq. (5-31) and Eq. (5-32) as for the standard sluice gate. The nondimensionalized pressure distributions P_G for the different angles of inclination α are shown for the relative gate opening $\varepsilon = 0.25$ in Figure 79 a). The nondimensionalized pressure distribution P_G is used to calculate the nondimensionalized dynamic pressure distribution P_{GD} with Eq. (5-41). The nondimensionalized dynamic pressure distribution is shown in Figure 79 b).

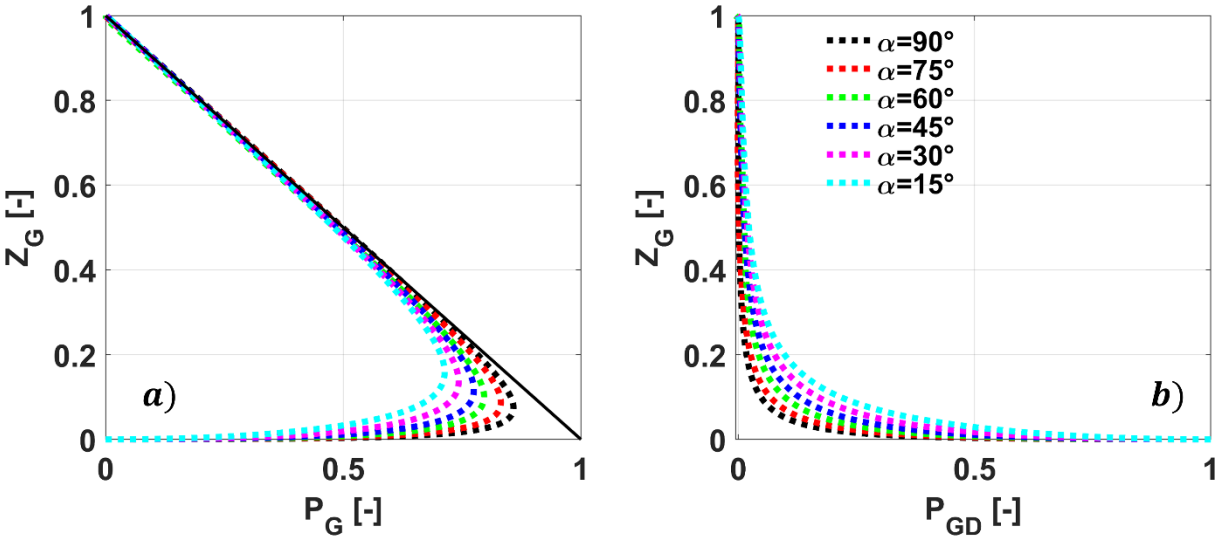

Figure 79: a) Dimensionless gate pressure distribution and b) dimensionless dynamic gate pressure distribution of inclined sluice gates for $\varepsilon = 0.25$ from CFD

The following statements can be made about the dependency of the angle of inclination α on the gate pressure distribution P_G and the dynamic gate pressure distribution P_{GD}:

- The gate pressure P_G and the maximum gate pressure P_{Gm} decrease with decreasing angle of inclination α
- The position of the maximum gate pressure Z_{Gm} increases upwards with decreasing angle of inclination α
- The pressure distribution deviates earlier from the hydrostatic pressure distribution as the angle of inclination α decreases.
- The dynamic pressure increases with decreasing angles of inclination already at larger Z_G

To parameterize the gate pressure distribution of the inclined sluice gate P_G, the dimensionless dynamic pressure P_{GD} is first parameterized using again Eq. (5-43) as for the standard sluice gate. The fitting parameter $k_G(\alpha)$ was determined with the non-linear least square method using the CFD values and is shown in Figure 80 (diamonds) as a function of the relative gate opening ε for the different angles of inclination α. The parameter k_G for the inclined gate pressure distribution can be parametrized in dependency of the relative gate opening ε with Eq. (5-46). Eq. (5-46) is a modified form of Eq. (5-44), which was used for the parameterization of the standard gate pressure distribution, and results from Eq. (5-46) for $k_{G2} = 1$.

$$k_G(\varepsilon, \alpha) = k_{G1} \cdot \varepsilon^{k_{G2}} \tag{5-46}$$

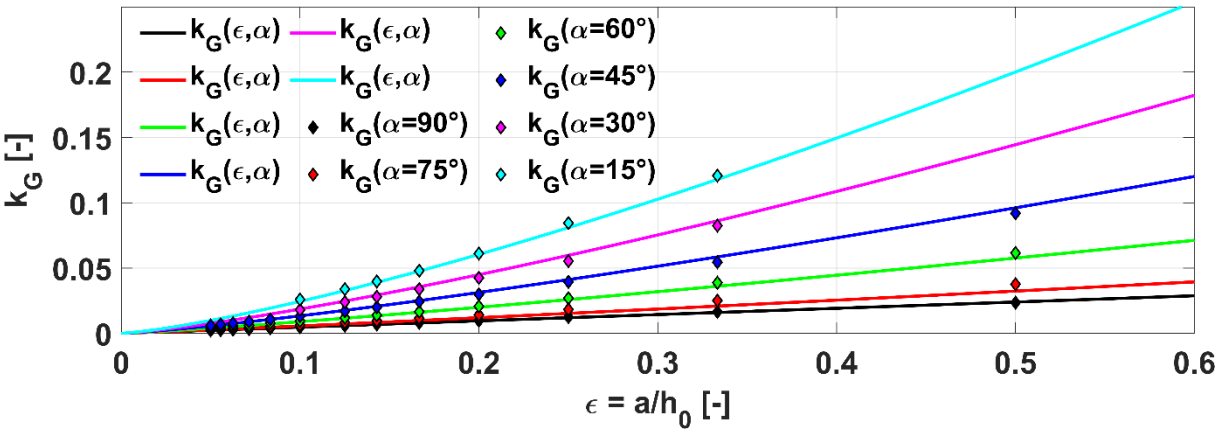

Figure 80: Parameter k_G for the parametrization of the inclined gate pressure distribution

The parameters of the parameterization formula (Eq. (5-46)) k_{G1} and k_{G2} are determined using the non-linear least square method and are shown in Table 10 together with the parameterization errors.

Table 10: Parameters k_{G1} and k_{G2} for inclined gate pressure parameterization

	$\alpha = 90$	$\alpha = 75$	$\alpha = 60$	$\alpha = 45$	$\alpha = 30$	$\alpha = 15$
k_{G1}	0.048	0.08008	0.139	0.2112	0.3314	0.5097
k_{G2}	1	1.076	1.174	1.211	1.274	1.308
SSE	$8.40 \cdot 10^{-7}$	$6.84 \cdot 10^{-7}$	$9.54 \cdot 10^{-7}$	$3.01 \cdot 10^{6}$	$2.71 \cdot 10^{6}$	$4.61 \cdot 10^{6}$
RMSE	0.0002646	0.0002493	0.0002945	0.000523	0.0007357	0.0009605

In the next step, a function must be found which describes the dependence of the parameters k_{G1} and k_{G2} on the angle of inclination α. For this purpose, the values determined in Table 10 are shown graphically in Figure 81 as a function of the angle of inclination α. Let us first consider the parameter k_{G1}, shown in Figure 81 a). It was found, that the parameter can be modeled using Eq. (5-47). The parameterization constant $k_{G,\alpha 1} = -0.6026$ was determined with the non-linear least square method, with the errors $RMSE = 0.01386$ and $SSE = 0.00096$. The constant $k_{G,90°} = 0.48$ was already determined in the previous chapter, where for $\alpha = 90°$ $k_{G1} = k_{G,90°}$. The course of the parameter k_{G1} determined with Eq. (5-47) as a function of the angle of inclination α is also shown in Figure 81 a). As can be seen from the figure and the small errors, the parameterization approach (Eq. (5-47)) is very well suited.

$$k_{G1} = k_{G,\alpha 1} \cdot (\sin(\alpha) - 1) + k_{G,90°} \tag{5-47}$$

To parameterize the parameter k_{G2}, the parameter is shown in Figure 81 b) as a function of the angle of inclination α. The dependence can be represented by Eq. (5-48). The parameterization constant $k_{G,\alpha 2} = 0.3164$ was determined with the errors $SSE = 0.0004413$

and RMSE = 0.009394. The parameterization formula for k_{G2} is also shown in Figure 81 b). This agrees well with the values from Table 10.

$$k_{G2} = 1 + k_{G,\alpha 2} \cdot \cos(\alpha) \tag{5-48}$$

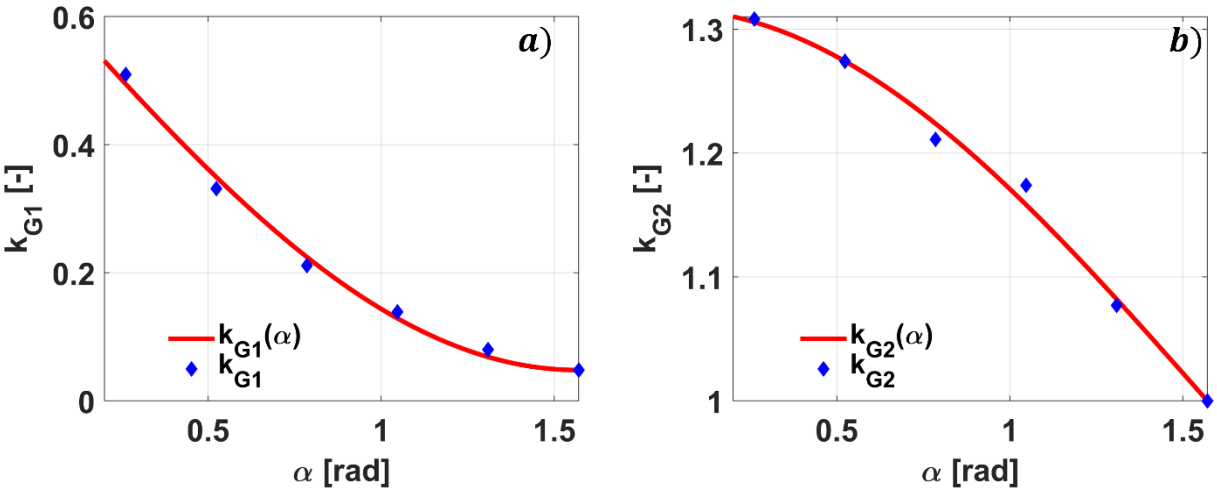

Figure 81: a) parameter k_{G1} and b) parameter k_{G2} for inclined gate pressure parameterization in dependency of angle of inclination α

Finally, substituting Eq. (5-47) and Eq. (5-48) into Eq. (5-46) yields the function shown in Eq. (5-49) for the parameter $k_G(\varepsilon, \alpha)$. For $\alpha = 90°$, Eq. (5-49) reduces to Eq. (5-44), the fitting parameter for the standard sluice gate parameterization. Eq. (5-49) is thus valid for both the standard and the inclined sluice gate. Figure 80 shows the course of the parameter $k_G(\varepsilon, \alpha)$.

$$k_G(\varepsilon, \alpha) = \left(k_{G,\alpha 1} \cdot (\sin(\alpha) - 1) + k_{G,90°}\right)\varepsilon^{1+k_{G,\alpha 2}\cdot\cos(\alpha)} \tag{5-49}$$

Substituting the parameter determined by Eq. (5-49) into Eq. (5-45), the formula for the dimensionless pressure distribution $P_G(Z)$ is obtained as a function of the relative gate opening ε and the angle of inclination α. With the help of Eq. (5-31) and Eq. (5-32) the gate pressure distribution p_G (z) can be determined from the dimensionless gate pressure distribution P_G (Z). In Figure 82, the newly determined pressure distribution is compared with the CFD results for the different investigated angles of inclination α. For the relative gate openings $\varepsilon = 0.25$ (Figure 82 a)) and $\varepsilon = 0.1$ (Figure 82 b)) the results generally agree very well. Only in the area of the maximum pressure p_{Gm} deviations occur for the angles $\alpha = 75°$ and $\alpha = 60°$.

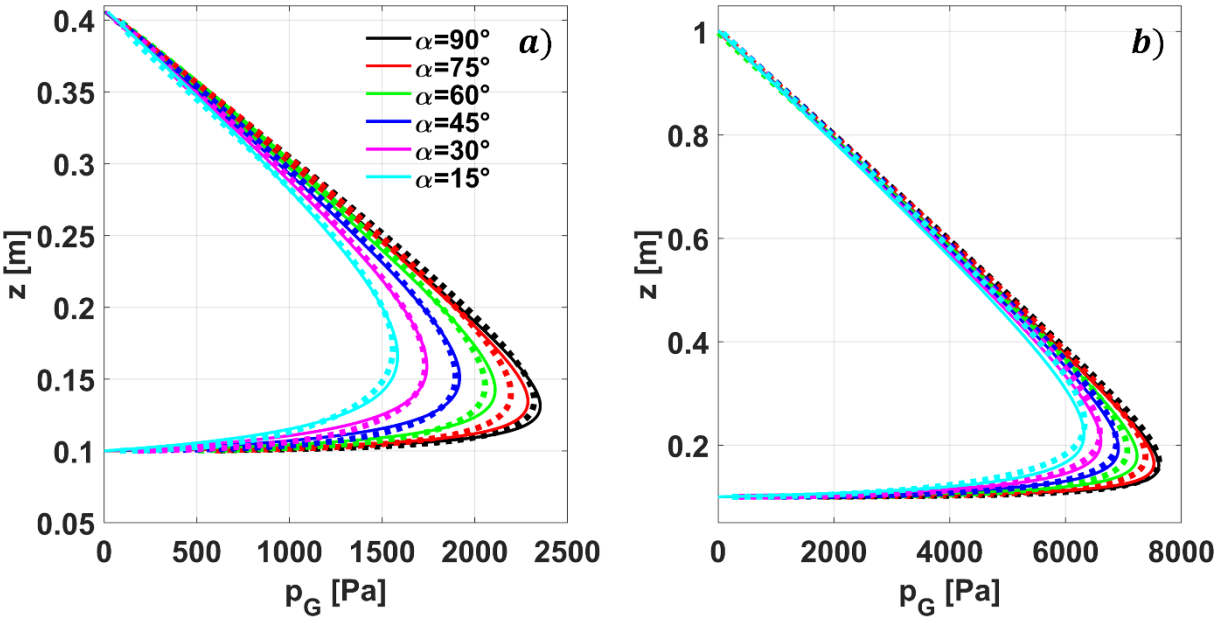

Figure 82: Comparison of the parametrization results (solid line) with CFD results (dashed line) of the gate pressure distribution for a) ε=0.25 and b) ε=0.1 for various angles of inclination α

The pressure distribution for the inclined sluice gate was also investigated by Gentilini [24] and Montes [35], for $\alpha = 45°$ and $\varepsilon = 0.2$. The parameterization are compared with the results of Gentilini [24] in Figure 83 a) and with the results of Montes [35] Figure 83 b). The parameterization results agree well with the results of Gentilini and Montes. The derived parameterization function for the gate pressure distribution could thus be confirmed for both the standard and the inclined sluice gates by comparison with literature values.

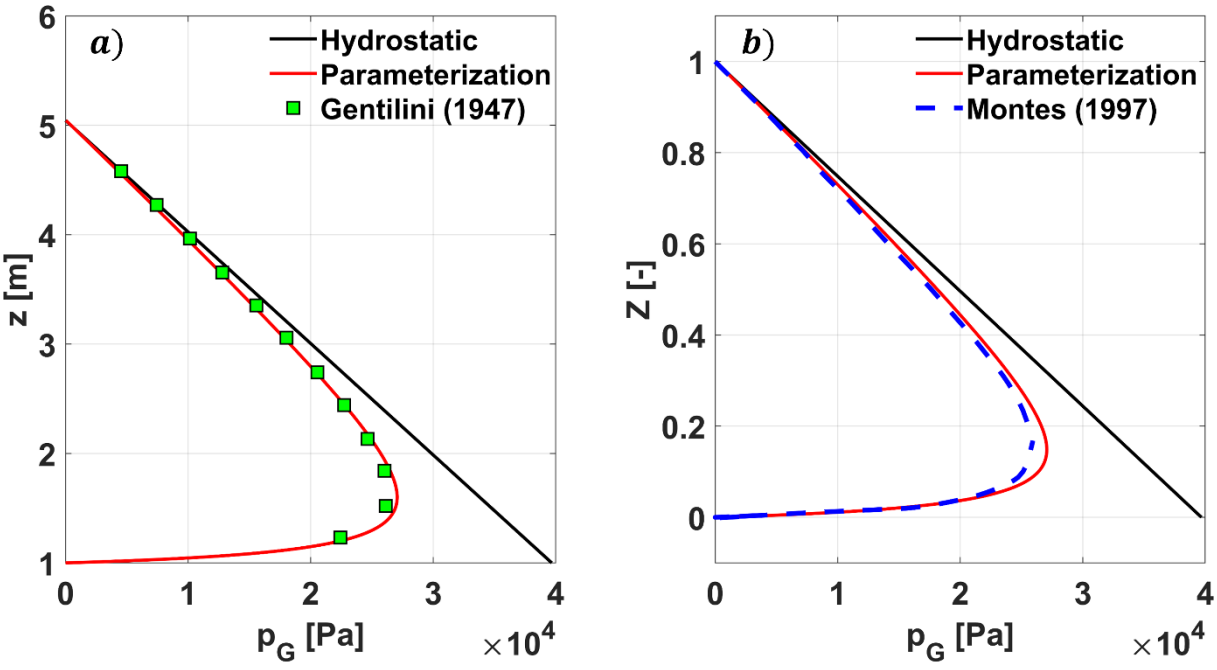

Figure 83: Comparison of the new inclined gate pressure distribution parameterization approach with data from a) Gentilini [24] and b) Montes [35] for α=45°

5.3.7 Gate Force

The force F_G acting on the sluice gate can be determined by integrating the pressure distribution along the sluice gate wall. For the calculation of the discharge from the momentum balance, see Eq. (3-15), the component of the pressure force parallel to the x-axis F_{Gx} is required. To determine this, we first integrate the pressure distribution $p_G(z)$ along the z-coordinate from the gate lip $z = a$ to the free water surface at the sluice gate wall $z = h_0 + \Delta h_G$. Since we assume a two-dimensional pressure profile and thus the pressure distribution is constant along the width (y-axis), the pressure integral can be directly multiplied by the width B. This results in the following equation for the pressure force F_{Gx} in x-direction on the sluice gate:

$$F_{Gx} = B \int_a^{h_0+\Delta h_G} p_G(z)\, dz \tag{5-50}$$

To solve this integral, it is first converted to the dimensionless form using Eq. (5-31) and Eq. (5-32). Where the hydrostatic pressure at the lower sluice gate edge $p_{GS} = \rho \cdot g \cdot (h_0 + \Delta h - a)$ and the wetted sluice gate surface $A_G = (h_0 + \Delta h - a) \cdot B$ are introduced for simplifications. This gives the formula shown in Eq. (5-51).

$$F_{Gx} = p_{GS}\, A_G \int_0^1 P_G(Z_G)\, dZ_G \tag{5-51}$$

The integral of the dimensionless pressure distribution (Eq. (5-45)) along the dimensionless gate coordinate Z_G is solved in detail below:

$$\int_0^1 P_G(Z_G)\, dZ_G = \int_0^1 \left(1 + k_G(\varepsilon,\alpha) \cdot Z_G - \left(Z_G + \frac{1}{\frac{1}{k_G(\varepsilon,\alpha)} \cdot Z_G + 1} \right) \right) dZ_G$$

$$= \int_0^1 1\, dZ_G + \int_0^1 k_G(\varepsilon,\alpha)\, Z_G dZ_G - \int_0^1 Z_G dZ_G - \int_0^1 \frac{1}{\frac{1}{k_G(\varepsilon,\alpha)} \cdot Z_G + 1} dZ_G$$

$$= 1 + \frac{1}{2} k_G(\varepsilon,\alpha) - \frac{1}{2} - k_G(\varepsilon,\alpha) \ln\left(\frac{1}{k_G(\varepsilon,\alpha)} + 1 \right)$$

$$= \frac{1}{2}\left(1 + 2\, k_G(\varepsilon,\alpha) \left(\frac{1}{2} - \ln\left(\frac{1}{k_G(\varepsilon,\alpha)} + 1 \right) \right) \right) \tag{5-52}$$

Finally, if the integral determined in Eq. (5-52) is substituted into Eq. (5-51), Eq. (5-53) is obtained for the pressure force F_{Gx} in the x-direction:

$$F_{Gx} = p_{GS} A_G \frac{1}{2}\left(1 + 2\, k_G(\varepsilon, \alpha)\, \left(\frac{1}{2} - \ln\left(\frac{1}{k_G(\varepsilon, \alpha)} + 1\right)\right)\right) \tag{5-53}$$

The parameter $k_G(\varepsilon, \alpha)$ can be determined with Eq. (5-49). For the case that the sluice gate is closed ($\varepsilon = 0$), the pressure force F_{Gx} must be equal to the hydrostatic pressure force F_{GSx} in x-direction, see Eq. (5-54). This can be confirmed since the parameter $k_G(\varepsilon, \alpha) = 0$ and for this case Eq. (5-53) is equal to Eq. (5-54).

$$F_{GSx} = \frac{1}{2} p_{GS} A_G = \frac{1}{2} \rho g B (h_0 + \Delta h - a)^2 \tag{5-54}$$

To compare the pressure forces for different relative gate openings ε, the dimensionless pressure force Π is introduced. This represents the ratio of the force F_{Gx} (Eq. (5-53)) acting on the sluice gate to the hydrostatic pressure force F_{GSx} (Eq. (5-54)). The dimensionless pressure force Π was also used in this way by Roth and Hager [28].

$$\Pi = \frac{F_{Gx}}{F_{GSx}} = \frac{F_{Gx}}{\frac{1}{2} \rho g B (h_0 + \Delta h - a)^2} \tag{5-55}$$

Figure 84 shows the CFD values and the newly determined parameterization approach of the dimensionless gate force Π as a function of the relative gate opening ε for the standard sluice gate ($\alpha = 90°$), where for the standard sluice gate the parameter $k_G(\varepsilon, 90°)$ reduces to the form shown in Eq. (5-44).

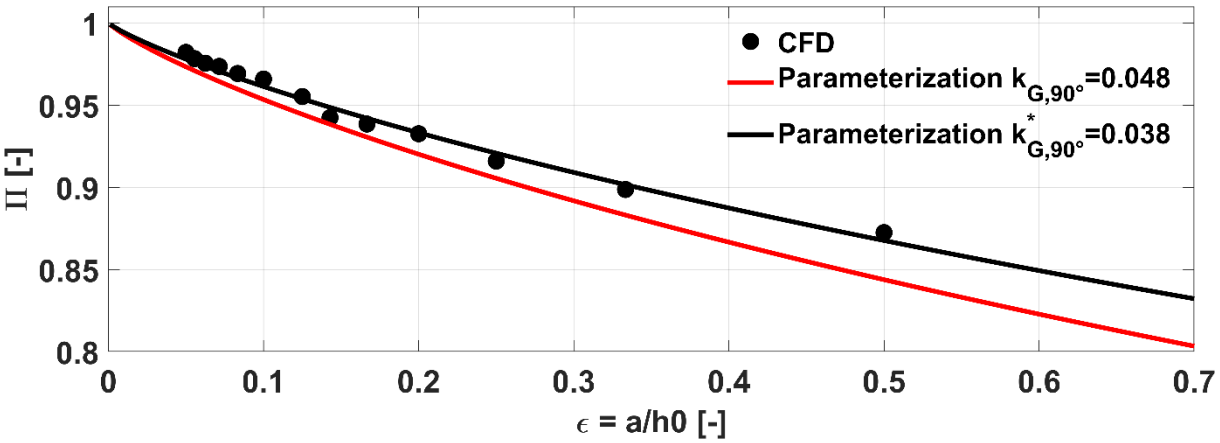

Figure 84: Dimensionless gate force Π of the standard sluice gate in dependency of the relative gate opening ε

The parameterization constant was originally determined with $k_{G,90°} = 0.048$. If one compares for this value ($k_{G,90°} = 0.048$) the values of the newly parameterized dimensionless

gate force Π with the CFD values, one finds that these correspond very well in the profile, but the values for the parameterization approach are smaller. In order to improve the parameterization of the pressure force, the parameterization constant $k_{G,90°}$ was redetermined on the basis of the pressure force determined in the CFD simulation. The parameterization constant $k^*_{G,90°} = 0.038$ was determined using the non-linear least square method. The dimensionless gate force determined with the newly determined parameter $k^*_{G,90°}$ is also shown in Figure 84. This agrees very well with the results of the CFD simulations, which is why the parameter $k^*_{G,90°}$ is used to determine the gate force in further calculations, to calculate the discharge via the momentum balance.

As already shown in chapter 5.3.5, the authors Roth and Hager [28], Belaud and Litrico [65] and Castro Orgaz and Hager [67] have published parameterization approaches for the determination of the gate pressure distribution for the standard sluice gate in their works, which have already been shown in Figure 78. By integrating these approaches, the pressure force can be determined for comparison with the pressure force determined in this work. Figure 85 shows the dimensionless pressure force Π determined by integrating the different approaches as a function of the relative gate opening ε. Considering the integral of the pressure distribution of Roth and Hager [28], it can be seen that it takes very large values compared to the other authors and for small relative gate openings ε the gate pressure force is larger than the hydrostatic pressure force ($\Pi > 1$), which is physically not possible. This inconsistency was already recognized by Roth and Hager [28] in the same paper, which is why they also proposed another independent function to parameterize the dimensionless gate force Π. This new function agrees very well with the CFD simulation values and the new parameterization for small relative gate openings $\varepsilon < 0.2$. For larger values of ε, there are some deviations between the parameterization formula of Roth and Hager and the new parameterization approach, but compared to the other works, they still agree well. The integrals of the pressure distributions of Belaud and Litrico [65] and Castro-Orgaz and Hager [67] run similarly over the whole range of the investigated relative gate openings ε, where for $\varepsilon < 0.1$ their values also agree with the pressure distribution of Roth and Hager [28] as well as the CFD values and the values of the new parameterization approach. For $\varepsilon > 0.1$, the dimensionless pressure force Π obtained by integrating the pressure distributions of Belaud and Litrico [65] and Castro-Orgaz and Hager [67] are smaller than the other values shown in Figure 85.

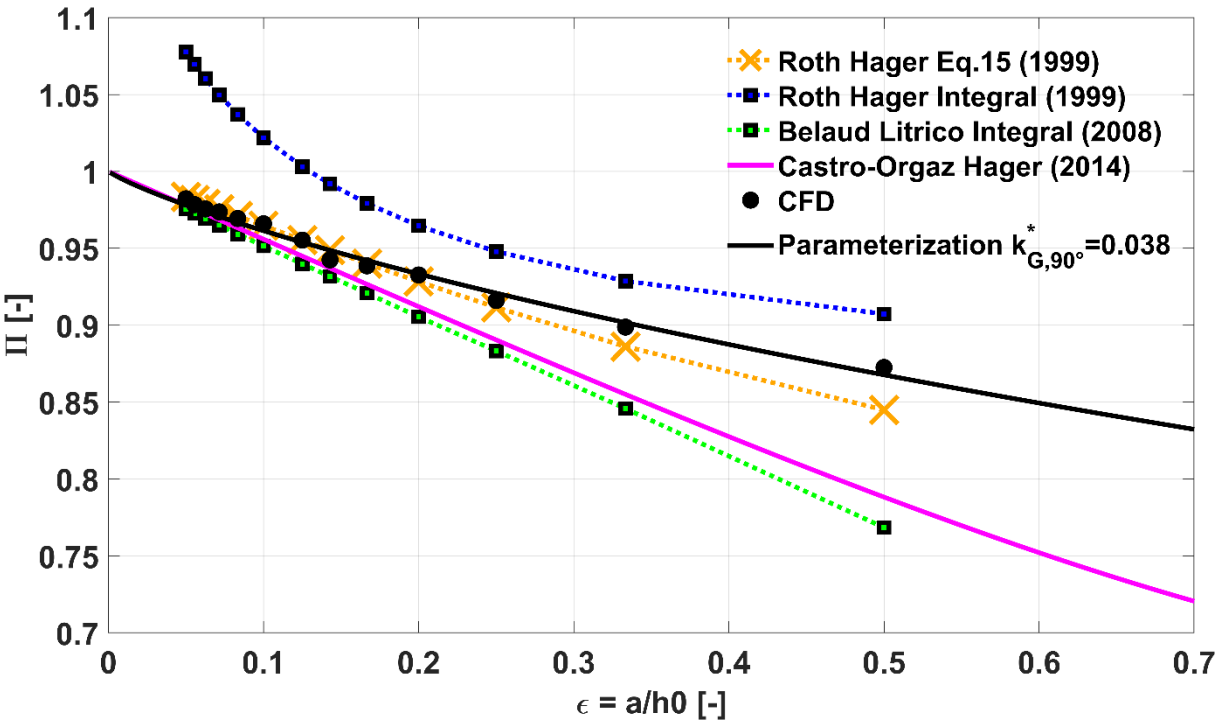

Figure 85: Comparison of dimensionless gate force Π of the standard sluice gate in dependency of the relative gate opening ε with results from the literature ([65] [67] [28])

In contrast to the parameterization formulas of the gate force from other authors, the parameterization formula for the x-component of the gate force (Eq. (5-53)) determined in this work is also valid for the inclined sluice gate. The dependency on the angle of inclination is considered by the parameter $k_G(\varepsilon, \alpha)$ (Eq. (5-49)). Figure 86 shows the dimensionless gate pressure force Π obtained by the new parameterization for the investigated angles of inclination α. For the parameterization constants occurring in Eq. (5-49), the previously determined values $k^*_{G,90°} = 0.038$, $k_{G,\alpha1} = -0.6026$ and $k_{G,\alpha2} = 0.3164$ were used. Also shown in Figure 86 is the dimensionless gate force Π determined from the CFD simulations. The parameterization values agree very well with the CFD simulation values. Literature values for the pressure force on the inclined sluice gate are not available, therefore the parameterization cannot be compared with these.

It was shown that the formula shown in Eq. (5-53) for adjusting the x-component of the pressure force on the sluice gate is well suited for both the standard sluice gate and the inclined sluice gate. With the new parameterization, it is possible for the first time to calculate the gate pressure force for the standard sluice gate and the inclined sluice gate.

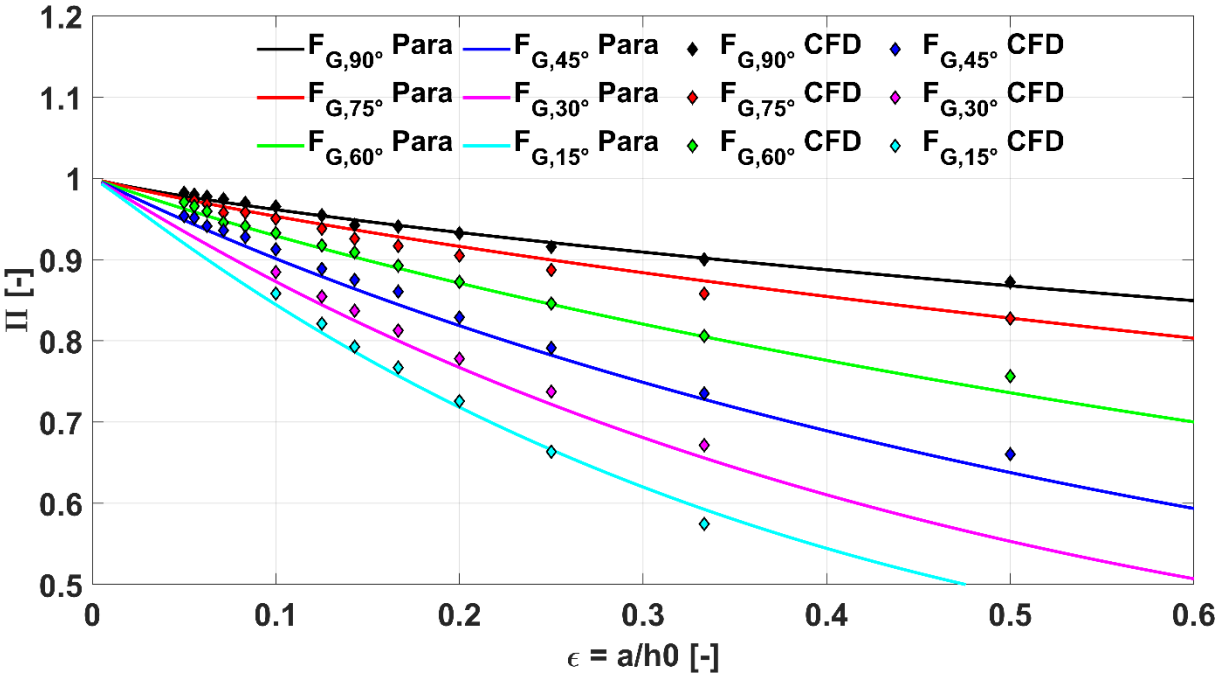

Figure 86: Dimensionless gate force Π of inclined sluice gate in dependency of the relative gate opening ε

The gate force in x-direction F_{Gx}, can also be used to calculate the total gate force F_G (Eq. (5-56)) and the force acting in z-direction F_{Gz} (Eq. (5-57)). These formulas can also be used, for example, in the mechanical design of the sluice gate and the drive.

$$F_G = \frac{F_{Gx}}{\sin(\alpha)} \tag{5-56}$$

$$F_{Gz} = \frac{F_{Gx}}{\tan(\alpha)} \tag{5-57}$$

6 Momentum Coefficient

The momentum coefficient has already been used for the introduction of the momentum balance for the sluice gate in chapter 3.2, but it will be discussed in more detail in this chapter. The profile of the momentum coefficient along the main flow direction (x-direction) for the vertical and inclined sluice gate will be analyzed. Further, a parameterization of the momentum coefficient at the opening β_O is performed, which is required for the determination of the discharge from momentum balance according to Eq. (3-15). But first, the definition of the momentum coefficient for incompressible flows is repeated here:

$$\int_A u^2 \, dA := \beta \, A \, \bar{u}^2 \tag{3-10}$$

Instead of the integral of the square of the velocity over the flow cross-section $\int_A u^2 \, dA$, the product of the square of the mean velocities and the flow cross-section $\bar{u}^2 A$ can be used in the momentum balance with the aid of the momentum coefficient β. This leads to significant simplifications, since the velocity does not have to be known at every point of the control volume boundary, but only one mean velocity and the momentum coefficient. Furthermore, the conservation of mass can also be written in terms of the average velocity $\bar{u}$ for incompressible fluids in hydraulics, which makes it easy to combine the two conservation equations. Assuming a very wide channel with cross section $h \cdot B$, the flow along the width B can be assumed to be constant and the influence of the sidewalls can be neglected. From this follows for the momentum coefficient β for wide channels:

$$\beta = \frac{B \int_0^h u^2 \, dz}{h \, B \, \bar{u}^2} = \frac{\int_0^h u^2 \, dz}{h \, \bar{u}^2} \tag{6-1}$$

where $z = 0$ is the channel bottom and $z = h$ is the water level. To evaluate the momentum coefficient profile from the CFD simulations, a plane must be created at each location X where a value for β is to be determined to evaluate the integral $\int_0^h u^2 \, dz$ and the surface-averaged velocity $\bar{u}$. Since both water and air are simulated in the CFD simulations, selecting the entire flow domain as the input part for the plane would result in an incorrect momentum coefficient. Therefore, a threshold part is first created that includes only cells with a volume fraction of water >0.5. This threshold part is then selected as input part for the plane. The water level $h(X)$ or the resulting flow cross section $A(X) = h \cdot B$ at the respective location X, is determined with a max report for the z-position. This gives the z-coordinate of the upper cell of the respective level, which is still in the threshold with a volume fraction of water >0.5.

As a result, the flow cross section cannot change continuously, but only by a cell size $\Delta_{grid} = \frac{a}{n_{grid}} = \frac{0.1\ m}{128}$. Due to this discontinuity, small fluctuations in the momentum coefficient curves shown in the following chapter occur occasionally. The momentum coefficient β_O required to solve the momentum balance for the control volume I, see Figure 27, can be evaluated exactly at the interface directly at the sluice gate opening ($X = 0$), where the flow cross section with $h = a$ is known exactly. The momentum coefficient at the opening β_O is therefore not affected by the described discretization errors.

6.1 Momentum Coefficient Profile

In this section, the profile of the momentum coefficient of sluice gate flows along the dimensionless X-coordinate is examined. Figure 87 shows the momentum coefficient for the standard sluice gate from $X = -15$ to $X = 3$ for three different relative gate openings ε. Looking at the upstream region ($X < 0$), it can be seen that far upstream of the sluice gate the momentum coefficient is $\beta_{\emptyset} \approx 1$. The value here depends on the velocity profile $u_{\emptyset}$ of the flow upstream of the sluice gate. If the velocity profile is undisturbed $u_{\emptyset} = \text{const.}$ there would be a block profile whose momentum coefficient $\beta = 1$. However, the real velocity profile differs from the block profile due to velocity changes in the boundary layer region. These changes are not directly influenced by the sluice gate, but by the channel properties upstream of the sluice gate. In the laboratory flume as well as in the CFD simulations carried out, the inlet channels are relatively short and smooth which makes the boundary layer less developed and thus the momentum coefficient close to one ($\beta_{\emptyset} \approx 1$). In river flows, the velocity profile $u_{\emptyset}$ can deviate much more from the block profile due to the roughness of the channel bottom and the length of the upstream flow, which can make the upstream momentum coefficient $\beta_{\emptyset}$ somewhat larger. For the logarithmic velocity profile, Malcherek [74] determined the momentum coefficient $\beta_{\emptyset}$ for various water depths and roughness and found that it is close to $\beta_{\emptyset} \approx 1$. Even for a very large roughness $r = 0.1$ m and a water depth of $h_{\emptyset} = 1$ m, i.e., the roughness corresponds to 10% of the water depth, the maximum momentum coefficient with $\beta_{\emptyset} = 1.14$ is relatively low. Previous studies on the sluice gate have not taken into account the velocity profile of the inflow for discharge calculations, which leads to the conclusion that its influence is comparatively small. However, if the momentum coefficient at the upstream region is known, it can be now considered in the momentum equation, Eq. (3-15).

If the sluice gate is approached from the upstream region, the momentum coefficient increases with decreasing distance to the sluice gate, similar to the sudden contraction studied by Malcherek and Müller [43], first gradually and then strongly. Immediately upstream of the sluice gate, the momentum coefficient reaches its maximum value.

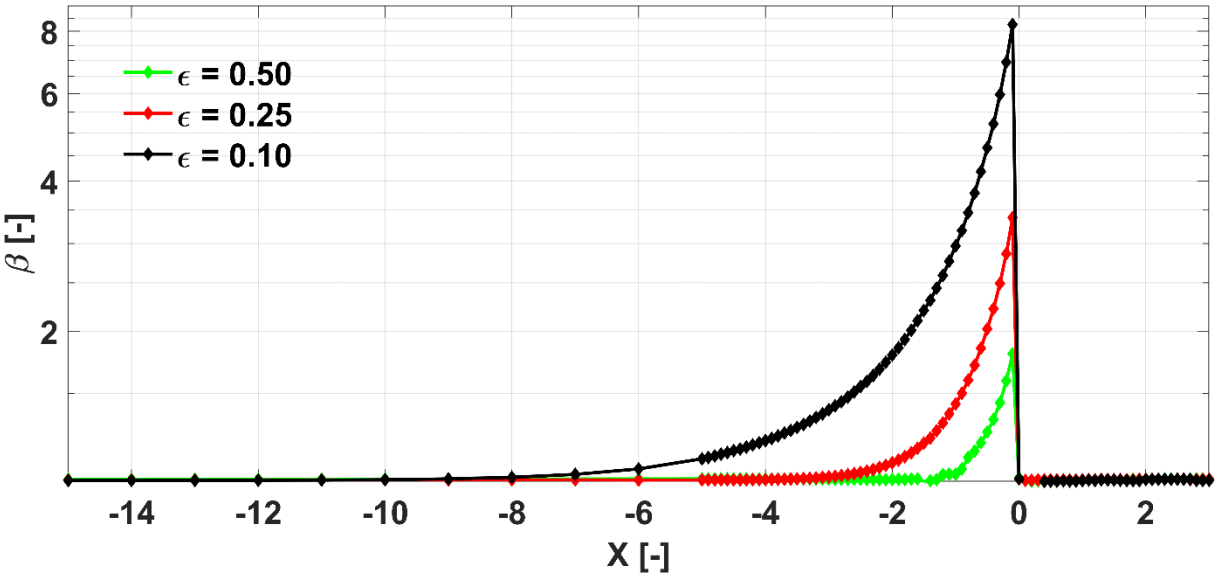

Figure 87: Momentum coefficient β along X-axis for standard sluice gate

This increase in momentum coefficient is due to the x velocity profile shown in Figure 88 at different positions of the dimensionless X coordinate.

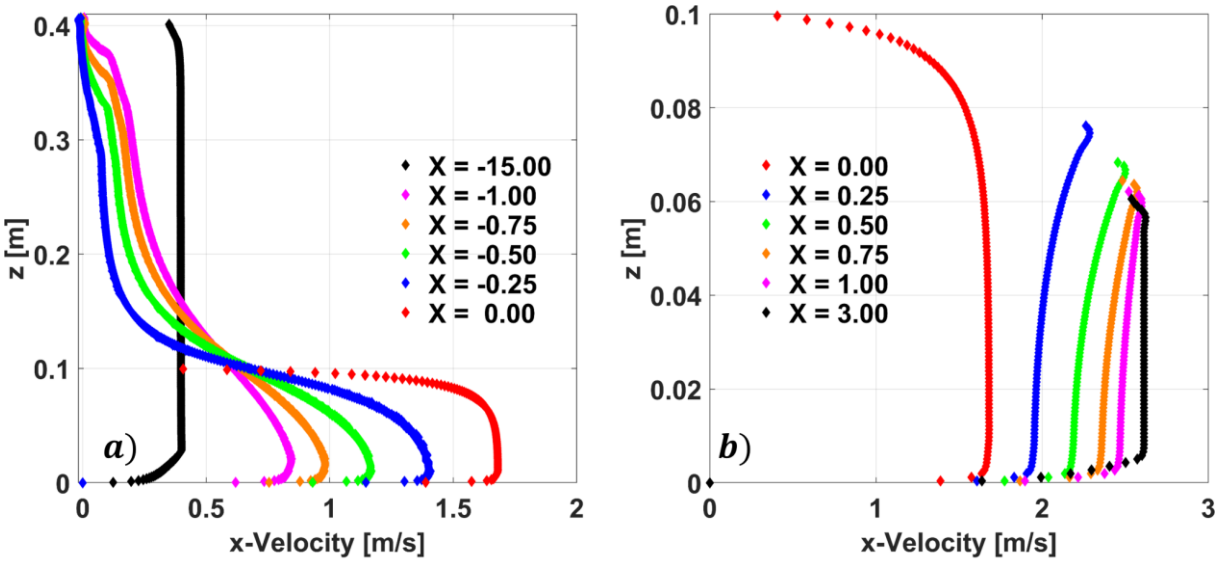

Figure 88: x-Velocity profile at different X-locations a) upstream Region b) downstream Region

In the upstream region (Figure 88 a)), it can be seen that as the distance to the sluice gate decreases, the x-velocity profile approaches more and more the x-velocity profile at the opening at $X = 0$, which means that the x-velocity approaches zero for $(z > a = 0.1\ m)$ and approaches the x-velocity profile at the opening u_O for $(0 < z < a)$. The theoretical maximum value of the momentum coefficient for the vertical sluice gate $\beta_{max,90°}$ can therefore be determined with the x-velocity profile at the opening and the water height at the sluice gate as follows:

$$\beta_{max,90°} = \frac{\int_0^a u_O^2 \, dz}{(h_0 + \Delta h_G)\left(\frac{Q}{(h_0 + \Delta h_G)B}\right)^2} = \frac{(h_0 + \Delta h_G)\int_0^a u_O^2 \, dz}{\left(\frac{Q}{B}\right)^2} \tag{6-2}$$

where $\int_0^a u_O^2 \, dz = \beta_O a \, \bar{u}_O{}^2 = \frac{\beta_O}{a}\left(\frac{Q}{B}\right)^2$ is. Substituting the relation into Eq. (6-2) one obtains:

$$\beta_{max,90°} = \frac{\int_0^a u_O^2 \, dz}{(h_0 + \Delta h_G)\left(\frac{Q}{(h_0 + \Delta h_G)B}\right)^2} = \frac{h_0 + \Delta h_G}{a}\beta_O \tag{6-3}$$

The maximum theoretically possible momentum coefficient $\beta_{max,90°}$ for the vertical sluice gate thus depends on the water height at the sluice gate, which can be calculated with Eq. (5-35) and the momentum coefficient at the opening β_O. The momentum coefficient at the opening β_O is derived in the following chapter and can be calculated using Eq. (6-9). Substituting the two equations into Eq. (6-3), the following equation finally results:

$$\beta_{max,90°} = \frac{h_0 + (h_0 - a)\,0.62\left(\frac{a}{h_0}\right)^{\frac{5}{2}}}{a}(0.02\,\frac{a}{h_0} + 1.032) \tag{6-4}$$

In Figure 89, the maximum momentum coefficient from Eq. (6-4) is compared with the CFD results for the standard sluice gate. For this purpose, a plane was created directly in front of the sluice gate at position $X = 0.001$ in the simulations. The results from the CFD simulations and those from Eq. (6-4) generally agree well, although as expected the CFD results slightly underestimate $\beta_{max,90°}$ from Eq. (6-4).

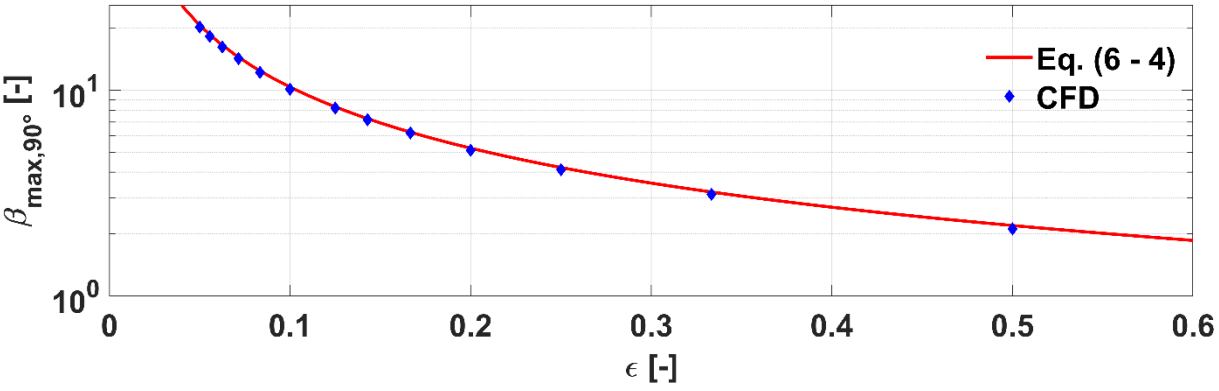

Figure 89: Comparison of maximum momentum coefficient from Eq. (6-4) with CFD results

Comparing the values for different relative gate openings ε in Figure 87, the increase of the momentum coefficient due to the sluice gate starts earlier with decreasing ε and also the

maximum value of the momentum coefficient becomes larger for smaller relative gate openings ε. This is due to the surface eddy already shown in Figure 41, which becomes longer and higher with smaller relative gate opening ε and thus reduces the effective flow cross section further upstream. This behavior is again like the sudden contraction observed by Malcherek and Müller [43], where the increase of the momentum coefficient for smaller contraction ratios also starts at the larger distance to the orifice. At the opening $X = 0$ where the flow cross section for the sluice gate suddenly reduces, the momentum coefficient drops abruptly to $\beta_0 \approx 1$. Since the momentum coefficient at the opening β_0 is needed for the momentum balance and is not exactly equal to one due to the small irregularity of the x-velocity profile, see Figure 88 b) at $X = 0$, it will be determined exactly in the following chapter. Considering the momentum coefficient in the tailwater of the sluice gate ($X > 0$), it remains at $\beta \approx 1$, since the x-velocity profile, see Figure 88 b), is also very uniform for ($X > 0$). Here the sluice gate differs from the sudden contraction, because for the sudden contraction the flow cross section in the downstream region does not change. In contrast to the sluice gate, a dead water zone with very low velocities forms directly behind the contraction, which causes the momentum coefficient to increase significantly before it drops again.

The momentum coefficient for inclined sluice gates is shown in Figure 90 for $\varepsilon = 0.25$. If the momentum coefficient is first observed in the upstream region, the maximum value of the momentum coefficient decreases as the angle decreases. In addition, the momentum coefficient does not drop abruptly at the opening, but initially rises to a maximum value and then drops again to near one at the opening.

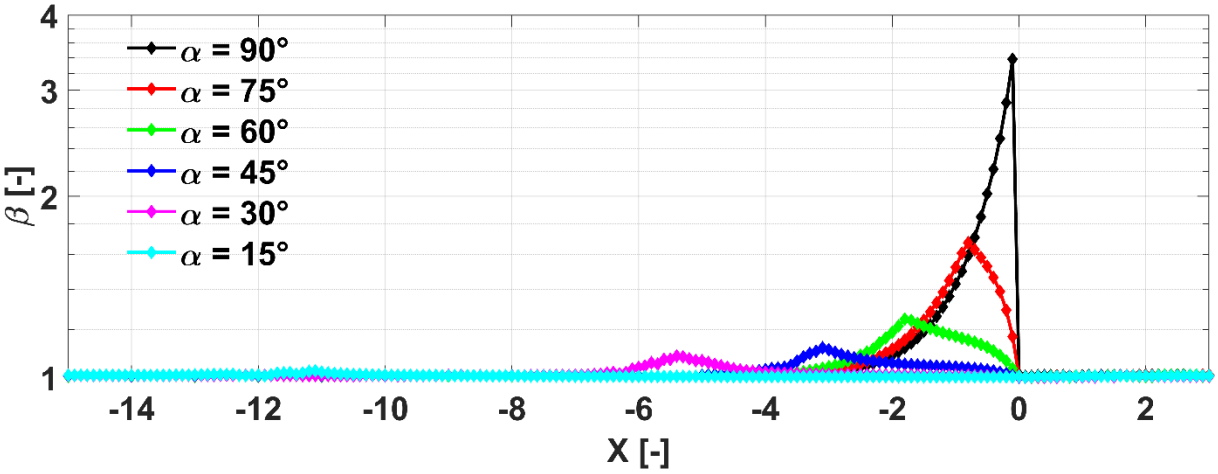

Figure 90: Momentum coefficient β along X-axis for inclined sluice gates (ε=0.25)

To explain this behavior, Figure 91 shows the inclined gate and the momentum coefficient curve. If we compare the position of the upper edge of the sluice gate with the

momentum coefficient profile, we can see that the maximum value of the momentum coefficient is reached at this point. The increase of the momentum coefficient upstream of the upper sluice gate edge can be explained by the fact that a surface eddy is also formed with the inclined sluice gate, but this is smaller than with the standard sluice gate, which also influences the velocity profile less. From the position of the upper sluice gate edge to the opening (X = 0), the momentum coefficient drops again. This is because with the inclined sluice gate, the flow cross-section through the gate is reduced and a kind of nozzle is formed. Through this "nozzle" the flow is accelerated more evenly than with the standard sluice gate. At the opening, the momentum coefficient drops to almost one and remains at about one in the downstream region. The momentum coefficient at the opening will be discussed in more detail in the following chapter since it is important for calculating the discharge from the momentum balance.

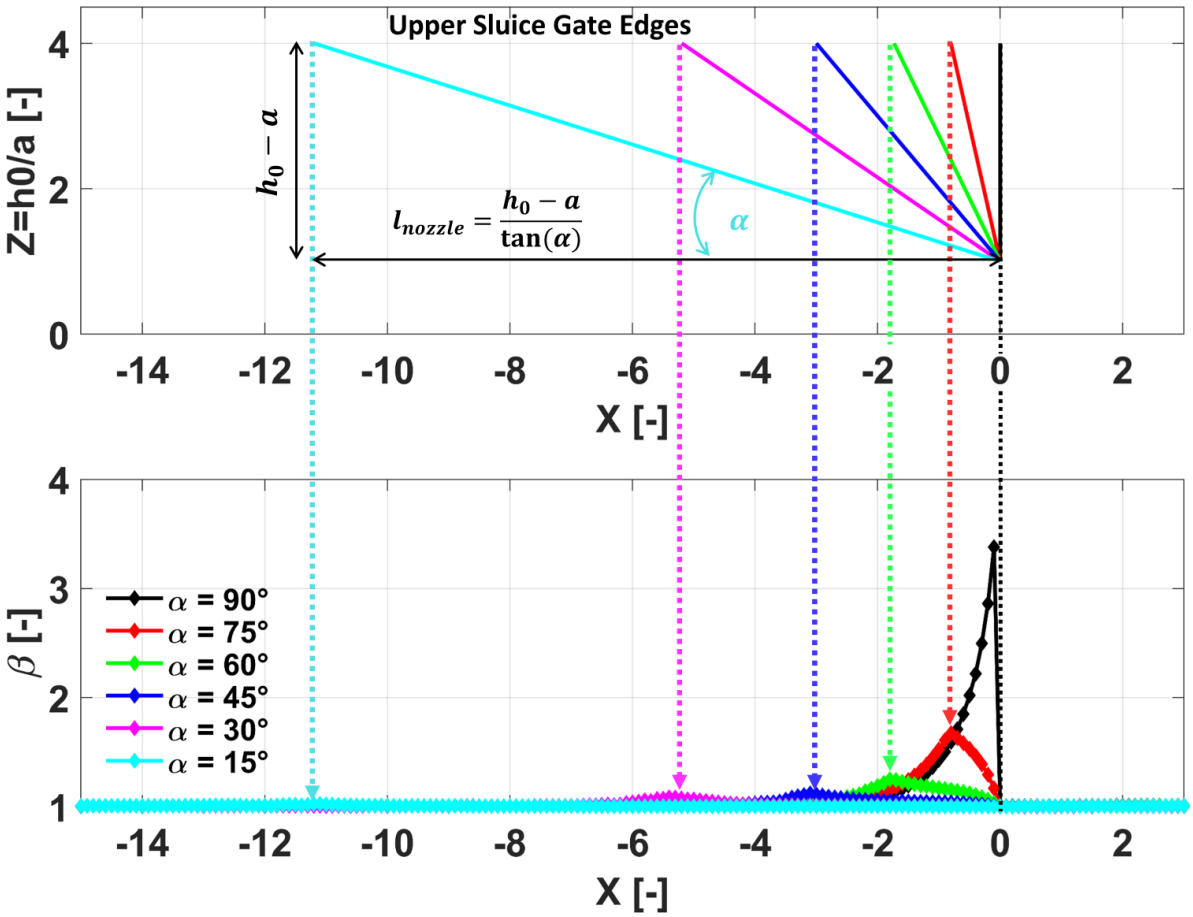

Figure 91: Position of upper sluice gate edge and β_{max} for inclined sluice gates

6.2 Momentum Coefficient at the Opening

The momentum coefficient at the opening, which is required to calculate the discharge from momentum balance, is determined in this chapter. In the previous chapter, the profile of the momentum coefficient was already shown, and it was shown that it is approximately one at the opening. The exact value, however, is slightly above one. The exact value from the CFD simulations for the momentum coefficient at the opening for the investigated relative gate openings ε and angles of inclination α is shown in Figure 92. If we first look at the momentum coefficient at the opening for the standard sluice gate ($\alpha = 90°$), we see that the maximum value is found here. The curve shows that the momentum coefficient at the opening is only slightly dependent on the relative gate opening ε. This dependency can be considered linear, whereby the slope is largest for $\alpha = 90°$ and decreases with decreasing angle of inclination α. The absolute value of β_O also decreases with decreasing α. At $\alpha = 45°$, the values are so close to one that the deviations can be neglected for the discharge calculation. For smaller angles, β_O increases minimally again, but is still so low that a value of one can also be assumed here for practical calculations.

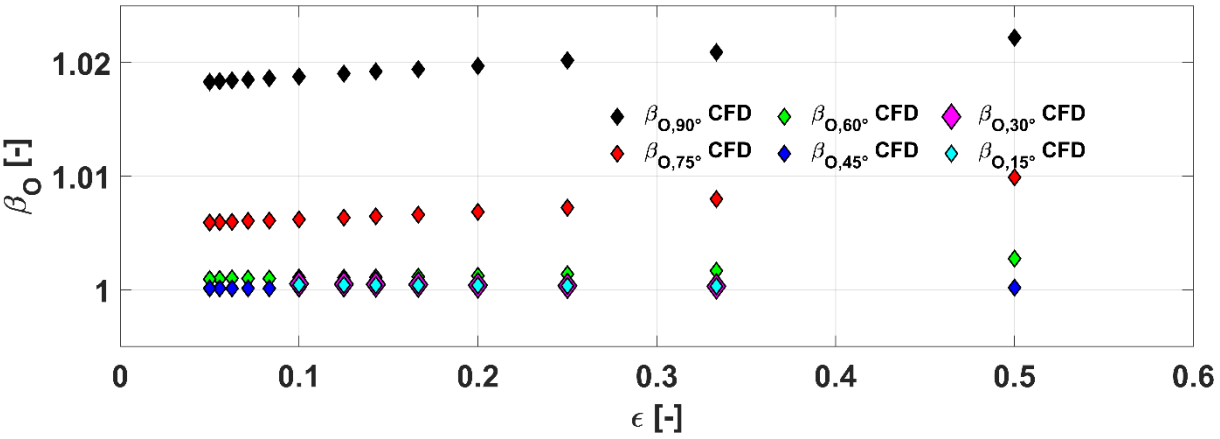

Figure 92: Momentum coefficient at opening β_O in dependency of the relative gate opening ε

This characteristic of β_O can be explained by looking at the velocity profile, shown in Figure 93 for $\varepsilon = 0.25$. While at the bottom at $Z_O = 0$ the velocity decrease due to the boundary layer is similar for all velocity profiles, the shape of the velocity profiles distinguishes near the lower sluice gate edge at $Z_O = 1$. For $\alpha = 45°$, the velocity profile is constant over a wide range of Z_O and has only a small decrease close to $Z_O = 1$. For angles of inclination larger than 45°, the velocity reduction near $Z_O = 1$ is more pronounced with increasing α and the reduction also starts at lower values of Z_O. For angles of inclination smaller than 45°, the x-velocity close to $Z_O = 1$ is also reduced but increases fast to a maximum in the region

$0.9 < Z_O < 1$ and then reduces again to a nearly constant velocity in the lower middle part of the x-velocity profile at the opening u_O.

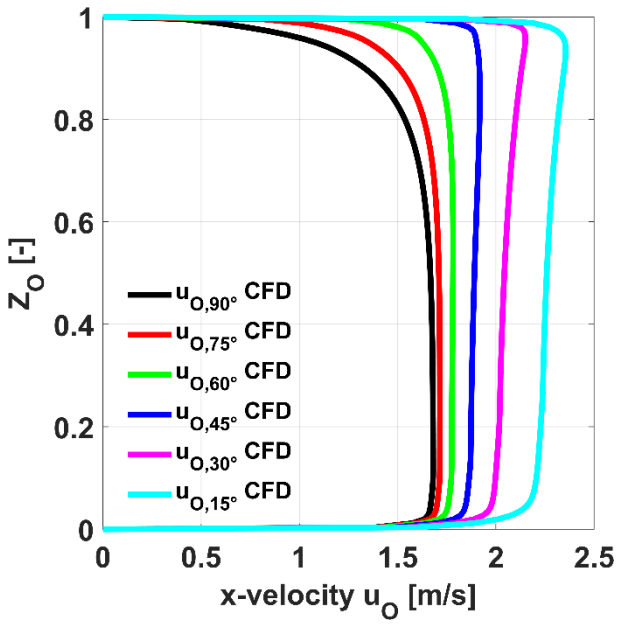

Figure 93: x-velocity profile u_O at the opening for ε=0.25

For the parameterization of the momentum coefficient at the opening, a sectional defined function is used, since, as already mentioned, β_O for $\alpha \leq 45\,^\circ$ can be assumed as constant one. Considering the momentum coefficient β_O for $\alpha > 45°$, as shown in Figure 94 a) for $\varepsilon = 0.5$ and in Figure 94 a) for $\varepsilon = 0.05$, the course can be approximated with a polynomial. The following equation is proposed as a parameterization function:

$$\beta_{O,\alpha>45°}(\alpha) = k_{\beta o} \cdot (\alpha[\mathrm{rad}] - b)^{\frac{5}{2}} + c \tag{6-5}$$

If we set as boundary conditions that the momentum coefficient $\beta_O = 1$ at the point $\alpha = 45° = \frac{\pi}{4}$ and at this point the slope $\frac{d\beta_{O,\alpha>45°}}{d\alpha}\left(\frac{\pi}{4}\right) = 0$, the parameterization function with the parameter $k_{\beta o}$ is obtained as follows:

$$\beta_{O,\alpha>45°}(\alpha) = k_{\beta o} \cdot \left(\alpha[\mathrm{rad}] - \frac{\pi}{4}\right)^{\frac{5}{2}} + 1 \tag{6-6}$$

The parameter for the momentum coefficient at the opening $k_{\beta o}$ is determined with the non-linear least square method using the data from CFD simulations. In Figure 94 a), the parameterization approach for the relative gate opening $\varepsilon = 0.5$ and in Figure 94 b) the parameterization approach for $\varepsilon = 0.05$ are shown graphically as an example. The results of the other relative gate openings investigated, as well as the SSE and RMSE, are summarized in

Table 11. The largest deviations occur for ε=0.5, but the deviations from the CFD values are generally small.

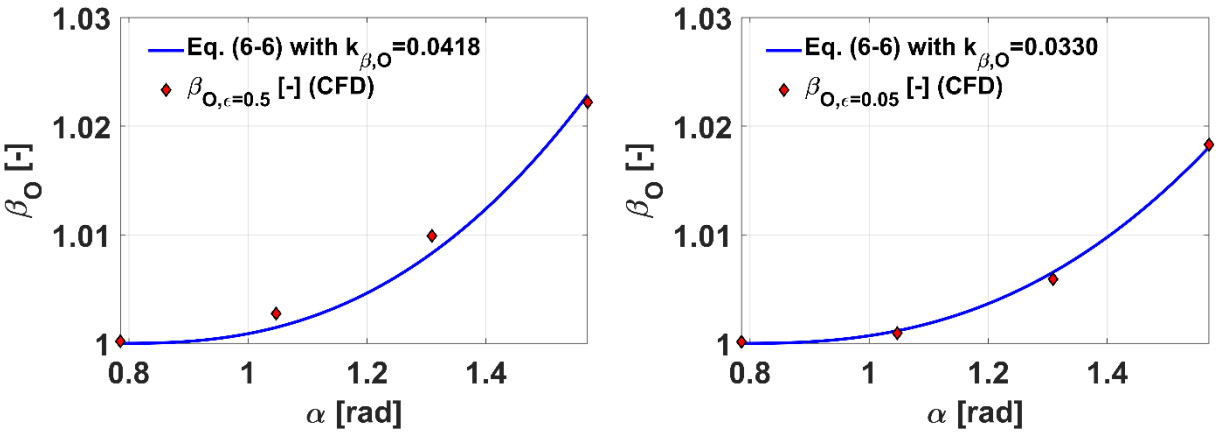

Figure 94: Opening momentum coefficient from CFD and parameterization approach (Eq. (6-6)) for a) $\varepsilon = 0.5$ and b) $\varepsilon = 0.05$

If the values determined for the parameter $k_{\beta o}$, shown in Table 11, are plotted in dependency of the relative gate opening ε, see Figure 95, a linear relationship can be seen. The following function was therefore selected as parameterization function for $k_{\beta o}$:

$$k_{\beta o}(\varepsilon) = k_{\beta o,1} \cdot \varepsilon + k_{\beta o,2} \tag{6-7}$$

Table 11: Parameter $k_{\beta o}$ for the parameterization of the momentum coefficient at the opening

	ε = 0.2	ε = 0.3	ε = 0.4	ε = 0.5	ε = 0.6	ε = 0.7	ε = 0.8
$k_{\beta o}$	$4.18 \cdot 10^{-2}$	$3.85 \cdot 10^{-2}$	$3.69 \cdot 10^{-2}$	$3.58 \cdot 10^{-2}$	$3.53 \cdot 10^{-2}$	$3.49 \cdot 10^{-2}$	$3.45 \cdot 10^{-2}$
SSE	$4.67 \cdot 10^{-6}$	$2.44 \cdot 10^{-7}$	$1.92 \cdot 10^{-8}$	$8.20 \cdot 10^{-8}$	$1.75 \cdot 10^{-7}$	$2.51 \cdot 10^{-7}$	$2.89 \cdot 10^{-7}$
RMSE	$1.25 \cdot 10^{-3}$	$2.85 \cdot 10^{-4}$	$8.00 \cdot 10^{-5}$	$1.65 \cdot 10^{-4}$	$2.41 \cdot 10^{-4}$	$2.89 \cdot 10^{-4}$	$3.11 \cdot 10^{-4}$
	ε = 1.0	ε = 1.2	ε = 1.4	ε = 1.6	ε = 1.8	ε = 2.0	
$k_{\beta o}$	$3.40 \cdot 10^{-2}$	$3.37 \cdot 10^{-2}$	$3.3510 \cdot 10^{2}$	$3.33 \cdot 10^{-2}$	$3.31 \cdot 10^{-2}$	$3.30 \cdot 10^{-2}$	
SSE	$3.56 \cdot 10^{-7}$	$4.32 \cdot 10^{-7}$	$4.18 \cdot 10^{-7}$	$4.79 \cdot 10^{-7}$	$5.00 \cdot 10^{-7}$	$5.25 \cdot 10^{-7}$	
RMSE	$3.44 \cdot 10^{-4}$	$3.79 \cdot 10^{-4}$	$3.73 \cdot 10^{-4}$	$4.00 \cdot 10^{-4}$	$4.08 \cdot 10^{-4}$	$4.18 \cdot 10^{-4}$	

The constants $k_{\beta o,1}$ and $k_{\beta o,2}$ were again determined using the non-linear least square method. Here, $k_{\beta o,1} = 0.02$ and $k_{\beta o,2} = 0.032$ were determined, with errors SSE $= 9.7336 \cdot 10^{-8}$ and RMSE $= 8.6530 \cdot 10^{-5}$. The parameterization approach for $k_{\beta o}$ is shown in Figure 95.

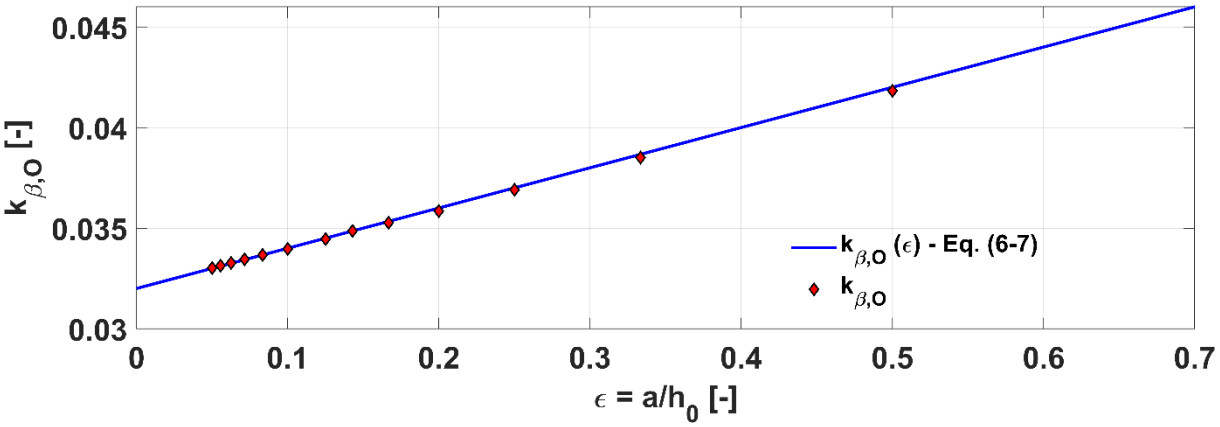

Figure 95: Parameter $k_{\beta o}$ in dependency of the relative gate opening ε

Summarizing the results of the parameterization, we finally obtain the following section-wise defined function for the momentum coefficient at the opening β_O:

$$\beta_O = \begin{cases} 1 & \text{for } \alpha \leq 45° \\ k_{\beta o}(\varepsilon) \cdot \left(\alpha[\text{rad}] - \frac{\pi}{4}\right)^{\frac{5}{2}} + 1 & \text{for } \alpha > 45° \end{cases} \tag{6-8}$$

Where the parameter$k_{\beta o}(\varepsilon)$ can be calculated as follows:

$$k_{\beta o}(\varepsilon) = 0.02 \cdot \varepsilon + 0.032 \tag{6-9}$$

In Figure 96 the new parameterization function (Eq. (6-8)) for the momentum coefficient is compared with the CFD values of the momentum coefficient. The parameterization agrees well with the CFD values both in course and in magnitude.

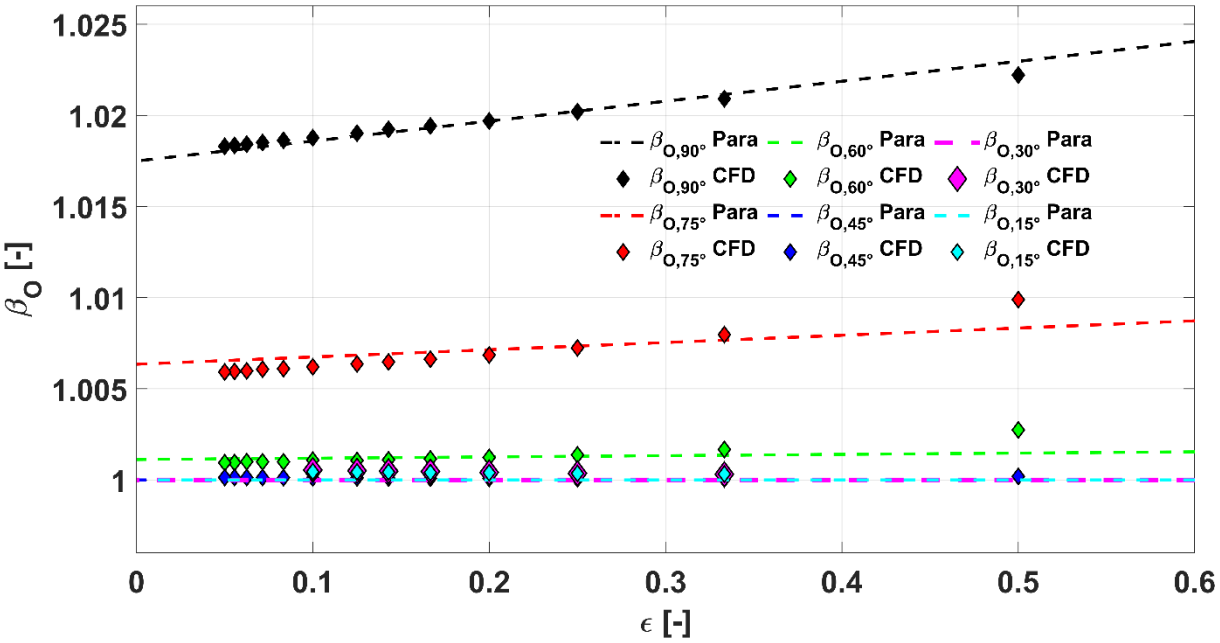

Figure 96: CFD values and parameterization approach of the momentum coefficient at the opening β_O

7 Discharge from Momentum Balance

In this chapter, the discharge of standard sluice gates and inclined gates are determined via the integral momentum balance. For this purpose, a MATLAB [75] program for determining the discharge is shown as an example. First, the forces and momentum coefficients are calculated and then used in the momentum balance for control volume I. In order to discuss the correctness of the discharge Q calculated by momentum balance, the discharge coefficient $c_{D,dB}$ is determined for it using Eq. (2-4) and compared with relevant experimental and analytical work from the literature.

7.1 Approach to Calculate the Discharge with the Momentum Balance

With the pressure forces and momentum coefficients determined in the previous chapters, the discharge can now be determined using Eq. (3-15) derived from the integral momentum balance, which is shown below:

$$Q = \sqrt{\frac{F_{\emptyset} - F_{Gx} - F_O}{\frac{\rho}{B}\left(\frac{\beta_O}{a} - \frac{\beta_{\emptyset}}{h_{\emptyset}}\right)}} \tag{3-15}$$

The pressure force at the left control volume boundary can be determined by the hydrostatic pressure force, with $F_{\emptyset} = \frac{1}{2} \cdot \rho \cdot g \cdot B \cdot h_0^2$. The velocity profile at the left control volume boundary is assumed as constant and hence the momentum coefficient is $\beta_{\emptyset} = 1$. The x-component of the gate force F_{Gx} can be calculated using Eq. (5-53). At the right control volume boundary, the pressure force at the opening F_O can be determined using Eq. (5-30) and the momentum coefficient at the opening β_O is determined using Eq. (6-8). If the equations are entered into a computer program, the discharge Q of the sluice gate can be calculated from them. The following is an example of a MATLAB program that calculates the discharge Q via the integral momentum balance by entering the opening height a, the upstream water level h_0, the angle of inclination α and the channel width B. To compare the discharge calculated from the integral momentum balance (Eq. (3-15)) with the CFD results, the MATLAB program shown below is used to calculate the discharge for $a = 0.1$ m, $h_0 = 0.11$ m to $h_0 = 2.2$ m, $\alpha = \{90°, 75°, 60°, 45°, 30°, 15°\}$ and $B = 1$ m. The results of the momentum balance are shown in Figure 97 as a function of the inverse relative gate opening $1/\varepsilon$. Also shown in Figure 97 is the discharge calculated in the CFD simulations. The results from the momentum balance and CFD agree very well. In the following chapters, the discharge calculated with the momentum balance is further compared with literature values, both for the standard sluice gate and for the inclined sluice gate.

```
%Sluice gate discharge from integral momentum balance
function Q=Sluice_Gate_Discharge(a,h0,alpha,B)
rho=1000;
g=9.81;
epsilon=a/h0;
% Bottom Pressure at Opening
kBO1=0.5829-0.06459*(1/tan(alpha)+2*cos(alpha)^2);
kBO2=0.1777*(alpha/(pi/2))^2;
KBO0=1-kBO1-kBO2;
pBO=rho*g*a*(KBO0+kBO1*(h0/a)+kBO2*(a/h0));
% Opening Pressure Force
kOstar=-0.6172;
kO=kOstar*(1-(h0/a)^kOstar);
FO=pBO*a*B*(-kO*(2/9)-rho*g*a/(6*pBO)+2/3);
% Gate Pressure Force
dh=(0.62*(epsilon)^2.5)*(h0-a);
kG90star=0.038;
kGa1=-0.6026;
kGa2=0.3164;
kG=(kGa1*(sin(alpha)-1)+kG90star)*epsilon^(1+kGa2*cos(alpha));
FG=0.5*B*rho*g*(h0+dh-a)^2 *(1+2*kG*(0.5-log(1/kG+1)));
% Opening Momentum Coefficient
if(alpha>pi/4)
Beta_O=((0.02*epsilon)+0.032)*(alpha-pi/4).^(5/2)+1;
else
Beta_O=1;
end
% Discharge
F=0.5*B*rho*g*h0^2-FG-FO;
Q=sqrt(F/((rho/B)*(Beta_O/a-1/h0)));
end
```

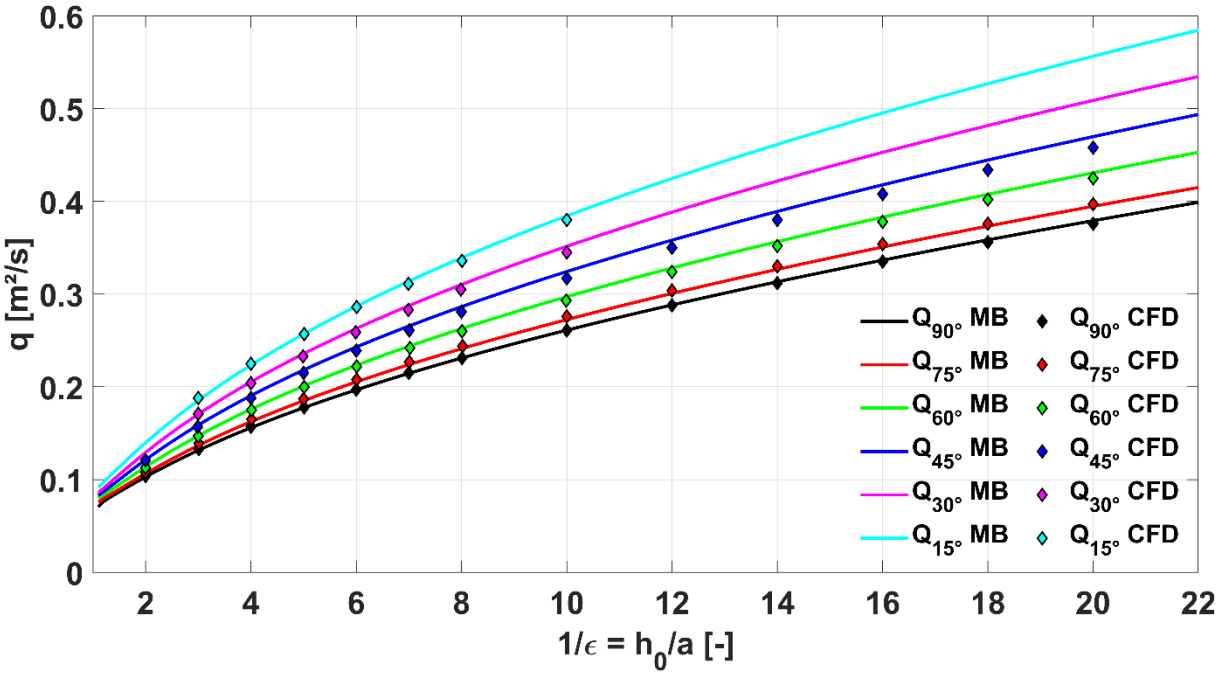

Figure 97: Comparison of specific sluice gate discharge q calculated by momentum balance (MB) and computational fluid dynamics (CFD) for various relative gate openings ε and angles of inclination α

7.2 Comparison of the Calculated Discharge from the Momentum Balance for the Standard Sluice Gate with Literature Values

The calculated sluice gate discharge from momentum balance is compared with the literature values of the standard sluice gate in Figure 98. For the comparison of the results, the du Buat discharge coefficient $c_{D,dB}$ was calculated with Eq. (2-4). Figure 98 consists of two graphs, where the works shown in the graph on the left (Figure 98 a)) have also studied the inclined sluice gate, while the works shown in the graph on the right (Figure 98 b)) have studied only the standard sluice gate.

Looking at the experimental results of Fawer [14], Gentilini [24] and Shivapur and Prakash [76] and the parameterization approach of Aigner et al. [25], which is based on the experimental data of Gentilini, it can be seen, that the momentum balance approach slightly underestimates the discharge coefficient $c_{D,dB}$ of these studies.

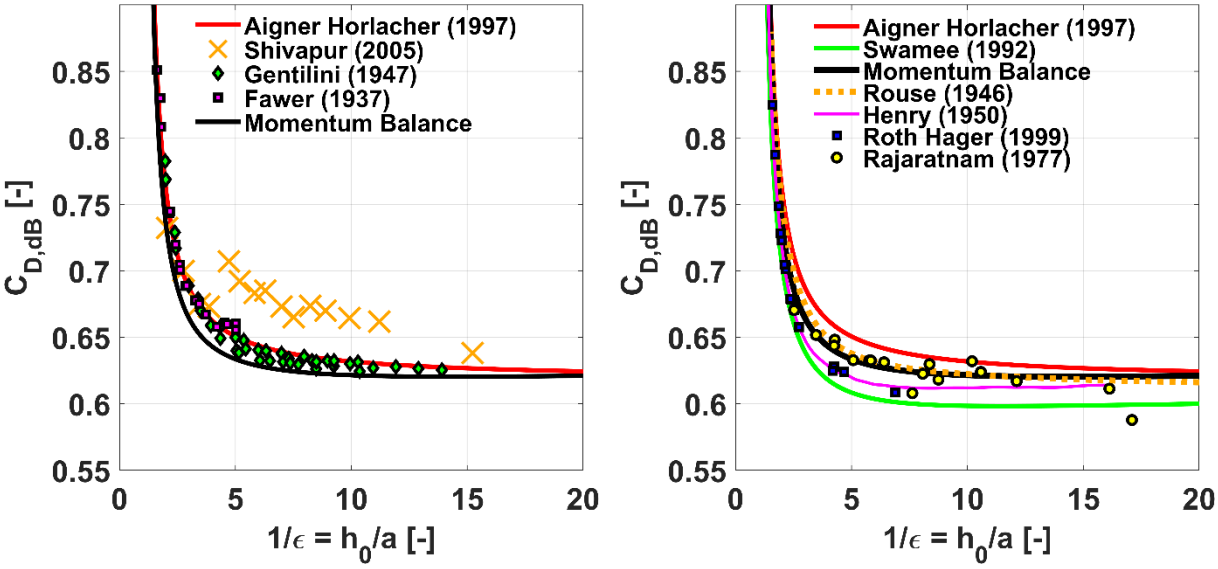

Figure 98: Discharge coefficient $c_{D,dB}$ from momentum balance compared with literature values in dependency of the inverse relative gate opening 1/ε for the standard sluice gate a) works that have also considered inclined sluice gates and b) works that have only considered standard sluice gates

The experiments of Fawer [14] were performed with opening heights of $a_{Fawer} = \{2\ cm, 3cm, 4cm\}$, the experiments of Gentilini [24] were performed with opening heights of $a_{Gentilini} = \{3\ cm, 4\ cm, 5\ cm, 7\ cm, 9\ cm\}$ and the experiments of Shivapur and Prakash [76] were performed with opening heights of $a_{Shivapur} = 4\ cm$. As described in Section 2.3, Nago [38] for $a_L < 6$ cm and Roth and Hager [28] for $a_L < 5$ cm found through their experiments that scaling effects occur for gate openings smaller than a_L. Roth and Hager [28] have derived a formula to account for scaling effects, see Eq. (2-36), which describes an increase of the discharge coefficient with decreasing gate opening a. The shown experiments

of Fawer [14] and Shivapur and Prakash [76] fall completely, as well as Gentilini [24] partially in the range in which according to Roth and Hager [28], as well as Nago [38] scaling effects occur. The larger values of the discharge coefficient $c_{D,dB}$ of Fawer [14], Gentilini [24] and Shivapur and Prakash [76] can be explained by the formula of Roth and Hager [28] (Eq. (2-36)), which takes into account the scaling effects that occur at the opening heights investigated by the authors mentioned before. This would also explain the deviations from the momentum balance, which is valid for sluice gate flows where the scaling effects have no significant influence. For the calculation of hydraulic structures, which are usually larger ($a > 6$ cm) and thus do not show scaling effects, the momentum balance should therefore provide more accurate results.

If we further compare the discharge coefficient from the momentum balance with the discharge coefficients determined from experiments by Henry [27], Rouse [3], Roth et al. [28] and Rajaratnam [32] and with the parameterization approaches of Swamee [26] and Aigner et al. [25] again, the discharge coefficient from the momentum balance approach lays between the values of these studies, while the approach of Aigner et al. [25] overestimates all other results. Using the parameterization approach of Swamee [26], a smaller discharge coefficient $c_{D,dB}$ over the whole range of the inverse relative gate opening $1/\varepsilon$ is obtained than all other values shown. Smaller values in comparison to the momentum balance, can be attributed to 3D effects in the experiment, which occur at small channel widths B. These 3D effects reduce the discharge Q through the sluice gate. The influence of 3D effects on the discharge will be explained in more detail in chapter 8.

7.3 Comparison of the Calculated Discharge from the Momentum Balance for the Inclined Sluice Gate with Literature Values

In Figure 99, the discharge coefficient $c_{D,dB}$ of the momentum balance is compared with the experimental work of Fawer [14], Gentilini [24] and Shivapur and Prakash [76] for the inclined sluice gate. For this purpose, a graph has been created for each angel of inclination α studied. Considering the angle of inclination $\alpha = 75°$ (Figure 99 a)), the discharge coefficient $c_{D,dB}$ of the momentum balance as for the standard sluice gate ($\alpha = 90°$), shown in Figure 98 a), is lower than the values published in the works of Fawer [14], Gentilini [24] and Shivapur and Prakash [76]. The difference could be explained by the fact that the experimental measurements of the aforementioned authors were performed in a region where scaling effects occur. For the inclined sluice gate, no work is available on whether and how strong scaling effects occur here. However, it can be assumed that scaling effects also occur for the inclined sluice gate. For the angle $\alpha = 60°$ (Figure 99 b)) the values Fawer [14], Gentilini [24] and Aigner and Horlacher [25] agree well with the momentum balance. For smaller angles $\alpha = 45°$, $\alpha = 30°$ and $\alpha = 15°$, the discharge coefficient $c_{D,dB}$ calculated with the momentum balance for $\frac{1}{\varepsilon} < 5$ also agrees very well with the literature values, see Figure 99 c), d) and e). For $\frac{1}{\varepsilon} > 5$, the discharge coefficient calculated with the momentum balance is higher than that of Gentilini [24] and Aigner and Horlacher [25]. The values measured by Shivapur and Prakash [76] are far above the other published results and will not be considered further.

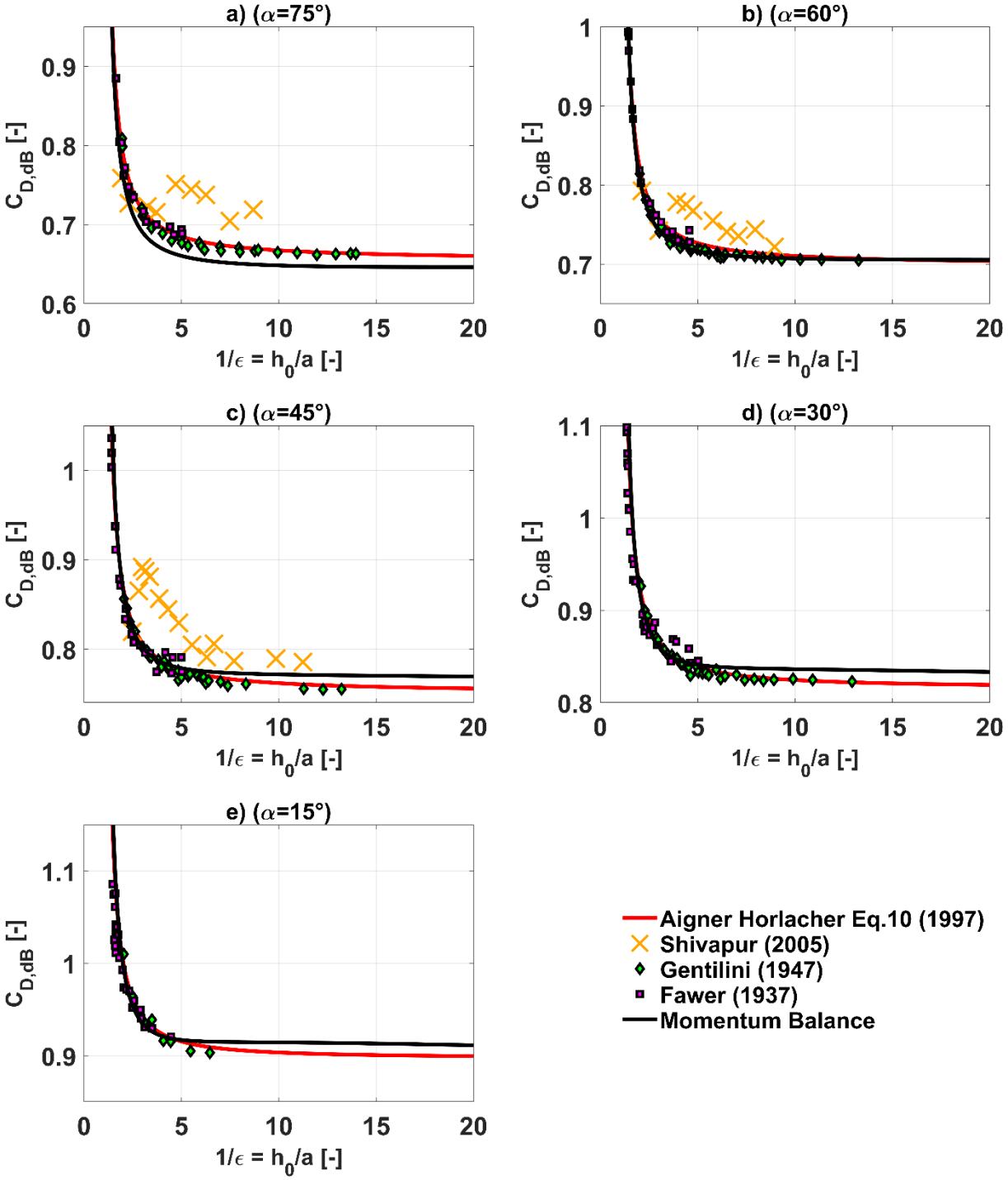

Figure 99: Discharge coefficient $c_{D,dB}$ from momentum balance compared with literature values in dependency of the inverse relative gate opening 1/ε for the inclined sluice gate a) $\alpha = 75°$, b) $\alpha = 60°$, c) $\alpha = 45°$, d) $\alpha = 30°$ and e) $\alpha = 15°$

Another way of representing the discharge coefficient is shown in Figure 100. Here the discharge coefficient $c_{D,dB}$ is plotted as a function of the angle of inclination α to illustrate this dependence. Figure 100 a) shows the momentum coefficient for $\varepsilon = 0.5$ and Figure 100 b) for $\varepsilon = 0.25$. The experimental results of Gentilini [24] and Fawer [14] were interpolated for the plot, since the authors did not exactly examine the relative gate openings ε=0.5 and ε=0.25. It

is clear how the parameterization formula of Aigner and Horlacher [25] and the momentum balance coincide for $\alpha \leq 45°$. For larger angles of inclination, the possible deviations due to scaling effects have already been explained.

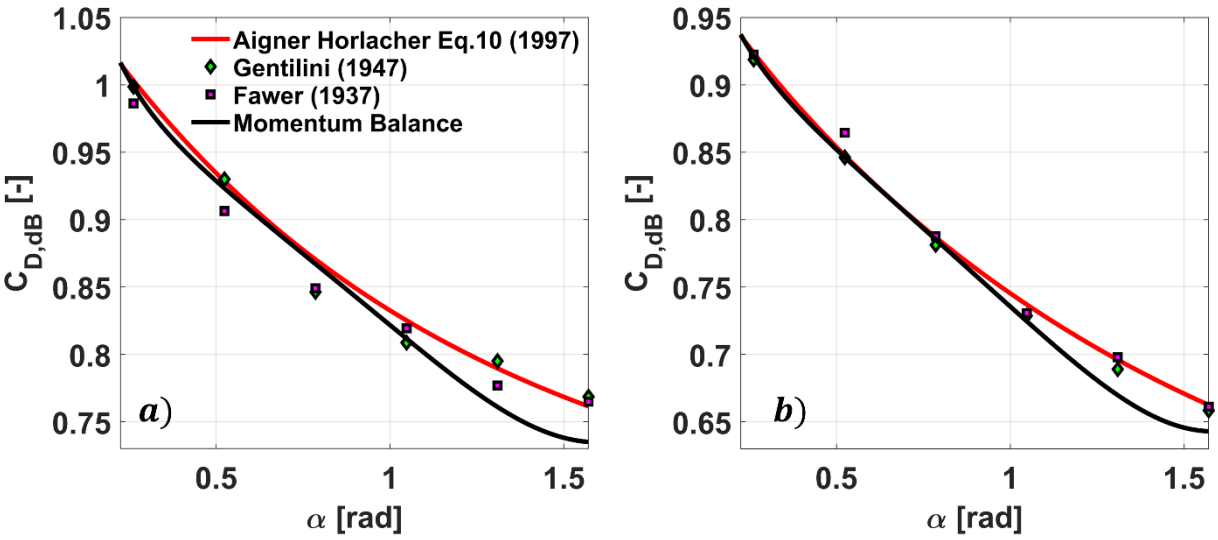

Figure 100: Discharge coefficient $c_{D,dB}$ from momentum balance compared with literature values in dependency of the angel of inclination α for a) $\varepsilon = 0.5$ $\left(\frac{1}{\varepsilon} = 2\right)$ and b) $\varepsilon = 0.25$ $\left(\frac{1}{\varepsilon} = 4\right)$

8 3D Effects on Sluice Gate Flows

In textbooks and in numerous publications on sluice gates, as well as in the previous chapters, sluice gate flows are considered as two-dimensional flows. This is a very good approximation for wide sluice gates, as they occur in many practical applications. Nevertheless, 3D flow effects occur, as already described in chapter 2.2. These 3D effects have significant influence on the flow of sluice gates with small relative gate widths ζ (Eq. (2-16)). The influence of 3D effects on the pressure distributions and the momentum coefficient at the opening β_O , is analyzed in this chapter for the relative gate widths $\zeta = \{0.125, 0.25, 0.5, 1.0, 2.0, 4.0, 6.0\}$ using the example for the standard sluice gate ($\alpha = 90°$) with $\varepsilon = 0.25$. In addition, the discharge calculation is modified using momentum balance to account for the 3D effect.

For this purpose, 3D flow simulations of the sluice gates with different relative channel widths ζ were performed. Figure 101 shows the Q-criterion to visualize the turbulent structures. RANS simulations (Figure 101 a)) and DES simulations (Figure 101 b)) were performed to analyze the 3D effects. The different turbulence patterns are clearly visible. Using the RANS approach, the turbulent structures are modeled, and the eddy structures are not resolved in detail. Looking at the DES simulation in Figure 101 b), eddy structures are clearly visible, and the (large scale) turbulent structures are more detailed. To analyze the 3D effects in this chapter, which are mainly due to the corner vortices, DES simulations were performed. The streamlines are shown in Figure 102, Figure 103 and Figure 104 for different relative gate widths ζ for the standard sluice gate with $h_0 = 0.4$, $a = 0.1$ and $\varepsilon = 0.25$. To generate the streamlines, a line seeding of the streamlines at the inlet at $z = 0.5\ h_0$, $z = 0.8\ h_0$, $z = 0.9\ h_0$, $z = 0.95\ h_0$ and $z = 0.99\ h_0$ was generated.

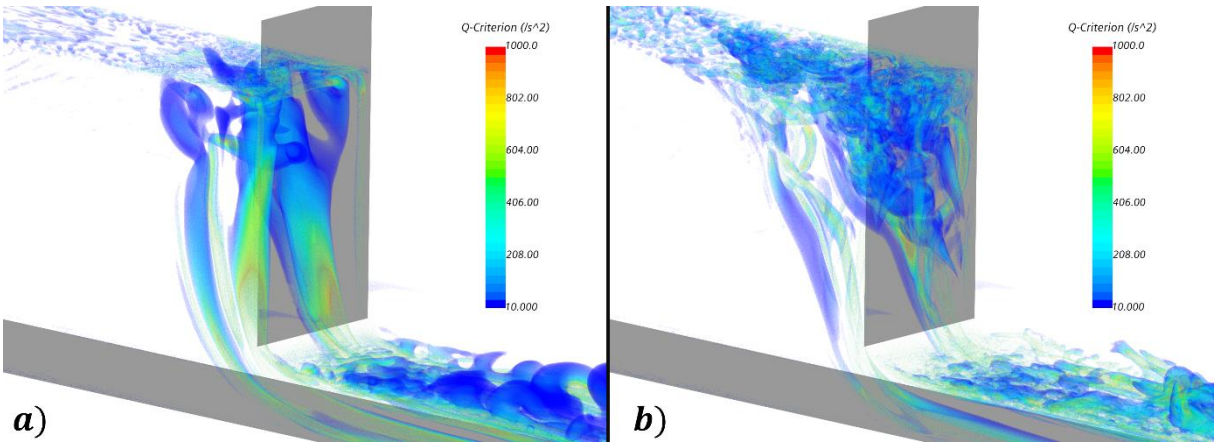

Figure 101: Visualization of turbulent structures of sluice gate flows using Q-Criterion for $\varepsilon = 0.25$ and $\zeta = 2$ a) RANS simulation and b) DES simulation

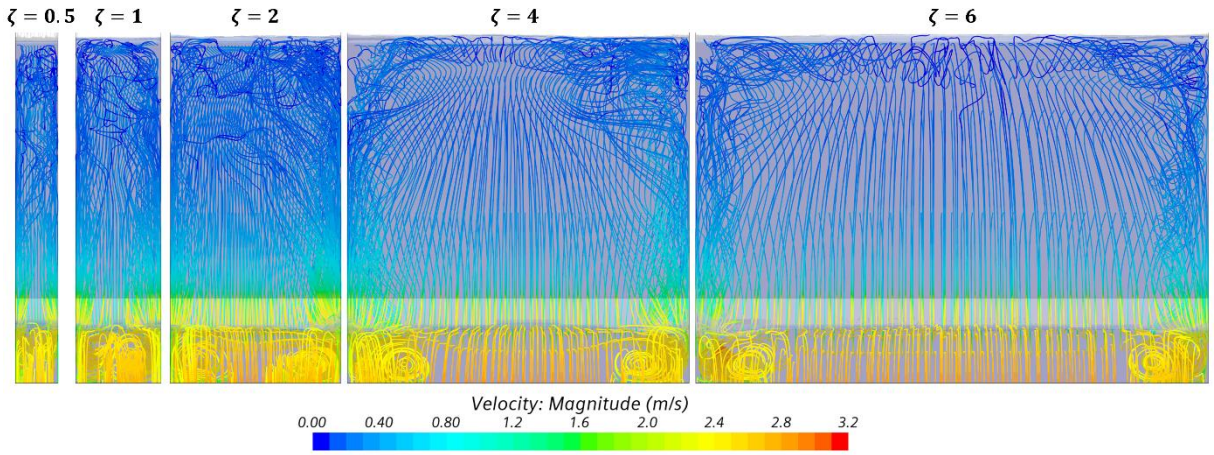

Figure 102: Frontal view of streamlines for different relative gate widths ($h_0 = 0.4$, $a = 0.1$ and $\varepsilon = 0.25$)

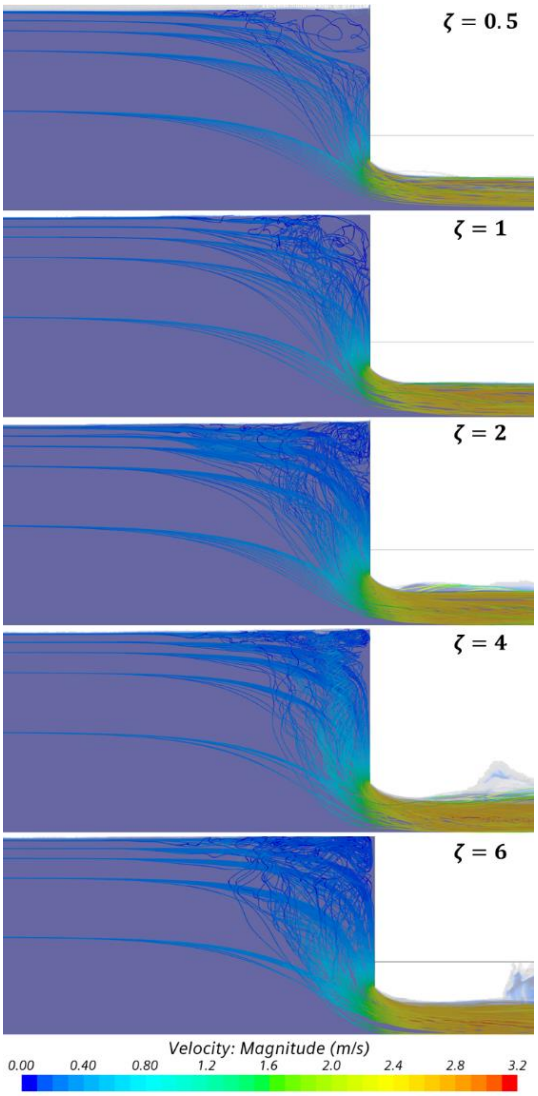

Figure 103: Side view of streamlines for different relative gate widths ($h_0 = 0.4$, $a = 0.1$ and $\varepsilon = 0.25$)

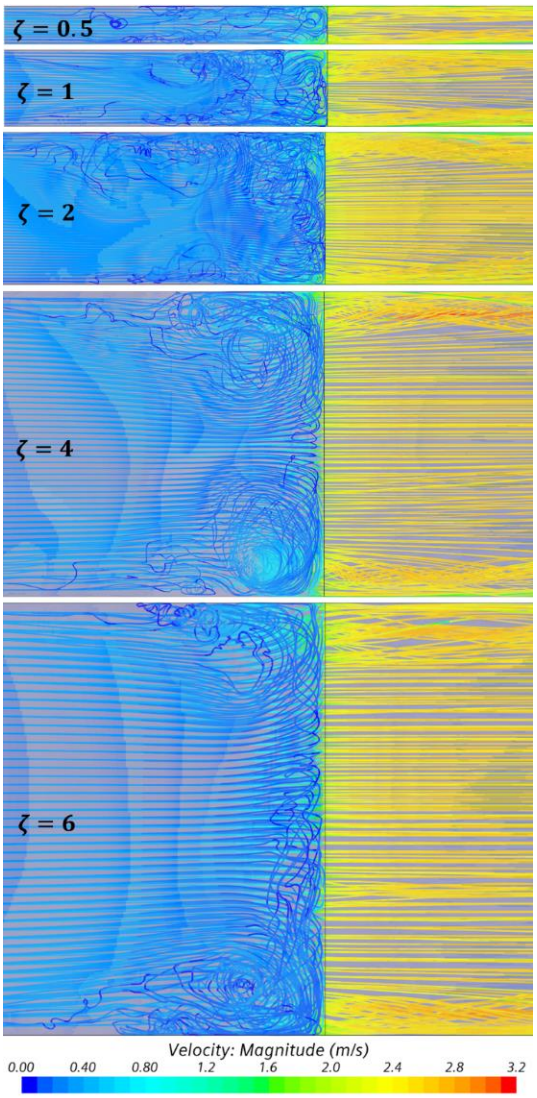

Figure 104: Top view of streamlines for different relative gate widths ($h_0 = 0.4$, $a = 0.1$ and $\varepsilon = 0.25$)

Figure 102 shows the frontal view of the streamlines. If we look at the corner vortices for $\zeta = 4$ and $\zeta = 6$, they are very similar to each other, but they are further away from each other due to the broader sluice gate. This similarity can also be seen in the side view Figure 103 and the top view Figure 104. For $\zeta = 2$, $\zeta = 1$ and $\zeta = 0.5$ the corner vortices mix in the upper half ($z > 0.5\ h_0$) and are no longer clearly separated. This is especially clear in the top view (Figure 104), which shows that the separated surface vortices are clearly separated for large relative gate widths $\zeta \geq 4$ and coincide for small relative gate widths $\zeta > 2$.

8.1 3D Pressure Distributions

In this section, the bottom pressure distribution p_B, the pressure distribution at the opening p_O and the pressure distribution at the sluice gate p_G are considered for the 3D case. In the previous 2D considerations, as with all other pressure distributions analyzed in previous work (e. g. [28] [60] [63] [64] [65] [66] [67]), a constant pressure profile along the width of the sluice gate was assumed. However, due to the corner vortices and the boundary layer, deviations occur in the edge region near the sidewalls, with the edge region dominating for sluice gates with very small relative channel width ζ.

A side view of the pressure distribution is shown in Figure 105 at several position along the width of the sluice gate for the example case $a = 0.1$ m, $h_0 = 0.4$ m and $B = 0.4$ m. In the middle plane ($Y = 0.5$), the pressure distribution is nearly undisturbed and comparable to the 2D pressure distribution. Also, in the tailwater downstream of the vena contracta, the pressure distribution in the middle area is hydrostatic. The strongest deviations of the pressure along the width are found in the intersection axis of the corner vortices at $Y = 0.08$ and $Y = 0.92$. Due to the larger velocities in the vortex, the pressure drops at the vortex and is lowest in the vortex core. In the downstream region, the pressure at the vortex core falls here even below ambient pressure. The water height in the downstream area is also influenced by the vortices and the pressure distribution is not hydrostatic. To illustrate that the pressure drop occurs around the corner vortices, the respective corner vortices were made visible with streamlines. In the upstream region at the sidewalls $Y = 0$ and $Y = 1$, a pressure decrease can also be observed in the surrounding of the corner vortices, but the pressure decrease is lower than in the vortex planes at $Y = 0.08$ and $Y = 0.92$. In the downstream region, the pressure distribution at the walls is also not hydrostatic and influenced by the shock waves, which are generated by the corner vortices. The position of the vortices depends strongly on the relative gate width ζ and is only valid for the shown example of the standard sluice gate with $a = 0.1$ m, $h_0 = 0.4$ m and $B = 0.4$ m ($\zeta = 4$) and should not be transferred to other cases.

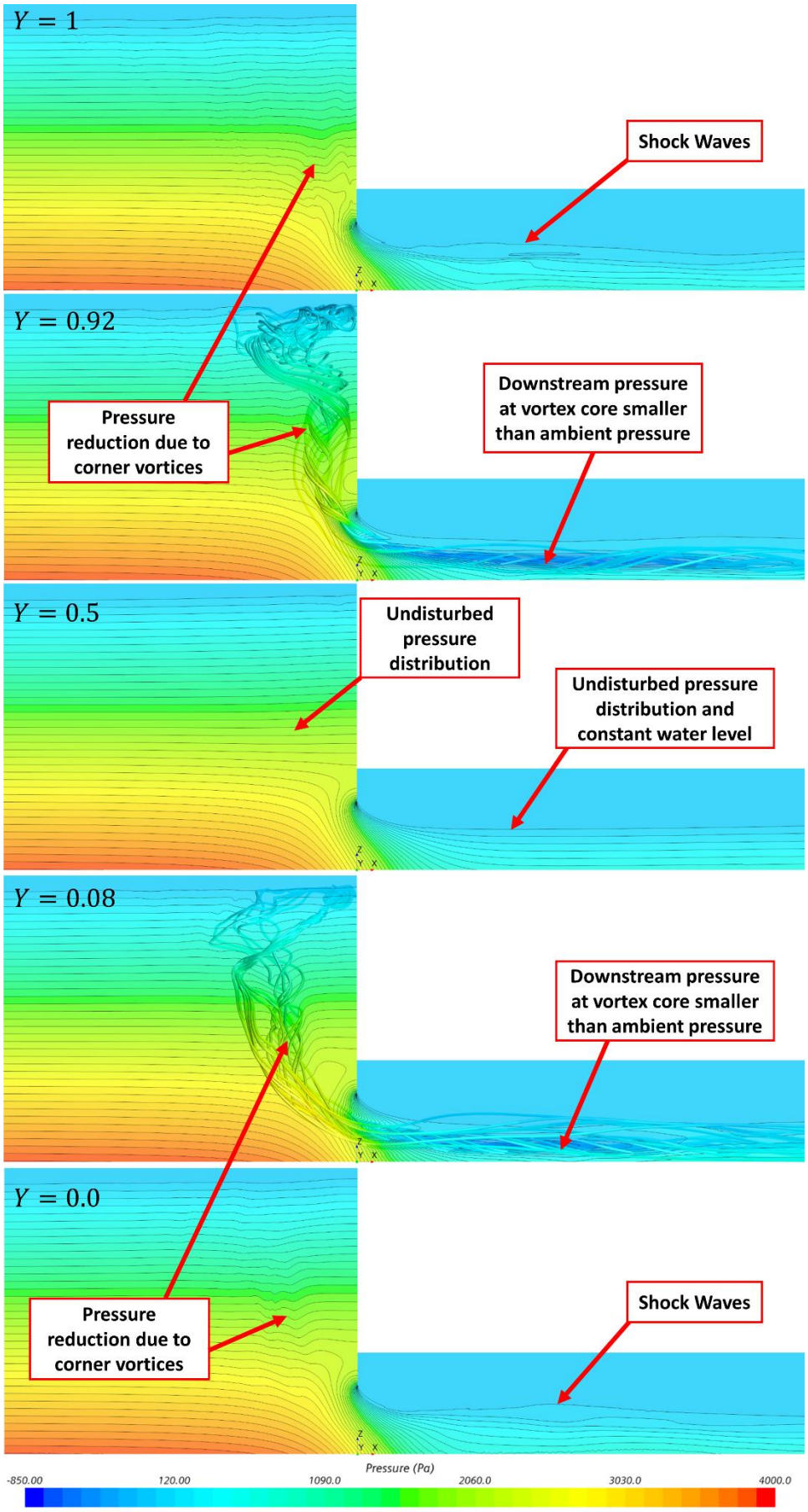

Figure 105: Side view of pressure contour plot at several positions of Y along the width

The 3D pressure distribution at the gate p_G and at the opening p_O associated with the example which was also shown in Figure 105 are shown in Figure 106. The contour plot in Figure 106 a) shows that there are deviations in the gate pressure distribution along the Y-coordinate along the axis of the corner vortices. At the opening, the vortices penetrate the control volume boundary. The pressure in the core of the vortex is very low and deviates significantly from the pressure distribution in the middle region, while at the corners between the bottom of the channel and the sidewalls the pressure is higher than at the bottom in the middle of the channel. The position of the vortices at which they penetrate the opening plane is also shown in Figure 106 a). The distance Y from the wall for both corner vortices is equal to $Y = 0.08$, the distance from the bottom in the opening z-coordinate for the left vortex core is $Z_O = 0.59$ and for the right vortex core is $Z_O = 0.68$. However, since this is a transient simulation, these quantities vary, which explains the errors in symmetry. Therefore, the shown 3D simulations should be considered as a momentary snapshot. The geometry of the corner vortices will not be discussed in detail in this work, but their influence on the pressure distributions, which are important for the momentum balance.

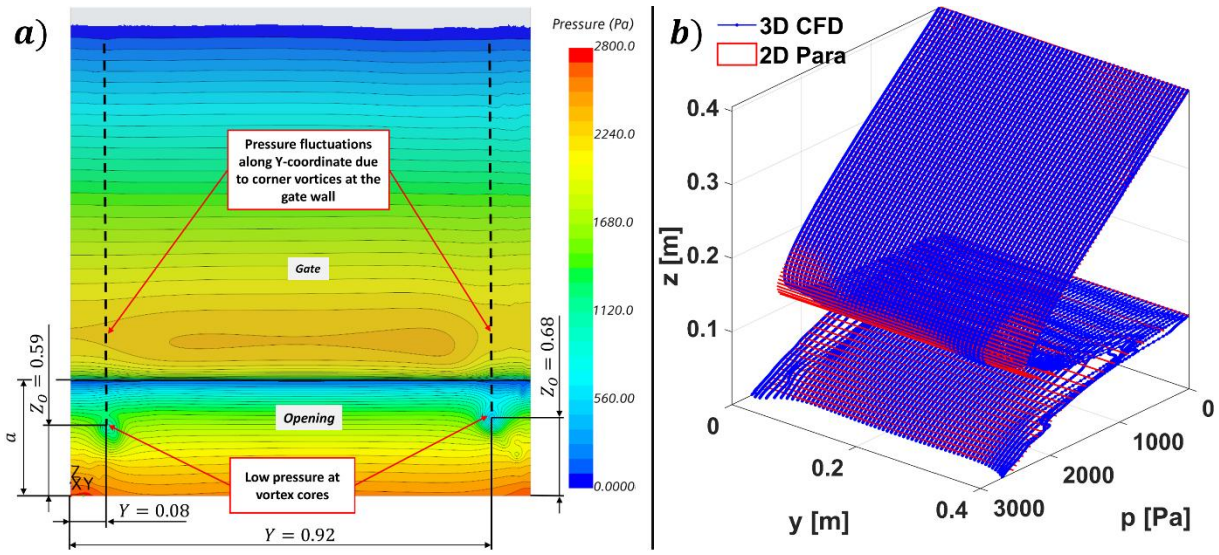

Figure 106: 3D Pressure distribution at gate and opening for $a = 0.1$, $h_0 = 0.4$ and $B = 0.4$ a) contour plot and b) 3D view

In Figure 101 b), the pressure distribution from the 3D CFD simulations is compared with the pressure distribution from the parameterization of the gate pressure distribution (Eq. (5-45)) and the parameterization of the opening pressure distribution (Eq. (5-25)). The pressure distributions largely agree, but there are deviations due to the corner vortices near the sidewalls. The largest deviations in the gate pressure distribution can be seen around the maximum pressure p_{GM}. At the opening one recognizes the clear deviations around the vortex

cores. Also, the increased pressure at the bottom ($z = 0$) of the 3D pressure distribution near the sidewalls is clearly visible. The following sections show the influence of the relative gate width ζ on the pressure distribution qualitatively and the integrals of the pressure distributions appearing in the momentum balance qualitatively.

8.1.1 3D Bottom Pressure Distribution

Although the bottom pressure distribution is only indirectly included in the momentum balance at the location $X = 0$ at the opening, it is nevertheless shown for the sake of completeness, since it is often assumed by the literature to be constant along the sluice gate width. For the 2D case, the bottom pressure distribution runs from the upstream hydrostatic pressure to the downstream hydrostatic pressure as it was described in chapter 5.1. Figure 107 shows the pressure contour plot of the 3D bottom pressure distribution for different relative gate widths ζ. Also shown are the streamlines to visualize the flow and the corner vortices. In general, the bottom pressure behaves similarly for all relative channel widths ζ investigated and is larger near the sidewalls than at the center of the flow. However, the influence of the sidewalls begins only immediately upstream of the sluice gate, where the vortices are generated. In the upstream region far from the sluice gate, the pressure distribution along the width is constant and hydrostatic ($p_B = \rho\, g\, h_0$). In the downstream region, a hydrostatic pressure distribution is present only in the middle region for the investigated channel length, see also Figure 107.

In Figure 108 a) the dimensionless bottom pressure distribution for the relative channel width $\zeta = 1$ and in Figure 108 b) the dimensionless bottom pressure distribution for $\zeta = 4$ are shown along the dimensionless gate width Y. Also shown in Figure 108 is the parameterization approach (Eq. (5-13)) of the bottom pressure distribution. In the upstream region ($X < 0$), the 3D bottom pressure is constant along the width and the two shown pressure distributions of the parameterization approach and the 3D CFD simulations agree well since the corner vortices arise only at the gate ($X = 0$) and propagate downstream. In addition, the z-distance of the corner vortices from the ground in the upstream region is very large, which is why the influence on the bottom pressure is smaller. In the downstream area it can be observed that near $Y = 0$ and $Y = 1$, the bottom pressure has strong variations, while in the center, the bottom pressure is nearly constant along the dimensionless channel width Y.

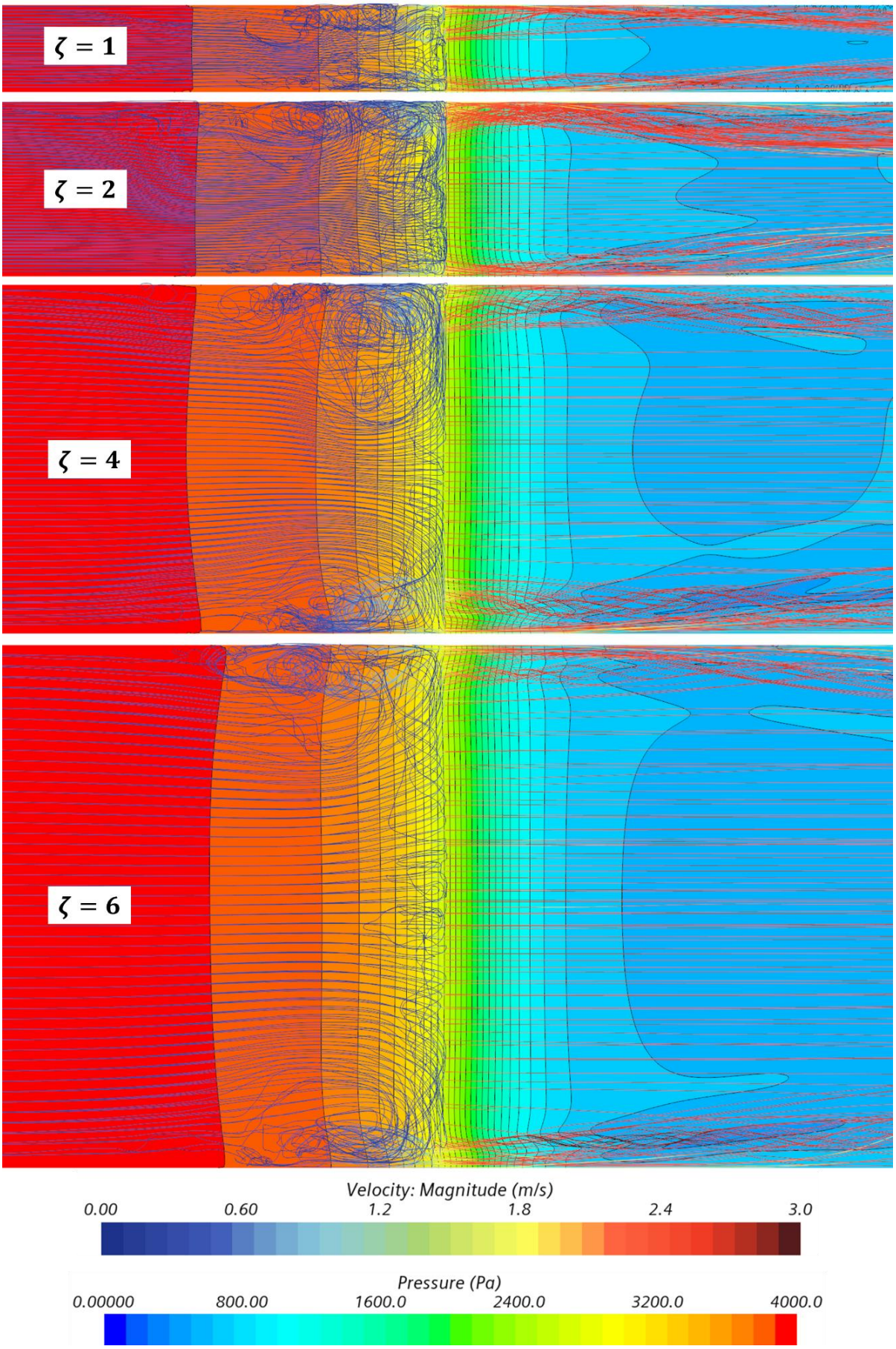

Figure 107: 3D bottom pressure contour plot and velocity streamlines for different relative gate widths ζ

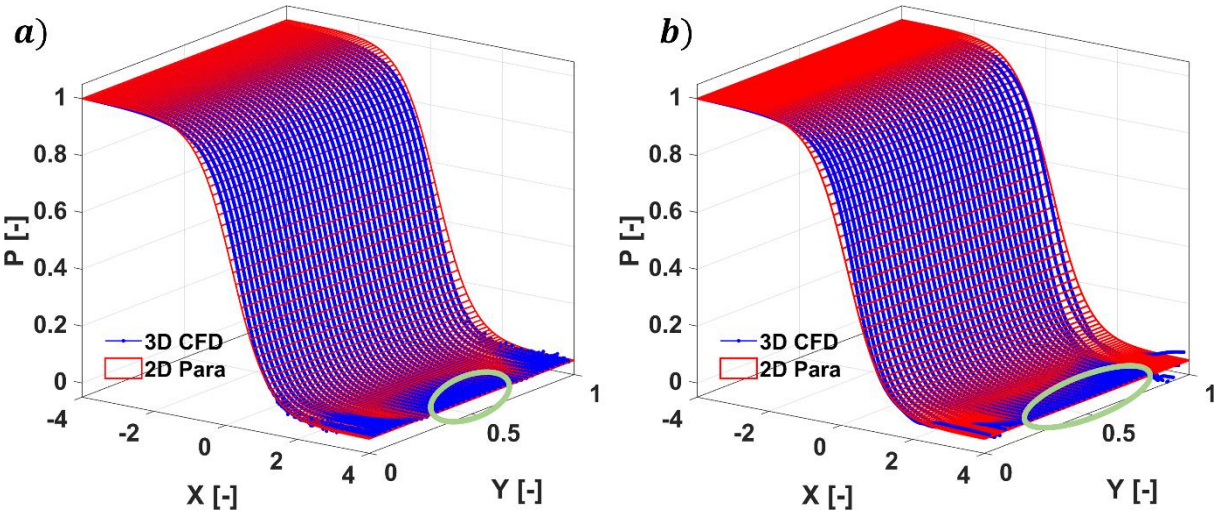

Figure 108: 3D bottom pressure profile and parameterization approach (Eq. (5-13)) for a) $\zeta = 1$ and b) $\zeta = 4$

8.1.2 3D Opening Pressure Distribution

The contour plots of the pressure distribution at the opening are shown in Figure 109. Deviations of the pressure distributions along the width are mainly visible at the side walls where the corner vortices penetrate the opening plane. The vortex cores are clearly visible due to the lower pressure in most of the cases shown. The corner vortices move upward away from the bottom towards the gate lip as the relative gate opening ζ becomes smaller. For very small relative gate widths ($\zeta = 0.125$), they are no longer visible in the contour plot and the pressure distribution is nearly constant across the entire width. For larger relative gate widths ζ, the pressure increase at the bottom near the side walls is also clearly visible.

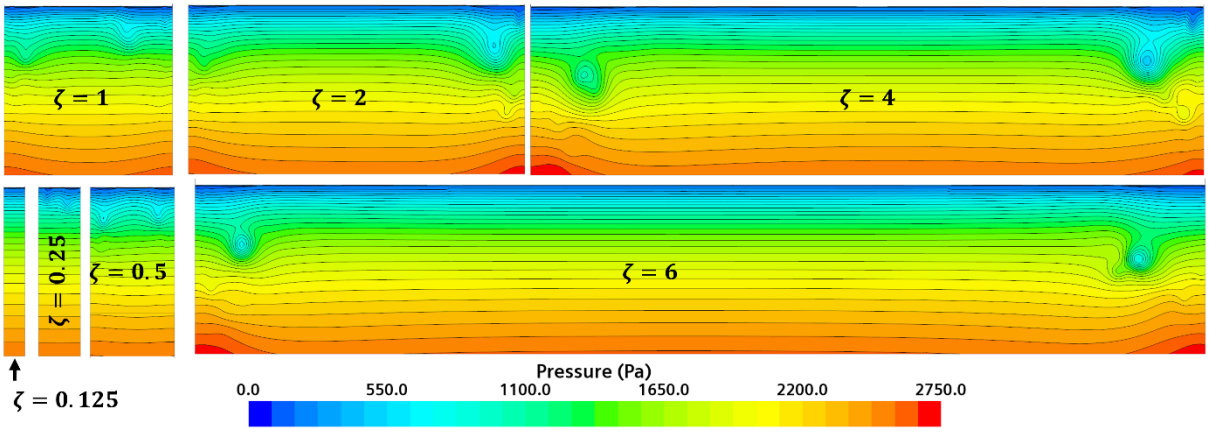

Figure 109: Contour plot of the pressure distributions at the opening for the studied relative gate widths ζ

Looking at Figure 110, where the 2D parameterization approach of the pressure distribution is compared with the 3D CFD simulations, there are larger deviations at the corner vortices on the pressure distribution for $\zeta = 4$ (Figure 110 b)) than for the case $\zeta = 1$ (Figure 110 a)). Conversely, the corner vortices occupy a larger part of the opening area for

$\zeta = 1$ than for $\zeta = 4$. That means, conversely, for $\zeta = 4$ there is a broader central region in which the opening pressure distribution agrees very well with the parameterization. This range becomes larger and larger with increasing relative gate width ζ.

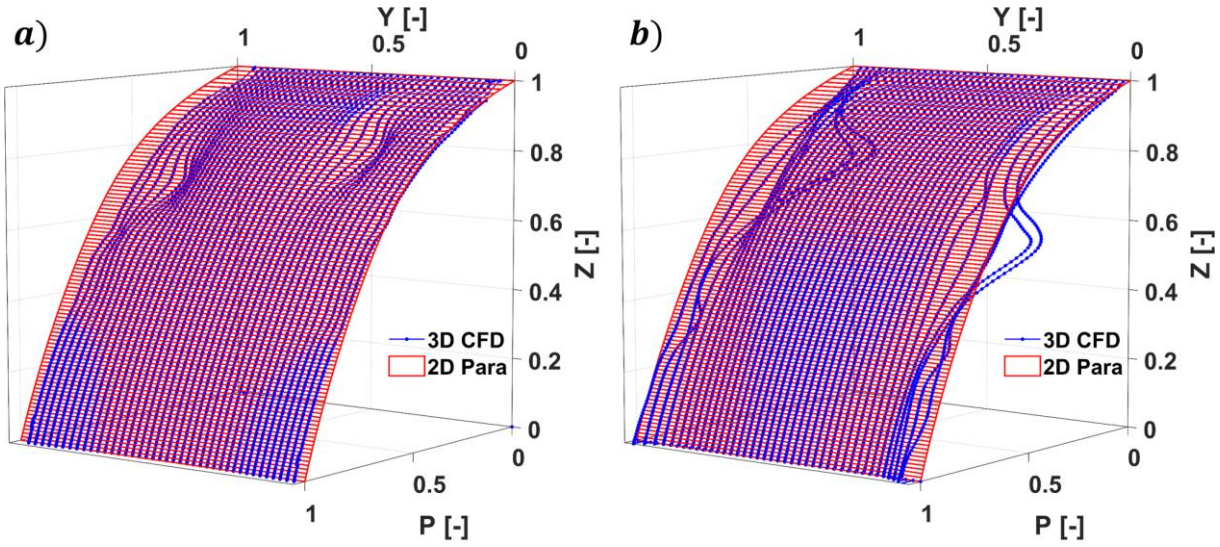

Figure 110: Opening pressure parameterization distribution from 3D CFD simulation and parameterization for $\varepsilon = 0.25$ a) $\zeta = 1$ and b) $\zeta = 4$

Looking at the normalized opening force F_O/B, shown in Figure 111, i.e. the integral of the opening pressure distribution over the area of the opening, it can be seen that from $\zeta = 1$ to $\zeta = 4$ the normalized opening pressure force is constant, since, as in Figure 110, the deviation of the pressure becomes smaller with decreasing relative gate width ζ, but extends over a larger part of the total area of the opening. The normalized opening force F_O/B is largest for the 2D case ($\zeta \to \infty$), since here no pressure drop through the corner vortices is considered. For $\zeta = 0.5$, the deviation is maximal and the value for F_O/B assumes a minimal value. For even smaller relative gate widths ζ, the normalized opening pressure force increases again as the corner vortices become much weaker. Also for $\zeta > 4$ the normalized opening pressure force increases again, because the area of the opening influenced by the corner vortices becomes smaller.

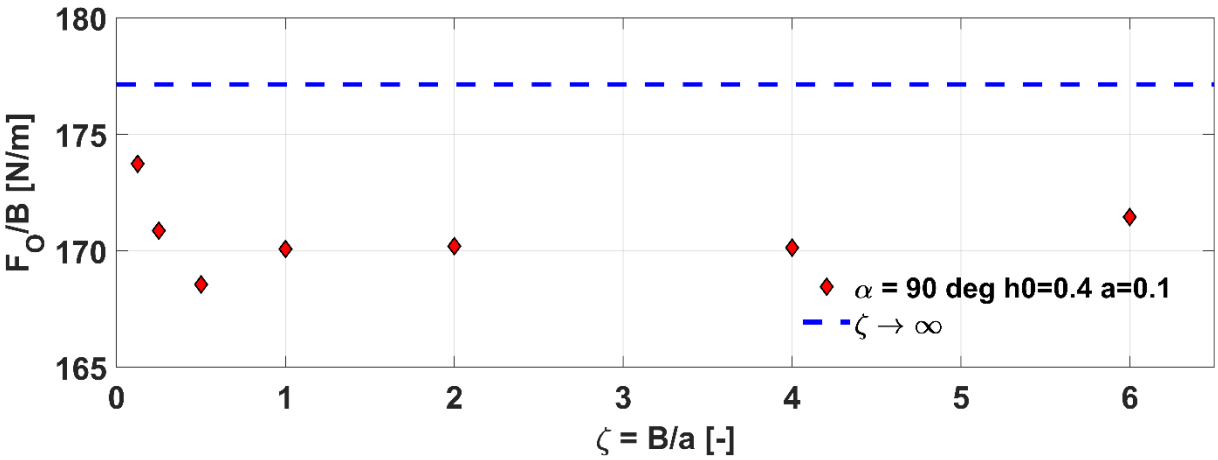

Figure 111: Normalized opening pressure force F_O/B depending on the relative gate width ζ for the standard sluice gate with $a = 0.1$ and $h_0 = 0.4$

8.1.3 3D Gate Pressure Distribution

Since the corner vortices are formed and located in the corners between the sluice gate and the side walls, they also influence the pressure distribution on the sluice gate. Figure 112 a) shows the pressure contour plot for different relative gate widths ζ. For relative gate widths $\zeta \geq 0.5$, it can be seen, that the gate pressure is reduced near the side walls. This reduction occurs in the area of the corner vortices which are shown in Figure 112 b), using streamlines. Also shown in Figure 112 b) is the pressure contour plot. The pressure reduction coincides with the location of the corner vortices and can be explained by the higher velocities and hence an increase in dynamic pressure at the vortices. For relative gate widths $\zeta < 0.5$, the pressure is more uniform along the width, because the gate pressure is influenced by the corner vortices over the entire width.

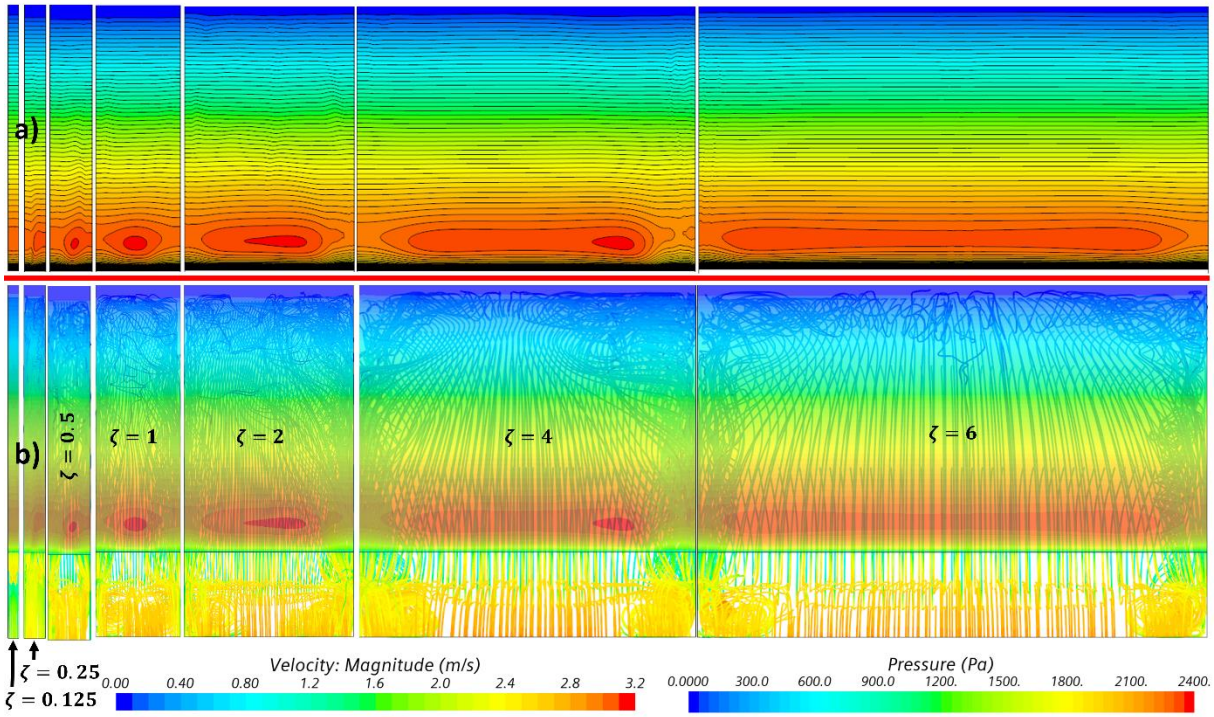

Figure 112: a) Gate pressure contour plot and b) gate pressure contour plot with streamlines for different relative gate widths ζ

However, the parameterization of the pressure distribution derived in the previous sections is compared with the CFD pressure distribution including 3D effects in Figure 113. For the dimensionless gate width $\zeta = 1$ (Figure 113 a)) and for $\zeta = 4$ (Figure 113 b)) the pressure distribution of the parameterization and the CFD simulations agree well in the middle part of the gate near $Y \approx 0.5$. At the sides, near $Y \approx 0$ and $Y \approx 1$, the pressure distribution from the parameterization does overestimate the actual 3D pressure distribution, because the parametrization does not take into account the dynamic pressure increases and hence the decreases in static pressure through the corner vortices. The middle part in which the pressure distributions from parameterization and CFD simulations coincide is larger for large relative gate widths ζ than for small relative gate widths, as in the case of the opening pressure distribution.

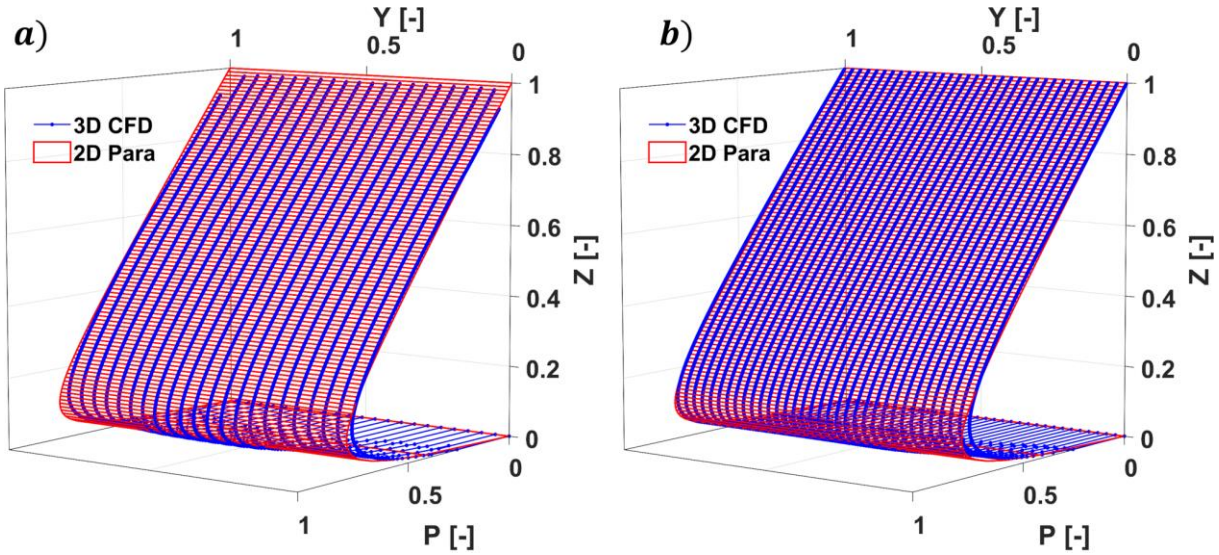

Figure 113: Comparison of gate pressure parameterization with 3D CFD pressure distribution for $\varepsilon = 0.25$ a) $\zeta = 1$ and b) $\zeta = 4$

Comparing the pressure integral of the gate pressure distribution for the 2D case with the 3D CFD simulations based on the nondimensionalized pressure force Π for different realtive gate widths ζ, see Figure 114, a very good agreement can be seen for large relative gate widths. From $\zeta \leq 2$, the nondimensionalized pressure force decreases slightly and then more and more. The decrease can be explained by the fact that for sluice gates with small channel widths the gate is influenced by the corner vortices over the entire width and thus the pressure decreases.

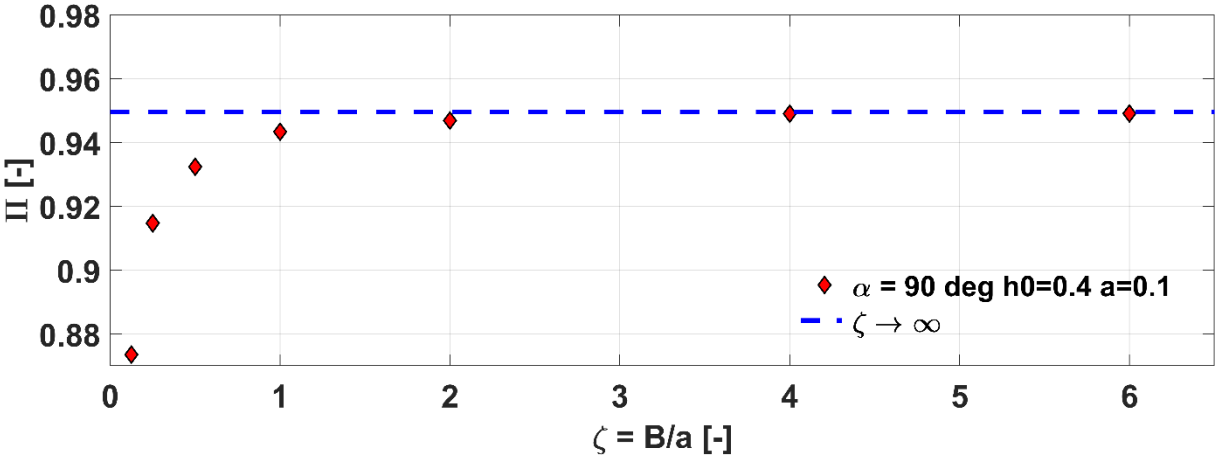

Figure 114: Dimensionless gate force Π depending on relative gate opening ζ for the standard sluice gate with $a = 0.1$ and $h_0 = 0.4$

8.2 3D Momentum Coefficient at the Opening

The momentum coefficient at the opening β_O describes the non-uniformity (deviation from block profile) of the velocity in x-direction. Due to the corner vortices, this non-uniformity, increases through the vortex cores. This is clearly visible in the velocity contour plot, see Figure 115. With decreasing relative gate width ζ the strength of the corner vortices decreases, but the relative area covered by the corner vortices increases. The boundary layer of the side walls has a further influence on the velocity field in the three-dimensional consideration and thus on the momentum coefficient. The influence of the boundary layer of the side walls on the momentum coefficient at the opening β_O becomes more and more important with decreasing relative gate opening ζ.

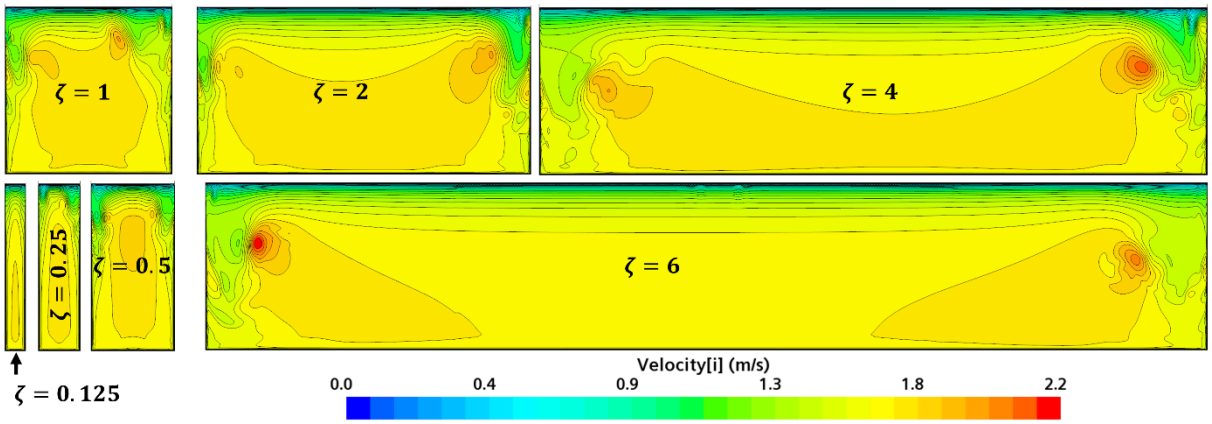

Figure 115: x-velocity contour plot at opening plane for different relative gate widths ζ

The momentum coefficient at the opening β_O determined from the velocity profile is shown in Figure 116. The momentum coefficient β_O is significantly larger for the 3D case than for the 2D case ($\zeta \to \infty$), but still small. Like the pressure integral at the opening F_O, the momentum coefficient deviates maximally from the 2D case at $\zeta = 0.5$. This is due to the same reasons as for the pressure integral at opening F_O. Since the corner vortices become weaker but affect a larger part of the area of the opening, the momentum coefficient increases evenly. For smaller relative gate widths $\zeta = 0.25$ the momentum coefficient decreases at first but increases again slightly due to the increasing influence of the side walls, see Figure 116 at $\zeta = 0.125$. The pressure integral at the opening, however, is not directly influenced by the boundary layer.

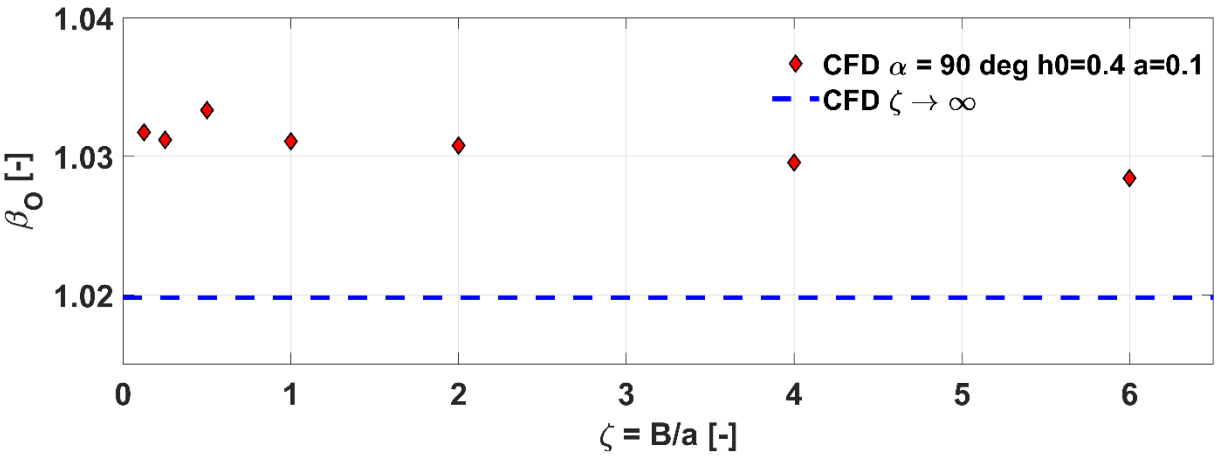

Figure 116: Momentum coefficient at opening β_O in dependency of relative gate width ζ for the standard sluice gate with $a = 0.1$ and $h_0 = 0.4$

8.3 Momentum Balance with 3D Effects

The calculation of the discharge using the integral momentum balance was carried out in chapter 7 for the 2D case, which theoretically corresponds to an infinitely wide sluice gate ($\zeta \rightarrow \infty$) and has also become a standard assumption in the literature. But as shown in the previous sections, the width of the channel has an influence on the pressure integrals at the opening F_O and at the gate F_G, as well as on the momentum coefficient at the opening β_O and thus also on the discharge Q. To show the dependence of the discharge on the channel width, the discharge coefficient $c_{D,dB}$, calculated from CFD, for various relative channel widths ζ is shown in Figure 117. The values shown here were again calculated for the standard sluice gate with $h_0 = 0.4$, $a = 0.1$ and $\varepsilon = 0.25$. For $\zeta \geq 2$ the discharge coefficient $c_{D,dB}$ shows no significant dependency on the relative channel width ζ, while for $\zeta < 2$ the discharge coefficient drops with decreasing ζ.

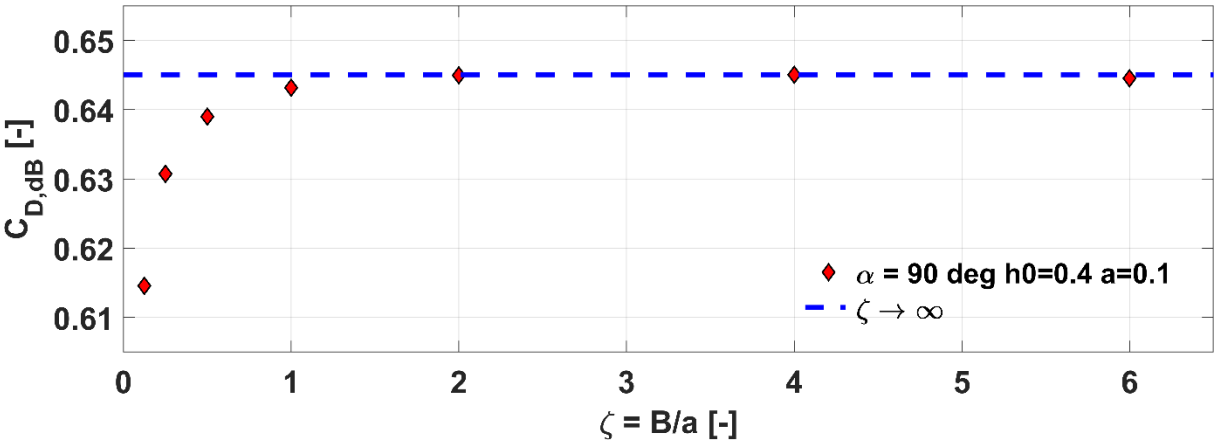

Figure 117: Discharge coefficient $c_{D,dB}$ in dependency of relative gate width ζ for the standard sluice gate with $a = 0.1$ and $h_0 = 0.4$

Using the forces and flux of momentum determined from the 3D CFD simulations, the integral momentum balance is now calculated using Eq. (3-9). In Table 12, the sum of the forces on the right hand side of Eq. (3-9) and the flux of momentum, on the left hand side of Eq. (3-9) are calculated for the different relative gate widths. Considering the case $\zeta \to \infty$ (2D case), it can be seen that the sum of the forces and the flux of momentum agree well and there is only a very small deviation of about 0.3 %. For the 3D cases studied, the deviations are much larger, and these deviations increase significantly with decreasing relative gate width ζ. These differences between the flux of momentum and the pressure forces are the viscous forces $\vec{F}_{viscous}$, that were neglected in the first approach, because they are low for large relative gate widths ζ as it can be seen for the 2D case ($\zeta \to \infty$) in Table 12.

Table 12: Flux of momentum, pressure forces and viscous forces for $a = 0.1$ m, $h_0 = 0.4$ m and $\varepsilon = 0.25$ from 3D CFD simulations for CV I

	Flux of Momentum	Pressure Forces	Viscous Forces
$\zeta = \frac{B}{a}$	$\frac{\beta_0 A_0 \bar{u}_0^2 - \beta_\emptyset A_\emptyset \bar{u}_\emptyset^2}{B}$	$\frac{F_\emptyset - F_G \cos(\alpha) - F_0}{B}$	$\frac{F_{viscous}}{B}$
∞	189.30	189.88	-0.58
6	190.65	194.61	-3.96
4	190.68	195.31	-4.63
2	191.21	196.69	-5.48
1	190.43	198.72	-8.29
0,5	188.29	204.87	-16.58
0,25	184.55	213.48	-28.92
0,125	176.87	232.71	-55.84

A graphical representation of the viscous forces $\vec{F}_{viscous}$ in dependency of the relative gate width ζ is shown in Figure 118. With increasing relative gate width ζ the viscous forces $\vec{F}_{viscous}$ relative to the channel width B are decreasing, as it can be seen in Figure 118, while for decreasing relative gate widths ζ the viscous forces are increasing rapidly. For 3D flows, the viscous forces are composed of the viscous forces of the two side walls and the bottom. Since the area of the side walls does not change with decreasing relative channel width ζ, the viscous forces on the side walls become dominant for small relative channel widths. A more detailed investigation of the viscous forces and the wall shear stress can be found in Appendix A.

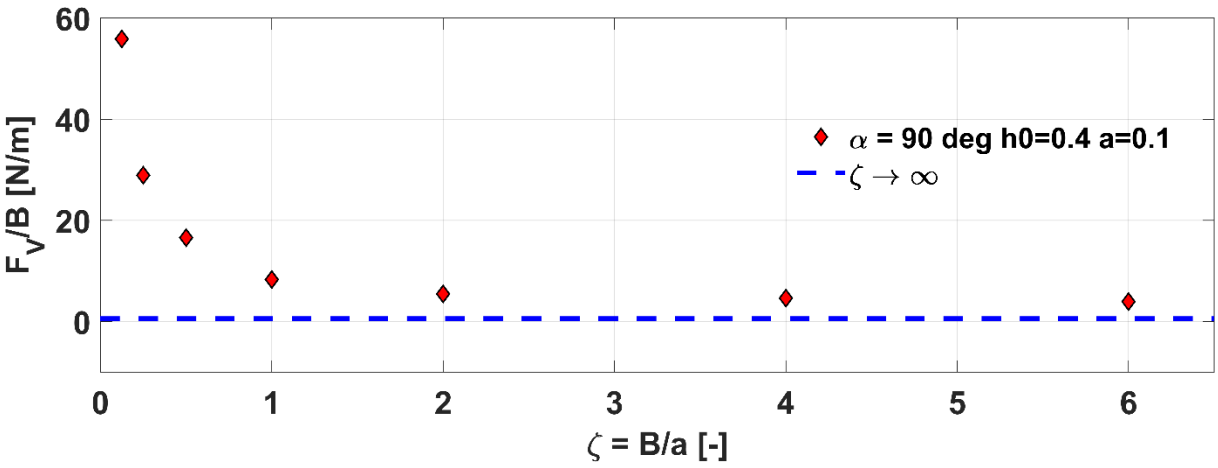

Figure 118: Normalized viscous forces in dependency of the relative gate width ζ for the standard sluice gate with $a = 0.1$ and $h_0 = 0.4$

To determine the exact discharge Q from the integral momentum balance, also when 3D effects are relevant, all the shown changes in forces and momentum coefficients must be considered by the integral momentum balance approach. The initially neglected viscous forces $\vec{F}_{viscous}$ must also be considered. To take these into account for practical applications, a 3D coefficient ϑ is therefore introduced which considers the aforementioned 3D influences. This 3D coefficient ϑ is defined in Eq. (8-1).

$$\vartheta = \frac{\beta_{O,\infty} - \frac{a}{h_0}}{\beta_{O,3D} - \frac{a}{h_0}} \left(\frac{F_{\emptyset} - F_{Gx,3D} - F_{O,3D} - F_{Viscous}}{F_{\emptyset} - F_{Gx,\infty} - F_{O,\infty}} \right) - 1 \tag{8-1}$$

Using the 3D coefficient ϑ from Eq. (8-1), the discharge Q, see Eq. (8-2), can be calculated precisely also for sluice gates with a small relative gate width ζ. The x-component of the pressure force on the sluice gate F_{Gx} appearing in Eq. (8-2) can be calculated using Eq. (5-53), the opening pressure force F_O can be determined using Eq. (5-30) and the momentum coefficient at the opening β_O is determined using Eq. (6-8). The 3D coefficient ϑ depends on the relative gate width ζ and it must consider for the case $\zeta \to \infty$ that $\vartheta = 0$. For this case then, Eq. (8-2) reduces to Eq. (3-15).

$$Q = \sqrt{\frac{\left(F_{\emptyset} - F_{G,x} - F_O\right)(1 + \vartheta)}{\frac{\rho}{B}\left(\frac{\beta_O}{a} - \frac{\beta_{\emptyset}}{h_0}\right)}} \tag{8-2}$$

In order to determine the 3D coefficient, it is first determined for the investigated relative gate widths using Eq. (8-1) from the values calculated in the CFD simulations. These are shown in Figure 119. For $\zeta \geq 2$ the 3D coefficent is $\vartheta \approx 0$, since the relative channel width

ζ has no significant influence on the discharge, see Figure 117. For $\zeta < 2$ the 3D coefficient decreases significantly with decreasing relative gate width ζ.

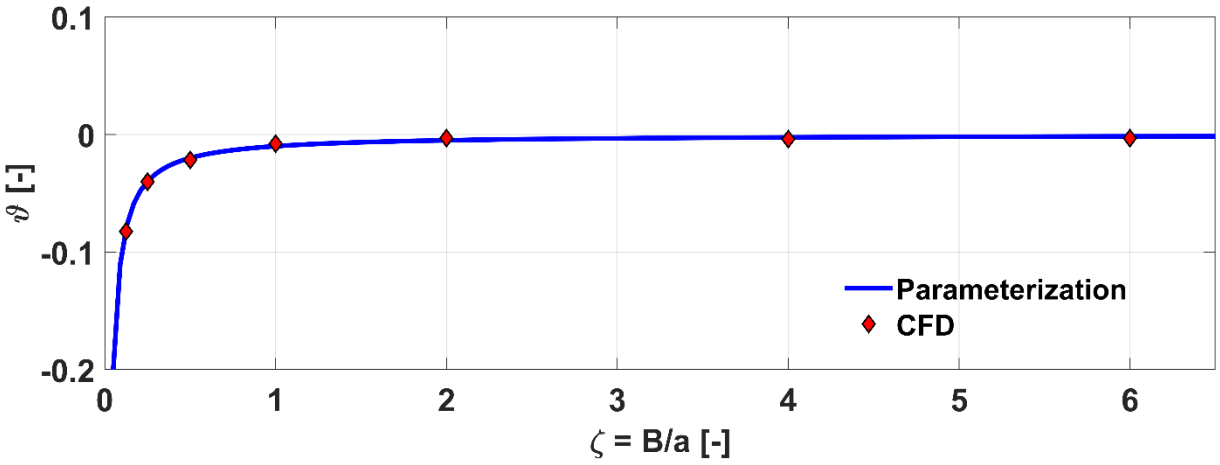

Figure 119: 3D coefficient ϑ in dependency of relative gate width ζ for the standard sluice gate with $a = 0.1$ and $h_0 = 0.4$

The function shown in Eq. (8-3) can be used to parameterize the 3D coefficient:

$$\vartheta(\zeta) = -\frac{k_\vartheta}{\zeta} \tag{8-3}$$

For the investigated standard sluice gate with $h_0 = 0.4$, $a = 0.1$ and $\varepsilon = 0.25$, the 3D coefficient was determined using the non-linear least square method with $k_{\vartheta,\varepsilon=0.25} = 0.01026 \approx 0.01$. For $k_{\vartheta,\varepsilon=0.25} = 0.01$, the errors were calculated with $SSE = 1.598 \cdot 10^{-5}$ and $RMSE = 1.632 \cdot 10^{-3}$. A graphical comparison of the CFD calculated 3D coefficient and the 3D coefficient from the new parameterization can be seen in Figure 119. The plot was validated only for relative channel widths of $\zeta \geq 0.125$. In practice, such small values are not relevant anyway. These were only shown for academic reasons and for the sake of completeness.

With Eq. (8-3) the discharge can now be calculated in dependency of the relative gate width ζ using Eq. (8-2). The specific discharge $q = Q/B$ calculated with the momentum balance in dependence of the relative channel width ζ is shown in Figure 120. Also shown in Figure 120 is the specific discharge q calculated in the CFD simulations. The values generally agree very well, although a minimally larger specific discharge was calculated in the CFD.

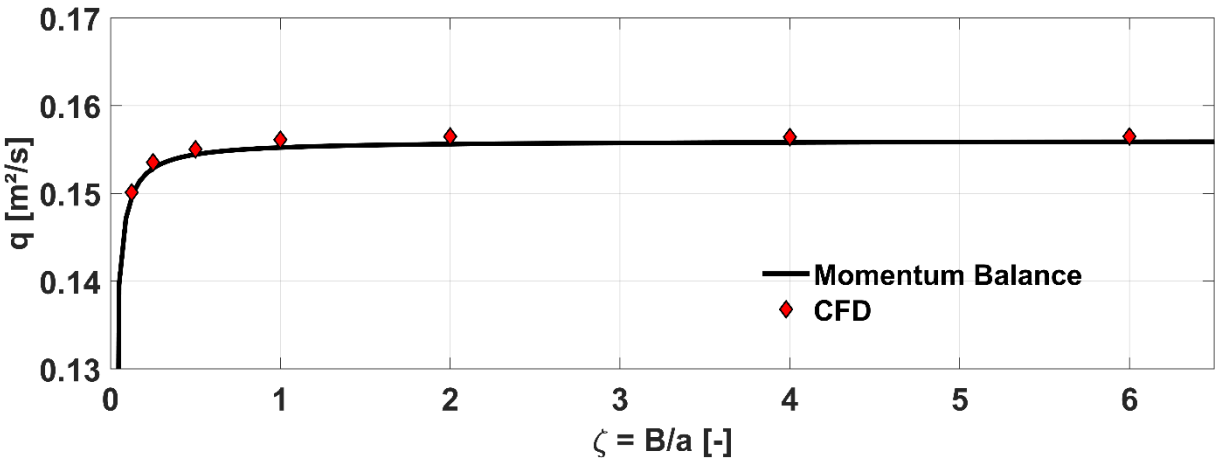

Figure 120: Specific discharge q from CFD and Momentum Balance in dependency of relative gate width ζ for the standard sluice gate with $a = 0.1$ and $h_0 = 0.4$

Looking at the discharge coefficient $c_{D,dB}$, shown in Figure 121, the momentum balance and CFD values also agree very well. As with the specific discharge q, the discharge coefficient calculated by momentum balance is somewhat smaller than that calculated by CFD.

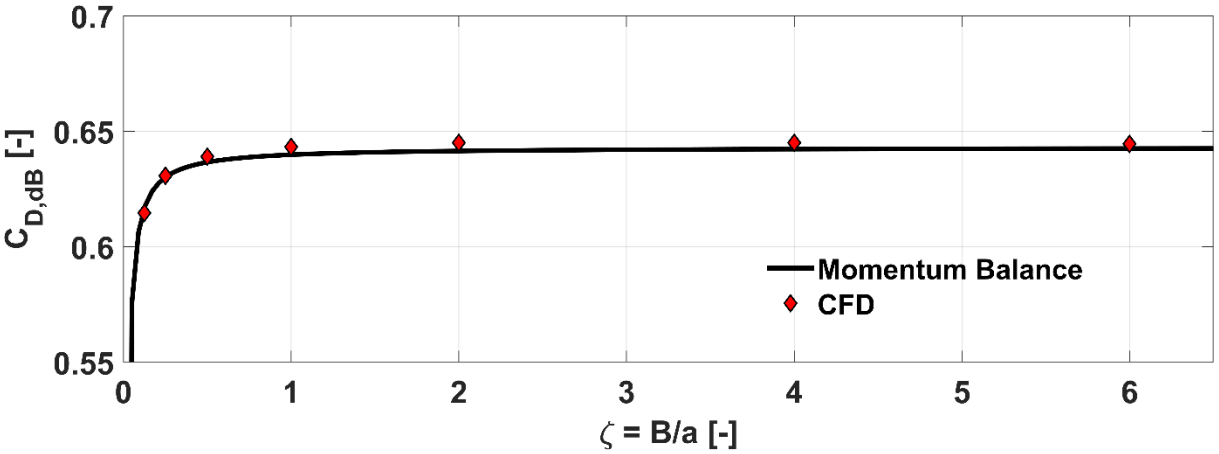

Figure 121: Discharge coefficient $c_{D,dB}$ from CFD and Momentum Balance in dependency of relative gate width ζ for the standard sluice gate with $a = 0.1$ and $h_0 = 0.4$

As shown in the example, the momentum balance can be further modified, e.g. to take into account 3D effects in sluice gates with a small relative channel width ζ. It is also possible to consider scaling effects and other influencing factors in the momentum balance.

9 Summary

In this work, the calculation of the discharge for standard and inclined sluice gates based on the conservation of mass and momentum was worked out. The approach was first worked out for an infinitely wide sluice gate i.e. the 2D case. This 2D approach has become established and is also used as standard in the literature, since it is suitable for most practical applications. To determine the pressure forces required for the momentum balance, the pressure distributions at the bottom, at the opening and at the gate were first parameterized based on CFD simulations. The parameterization was carried out for both the standard and the inclined sluice gate, i.e., the respective pressure distributions can be calculated as a function of the angle of inclination α. Previous work, on the other hand, has only dealt with the standard sluice gate. In addition, the dependence on the relative gate opening ε was always considered in the new approaches. The new parameterization approaches can be found in the following equations:

- Bottom pressure at opening P_{BO}: Eq. (5-9).
- Upstream bottom pressure P_{BU}: Eq. (5-18)
- Opening pressure distribution P_O: Eq. (5-27)
- Gate pressure distribution P_G: Eq. (5-45)

By integrating the parameterized pressure distributions, it was then possible to derive formulas for calculating the pressure forces at the gate and at the opening. These formulas are valid for both the standard sluice gate and the inclined sluice gate, while the previous approaches were limited to the standard sluice gate. The equations are listed below:

- Opening pressure force F_O: Eq. (5-30)
- Gate pressure force F_{Gx}: Eq. (5-53)

The course of the momentum coefficient was also analyzed in this work and a parameterization of the momentum coefficient at the opening was performed. The parameterization formula for the momentum coefficient at the opening β_O can be found in Eq. (6-8).

With the equations above, the discharge Q can be calculated using the momentum balance Eq. (3-15) for CV I, shown in Figure 27. The results were presented as a function of the relative gate openings ε and the angles of inclination α. The discharge calculated by Eq. (3-15) could be confirmed with relevant literature values.

It was also shown, how the momentum balance can be extended to include 3D effects, whereby also sluice gates with small width can be calculated. For this purpose, DES simulations were performed in CFD and the influence of the 3D effects on the pressure distributions, pressure forces and momentum coefficient were shown. Previous work has always assumed the pressure distribution to be constant along the width. In this work, however, it was shown that significant deviations can be observed, especially around the corner vortices. In addition, the pressure forces and the momentum coefficients also depend on the channel width. Based on an example case, the influence of 3D effects on the sluice gate discharge was shown in detail. In addition, the influence of 3D effects on the gate pressure distribution, the gate pressure force, the opening pressure distribution, the opening pressure force and on the opening momentum coefficient was shown.

The approach can be extended to include other factors such as scaling effects, other designs, and submerged flows. By making appropriate adjustments to the parameterization formula for the pressure distributions and the momentum coefficient, all these effects can be captured with the integral momentum balance approach.

In addition, a formula for calculating the maximum momentum coefficient $\beta_{max,90°}$ (Eq. (6-4)) for the vertical sluice gate was developed, with which the maximum momentum coefficient immediately in front of the opening can be calculated as a function of the relative gate opening ε. Furthermore, the course of the momentum coefficient in front and behind the sluice gate was analyzed for different angles of inclination α and relative gate openings ε.

Moreover, the detailed 3D simulations showed the influence of the gate width B on the vortex structures. It was shown that the corner vortices interact more strongly for small than for large relative gate widths ζ. Thus, for the first time, the influence of the corner voritces on the pressure distributions at the sluice gate and at the opening can be shown in dependency of the relative gate width ζ. Likewise, the 3D velocity profile at the opening was shown and analyzed in dependency of the relative gate width ζ. A dependence of the viscous forces on the side walls and the bottom wall in an area around the sluice gate as a function of the relative gate width ζ was also shown and the influence of the corner vortices on the wall shear stress was shown and analyzed.

With the momentum balance approach shown in this work, the discharge of standard and inclined sluice gates can be calculated accurately and fast. The discharge can be determined, for example, with the MATLAB program shown on p. 115, without interpolating discharge coefficients from graphs, which not only brings the described advantages from an academic point of view, but also a practical time saving for engineers. In the future, this approach can be extended for the submerged sluice gate and other sluice gate designs, such as those shown in chapter 2.1.3. Likewise, from the knowledge gained in this work, it can be said with a fair degree of certainty that the integral momentum balance can also be used to accurately calculate other hydraulic structures such as weirs, which is also a topic for future research. For other fluid mechanics problems such as the outflow of vessels [77] or the calculation of sudden contractions and sudden expansions [78], great progress has recently been made with the integral momentum balance. For the future, it is also conceivable that the integral momentum balance approach will be applied for more and more fluid mechanic problems. A possible example could be the calculation of the lift of airfoils in aerodynamics.

APPENDIX A: 3D Shear Stress and Shear Force

In this appendix, the shear forces, and stresses of the side and bottom walls, of a sluice gate with geometric dimensions $a = 0.1$ m, $h_0 = 0.4$ m and $\alpha = 90°$ are analyzed for different relative gate widths from $\zeta = 0.125$ to $\zeta = 6$ based on CFD simulations. The investigations were carried out in the range of the dimensionless x-coordinate from $X = -10$ to $X = 3$. The viscous forces at the bottom relative to the channel width B are shown below in Figure 122. For the relative gate widths $\zeta = 1$ and $\zeta = 2$, the normalized bottom shear force $F_{V,B}/B$ is largest and decreases slightly with increasing ζ. For relative gate widths $\zeta < 1$, the normalized bottom shear force $F_{Vs,B}/B$ drops suddenly, although in terms of magnitude the decrease is moderate. To explain this behavior, the wall shear stress magnitude at the bottom of the channel was plotted on a contour plot in Figure 123.

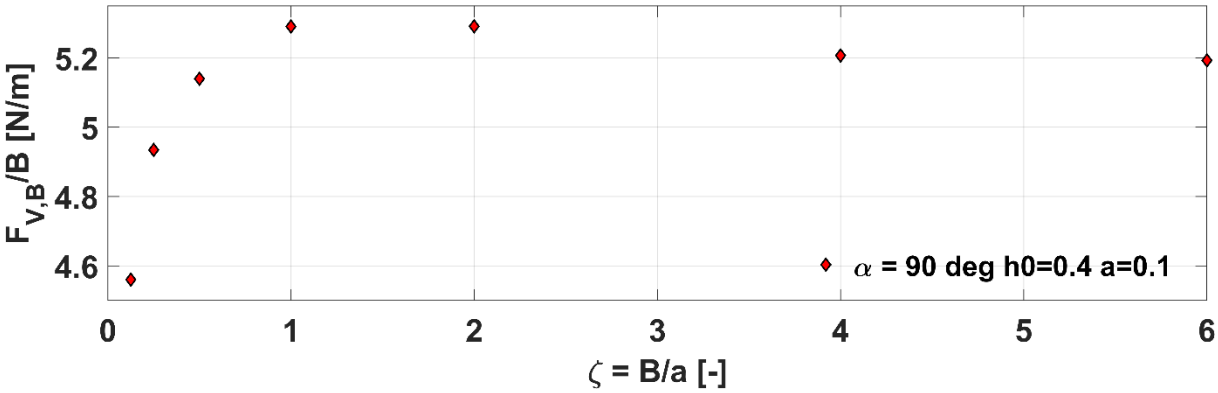

Figure 122: Normalized bottom shear force in dependency of the relative gate width for the standard sluice gate with $a = 0.1$ and $h_0 = 0.4$ between $X = -10$ and $X = 3$

Upstream ($X < 0$), the wall shear stress profile is similar for all investigated relative gate widths ζ, whereas downstream, significant differences are evident in the sidewall area. These differences are due to the corner vortices, which are shown in Figure 124 together with the bottom and sidewall wall shear stress. For $\zeta \geq 1$ large values of wall shear stress can be seen around the corner vortices. The shear forces at the bottom $F_{V,B}$ correspond to the integral of the wall shear stress over the bottom surface. As the relative gate width ζ increases, the area influenced by the corner vortices with large wall shear stress values becomes smaller, the shear force also gradually decreases. For $\zeta < 1$, the wall shear stress is not so strongly influenced by the corner vortices, which means that the maximum values of the wall shear stress are smaller for these relative gate widths, see Figure 123. As a result, the shear force $F_{V,B}$, as shown in Figure 122, also becomes smaller with decreasing relative gate width ζ.

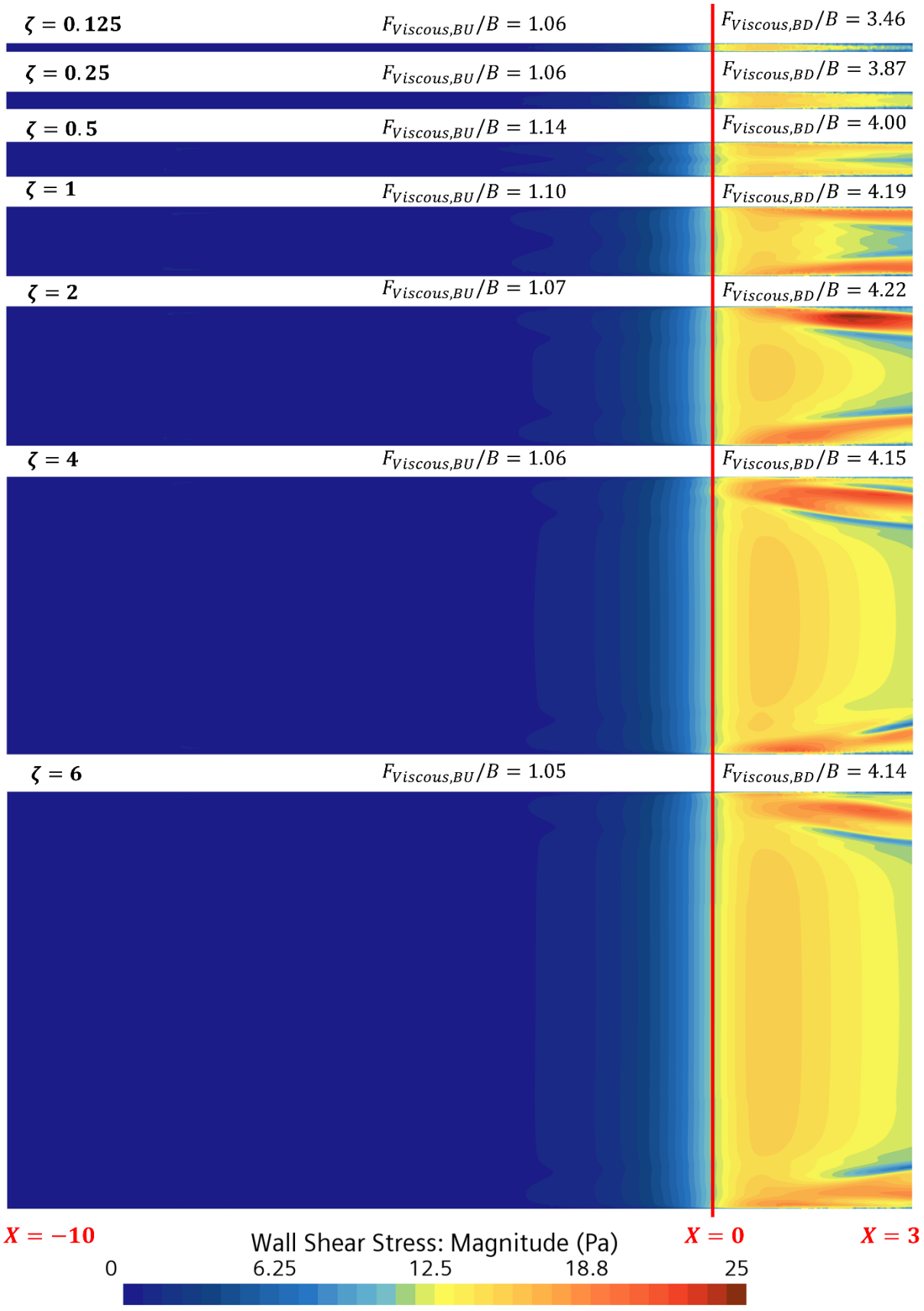

Figure 123: Bottom wall shear stress contour plot for different relative gate widths ζ

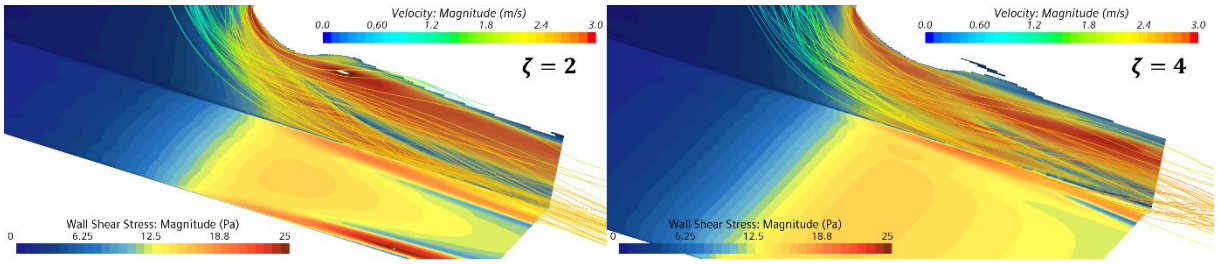

Figure 124: Streamlines and wall shear stress at the bottom and sidewall to demonstrate the influence of corner vortices on wall shear stress

The shear forces of the two sidewalls $F_{V,SW}$ are shown in Figure 125. The shear forces of the side walls generally increase with decreasing ζ. Influenced mainly by the transient corner vortices and other 3D effects, the values of the right and left sidewall shear forces fluctuate, which explains the small differences between the left and right sidewalls despite the same relative gate width ζ. Since the area of the side walls does not change with the channel width B, the shear force of the side walls was not normalized in the figure.

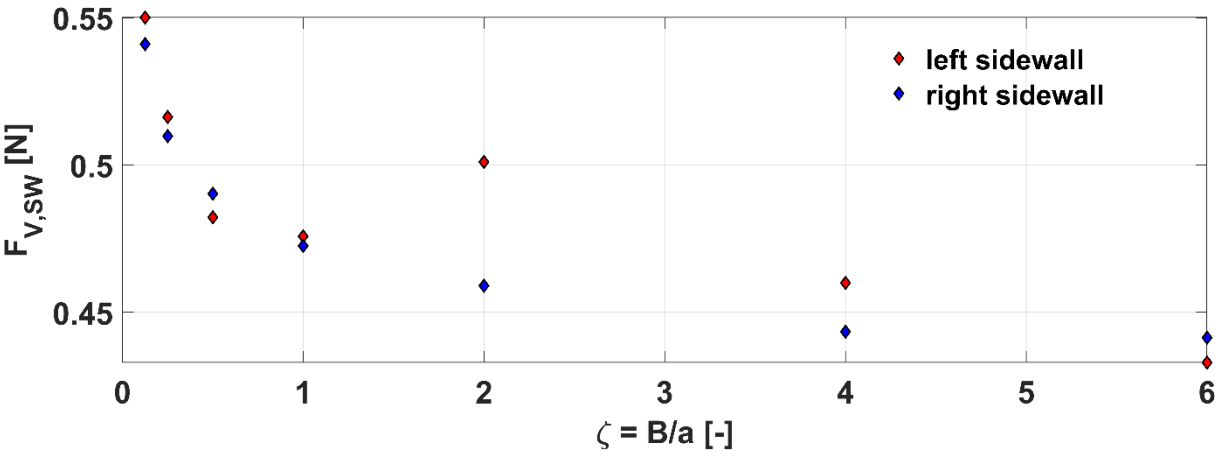

Figure 125: Side wall shear force in dependency of the relative gate width for the standard sluice gate with $a = 0.1$ and $h_0 = 0.4$ between $X = -10$ and $X = 3$

Figure 126 shows the shear stress contour plot of the sidewalls for the different relative gate widths ζ investigated. As with the wall shear stress at the bottom, it can be seen that in the downstream area, the corner vortices have an influence on the side wall shear stress, which can also be seen in Figure 124. For small relative gate widths ζ this influence becomes smaller. If we look at the values of the downstream shear force $F_{V,SWD}$, we see that for small relative gate widths ζ, the influences of the corner vortices on the viscous forces $F_{V,SWD}$ are smaller than for large relative gate widths ζ. These fluctuations tend to contradict the course of the viscous force $F_{V,SW}$ on the side wall shown in Figure 125. In terms of magnitude, however, these deviations from $F_{V,SWD}$ are relatively small and are overlaid by the larger deviations of the viscous forces

in the upstream region $F_{V,SWU}$. These are larger for small relative gate widths ζ and decrease with increasing relative gate with ζ.

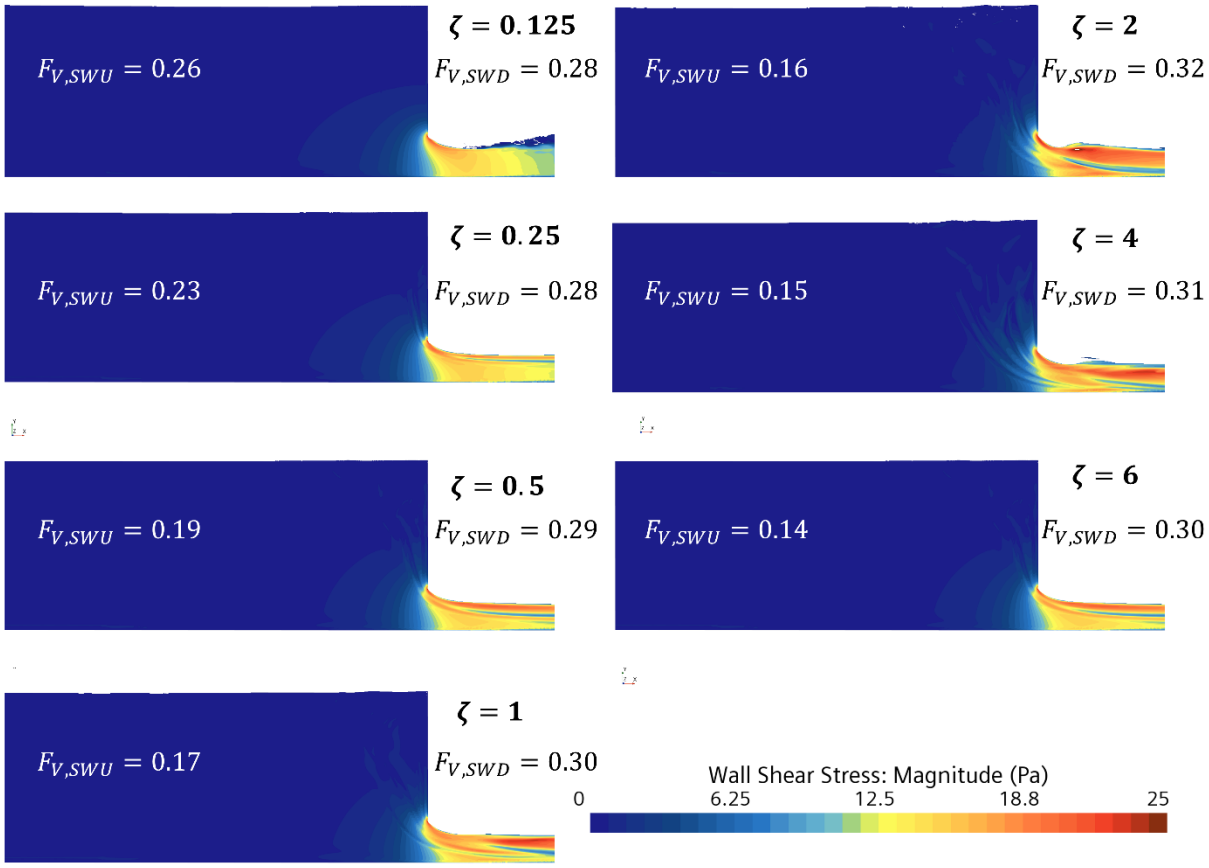

Figure 126: Side wall shear stress contour plot for different relative gate widths ζ

Since this behavior is not evident from the curves shown in Figure 126, the wall shear stress contour plot of the upstream region in the range between 0 Pa and 2 Pa is shown again in Figure 127 as an exemplary case for $\zeta = 0.125$ and $\zeta = 4$. Figure 127 shows that for $\zeta = 0.125$ the wall shear stress is greater in the area far upstream of the gate opening than at $\zeta = 4$. Although the wall shear stress is locally increased near the gate opening due to the corner vortices for $\zeta = 4$, since the viscous forces represent the integral over the surface and the surface influenced by the corner vortices in the upstream region is relatively small, the sum of the viscous forces is also greater for small relative gate widths ζ.

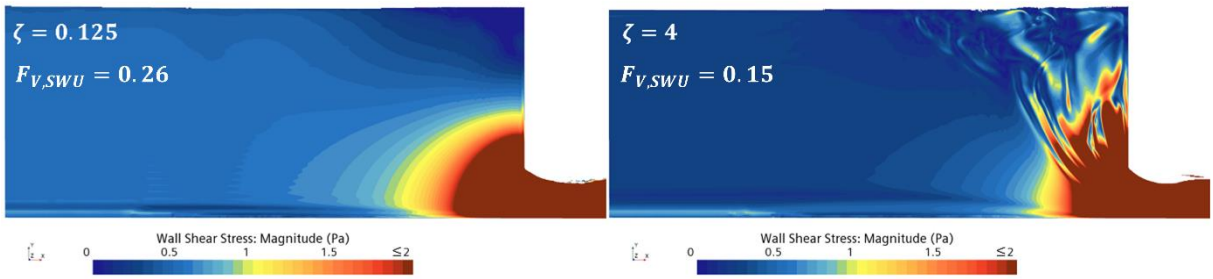

Figure 127: Upstream side wall shear stress contour plot (small pressure range)

Figure 128 shows the normalized shear force of the bottom and the normalized shear force of the sidewalls, as well as the sum of the total shear force as a function of the relative gate width ζ. It is clearly visible that for small relative gate widths ζ, the proportion of the shear force of the sidewalls assumes a large proportion of the total forces. For $\zeta = 2$, the shear forces of the sidewalls and the bottom are approximately equal, while for $\zeta > 2$, the proportion of the bottom on the total force is greater than that of the sidewalls.

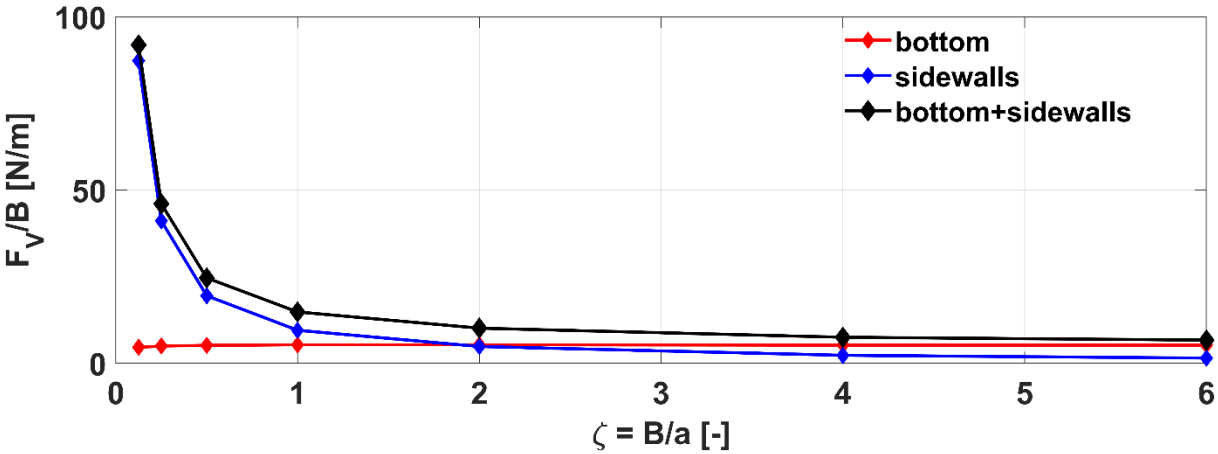

Figure 128: Normalized bottom shear force and side wall shear force in dependency of the relative gate width for the standard sluice gate with $a = 0.1$ and $h_0 = 0.4$ between $X = -10$ and $X = 3$

This analysis on the wall shear stress of sluice gates is limited to the investigated case $a = 0.1$ m, $h_0 = 0.4$ m and $\alpha = 90°$ and valid in the range between $X = -10$ to $X = 3$. For other cases and ranges of X, the values may shift somewhat, but these were not investigated, as the investigation of wall shear stress is not the main subject of this research work. Nevertheless, the analysis gives an impression of how the viscous forces of the side walls and the bottom change depending on the relative gate width ζ and how the corner vortices influence the wall shear stress.

APPENDIX B: Fitting Error Calculation - SSE and RMSE

For the quantitative evaluation of a model function, the sum of squared errors (SSE) and the root mean squared error (RMSE) were used in this work. These sum of squared errors (SSE) and the root mean squared error (RMSE) are introduced in the following and an example is shown, how the SSE and the RMSE is calculated.

The sum of squared errors (SSE) is defined in Eq. (B-1) [79].

$$\mathrm{SSE} = \sum_{i=1}^{n} (y_i - \hat{y}_i)^2 \tag{B-1}$$

Where y_i it the i^{th} value of the variable to be modeled and $\hat{y}_i$ is the predicted value of y_i from the model equation. A small value of the SSE means that the deviations of the model from the data to be modeled are small. This means that the smaller the SSE the better the model is suited to model the data set.

The mean squared error (MSE) is defined as the sum of squared errors divided by the residual degree of freedom v and is shown in Eq. (B-2) [79].

$$\mathrm{MSE} = \frac{\mathrm{SSE}}{v} \tag{B-2}$$

Where the residual degrees of freedom v is equal to the number of data points n minus the number of coefficients of the model equation m, see Eq. (B-3).

$$v = n - m \tag{B-3}$$

From the mean squared error (MSE) the root mean squared error (RMSE) can be determined as shown in Eq. (B-4).

$$\mathrm{RMSE} = \sqrt{\mathrm{MSE}} = \sqrt{\frac{\mathrm{SSE}}{v}} \tag{B-4}$$

The RMSE can also be referred to as the standard error of the fit and is an estimate of the standard deviation of the random component in the data. As with the SSE, the closer the value of the MSE or RMSE is to zero, the better is the model function suited to predict the data [79]. In the following, an example for the calculation of the sum of squared errors and the root mean squared error is shown.

Example

The following example is based on the parameterization of the coefficient for the opening pressure distribution k_O by using Eq. (5-26) and is intended to show the calculation of the RMSE and the SSE. The parameter k_O shall be modeled by Eq. (5-26). The numerical values of the parameter k_O to be modeled for the different relative gate openings are shown in Table 13. A graphical representation of the parameter k_O to be modeled can be seen in Figure 129 (red diamonds).

$$k_O(\varepsilon) = k_O^* \left(1 - \left(\frac{1}{\varepsilon}\right)^{k_O^*}\right) \tag{5-26}$$

The constant k_O^* occurring in Eq. (5-26) was determined using the non-linear least square method, as $k_O^* = -0.6172$, based on the data of k_O shown in Table 13. Using Eq. (5-26), $k_O(\varepsilon)$ can now be determined. This is also shown in Table 13 as well as in Figure 129.

Table 13: Example of error calculation using the opening pressure distribution parameter k_O

i	$1/\varepsilon$	k_O	$k_O(\varepsilon)$ from Eq. (5-26)	$\left(k_0 - k_0(\varepsilon)\right)^2$
1	2	-0.209288695	-0.21483	$3.06587 \cdot 10^{-5}$
2	3	-0.295136018	-0.30391	$7.69809 \cdot 10^{-5}$
3	4	-0.348206835	-0.35488	$4.45062 \cdot 10^{-5}$
4	5	-0.385784606	-0.38863	$8.08907 \cdot 10^{-6}$
5	6	-0.411376119	-0.41296	$2.49356 \cdot 10^{-6}$
6	7	-0.43154402	-0.43149	$2.74157 \cdot 10^{-9}$
7	8	-0.447213047	-0.44618	$1.06059 \cdot 10^{-6}$
8	10	-0.470386347	-0.46819	$4.83978 \cdot 10^{-6}$
9	12	-0.493222143	-0.48405	$8.42074 \cdot 10^{-5}$
10	14	-0.498733646	-0.49613	$6.77774 \cdot 10^{-6}$
11	16	-0.509081743	-0.50571	$1.13810 \cdot 10^{-5}$
12	18	-0.515612463	-0.51353	$4.35519 \cdot 10^{-6}$
13	20	-0.519191321	-0.52005	$7.42178 \cdot 10^{-7}$

From the values for k_0 and $k_0(\varepsilon)$ in Table 13, the squared error is now calculated for each row using the formula $\left(k_0 - k_0(\varepsilon)\right)^2$. The squared error is also shown in Table 13. The sum of squared erros can be calculated by adding up the 13 rows as follows:

$$\mathrm{SSE} = \sum_{i=1}^{n=13} \left(k_0 - k_0(\varepsilon)\right)^2 = 2.761 \cdot 10^{-4}$$

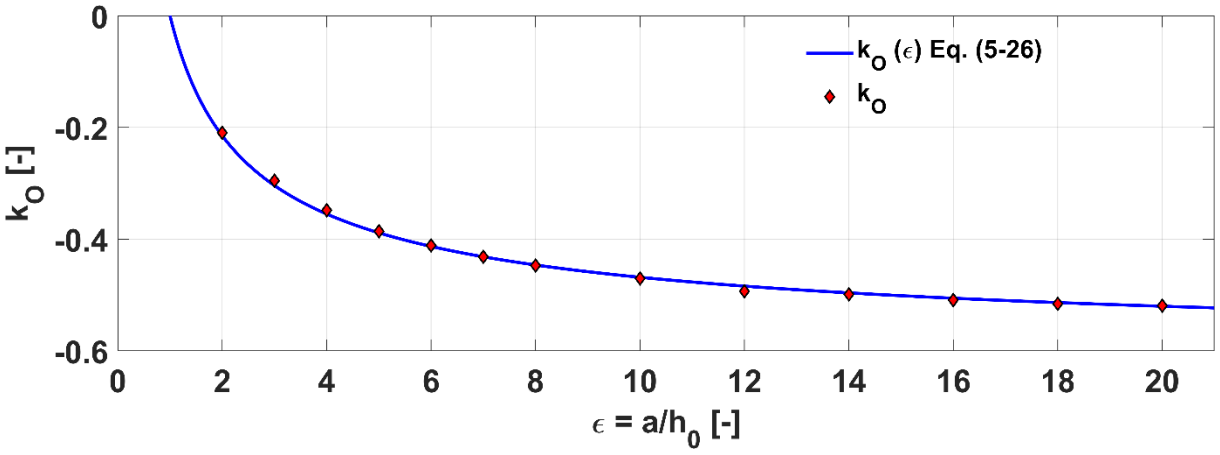

Figure 129: Parameter k_O and model function $k_O(\varepsilon)$ with $k_O^* = -0.6172$

To calculate the root mean squared error (RMSE), the residual degrees of freedom v must first be determined. This is the difference of the number of data points $n = 13$ minus the number of coefficients of the model equation $m = 1$ (one parameter k_O^* in the model equation).

$$v = n - m = 13 - 1 = 12$$

The root mean squared error RMSE can then be determined from the sum of squared error SSE and the residual degrees of freedom v as follows:

$$RMSE = \sqrt{\frac{SSE}{v}} = \sqrt{\frac{2.761 \cdot 10^{-4}}{12}} = 4.797 \cdot 10^{-3} \tag{B-5}$$

Figure 130 also shows the SSE and RMSE for other values of the constant k_O^*. It is obvious that the SSE and RMSE are smallest for $k_O^* = -0.6172$, which was ensured by non-linear least square method.

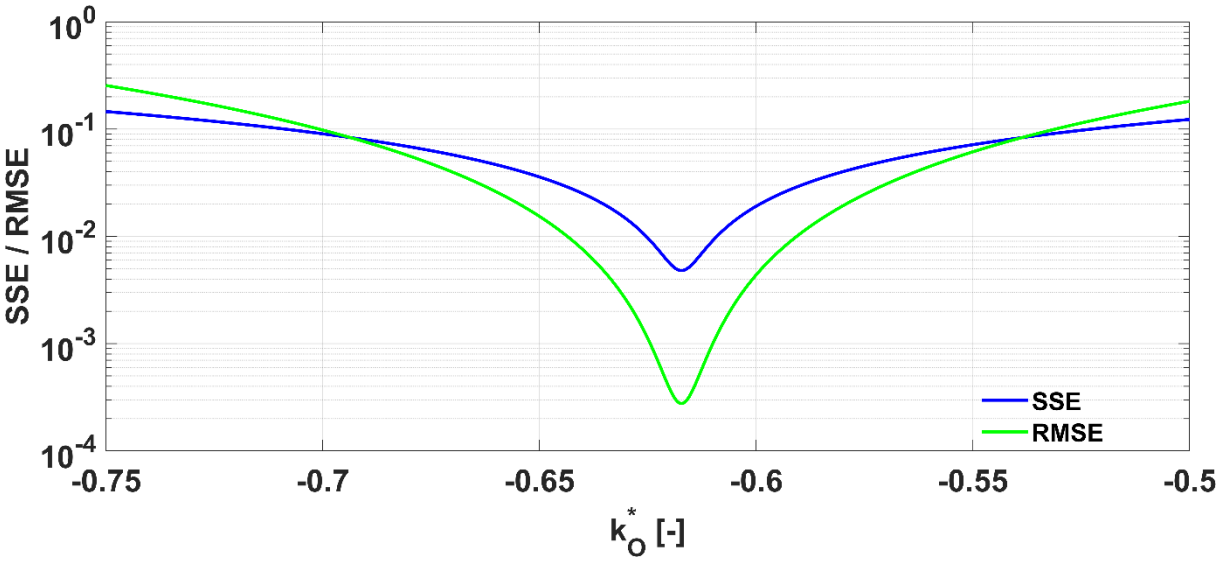

Figure 130: Sum of squared errors and root mean squared error for different values of k_O^*

Figure 131 also shows the model equation (Eq. (5-26)) graphically for the values $k_O^* = 0.6$ and $k_O^* = 0.65$, where for $k_O^* = 0.6$ the errors $SSE = 4.3756 \cdot 10^{-3}$ and $RMSE = 1.9095 \cdot 10^{-2}$ were calculated and for $k_O^* = 0.65$ the errors $SSE = 1.5372 \cdot 10^{-2}$ and $RMSE = 3{,}5791 \cdot 10^{-2}$ were calculated. Comparing the curves of the model function with different constants k_O^* with the data k_O to be parameterized in Figure 131, it is clear that the model function with $k_O^* = -0.65$ shows the largest deviations from the data. Figure 124 also shows that the best agreement is obtained with $k_O^* = -0.6172$, where the errors are also the smallest.

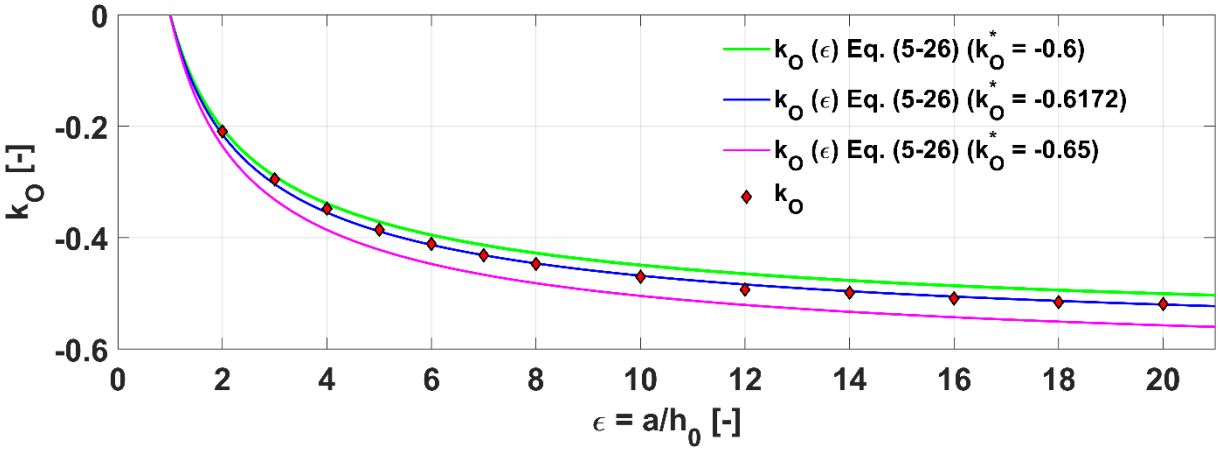

Figure 131: Model function $k_O(\varepsilon)$ (Eq. (5-26)) for different fitting constants k_O^*

List of Figures

List of Tables

Bibliography

[1] A. Malcherek, Fließgewässer - Hydraulik, Hydrologie, Morphologie und Wasserbau, Berlin: Springer-Verlag, 2019.

[2] P. Epple, H. Babinsky, M. Steppert und M. Fritsche, „On How the Generation of Lift Can Be Explained in a Closed Form Based on the Fundamental Conservation Equations," Proceedings of the ASME 2020 Fluids Engineering Division Summer Meeting, pp. FEDSM2020-20261, 13-15 7 2020.

[3] H. Rouse, Elementary Mechanics of Fluids, New York: Dover Publications, Inc., 1946.

[4] K. Subramanya, Flow in Open Channels, New Delhi: Tata McGraw-Hill Publishing Company Limited, 2009.

[5] E. Naudascher, Hydraulik der Gerinne und Gerinnebauwerke, Wien New-York: Springer-Verlag Wien, 1992.

[6] C. Keutner, „Wasserabführungsvermögen von scharfkantigen und abgerundeten Planschützen," in Die Bautechnik, Berlin, Ernst & Sohn Verlag für Architektur und technische wissenschaften GmbH & co., 1932, pp. 266-269.

[7] J. L. Weisbach, Die Experimental-Hydraulik, JG Engelhardt, 1855.

[8] K. R. Bornemann, „Über den Ausfluss bei Schützen und schützenartigen Mündungen," Der Civilingenieur 26, pp. 297-376, 1880.

[9] K. R. Bornemann, „Versuche über den Ausfluss unter Wasser bei Schützen," Der Civilingenieur 17, pp. 45-60, 1871.

[10] P. P. Boileau, Traité de la mésure des eaux courants ou expériences, observations et méthodes, Paris: Mallet-Bachelier, 1854.

[11] J. Weisbach, Ingenieur und Maschinen Mechanik - Vierte verbesserte und vervollständigte Auflage, Braunschweig: Friedrich Vieweg und Soh, 1862.

[12] A. Linnebrügge, „Wassermessung bei Schützenöffnungen unter Wasser," in Der Civilingenieur, Leipzig, Verlag von Arthur Felix, 1879, pp. 25-40.

[13] M. Rühlmann, Hydromechanik, Leipzig: Arnold'ische Buchhandlung, 1857.

[14] C. Fawer, Etude de Quelques Ecoulements Permanents a Filets Courbes, Lausanne: Imprimerie La Concorde, 1937.

[15] P. L. G. du Buat, Principes d'Hydraulique, Tome I., Paris: Imprimerie de Monsieur, 1786.

[16] H. Müller, „Rechnerische Ermittlung der Strömungsvorgänge an scharfkantigen Planschützen," Wasserkraft und Wasserwirtschaft 24. Heft 30. Jahrgang, pp. 281 - 284, 16 Dezember 1935.

[17] A. Kiczko und J. Kubrak , „Experimental and numerical investigation of non-submerged flow under a sluice gate," Annals of Warsaw University of Life Sciences – SGGW Land Reclamation No 47 (3), pp. 187-201, 2015.

[18] O. Silva und M. Rijo, „Flow Rate Measurements under Sluice Gates," Journal of Irrigation and Drainage Engineering / Volume 143 Issue 6, p. 06017001, June 2017.

[19] K. Y. Li, L. X. He, L. C. Qiu, J. Chen und Y. Han, „Experimental investigation of discharge characteristics of float type sluice gate," IOP Conference Series: Earth and Environmental Science, Volume 191, The 4th International Conference on Water Resource and Environment (WRE 2018), Kaohsiung City, Taiwan, 17-21 July 2018.

[20] U. Zanke, Hydraulik für den Wasserbau 3. Auflage, Berlin Heidelberg: Springer-Verlag Berlin Heidelberg, 2013.

[21] R. Freimann, Hydraulik für Bauingenieure - Grundlagen und Anwendungen, München: Carl Hanser Verlag, 2014.

[22] W. Werner, „Ableitung einer kinematischen Beziehung zur Berechnung des Durchflusses unter Planschützen nach der Theorie freier Stromlinien," Wissenschaftliche Zeitschrift der Technischen Universität Dresden 12 - Heft 6, pp. 1693-1699, 22 Juli 1963.

[23] H. Voigt, Abflußberechnung gleichzeitig über- und unterströmter Stauelemente, Dresden: Dissertation Technische Universität Dresden, 1971.

[24] B. Gentilini, „ECOULEMENTS SOUS LES VANNES DE FOND INCLINEES OU A SECTEUR - RESULTATS TECHNIQUES ET EXPERIMENTAUX," La Houille Blanche, pp. 145-149, MARS-AVRIL 1947.

[25] D. Aigner und H. B. Horlacher, „Optimum Design of Self-Regulating Spring Steel Throttles for Sewer Overflow Tanks," Managing Water: Coping with Scarcity and Abundance, 1997.

[26] P. K. Swamee, „Sluice-Gate Discharge Equations," Journal of Irrigation and Drainage Engineering, pp. 56-60, January 1992.

[27] H. R. Henry, „Discussion of Diffusion of submerged jets," Transactions of the American Society of Civil Engineers 115, pp. 687 - 694, 1950.

[28] A. Roth und W. H. Hager, „Underflow of standard sluice gate," Experiments in Fluids 27, pp. 339-350, 1999.

[29] N. Rajaratnam, „Free Flow Immediately Below Sluice Gates," Journal of the Hydraulics Division HY4, pp. 345-351, April 1977.

[30] D. Aigner und G. Bollrich, Handbuch der Hydraulik: für Wasserbau und Wasserwirtschaft, Berlin: Beuth Verlag GmbH, 2021.

[31] M. Steppert, P. Epple und A. Malcherek, „Impact of Flow Characteristics on the Pressure Distribution on Sluice Gates," Proceedings of the ASME 2021 - Fluids Engineering Division Summer Meeting, pp. 1-11, accepted.

[32] N. Rajaratnam und J. A. Humphries, „Free Flow Upstream of Vertical Sluice Gates," Journal of Hydraulic Research 20, pp. 427-437, 1982 no. 5.

[33] C. D. Harber und J. S. Gulliver, „Surface films in laboratory flumes," Journal of Hydraulic Research, Vol. 30, No. 6, pp. 801-815, 1992.

[34] L. Cassan und G. Belaud, „Experimental and numerical studies of the flow structure generated by a submerged sluice gate," Proceedings from First IAHR European Congress-Edinburgh, Scotland, May 2010.

[35] J. S. Montes, „Irrotational Flow and Real Fluid Effects Under Planar Sluice Gates," Journal of Hydraulic Engineering Vol. 123, No. 3, pp. 219-232, March 1997.

[36] H. von Helmholtz, „Über Integrale der hydrodynamischen Gleichungen, welche den Wirbelbewegungen entsprechen," Journal für die reine und angewandte Mathematik, pp. 25-55, 1858.

[37] W. F. Durand, Aerodynamic Theory - Volume I Mathematical Aids, Fluid Mechanics, Historical Sketch, New York: Dover Publications, Inc., 1934.

[38] H. Nago, „Symposium on Scale Effects in Modelling Hydraulic Structures," in Scale Effects in Free Efflux from an Underflow Gate, 1984, 1984.

[39] M. Steppert, P. Epple und A. Malcherek, „Sluice Gate Discharge From Momentum Balance," Journal of Fluids Engineering Vol. 144, pp. 041101-1 - 041101-17, April 2022.

[40] F. M. White, Fluid Mechanics, Seventh Edition, New York, NY: McGraw-Hill, 211.

[41] A. Malcherek, „A New Approach to Hydraulics Based on the Momentum Balance: Sharp Edged Outflows and Sluices," Proceedings of the 37th IAHR World Congress, pp. 1515 - 1521, August 2017.

[42] A. Malcherek, „Eine neue, auf der Impulsbilanz basierende Theorie zur Hydraulik des Schützes," Wasserwirtschaft 5, pp. 40-44, 2018.

[43] A. Malcherek und S. Müller, „The Application of the Integral Momentum Balance on the Pressure Drop of a Sudden Contraction," Journal of Fluids Engineering Vol. 143 / 011302-1, JANUARY 2021.

[44] Siemens Digital Industries Software, „Simcenter STAR-CCM+ Documentation Version 2022.1," Siemens, 2022.

[45] J. H. Ferziger und M. Peric, Numerische Strömungsmechanik, Berlin Heidelberg: Springer-Verlag, 2008.

[46] F. R. Menter, „Zonal two-equation k-ω turbulence model for aerodynamic flows," AIAA Paper 1993-2906, 1993.

[47] F. R. Menter, „Two-equation eddy-viscosity turbulence models for engineering applications," AIAA Journal 32 No. 8, pp. 269-289, August 1994.

[48] F. R. Menter, M. Kuntz und R. Langtry, „Ten Years of Industrial Experience with the SST Turbulence Model," Turbulence, Heat and Mass Transfer 4 Nr. 1, pp. 625-632, 2003.

[49] D. C. Wilcox, „Formulation of the k-ω Turbulence Model Revisited," AIAA Journal Vol. 46, No. 11, pp. 2823-2837, November 2008.

[50] W. P. Jones und B. E. Launder, „The Prediction of Laminarization with a Two-Equation Model of Turbulence," Int. J. Heat and Mass Transfer Vol. 15, pp. 301-314, 1972.

[51] T. -H. Shih, W. W. Liou, A. Shabbir, Z. Yang und J. Zhu, „A New k-ε Eddy Viscosity Model for High Reynolds Number Turbulent Flows-Model Development and Validation," NASA Technical Memorandum106721, August 1994.

[52] P. Spalart und S. Allmaras, „A one-equation turbulence model for aerodynamic flows," in AIAA 30th Aerospace Sciences Meeting and Exhibit, Reno, NV, USA, 1992.

[53] C. W. Hirt und B. D. Nichols, „Volume of Fluid (VOF) Method for the Dynamics of Free Boundaries," Journal of Computational Physics 39, pp. 201-225, 1981.

[54] D.-G. Kim, „Numerical Analysis of Free Flow Past a Sluice Gate," KSCE Journal of Civil Engineering Vol. 11, No. 2, pp. 127-132, March 2007.

[55] A. A. Oner, M. S. Akoz, M. S. Kirkgoz und V. Gumus, „Experimental Validation of Voume of Fluid Method for a Sluice Gate Flow," Advances in Mechanical Engineering Volume 2012, 2012.

[56] G. Wellein, „Emmy parallel cluster (Tier3)," Erlangen National High Performance Computing Center (NHR@FAU), [Online]. Available: https://hpc.fau.de/systems-services/systems-documentation-instructions/clusters/emmy-cluster/. [Zugriff am 05 04 2022].

[57] L. F. Richardson, „The Approximate Arithmetical Solution by Finite Differences of Physical Problems Involving Differential Equations, with an Application to the Stresses In a Masonry Dam," Transactions of the Royal Society of London, Series A, 210, pp. 307-357, 1910.

[58] L. F. Richardson und J. A. Gaunt, „The Deferred Approach to the Limit," Philosophical Transactions of the Royal Society of London, Series A, 226, pp. 299-361, 1927.

[59] F. Valentin, Einfluß des Unterwasserstandes auf die Strömungsverhältnisse beim Ausfluß unter einer Schütze, München: Institut für Hydraulik und Gewässerkunde Technische Hochschule München - Hrsg. Prof. Dr.-Ing P.-G. Franke, 1968.

[60] T. Y. Han und W. L. Chow, „The Study of Sluice Gate and Sharp-Crested Weir Through Hodograph Transformations," Journal of Applied Mechanics VOL. 48, pp. 229-238, June 1981.

[61] A. Koch und M. Carstanjen, Von der Bewegung des Wassers und den dabei auftretenden Kräften, Berlin: Verlag von Julius Springer, 1926.

[62] H. Kulka, Der Eisenwasserbau Band 1: Theorie und Konstruktion der beweglichen Wehre, Berlin: Verlag von Wilhelm Ernst & Sohn, 1928.

[63] G. Pajer, „Über den Strömungsvorgang an einer unterströmten scharfkantigen Planschütze," Zeitschrift für angewandte Mathematik und Mechanik - Band 17 Heft 5, pp. 259-269, Oktober 1937.

[64] A. Cheng, J. A. Liggett und P. L.-F. Liu, „Boundary Calculations of Sluice and Spillway Flows," Journal of the Hydraulics Division Vol. 107 - Issue 10, pp. 1163-1178, 1981.

[65] G. Belaud und X. Litrico, „Closed-form solution of the potential flow in a contracted flume," Journal of Fluid Mechanics, pp. 1-9, 2008.

[66] J. I. Finnie und R. W. Jeppson, „Solving Turbulent Flows Using Finite Elements," Journal of Hydraulic Engineering - Vol. 117, No. 11, pp. 1513-1530, November 1991.

[67] O. Castro-Orgaz und W. H. Hager, „Transitional flow at standard sluice gate," Journal of Hydraulic Research, 52:2, pp. 264-273, August 2014.

[68] K. Woycicki, Wassersprung, Deckwalze und Ausfluss unter einer Schütze, Warschau: Verlag der polnischen Akademie der technischen Wissenschaften, 1931.

[69] Dr. S., „Ausfluß aus Seitenöffnungen am Boden, die ganz oder teilweise unter Unterwasser liegen," Zentralblatt der Bauverwaltung 50. Jahrgang Nummer 31, p. 560, 6 August 1930.

[70] R. V. Southwell und G. Vaisey, „Relaxation Methods Applied to Engineering Problems XII. Fluid Motions Characterized by 'Free' Stream-Lines," Philosophical Transactions of the Royal Society A, pp. 117-161, 01 January 1946.

[71] T. B. Benjamin, „On the flow in channels when rigid obstacles are placed in the stream," Journal of Fluid Mechanics, Volume 1, Issue 2, pp. 227-248, July 1956.

[72] E. Naudascher, „Scale Effects in Gate Model Tests,“ Symposium on Scale Effects in Modelling Hydraulic Structures, 1985.

[73] D. Fangmeier und T. S. Strelkoff, „Solution for gravity flow under a sluice gate,“ Journal of the Engineering Mechanics Division Vol. 94 - Issue 1, pp. 153-176, 1968.

[74] A. Malcherek, „Hydraulik 21: Der Impulsbeiwert,“ 25 01 2016. [Online]. Available: https://www.youtube.com/watch?v=WJtSwRi14qM. [Zugriff am 26 04 2022].

[75] The MathWorks, Inc, „MATLAB R2020a“.

[76] A. V. Shivapur und M. N. Shesha Prakash, „Inclined Sluice Gate for Flow Measurement,“ ISH Journal of Hydraulic Engineering. Vol. 11. No. 1, 2005.

[77] A. Malcherek, „A General Outflow Theory Based on Momentum Balance,“ Journal of Fluids Engineering, Volume 144, Issue 1, pp. FE-20-1710, January 2022.

[78] S. Müller und A. Malcherek, „A Unified Theory for the Pressure Change of Sudden Expansions and Contractions Based on the Momentum Balance,“ Proceedings of the ASME 2021 Fluids Engineering Division Summer Meeting. Volume 2, pp. FEDSM2021-65703, 10-12 August 2021.

[79] The MathWorks, Inc., „MathWorks: Evaluating Goodness of Fit,“ 2022. [Online]. Available: https://www.mathworks.com/help/curvefit/evaluating-goodness-of-fit.html. [Zugriff am 20 10 22].